Chair of Mining Engineering and Mineral Economics

Doctoral Thesis

A Breakage Model for Discrete Element Simulations Applied to Iron Ore Sinter

Dipl.-Ing. Michael Alexander Denzel, BSc

March 2023

AFFIDAVIT

I declare on oath that I wrote this thesis independently, did not use other than the specified sources and aids, and did not otherwise use any unauthorized aids.

I declare that I have read, understood, and complied with the guidelines of the senate of the Montanuniversität Leoben for "Good Scientific Practice".

Furthermore, I declare that the electronic and printed version of the submitted thesis are identical, both, formally and with regard to content.

Date 07.03.2023

Signature Author
Michael Alexander Denzel

Bibliographic data

Title:	A Breakage Model for Discrete Element Simulations Applied to Iron Ore Sinter
Author:	Michael Denzel
Year:	2023
Place:	Leoben, Austria
Type:	Doctoral (PhD) Thesis / Dissertation, University of Leoben
Pages:	228
DOI:	https://doi.org/10.34901/mul.pub.2023.01
Supervisor:	Univ.-Prof. Dipl.-Ing. Dr.mont. Nikolaus August Sifferlinger
Co-Supervisor:	Univ.-Prof. Dipl.-Ing. Dr.mont. Thomas Antretter
Reviewers:	Univ.-Prof. Dipl.-Ing. Dr.techn. Georg Kartnig
	Univ.-Prof. Dipl.-Ing. Dr.techn. Johannes Schenk

Copyright

Acknowledgment

Funding

Publications

Several contents of this thesis were previously published in journal articles in:

- Minerals Engineering 175 (2022), Elsevier. [1]

- Bergbau - Zeitschrift für Rohstoffgewinnung, Energie, Umwelt 73 (2022), Ring deutscher Bergingenieure e.V. [2] (republication of [9])

- Stein & Kies 180 (2022), Forum mineralische Rohstoffe. [3]

- BHM Berg- und Hüttenmännische Monatshefte 168 (2023) [4]

- BHM Berg- und Hüttenmännische Monatshefte 167 (2022) [5]

- BHM Berg- und Hüttenmännische Monatshefte 166 (2021), ASMET Research GmbH, BVÖ. [6]

Further content of this thesis was published in conference papers with corresponding presentations at:

- MHCL 2022 - 24th International Conference on Material Handling, Constructions and Logistics. Belgrade, Serbia. [7]

- CHoPS 2022 - 10th International Conference on Conveying and Handling of Particulate Solids. Salerno, Italy. [8]

- 10. Kolloquium Fördertechnik im Bergbau 2022. TU Clausthal, Germany. [9]

- ESTEP Dissemination Event 2022 - Beyond Steel Research Projects. Brussels, Belgium / online. [10]

- 25. Fachtagung Schüttgutfördertechnik 2021. University of Magdeburg, Germany. [11]

Some content was also previously submitted in project reports to the EU and the research consortium, which will be published collectively after project closing in [12–16].

Additionally, two Workshops were held online in [17] and [18], which were open to public and mainly attended by industry stakeholders.

Abstract

Due to mechanical stress during transport and storage, bulk material partly degrades and fines are produced. This can be problematic in various applications and is especially critical for blast furnace sinter. Fines have to be re-sintered and are responsible for additional high costs, energy demand and emissions.

To analyze breakage behavior of blast furnace sinter a highly automated test rig for rapid single particle impact testing with integrated fragment analysis was developed. Fragment size distribution, fines production and breakage probability were investigated and clear trends were able to be determined. A general fines production curve was able to be calculated by introducing a size factor. A size-independent description with the t_n-model was also performed.

Neither a post-processing procedure nor bonded particle models were considered suitable to simulate the degradation of blast furnace sinter during transport and storage processes. A novel breakage model for the discrete element method using polyhedral particles is presented. The breakage model is based on a probabilistic particle replacement with Voronoi-tessellated fragments. In contrast to other particle replacement models with spheres, mass and volume remain constant. High mass flows and multiple breakage for processes with several damaging events, as found in industrial applications, can be simulated. The breakage model was verified and validated by a series of shatter tests and trials with two different transfer systems with different batches of sinter from two different manufacturers. Simulation and test results are consistent. Especially the fines are predicted with high accuracy. The breakage model was successfully applied to quantify particle breakage in a solid state material turbine used to reduce segregation effects during bunker filling.

Kurzfassung

Aufgrund von mechanischen Belastungen während Transport- und Lagerprozessen zerfällt Schüttgut teilweise und es entsteht Feinmaterial. Dies kann in verschiedenen Anwendungen problematisch sein und ist bei Hochofensinter besonders kritisch. Feinmaterial muss erneut gesintert werden, was zu zusätzlich hohem Energiebedarf, hohen Kosten und Emissionen führt.

Zur Analyse des Bruchverhaltens von Hochofensinter wurde ein hochautomatisierter Prüfstand für Einzelpartikelprallversuche mit integrierter Fragmentanalyse entwickelt. Die Partikelgrößenverteilung nach dem Bruch, die Produktion von Feinmaterial und die Bruchwahrscheinlichkeit wurden untersucht und es konnten klare Trends ermittelt werden. Durch die Einführung eines Größenfaktors konnte eine allgemeine Kurve für die Produktion von Feinmaterial berechnet werden. Eine größenunabhängige Beschreibung mit dem t_n-Modell wurde ebenfalls durchgeführt.

Weder eine Methode im Post-Processing noch Bonded Particle Modelle wurden als geeignet angesehen, um die Degradation von Hochofensinter während Transport- und Lagerprozessen zu simulieren. Ein neues Bruchmodell für die Diskrete-Elemente-Methode unter Verwendung polyedrischer Partikel wird präsentiert. Das Bruchmodell basiert auf einem probabilistischen Particle Replacement mit Voronoi-tessellierten Fragmenten. Im Gegensatz zu anderen Particle Replacement Modellen mit Kugeln, bleiben Masse und Volumen konstant. Hohe Massenströme und wiederholter Bruch von Fragmenten für Prozesse mit mehreren Schadensereignissen, wie sie in industriellen Anwendungen vorkommen, können simuliert werden. Das Bruchmodell wurde anhand einer Versuchsreihe mit Fallversuchen und zwei Versuchsreihen mit verschiedenen Schurrensystemen mit unterschiedlichen Sinterchargen von zwei verschiedenen Herstellern verifiziert und validiert. Die Simulations- und Versuchsergebnisse sind konsistent. Insbesondere der Feinanteil wird mit hoher Genauigkeit vorhergesagt. Das Bruchmodell wurde erfolgreich zur Quantifizierung des Partikelbruchs in einer Feststoffturbine eingesetzt, welche zur Reduzierung von Entmischung beim Befüllen von Bunkern dient.

Contents

List of abbreviations

API	Application Programming Interface
BPM	Bonded Particle Model
CSIRO	Commonwealth Scientific and Industrial Research Organisation
CF	Compressive Force
CFD	Computational Fluid Dynamics
CDT	Constant Directional Torque
DBM	Discrete Breakage Model
DEM	Discrete Element Method
DE	Discrete Element
DRI	Direct Reduced Iron
EU	European Union
FBM	Fast Breakage Model
FEM	Finite Element Method
HBI	Hot Briquetted Iron
JKMRC	Julius Kruttschnitt Mineral Research Centre
JKR	Johnson-Kendall-Roberts
JKRBT	Julius Kruttschnitt Rotary Breakage Tester
LOWESS	Locally Weighted Scatterplot Smoothing
MinSiDeg	Minimise Sinter Degradation
PBM	Population Balance Model
PRM	Particle Replacement Model
PSD	Particle Size Distribution
RFCS	Research Fund for Coal and Steel
SILC	Short Impact Load Cell
SPH	Smoothed Particle Hydrodynamics
STD	Standard Deviation
TES	Thermal Energy Storages
UCS	Unconfined Compressive Strength
UFLC	Ultra-Fast Load Cell
UFRJ	Federal University of Rio de Janeiro

1 Introduction

Due to mechanical stress during transport and storage, bulk material partly degrades and fines are produced. This can be problematic in various applications. Especially at transfer points, the bulk material has a high energy content due to transfer heights and conveying velocities. During transfer processes bulk material can be strongly decelerated and kinetic energy is mainly transferred into material degradation and equipment wear. High equipment wear could lead to short maintenance intervals, increased downtimes and thus to high costs and loss of profit. Also, various treatment processes lead to particle breakage, which can either be desired like in mills and crushers or undesired like in screens.

Undesired particle breakage and fines generation also lead to air pollution as dusts often escape from the plant. When inflammable material is handled like in coal mining, for example, material degradation also increases the risk of dust explosions.

Particle breakage is particularly critical during transport and storage of blast furnace sinter. To ensure a sufficient gas flow in the blast furnace a minimum grain size is required. For this purpose, fine-grained input materials must be agglomerated by sintering. Between the sinter plant and the blast furnace the sinter passes through various conveying systems, coolers, sieves and bunkers, where it partly degrades due to mechanical stress. Before charging the blast furnace, resulting fines below minimum grain size are screened out and returned to the sinter plant to be re-sintered. These so-called return fines due to transport and storage are 6.3% of the total mass flow on EU average [19]. Sintering is a highly energy-consuming process and thus leads to high costs and emissions. For sinter production up to 2265 MJ/t sinter are required [19]. Thus, a savings potential of 143 MJ/t sinter regarding conveying technology exists. This is roughly equivalent to the calorific value of 4 l of diesel. With an annual sinter production of 93 million t on EU average [19], this results in an annual savings potential of 375 million l of diesel only in the EU [3]. According to [19], the average process costs are 20 €/t return fines. Besides massive savings in energy and CO_2 emissions, a reduction of return fines of only 1% would result in annual savings of 18.6 million € in the EU [6].

The following work was conducted within the project MinSiDeg. The aim of the project was to minimize sinter degradation between the sinter plant and the blast furnace in order to reduce costs, energy consumption and emissions [20]. During MinSiDeg existing sinter conveyor systems were analyzed and critical points in regard to material degradation were detected. Most of the sinter plants in Austria and Germany were built decades ago and mass fluxes have been increased by simply increasing belt conveyor speeds. This leads to undesired additional impacts on conveying equipment and disadvantageous material flow. As blast furnaces and sinter plants operate nearly continuously, downtimes are short and rare. As the discrete element method (DEM) has been proven to be most suitable for bulk material simulations, a model for DEM was demanded in order to identify and optimize critical points in terms of particle breakage. Furthermore, innovative particle-preserving conveying systems were developed or tested during the project MinSiDeg. For this purpose, a precise understanding of sinter breakage behavior and a model to simulate particle breakage was essential.

2 State of the art

2.1 Iron ore sinter

For blast furnace operation a minimum grain size is required to ensure a sufficient gas flow through the blast furnace. For this purpose, fine-grained input materials must be agglomerated by sintering. These input materials are mainly fine ores, but other iron-containing materials like concentrates, combustion products and waste materials of steel plants (furnace dust, mill scale etc.) are used too [21]. In the sintering process the fine-grained iron-containing materials, coke breeze, limestone and return fines are converted into agglomerates of suitable size for charging into the blast furnace. Agglomeration is achieved by forced draft combustion of an admixed fuel, in this case coke. Superficial melting leads to adhesion between particles [22]. This results in a highly porous, heterogeneous and a cracked material with crumbly breakage characteristics, which are shown in Figure 2.1 [1].

Nowadays sinter is only used in blast furnaces and is produced on the steel plant site. Due to various chemical effects, basicity has a great influence on sinter strength [23, 24]. Depending on sinter basicity CaO is added to the sinter mixture, which limits transport and storage properties. CaO hydrates to $Ca(OH)_2$ due to air humidity, which reacts to $CaCO_2$ with CO_2 from the air. This leads to weakening and degradation of sinter particles. [21]

Due to mechanical excavation methods the percentage of fine ore has substantially increased in the last decades in comparison to lump ore, which makes agglomeration processes essential for steel production. Compared to iron ore pellets, sinter is more reactive due to its porosity and large surface area but also more fragile and heterogeneous than pellets.
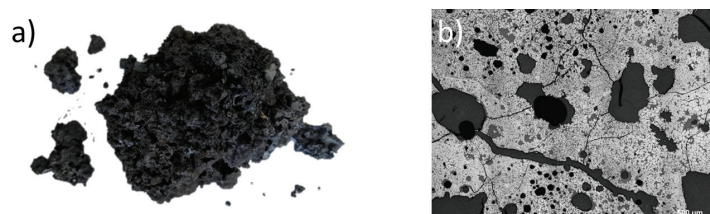
Figure 2.1: a) Sinter with fragments [1] b) Microscope image of sinter [25]

2.2 Sintering process

Sintering of fine ores was first applied discontinuously in a sinter pot in 1905. In 1911 the first sinter plant with a sinter strand for a continuous process commenced operation [26]. A simplified flow diagram of a sinter plant is shown in Figure 2.2. In the EU (EU-28) sinter is produced exclusively by down draft sintering on continuously-traveling grates. In this so-called Dwight-Lloyd process the continuously-traveling grates are formed by a series of pallet cars of fixed length and width. These pallet cars pass below a charging hopper at the beginning of the process. Already sintered coarse material of 10-25 mm is fed first into the pallet cars to form a hearth layer of 30-60 mm thickness. This hearth layer protects the steel grates from overheating in the process. Then the cars are fed with fine raw sinter mix (0-8 mm), which forms the main part of the sintering bed above and is the result of a pre-processing step of granulation. [27–29]
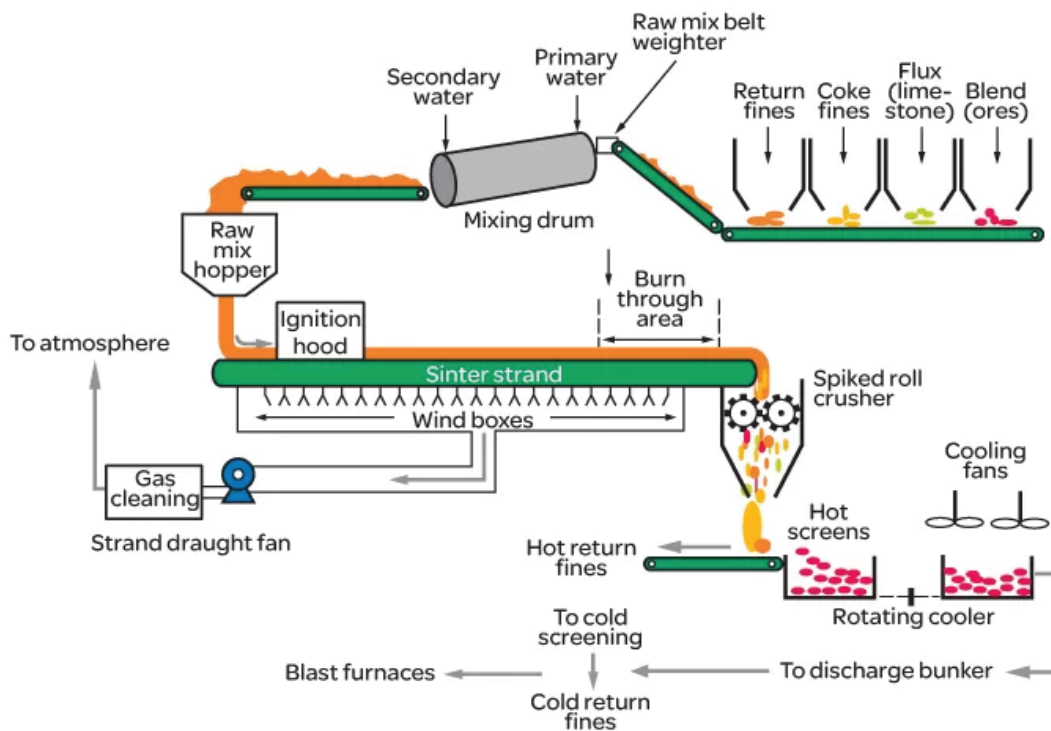
Figure 2.2: Simplified diagram of a sinter plant [30]

The following description of a sinter plant is based on [21] and [29]. With dosing bins a mixture of iron ore blend, coke fines, flux and return fines is produced. Fine ores are homogenized in blending beds to compensate chemical and physical differences. As flux, mainly basic materials like $CaCO_3$, $(Ca,Mg)CO_3$ and CaO are used to compensate the acidity of most ores and to provide a blast furnace

slag with the desired basicity. Return fines are material which has already been sintered and whose grain size is below the minimum of 6.3 mm (sometimes 5 mm), and therefore, has to be re-sintered. 30-40 % of the total sinter mass flow is screened out as return fines at hot and cold screening [6].

Water is added to the mixing drum to bind fine particles (<0.2 mm) to coarse particles. This leads to a pre-agglomeration, which raises gas permeability and is required for combustion in the following process steps [27]. The mixing and granulation drums can either be separate or combined.

This pre-agglomerated fine raw sinter mix is placed on the hearth layer and travels towards the ignition hood. In the ignition hood the fuel material is ignited, in this case coke. For ignition, coke oven or blast furnace gas is used, which is mixed with natural gas to adjust the heat value. After ignition on the surface of the sinter strand, underlying wind boxes apply suction at the bottom of the sinter strand. This leads to a downward propagation of the combustion front through the porous bed of raw materials. At the combustion front, temperatures between 1200 and 1480 °C convert the raw material into a semi-molten mass, which solidifies into a porous sinter material. Vertical movement of the combustion front is typically 10-30 mm/min until it reaches the bottom. This so-called burn-through-point should ideally be at the end of the sinter strand. Process times for bed heights of 500-600 mm are usually around 25 min. The sinter strand with the ignition hood at the rear is depicted in Figure 2.3a). [31–34]

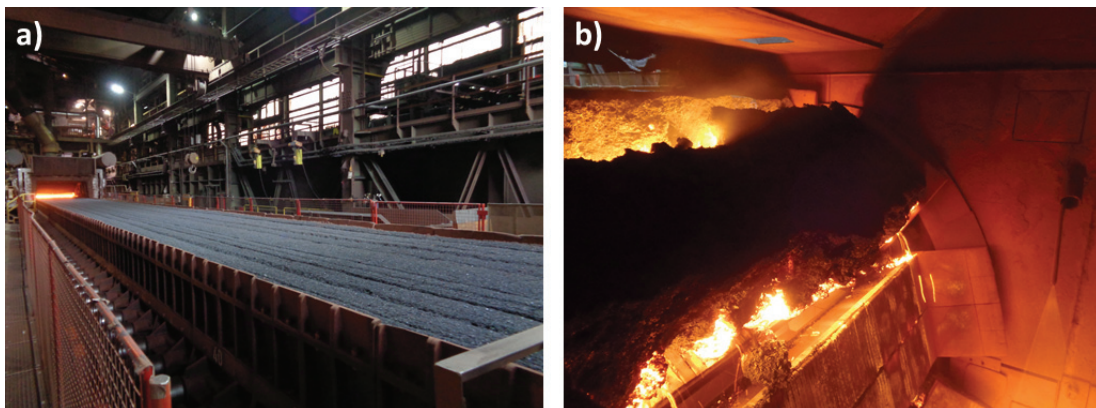**Figure 2.3:** a) Sinter strand with ignition hood b) End of sinter strand with dropping sinter cake clods

At the end of the sinter strand, the so-called sinter cake falls off the strand in large clods (see Figure 2.3b), which are then crushed in a spike roll crusher. Grain sizes of 6.3-50 mm are desired after the crusher. All particles below 6.3 mm are screened out and returned to the sinter plant as hot return fines (hot screening).

The rest of the material is conveyed into a rotating cooler. After these steps, the material usage depends on its grain size. Material under 5 mm is returned as return fines to be re-sintered. A small percentage of the coarser particles are returned for utilization as hearth layer in the sintering process. The majority of the material is used as sinter burden in the blast furnace and is further subject to handling, which includes transportation, storage and sieving. [31][29]

The efficiency of the sintering process can be described by two parameters: specific sinter production in $[t/m^2]$ and specific coke consumption in [kg coke/t sinter]. The specific sinter production is defined as the sinter produced per unit of area of the sinter strand in a given period of time. Typical values for European sinter plants are around 35-40 t/m^2 and day [19][34]. The specific coke consumption is a value for the energetic demand, given as a certain mass of coke required to produce a mass of sinter. Typical values in Western Europe are 38-64 kg coke/t sinter [19, 34, 35].

2.3 Path of the sinter

As the sinter plant and the blast furnace are usually hundreds of meters apart, the sinter has to be conveyed over long distances. This is commonly accomplished by belt conveying systems. For buffering and because there is mostly more than one blast furnace, the sinter is stored in bunkers or stockpiles. This leads to a complex system, where the sinter passes through various conveying systems, transfer points, switches, bunkers and screens. Due to mechanical stress during conveying and storage the sinter partly degrades. Before charging the blast furnace, resulting fines are screened out and returned to the sinter plant. According to [19] 60 kg fines per ton sinter on EU average are screened out before being charged into the blast furnace. Thus, 6% of the mass flow are conveyed in a circuit. The path of the sinter is illustrated in Figure 2.4. [1, 6, 12]
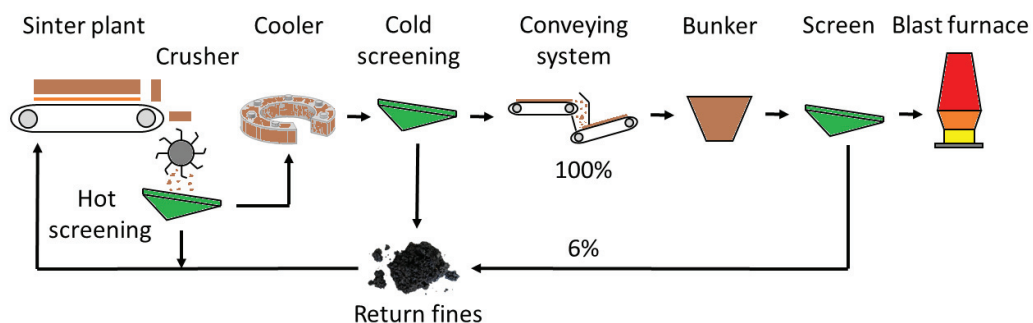
Figure 2.4: Path of sinter [6]

As sinter is a very abrasive material, rock boxes are frequently used at transfer points. A rock box causes a desired material accumulation, which reduces wear on the equipment, but can lead to an increase in material degradation. A sketch and a rock box in operation are shown in Figure 2.5. In most of the plants mass flows have been increased over the years by simply increasing belt conveyor speeds. Furthermore, installations for reducing equipment wear, measuring and sampling have been added to conveying systems. All this leads to undesired material flow, material accumulations and additional impacts on equipment in some cases, which further increases material degradation. [6, 12]
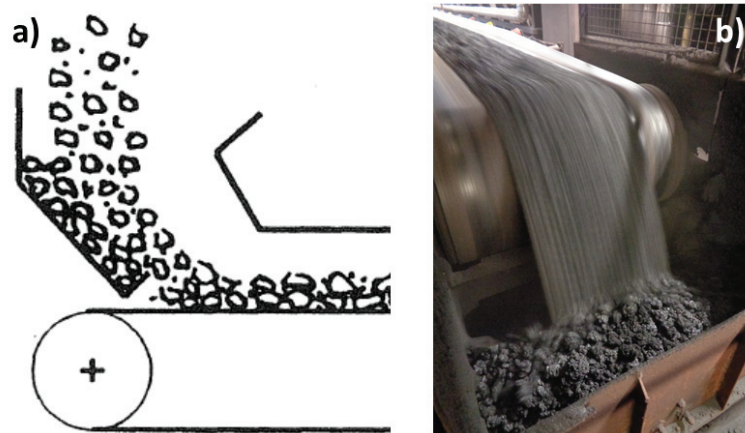
Figure 2.5: a) Sketch of a rock box [36] b) Rock box with sinter in operation

Sinter is either stored in large stockpiles outside or in bunkers inside the plant. For this purpose, square-shaped bunkers are often used, which are filled by a belt conveyor (see Figure 2.6a). Especially at low filling levels, high drop heights occur, which leads to significant material degradation. Furthermore, segregation effects due to bunker filling by belt conveyors are noticed. This is a common phenomenon. Large particles accumulate at the top of the belt conveyor and small particles accumulate at the bottom. Thus, at belt discharge large particles accumulate in conveying direction of the filling belt conveyor and small particles accumulate against conveying direction in the bunker (see Figure 2.6b). This leads to fluctuations in blast furnace operation. [6, 12, 20]

2.4 Degradation of steel-making materials

The following Section 2.4 is based on [37] and is also referred to in [1]. Several studies have been carried out dealing with degradation during the handling of
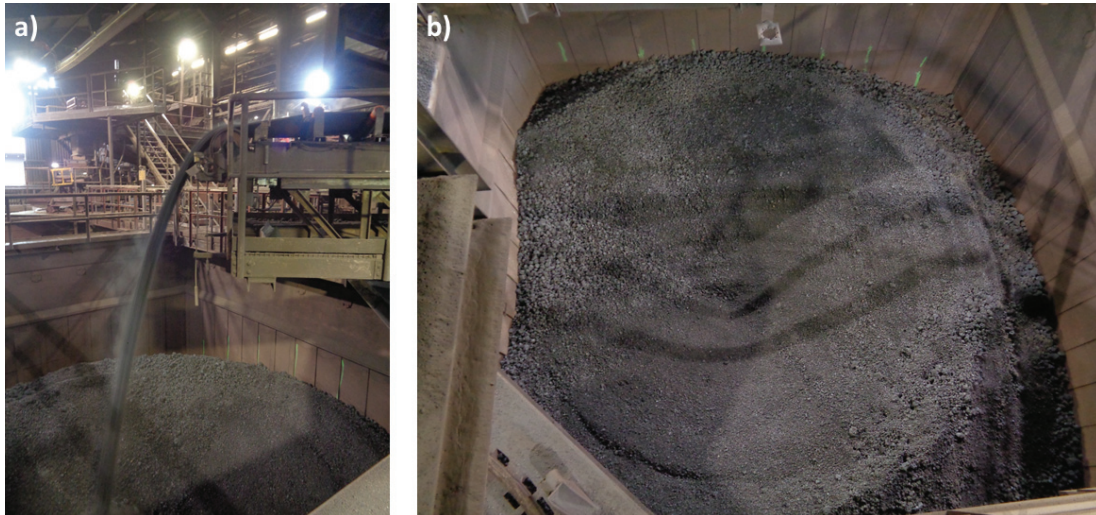
Figure 2.6: a) Bunker filling [6] b) Segregation effects in bunkers [6]

steel-making materials, which include coal, coke, iron ore sinter and iron ore lumps [38–50]. [37] is a review article. As handling processes and problems like fines generation are similar for all of these materials, steel-making materials are often analyzed collectively. The aim of all these studies was to reduce undesired degradation effects and fines production. Thus, models and conclusions are usually valid for all of these materials, including sinter. As sinter is a product of a process (see Section 2.2), sinter degradation characteristics are also dependent on process parameters, composition and phase chemistry. These factors are not subject of this thesis. They are assessed in regard to fines production in [51]. A detailed study on the degradation of iron ore pellets due to impacts during transportation and handling is provided in [52].

In [53–55] degradation is defined as the reduction of a given size fraction to smaller size fractions found in the range of final products expressed as mass fractions. In [56] the particle size degradation during impacts in pneumatic conveying circuits was investigated and it was concluded that the rate of degradation was directly proportional to the number of impacts encountered by the particles. Vogel and Quass [57] investigated the degradation of coal lumps during mining and handling operations and concluded that the impact forces were the key factor when the lumps fell freely from different heights. An influence of the lump size on the degradation was also noticed. [37]

2.4.1 Drop tests

In [55] the degradation of coal, iron ore sinter and coke due to drops at transfer points, stockpiling and reclaiming was investigated. In tumbler drum tests it was

noticed that size degradation was due to both volume and surface breakage. It was also concluded that a drop test method was more suitable for steel-making materials, such as sinter and coke, due to limitations of the tumbler drum test and easy application of the drop test.

A series of drop tests was conducted in [42, 43, 49] to determine the critical drop height of coal for the iron-making process. All of these drop series were selected to have a total drop height of 30 m (30 drops at 1 m, 15 drops at 2 m, 10 drops at 3 m etc.). The results of this trial are shown in Figure 2.7. The degradation decreases when a large drop is replaced by several smaller drops, which is also consistent with the findings in [39, 40, 58, 59].
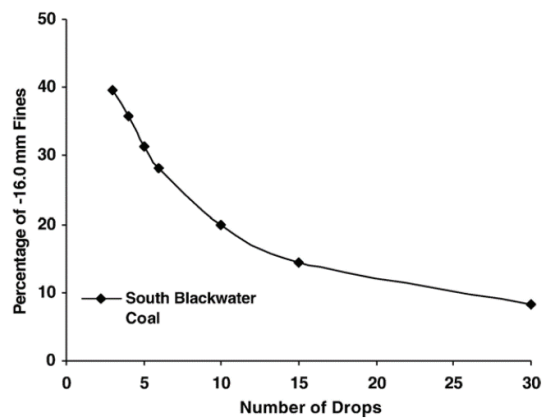
Figure 2.7: Percentage of generated coal fines after different drop series with the same total drop height in dependence on the number of drops [43]

2.4.2 Cushioning tests

Several studies were carried out investigating cushioning effects of fines on degradation [42, 43, 58–60]. Fagerberg and Sandberg [60] showed that 30% initial fine content reduced the degradation of lump iron ore by 40%, which is consistent with the results in [58]. Waters and Mikka [59] showed that the cushioning effects on fines generation were more significant at higher drop heights than at lower ones. In [42, 43] Sahoo tested the cushioning effects of fines on coal degradation during handling and concluded that coal samples with higher percentages of initial fines reduced overall coal degradation.

2.4.3 Influence of impact surfaces

In [39] the effect of different impact surfaces on the degradation of iron ore sinter due to drops at various transfer points was examined. The results showed that

degradation decreased by 66% when the sinter was dropped onto a sinter bed compared to a drop onto a steel surface. In [41, 44] the effect of different impact surfaces on the degradation of coal was investigated (see Figure 2.8). The study revealed that the drop onto a steel surface produced 9% more fines (<16 mm) than the drop onto a conveyor surface and 13.4% more fines than the drop onto a coal surface at a drop series with 6 drops at 5 m.
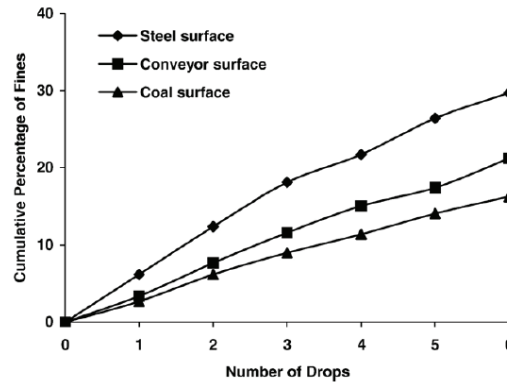
Figure 2.8: Cumulative percentage of fines after several drops of coal onto different surfaces [41]

2.4.4 Influence of lump sizes

Various studies revealed that large lump sizes of iron making materials were more likely to break [50, 59, 61–63]. This is in agreement with Griffith's theory of fracture [64, 65], which implies that larger particles are more likely to contain larger cracks and thus are more susceptible to breakage.

2.4.5 Stabilization effects

Physical stresses on bulk material have a two-sided effect: on the one hand stresses may lead to degradation and fines generation, but on the other hand this stabilizes the strength of the remaining material [20]. The so-called sinter stabilization effect [66] prevents particle degradation in the blast furnace. It is due to mechanical stress during handling, sieving and storage. This leads to an early dropout of weak material and an increase of particle roundness due to abrasion. The same effect was noticed for iron ore lumps in [55, 59, 60, 62, 63] and for coal in [41].

2.4.6 Tumbler tests

The friability of coal was defined by Yancy and Zane [67] as the physical property of coal being reduced in size during handling due to impacts and attrition. In their work the tumbler test was suggested as a suitable method to estimate the friability of coal. Fagerberg and Sandberg [60] evaluated the abrasion of iron ore lumps in a tumble drum test. Lister et al. [68, 69] investigated the degradation of coke in a tumbler test and suggested that there are three mechanisms for fines production: (1) particle-particle abrasion, (2) particle-drum abrasion and (3) fines produced by impacts as particles drop from lifters and collide with the rotating drum. In [47] the size degradation of coal was tested. The results showed an initial high rate of degradation due to volume breakage along existing cracks. After a few minutes of tumbling, volume breakage decreased and the coal lumps stabilized (see Figure 2.9). Further tumbling lead to fines generation due to abrasion. These findings were confirmed in [61] for coke. Further investigations to measure the degradation of coal, coke, lump iron ore and sintered iron ore using the tumbler test were conducted in [49, 50, 61].

In [70] the surface breakage of fired iron ore pellets due to impacts in tumbler drum tests was investigated for five types of industrial iron ore pellets. The results revealed that attrition occured at variable impact angles and at energies higher than 5 J/kg for iron ore pellets. Also, a model was developed to quantify the relative mass loss due to surface breakage (see Section 2.9.3). [70].
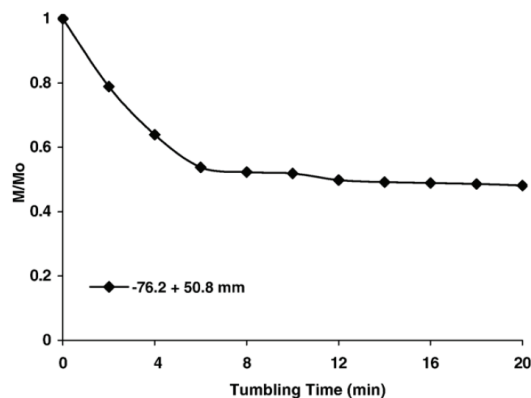

Figure 2.9: Degradation of coal tested in a tumbler drum [47]

2.4.7 Chute design

First investigations regarding factors affecting the degradation of sinter at a belt conveyor transfer point were made in [71]. In [72] it was suggested that the factors

affecting degradation at transfer points were mainly the height of the transfer point, impacts on the chute and change in direction from loading to receiving. Goodwin and Ramos [53] analyzed various types of chutes with regard to the degradation of coal and concluded that the best chute design was a curved-profile variable geometry, developed by [73]. In [38] a baffle plate chute is suggested as one way to avoid degradation at conveyor transfer points (see Figure 2.10a). Baffle plate chutes exploit the same cushioning effect (see Section 2.4.2) as rock boxes, described in Section 2.3. In [39] it was shown that the degradation of sinter dropped by 1% when using a baffle plate chute during ship loading. The least degradation occurs when slide chutes are used. As mentioned in Section 6.2, most studies in this field revealed that large drop heights should be avoided and replaced by multiple smaller drop heights [37]. Especially when feeding a fast-moving belt conveyor, the material should first be accelerated to the speed of the receiving belt conveyor, as illustrated in Figure 2.10b). This avoids rolling and bouncing, which increases material degradation and equipment wear. [37, 38]
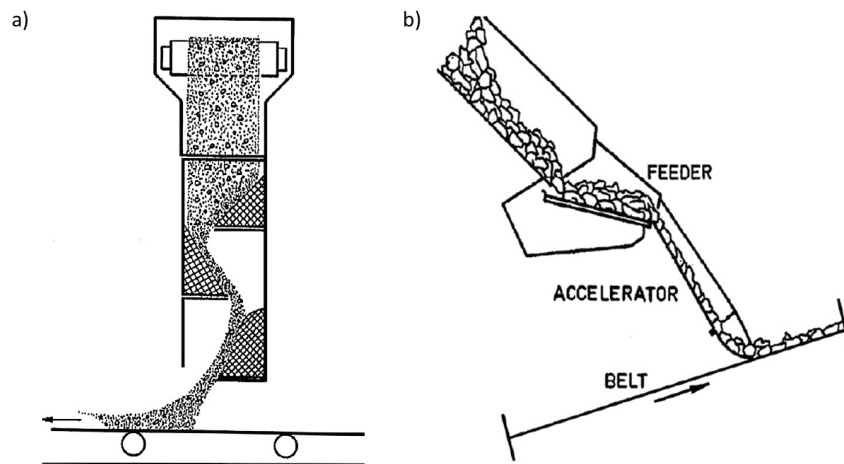
Figure 2.10: a) Baffle plate chute [38] b) Accelerator for fast conveyors [38]

In earlier days the design of chutes was based on a rule of thumb or experience. Nowadays computer aided design with DEM (discrete element method, see Section 2.10) allows optimum operation for every specific application in terms of degradation, equipment wear, dust emissions and plugging. Investigations regarding chute design by means of DEM and experimental studies were conducted by Kessler and Prenner in [74]. As every material has different flow properties, a proper material calibration and accurate knowledge of input parameters is crucial. As long as not all parameters can be measured independently, they have to be estimated initially. In [74] accurate calibration was achieved with test simulations

and comparison studies of computer simulations and laboratory tests. With this approach meaningful results were achieved, which were confirmed by trouble-free operation of designed chutes for a period of several years. Fundamentals and the early development of methods for chute optimization by means of DEM are documented in [75–81]. A characterization of sinter and pellet particles including dynamic angle of repose and an estimation of rolling friction for non-spherical particles is provided in [82, 83]. Parameters for binary mixtures of sinter and pellets were investigated in [84]. Recent studies in the field of chute design using DEM were conducted in [85–91] (see Figure 2.11).
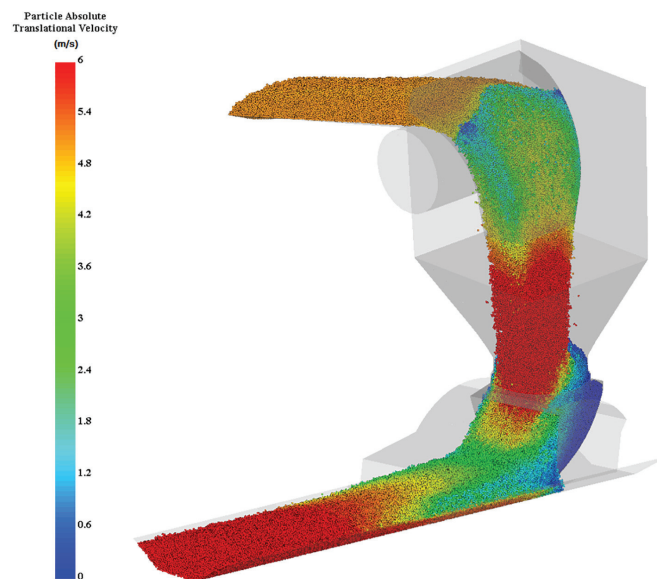
Figure 2.11: Optimized chute with hood and spoon by means of DEM at steady state. Colour scale represents particle translational velocity. [88]

2.4.8 Further investigations focused on sinter

Nistala et al. [92] assumed that the effect of transport parameters such as drop height and conveying length on the generation of return fines cannot be predicted by conventional tests such as tumbler and shatter tests. Thus, various steps involved in transportation were simulated by customized drop and vibration tests in the work of Nistala et al. [92] to investigate the effect of sinter size, drop height and conveying time on the percentage of return fines and volume breakage. The following findings were obtained.

Drop and vibration tests showed that the extent of volume breakage is higher for large sinter particles, which is consistent with the conclusions in [50, 59, 61–63] (see Section 2.4.4). Contrary to volume breakage, the percentage of generated

fines does not increase with particle size. The highest relative fines production was determined in the size fraction 5-10 mm, followed by 20-30 mm, 30-40 mm and 10-20 mm. The volume breakage constant (see Section 2.9.1) for all size fractions of sinter is logarithmically related to drop height and the time of vibration (see Figure 2.12). This confirms first-order breakage behavior (see Section 2.9.1) and agrees with conclusions in [49, 50, 55, 61, 62]. For all size fractions a linear relation between the percentage of generated return fines and drop height was observed. In the case of vibration tests, a logarithmical relation between vibration time and percentage of generated return fines was found (see Figure 2.13). While significant cushioning effects were provided by sinter fines (<5 mm) during tumbler tests, low cushioning effects during drop tests and negligible cushioning effects in vibration tests were noticed. [92]

As the size fraction 5-10 mm contributes most to return fines generation, it is suggested to use the sinter sized 5-10 mm instead of 10-25 mm as hearth layer to reduce overall fines generation. As the clearance between the grate bars on sinter pallets is usually 4-6 mm, it is assumed that a hearth layer sized 6-10 mm would not adversely affect gas flow through the sinter bed, but this has to be confirmed in further investigations. [92]
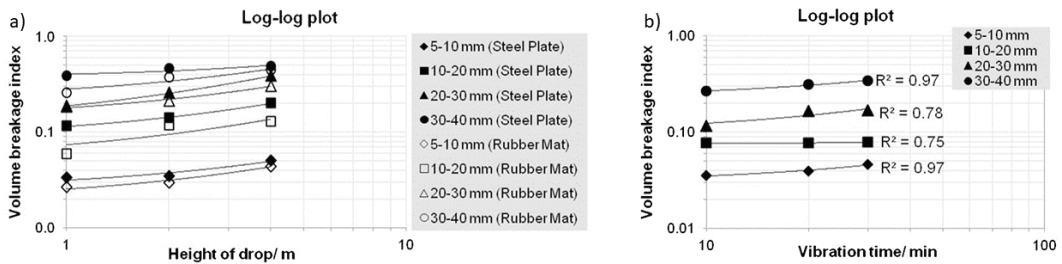
Figure 2.12: Volume breakage index for a) drop tests b) vibration tests [92]
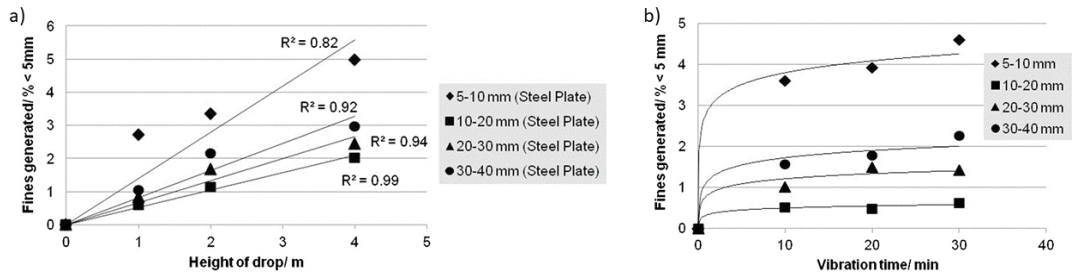
Figure 2.13: Relative fines generation by a) drop tests b) vibration tests [92]

2.4.9 Hot sinter

In [93] an attempt was made by Öfner and Zaunrith to characterize the breakage behavior of hot sinter by single particle tests with a drop weight. Non-consistent results regarding energy input compared to parallel tests in a jaw crusher point out some problems and challenges when testing materials with widely varying properties. Especially the great heterogeneity of sinter demands a high sample number. The jaw crusher tests revealed the influence of sinter temperature on breakage behavior. Before crushing, the specimen temperature was measured by thermal imaging. The percentages passing after crushing 6.3, 2 and 0.5 mm mesh size was plotted against the maximum specimen temperature and a linear increase in fines generation with sinter temperature was determined (see Figure 2.14). [93] [1]
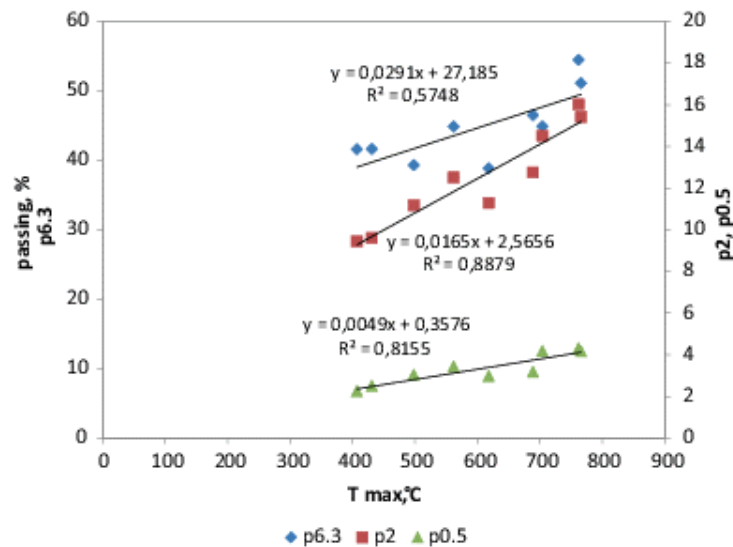
Figure 2.14: Influence of sinter temperature on fines generation [93]

2.5 Fundamentals of impact processes

In this Section some fundamentals of impact processes are briefly explained as some of the content of this thesis is based on impacts.

2.5.1 Principle of linear impulse and momentum

Generally, at an impact between two bodies relatively high forces occur during a very small time interval. The integral of the F(t) curve $\int F(t)\,dt$ is defined as

linear impulse or force impact (see Figure 2.15a). The principle of linear impulse and momentum is fundamental in dynamics (see Equation 2.2). It is obtained by integrating the equation of motion (Equation 2.1) for a particle of mass m with respect to time between t_1 and t_2. It states that the initial momentum of a particle at time t_1 plus the sum of all impulses applied to the particle from t_1 to t_2 equals the final momentum of the particle at time t_2. In a system of particles moving relatively to an inertial reference (see Figure 2.15b), Equation 2.3 is applied. The internal forces $\vec{f_i}$ do not appear in this equation, since by Newton's third law (actio=reactio) they occur in pairs of equal values but in opposite directions and thus cancel out. Only the external forces $\vec{F_i}$ are relevant in this case. [94]

$$\sum_i \vec{F_i} = m\frac{d\vec{v}}{dt} \tag{2.1}$$

$$m\vec{v_1} + \sum_i \int_{t_1}^{t_2} \vec{F_i} dt = m\vec{v_2} \tag{2.2}$$

$$\sum_i m_i(\vec{v_i})_1 + \sum_i \int_{t_1}^{t_2} \vec{F_i} dt = \sum_i m_i(\vec{v_i})_2 \tag{2.3}$$

m	Particle mass	$[kg]$
v	Particle velocity	$[m/s]$
t	Time	$[s]$
F	External force	$[N]$

2.5.2 Central impact

In general, a distinction is made between two types of impacts. At a straight impact the velocity vectors of both colliding particles before the impact are along a line passing through both mass centers (see Figure 2.16a). This line is called the line of impact and is perpendicular to the plane of contact. If one or both velocity vectors form an angle to the line of impact, the impact is referred to as
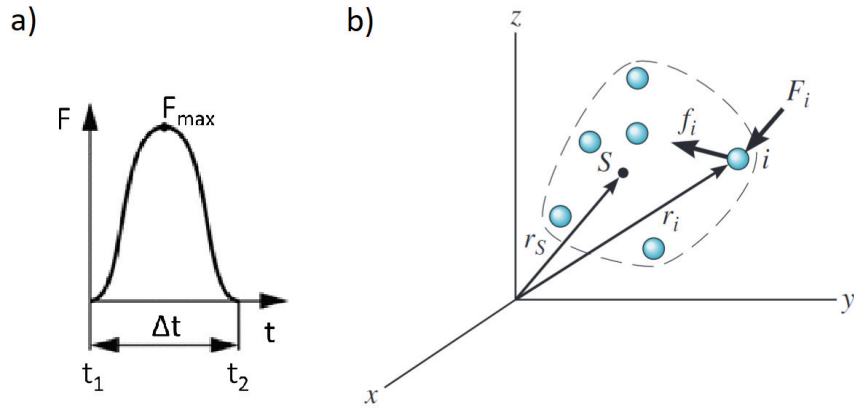
Figure 2.15: a) Linear impulse [95] b)Inertial coordinate system [94]

an oblique impact (see Figure 2.16b). If the line of impact passes through both mass centers of the particles, a central impact occurs, otherwise, it is referred to as an eccentric impact. [94]
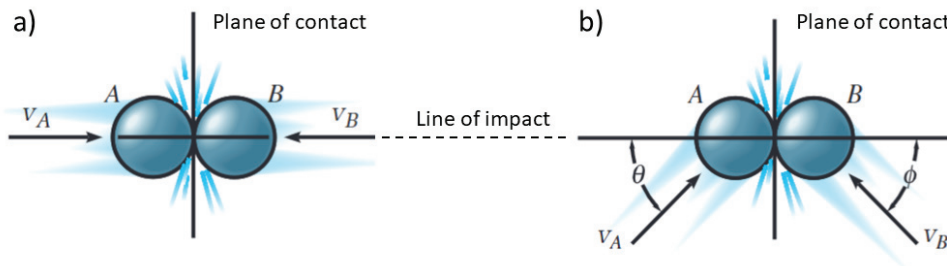
Figure 2.16: a) Straight central impact b) Oblique central impact [94]

The mechanics of an impact process are described by means of the following case involving two straightly and centrally colliding particles A and B (see Figure 2.17). In Figure 2.17a) the particles have the initial impulses $m_A(\vec{v_A})_1$ and $m_B(\vec{v_B})_1$ before the impact. During the impact in Figure 2.17b) the particles are considered as locally deformable and are compressed at the contact point. This leads to the deformation impulses $\int \vec{K}\,dt$, which are the same in value but in opposite directions. Only when compression reaches the maximum, both particles move with the same velocity $\vec{v}$ as their relative movement becomes zero (see Figure 2.17c). Then the period of restitution occurs (see Figure 2.17d). The particles either return to their original shapes or remain partly or fully deformed. The equal but opposite restitution impulse $\int \vec{R}\,dt$ pushes the particles apart. Due to the physical properties of the particles the restitution impulse is always smaller than the deformation impulse $\int \vec{K}\,dt > \int \vec{R}\,dt$. After the impact the particles have the resulting impulses $m_A(\vec{v_A})_2$ and $m_B(\vec{v_B})_2$, shown in Figure 2.17e), with $(\vec{v_B})_2 \geq (\vec{v_A})_2$. At an oblique impact the particle velocities $(\vec{v_A})_2$ and $(\vec{v_B})_2$ change

in value and direction due to the impact (see Figure 2.18). When initial velocities and directions are known, four variables v_A, v_B, ϕ_2, θ_2 need to be caluclated. [94]
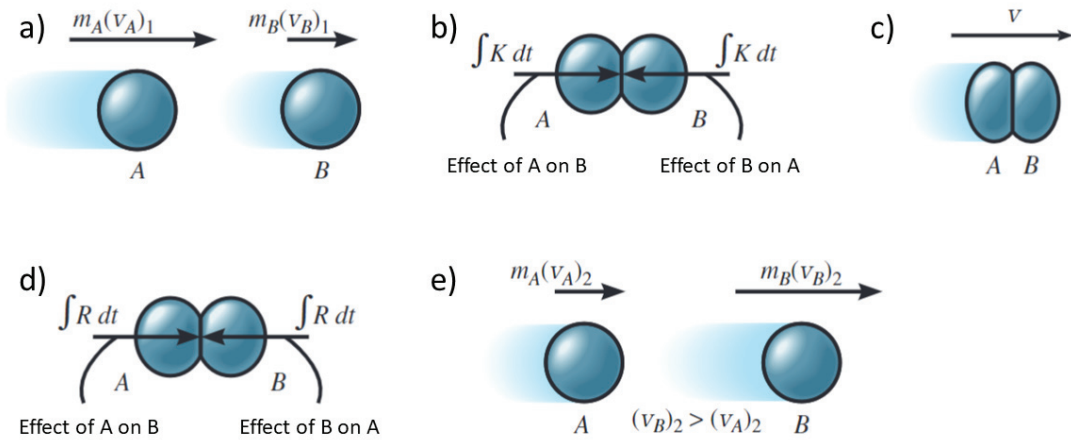
Figure 2.17: a) Before impact b) Deformation impulse c) Maximum deformation d) Restitution impulse e) After impact [94]
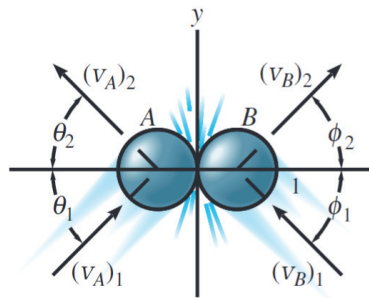
Figure 2.18: Oblique impact [94]

2.5.3 Coefficient of restitution

The coefficient of restitution is defined as relationship between restitution and deformation impulse (see Equation 2.4). The unknown velocity v can be eliminated, which leads to Equation 2.5. Thus, the restitution coefficient is a value between 0 and 1, with the following two borderline cases. At the fully plastic or fully inelastic impact (e=0), no restitution impulse exists and both particles move together with the same velocity in direction of the line of impact. At a fully elastic impact (e=1) the restitution impulse equals the deformation impulse. In reality no fully elastic impact exists because some energy is always dissipated and transferred into heat, acoustic emissions and local plastic deformations. The coefficient of resitution can be determined by drop tests, in which a particle with mass m_A is

dropped onto a surface of a body with mass $m_B \gg m_A$. Considering $m_B \to \infty$ and thus $(\vec{v_B})_2 \to 0$, Equation 2.6 can be applied when the rebound height $(h_A)_2$ is measured. The dissipated energy ΔT can be calculated by means of the difference of kinetic energies (see Equation 2.7). [94]

$$e = \frac{\int \vec{R}\, dt}{\int \vec{K}\, dt} = \frac{\vec{v} - (\vec{v_A})_2}{(\vec{v_A})_1 - \vec{v}} = \frac{(\vec{v_B})_2 - \vec{v}}{\vec{v} - (\vec{v_B})_1} \tag{2.4}$$

$$e = \frac{(\vec{v_B})_2 - (\vec{v_A})_2}{(\vec{v_A})_1 - (\vec{v_B})_1} \tag{2.5}$$

$$e = \sqrt{\frac{(h_A)_2}{(h_A)_1}} \tag{2.6}$$

$$\Delta T = \sum T_1 - \sum T_2 = \frac{1 - e^2}{2} \cdot \frac{m_A m_B}{m_A + m_B} \left[(\vec{v_A})_1 - (\vec{v_B})_1\right]^2 \tag{2.7}$$

e	Coefficient of restitution	$[-]$
R	Restitution force	$[N]$
K	Deformation force	$[N]$
v	Particle velocity at maximum deformation	$[m/s]$
$v_{A/B}$	Velocity of particle A or B	$[m/s]$
$(v_{A/B})_1$	Particle velocity before impact	$[m/s]$
$(v_{A/B})_2$	Particle velocity after impact	$[m/s]$
$(h_A)_1$	Drop height	$[m]$
$(h_A)_2$	Rebound height	$[m]$
ΔT	Dissipated energy	$[J]$
T_1	Kinetic energy before the impact	$[J]$
T_2	Kinetic energy after the impact	$[J]$
$m_{A/B}$	Particle mass of particle A or B	$[kg]$

2.5.4 Impact against a wall

At an oblique impact of a particle with mass m_1 on a smooth wall with mass $m_2 \to \infty$, the resulting velocity parallel to the wall surface v_{1y} remains constant. The velocity perpendicular to the wall surface v_{1x} decreases depending on the coefficient of restitution $0 < e < 1$. Thus, the rebound angle α^* also depends on the damping behaviour. Three cases are distinguished (see Figure 2.19). [95]
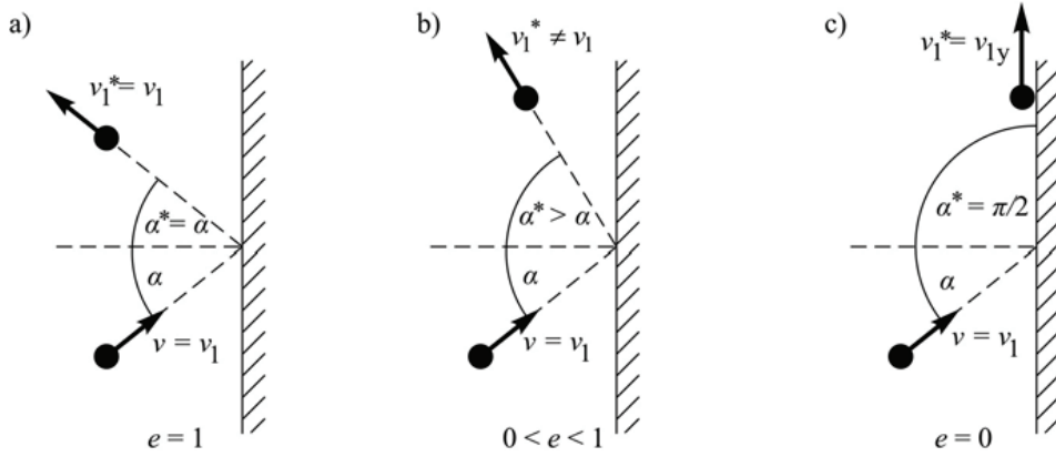
Figure 2.19: Impact on a wall with a) fully elastic b) partly elastic c) fully inelastic [95]

2.6 Particle breakage mechanism

Particle breakage in degradation and comminution processes is the result of various poorly understood microprocesses. The outcome of these processes depends on complex interactions between stressing conditions, material characteristics and environmental conditions. Stressing conditions can be classified by the type of stress applied (compressive or shear), stressing intensity, stressing rate and the number of loading points. The most relevant material characteristics for particle breakage are the fracture strength and the deformation behavior. The fracture strength can either be defined by the required energy to cause fracture or by the critical tensile stress. Material deformation behavior can be classified as elastic (brittle) or inelastic, which includes semi-brittle, plastic [96] and quasi-brittle. Quasi-brittle behavior is characterized by gradual accumulation of crack-like damage [97]. Environmental contributions are generally associated with the presence of surface-active agents or moisture. [98]

As in most industrial applications only the outcome is relevant, a complete understanding of the detailed breakage process is not required in many cases. A complete understanding of all these interactions is not possible anyway unless the most elementary breakage micro event is analyzed. The fundamental properties of the fracture process can be investigated most effectively by well-controlled single particle experiments. Many single particle fracture studies have been conducted and there is a general agreement in literature on the basic model description [99]. The particle is stressed by the initial contact with the tools, such as a drop weight and a hard anvil, and the energy is stored in the particle as strain energy. The small amount of plastic deformation at the loading points is not considered significant for most materials. During this initial period the particle deformation can be described by the Hertzian model [99, 100]. Beyond a certain stress, for most materials crack-like damage starts to accumulate within the particle. When failure criteria are met, a macro crack grows unstably and increasingly rapidly and which may eventually branch [97]. When cracks advance to the particle surface, several progeny particles are formed. The size and number of the resulting progeny particles depends on the location and size of the initiating flaw, the extent of crack branching and the material micro structure. [98]

Initiation of unstable crack growth is defined by the Griffith criterion [64], which states that a crack will unstably propagate when the reduction in strain energy that occurs due to crack growth is greater or equal to the increase in surface energy due to the creation of new free surfaces [101] (see Equation 2.8). For the simple case of a thin rectangular plate with a crack perpendicular to the load (see Figure 2.20), the strain energy W_{str} is given by Equation 2.9. The surface energy W_{surf} for both fracture surfaces is given in Equation 2.10. Thus, the crack propagation criterion results in Equation 2.11 and the required stress σ_c for crack propagation is defined by Equation 2.12. [64, 101]
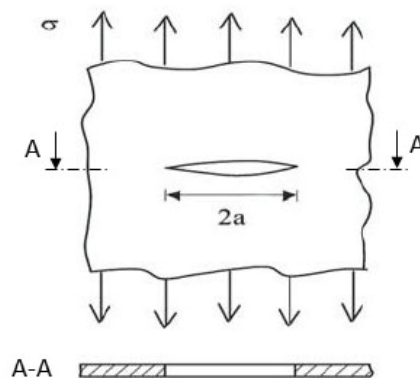

Figure 2.20: The Griffith crack (flaw) of length 2a perpendicular to the load is in the middle of a thin infinite large material [102]

This theory can be applied to linear elastic materials that fracture in a brittle fashion [101], but conventional fracture mechanics techniques cannot be used for particle breakage because of the great difficulty in calculating the stress field inside an irregularly shaped particle. In the case of particle breakage, the energy required for crack propagation comes entirely from stored strain energy, which is available at crack initiation. This energy is defined as particle fracture energy. This theory is based on the fact that no other energy source is available to provide energy at the required rate during crack growth. The required rate is generally much larger than the rate at which energy is delivered to the particle during a stressing event. Thus, the stored particle fracture energy must be at least as large as the total energy that is dissipated at the growing crack tip. In most cases the stored particle fracture energy exceeds the dissipated energy at the crack tip. When the fracture is complete, the remaining energy is dissipated as kinetic energy of progeny fragments. This can either result in further breakage of fragments or stressing of tools [99]. [98]

$$\frac{dW_{str}}{da} \geq \frac{dW_{surf}}{da} \tag{2.8}$$

$$W_{str} = \frac{a^2 \pi \sigma^2}{E} \tag{2.9}$$

$$W_{surf} = 4a\gamma \tag{2.10}$$

$$\frac{2a\pi\sigma^2}{E} \geq 4\gamma \tag{2.11}$$

$$\sigma_c = \sqrt{\frac{2E\gamma}{\pi a}} \tag{2.12}$$

W_{str}	Strain energy	$[J]$
W_{surf}	Surface energy	$[J]$
a	Crack length	$[m]$
σ	Stress	$[Pa]$
E	Young's modulus	$[Pa]$
γ	Surface tension	$[N/m]$

Teo and Waters [63] showed that the degradation of iron making agglomerates is caused by the following two mechanisms: volume breakage, in which the individual lumps fracture, and surface breakage due to chipping or abrasion. These mechanisms are distinguished by the size distribution of the degradation products (see Figure 2.21). Volume breakage occurs when the particle is subject to compressive stresses resulting in disintegrative fracture. In the case of surface breakage, the particle suffers gradual wearing of its surface, leaving the initial particle mostly intact but usually more rounded due to stress concentrations on the corners of protrusions. [37, 98]

A review article regarding particle attrition mechanisms including different incfluences of particle morphology such as failure modes, material characteristics, geometry and response to different loading conditions is provided in [103].
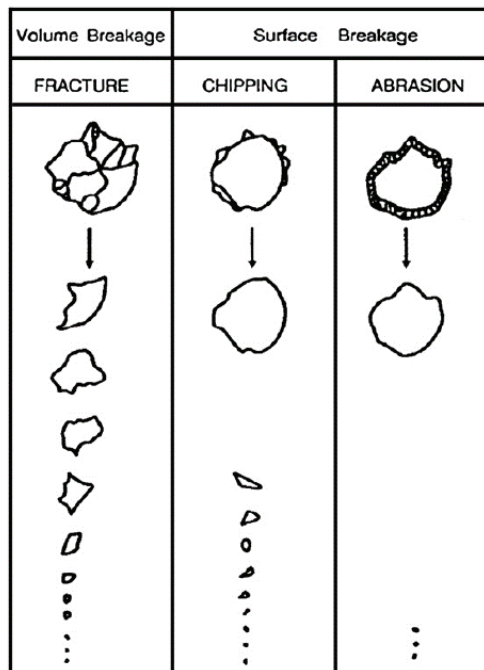

Figure 2.21: Breakage mechanisms [63]

2.7 Bulk sample breakage tests

In the following Chapter selected bulk sample test methods to investigate particle breakage are described. Generally, a distinction is made between bulk sample tests with a large number of particles and single particle tests. Bulk sample breakage tests are usually less effort compared to single particle tests as statistical significance in terms of particle breakage behavior can be achieved with a lower number of tests. Furthermore, bulk sample tests take into account the influence of particle-particle interactions, like cushioning effects and abrasion. To determine the breakage behavior more precisely single particle tests are often required.

2.7.1 Tumbler test

For the tumbler test, a bulk sample is placed into a rotating steel drum and the PSD after a specific number of revolutions is measured by a screening procedure. Depending on the region, there are several standardized procedures for this test, which mainly differ in bulk sample mass, initial particle size and number of revolutions. In North America the ASTM Tumbler Test based on ASTM D 3402 [104] and in Japan the Japanese Drum Test after JIS K2151 [105] is commonly used. In Europe the Micum (see Figure 2.22) and Irsid Test are nowadays standard to determine the strength of sinter and coke. They are based on ISO 556 [106]. In the Micum and Irsid Test a bulk sample of 25 kg is placed in the drum and rotated for 100 (Micum) or 500 (Irsid) revolutions. The M_{40}, M_{20} and M_{10} values represent the percentage of the remaining material passing the 40, 20 or 10 mm aperture test sieve. Similar to the Micum test, the Irsid test reveals the I_{40} to I_{10} values after 500 drum revolutions. [106]

2.7.2 Shatter test

A shatter test is a simple bulk sample test method. In a shatter test, a bulk sample is placed in a box and dropped from a certain height onto a baffle plate. The baffle plate is usually of steel, but is often replaced by other materials to investigate the interaction with other equipment materials. With the change in PSD due to the drop, conclusions regarding particle strength and interaction parameters are drawn.
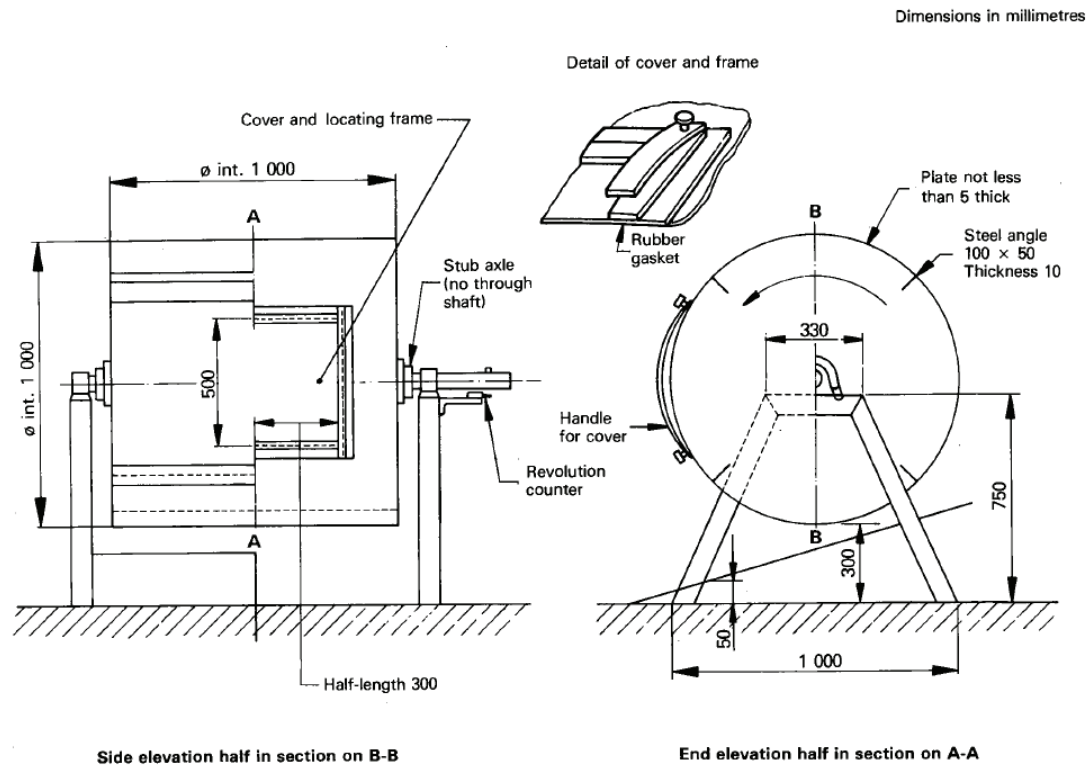
Figure 2.22: Standardized Micum drum for tumbler tests [106]

2.7.3 Crushers

To determine the fracture energy of bulk materials, conventional crushers from mineral processing can be used. There are various types of crushers, like jaw crushers, impact crushers, hammer crushers, cone crushers and roller crushers. For fracture energy investigations, laboratory jaw crushers are usually used. A jaw crusher uses two jaws. One jaw is stationary and the other jaw is moving in an oscillatory motion with the help of an eccentrically mounted rod (pitman) and a toggle mechanism [107] (see Figure 2.23). By measuring the increase in electric power consumption of the drive motor, the fracture energy for the feeded material can be determined. [108, 109]

2.8 Single particle breakage tests

Various testing methods have been developed to measure the breakage characteristics of single particles subject to compression. Each test method allows investigation over a restricted range of deformation rates. Single particle test methods can be classified according to the number of contact points and the stress application mode (see Figure 2.24). [98]
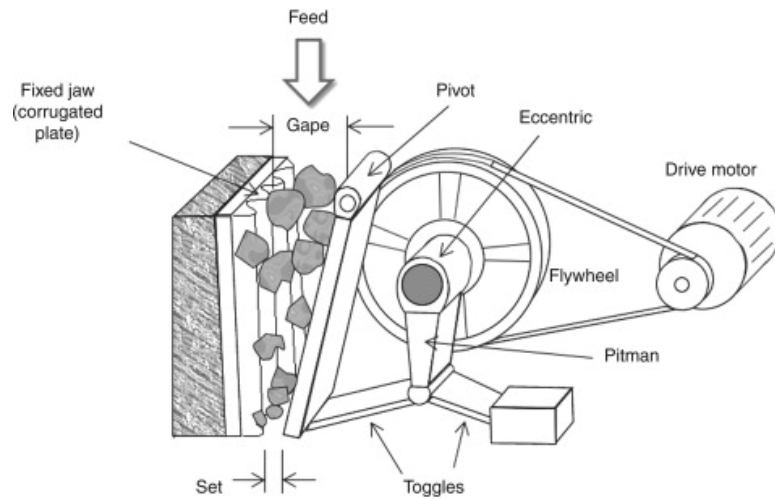
Figure 2.23: Double toggle jaw crusher [110]
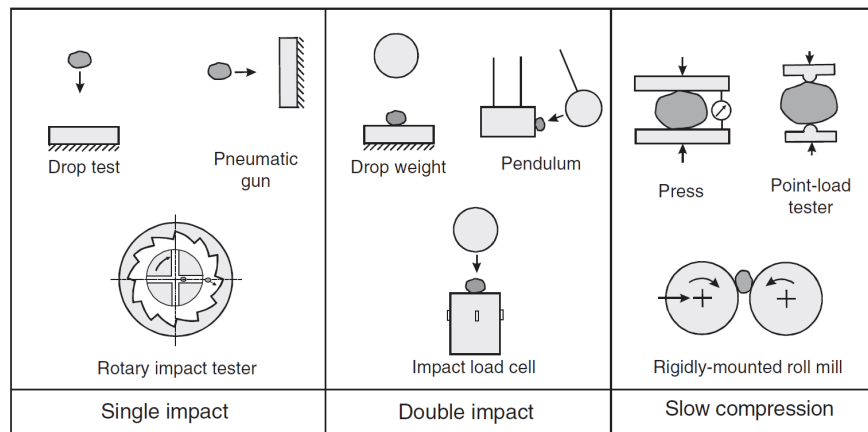
Figure 2.24: Different types of sinlge particle breakage tests [98]

Single impact tests can be conducted by drop tests [111–113], by propelling particles at a target with a pneumatic gun [114] or by a rotary impact tester [115], for example. In each of these cases the mass-specific impact energy E_{cs} is only dependent on the impact velocity of the particle itself and is calculated by Equation 2.13. The remaining energy after the crushing event is converted into kinetic energy of the fragments. This energy eventually causes secondary breakage, especially if the velocity vectors of the fragments are directed towards the impact surface. In double impact tests the specimen is crushed between two hard surfaces with a moderate deformation rate. This can be a simple drop test or a pendulum test, for example. In this case the available impact energy can be calculated precisely with classic mechanics. Modified versions with proper instrumentation also allow to determine the absorbed energy by the particle during impact (see

Section 2.8.2). Slow compression tests are performed by uniaxial compression presses or by a rigidly mounted roll mill at a very slow deformation rate. [98] Techniques where the particle is loaded at rates so low that the duration of the contact is sufficient to allow the stress to propagate and equilibrate throughout the particle are called quasi-static [98]. This is the case in most test methods except high-velocity impact tests by a pneumatic gun or a rotary impact tester or drop tests from large drop heights. Comprehensive reviews about early contributions to single particle breakage are found in [116, 117]. In [118] common methods for single particle breakage tests were evaluated. As a result, the SMC-test [119], which is a method based on a drop weight tester, and the relatively expensive rotary impact tester (see Section 2.8.6) were considered most practicable to dertermine ore comminution behavior [118]. In the following, selected single particle impact tests are described in detail, as already published in [1]. A review article comparing different experimental techniques for measuring particle attrition is provided in [103].

$$E_{cs} = \frac{v^2}{2} = gh \qquad (2.13)$$

E_{cs}	Specific impact energy	$[J/kg]$
v	Impact velocity of the particle	$[m/s]$
g	Gravity	$[m/s^2]$
h	Drop height of particle	$[m]$

2.8.1 Simple drop weight test

Most common for single particle breakage testing is the simple drop weight test. In this test, a weight is released from a certain height onto the sample placed on a rigid anvil underneath (see Figure 2.25). The amount of energy available at impact is simply calculated by Equation 2.14 and can be adjusted by the drop height. Various test rigs were designed in [120–123] with the JKMRC drop test being the most well-known. In [93] an attempt was made to characterize breakage behavior of hot sinter by sinlge particle tests with a drop weight (see Section 2.4.9). The drop weight tester was also used in [124] for calibration of

a bonded particle model (see Section 2.11.1) in discrete element simulations of rocks in a cone crusher. To investigate particle bed fracture with finer particles, the anvil is replaced by a die [125]. In [126] a method to determine fine particle breakage behavior was developed by means of a drop weight tester. [1, 118]
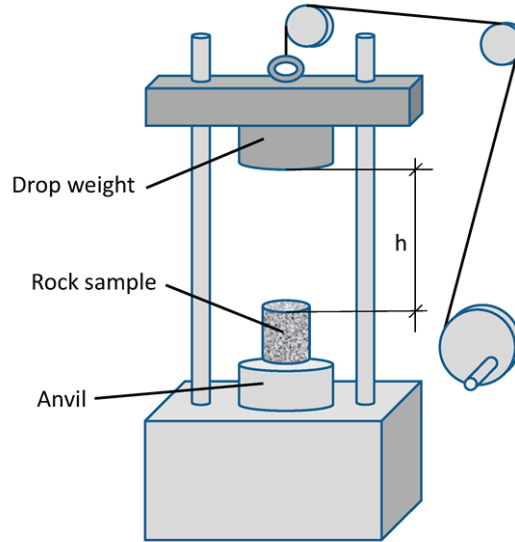
Figure 2.25: a) Schematic illustration of a simple drop weight test apparatus [118]

$$E_c = m_w g h_d \qquad (2.14)$$

E_c	Comminution energy	$[J]$
m_w	Mass of drop weight	$[kg]$
g	Gravity	$[m/s^2]$
h_d	Drop height	$[m]$

2.8.2 Instrumented drop weight test

By adding measurement instrumentation to the drop weight tester, the well-established instrumented drop weight tester called the Ultra-Fast Load Cell device (UFLC) was developed in [99, 127, 128] (see Figure 2.26a). In this device, the sample consisting of individual particles or a bed of particles is placed on a

vertical steel bar and impacted by the drop weight. The impact waves are detected by strain gauges, which are placed on the vertical steel bar. This allows to determine the actual load applied to the sample. With the load-time curves and the calculated deformation, the actual transferred energy can be estimated instead of using the potential energy of the drop weight (see Equations 2.15 to 2.18). E_c is the total energy loss, which is the sum of the energy consumed in particle breakage and other losses such as friction, plastic deformation and heat [128]. With Equation 2.18 and the momentum balance of the falling steel ball, the coefficient of restitution can be calculated by Equation 2.19 in this case, which is an important parameter for DE simulations of ball and rod mills. In Equation 2.19 the terms in square brackets represent the energy of the drop weight after impact [99]. A portable impact load cell device called the Short Impact Load Cell device (SILC), which uses the same principles as the UFLC, was developed in [129] for in-situ quantification of ore breakage behavior. [118, 128]
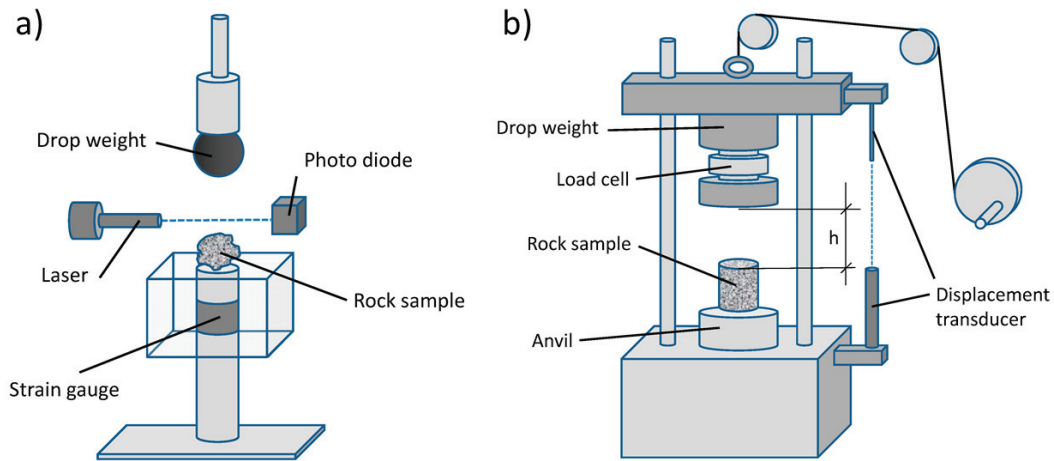
Figure 2.26: Instrumented drop weight tester a) Ultra-Fast Load Cell device b) with load cell on drop weight and inductive displacement transducer [118]

Another instrumented drop weight tester was designed in [130]. It is based on the simple drop weight test and was initially designed for the investigation of particle compaction processes. In this test device a load cell is mounted directly onto the drop weight. The load cell and an inductive displacement transducer allow to create time-dependent measurement profiles for the primary impact and the following rebounds (see Figure 2.26b). The comminution energy transferred to the sample can then be calculated by integration of load-displacement curves. [118]

$$E_i = E_c + E_r + E_{res} \tag{2.15}$$

$$E_r = \frac{1}{\rho AC} \int_0^{t_f} F^2(t)dt \tag{2.16}$$

$$E_i = \frac{m_b v_0^2}{2} \tag{2.17}$$

$$E_c = E_i(1 - e^2) - \frac{1}{\rho AC} \int_0^{t_f} F^2(t)dt \tag{2.18}$$

$$e = \left[E_i - v_0 \int_0^{t_f} F(t)dt - g \int_0^{t_f} F(t)tdt - \frac{1}{m_w} \left(\int_0^{t_f} F(t)dt \right)^2 \right]^{\frac{1}{2}} E_i^{-\frac{1}{2}} \tag{2.19}$$

E_i	Input energy	$[J]$
E_c	Comminution energy	$[J]$
E_r	Energy absorbed in deformation of the rod	$[J]$
E_{res}	Residual energy of the striker	$[J]$
ρ	Density of the rod	$[kg/m^3]$
A	Cross-Sectional area of the rod	$[m^2]$
C	Wave propagation velocity	$[m/s]$
t_f	Final time of contact	$[s]$
e	Coefficient of restitution	$[-]$
m_w	Mass of drop weight	$[-]$
v_0	Velocity of drop weight at instant of impact	$[-]$
g	Gravity	$[m/^2]$

2.8.3 Twin pendulum test

In a twin pendulum tester the particle is crushed between two pendulum-mounted hammers, which are released simultaneously from a certain height [131]. A single particle is placed on a socket and hit simultaneously by both hammers. This procedure is repeated with an incremental increase in the deflection angle of the hammers until the particle breaks. This method is well established to determine the Bond Crushing Work Index C_{WI} of larger particle sizes (50-75 mm), introduced by Bond in [132–134]. Strictly following Bond's measurement standards [132], the C_{WI} is defined by Equation 2.20, with Equation 2.21 for the impact energy per particle thickness. This procedure has been established to test the crushability of ore and was also used to determine coal degradation in [48]. Tavares and Carvalho developed a continuum damage model using particle fracture and a parameter to characterize particle breakage by repeated impacts to predict the C_{WI} in [135]. In [131, 136] the twin pendulum tester was extended by adding instrumentation, which allows to record the pendulum motion. By only lifting one pendulum hammer and mounting the sample on the other, the actually transferred energy to the particle can be determined by evaluating the rebounds of the pendulums after collision. [118]

$$C_{WI} = \frac{53.5 \cdot C_B}{\rho_P} \tag{2.20}$$

$$C_B = \frac{117 \cdot (1 - \theta)}{d_p} \tag{2.21}$$

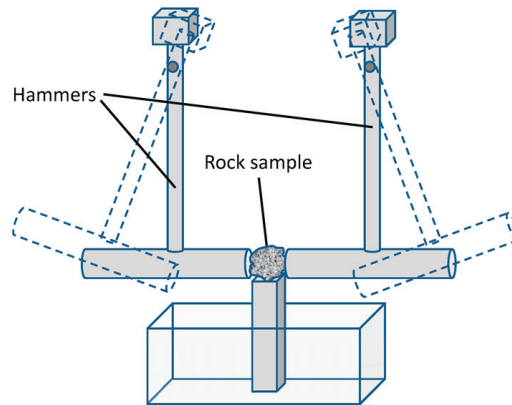|		
C_{WI}	Crushing Work Index	$[kWh/t]$
C_B	Impact energy per particle thickness	$[J/mm]$
ρ_p	Particle density	$[g/cm^3]$
d_p	Particle thickness	$[mm]$
ρ	Density of the rod	$[kg/m^3]$
θ	Deflection angle	$[deg]$

Figure 2.27: Twin pendulum tester [118]

2.8.4 Split Hopkinson pressure bar test

In the Split Hopkinson pressure bar - originally designed for analyzing stress propagation in materials due to detonation of explosives in [137] - the sample is placed between two bars of which one is linked with a rigid block and the other is accelerated by a gas gun (see Figure 2.28). With some modifications, it was also used for particle breakage investigations in [138], where it was named the CSIRO Hopkinson pressure bar. [1, 118]
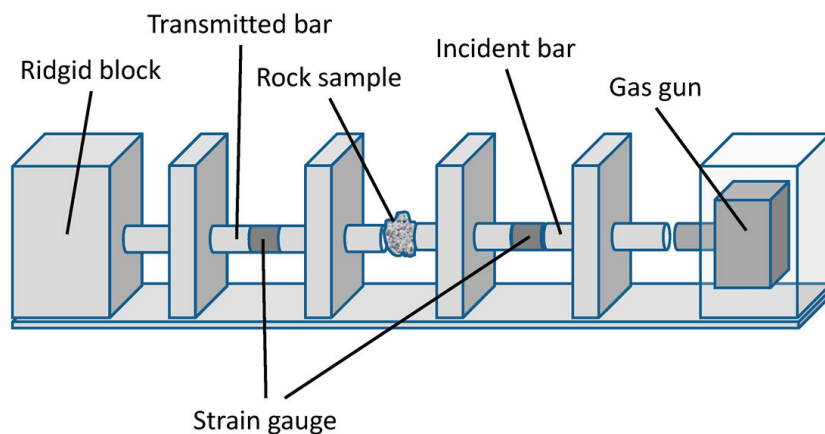

Figure 2.28: Split Hopkinson pressure bar [118]

2.8.5 Pneumatic guns

To describe the fragments of rock cores produced by single particle impact, a test rig where samples are accelerated pneumatically and shot at a steel target was used in [139] and is described in detail in [140]. An air jet device to investigate

single particle impacts of fine grains is presented in [141]. An apparatus for conducting single particle impact tests with iron ore pellets in the size range of 9 to 16 mm was designed in [142] (see Figure 2.29). In these tests a PVC tube is used to propel the pellets against an adjustable steel plate, by compressed air through a solenoid valve. Results in [142] are consistent with those in drop tests, with the advantage that this test method is able to cover a wider range of impact velocities under controlled conditions. [1]
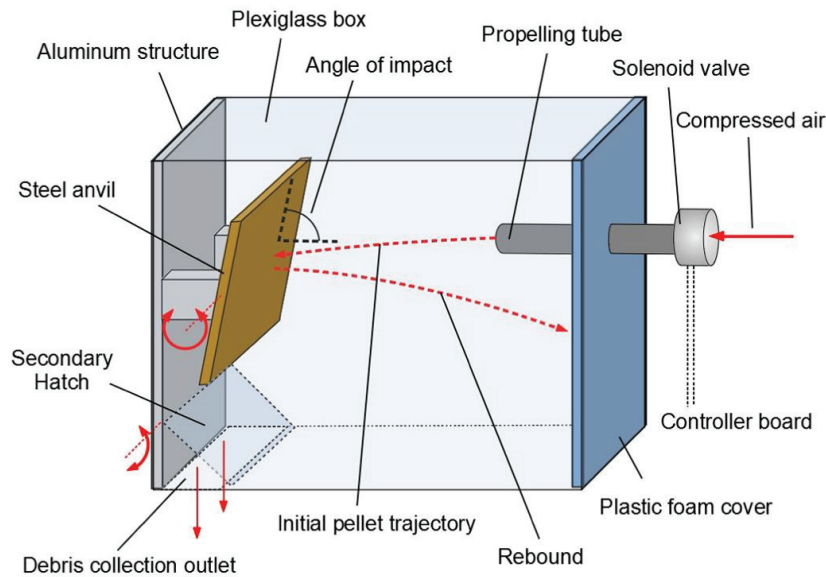

Figure 2.29: Pneumatic impact device [142]

2.8.6 Rotary impact tester

A rapid method for impact testing is the rotary impact tester, first presented by Schönert and Marktscheffel in [115] (see Figure 2.30) and commercially adapted for ore testing by Shi and Kojovic in [143] as the JKRBT. The rotary impact tester mainly consists of a rotor and a surrounding stator (target ring) with a specially formed inner surface to act as an anvil for the accelerated particles. The particles are fed into a chamber in the middle of the rotor, are accelerated in one of the four radial channels by centrifugal forces, travel through the channels in the rotor and crash against the inner surface of the target ring. The inner surface of the target ring is designed to act as impact surface, which is perpendicular to impact velocities at usual rotation speeds. As a feeding device usually a vibrating feeder is used. Particle velocity for each moment consists of a radial and a circumferential component of the same value. When the particles reach the outer diameter d of the rotor, they are ejected with a radial and tangential

component, which are both equal to the circumferential speed of the rotor. As the grinding and feed chamber are evacuated to avoid any disturbing influence of air flows and friction during accelerating and can be neglected, the impact velocity v can be obtained as a function of rotational speed n by Equation 2.22. In the work of Vogel and Peukert [144] small polymer particles were accelerated to high velocities this way. In [145] a test procedure for ore breakage behavior characterization with particle sizes 13.2–45 mm is described by using the JKRBT. [1, 144]
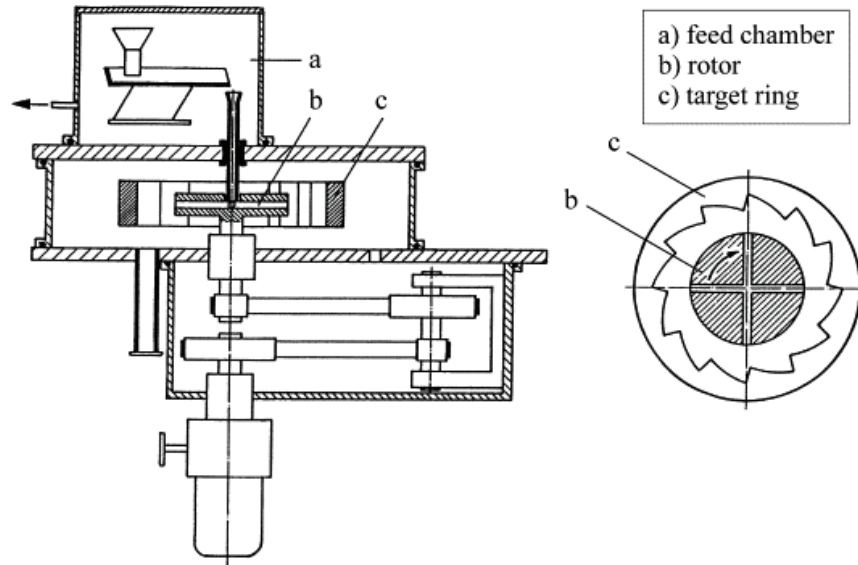
Figure 2.30: Rotary impact tester [115]

$$v = \sqrt{2} \cdot \pi dn \qquad (2.22)$$

v	Impact velocity	$[m/s]$
d	Diameter of the rotor	$[m]$
n	Rotational speed	$[s^{-1}]$

2.8.7 Compression tests

In compression tests the specimen is pressed between two parallel plates and is loaded until failure of the sample. Displacement and load are recorded over the test procedure. Compression tests are mostly used for rock mechanical testing,

where a drill core or samples of regular shapes are tested. For regular shapes, the particle strength can easily be calculated. The particle strength of irregularly-shaped particles due to compression was investigated by Hiramatsu and Oka in [146]. In these investigations, it was shown with photo-elastic methods that the stress states of a sphere, a prism and a cube subject to a pair of concentrated loads are similar. In [146] the stresses of an elastic sphere subject to point load compression were analyzed and after simplifications, the tensile strength can be obtained by Equation 6.2. Various standard test methods are used, which differ in the loading conditions applied [147]. These include the uniaxial compressive test (Figure 2.31a), triaxial test, point load test and indirect tensile strength tests (Figure 2.31b).

If the specimen is not further supported, the test is referred to as the unconfined compressive strength (UCS) test. The UCS is one of the most important mechanical properties of rocks and widely used in mining engineering.

For triaxial compression tests, the specimen is enveloped in a membrane in order to seal it from the surrounding pressure medium, usually oil. Then axial compressive load and oil pressure are increased until failure. Triaxial tests are usually used to measure shear properties of deformable solids, especially soils, granular materials or powders.

In the point load test, the compressive load is applied between the tips of two cones instead of using parallel planes. Point load test devices are relatively compact and are often used in the field to determine the point load strength index, which can further be converted into uniaxial compressive strength, using a material-specific predetermined linear conversion factor [148].

For the indirect tensile strength test, cylindrical specimens are loaded radially between two cushioned plates or curved clamps. This induces an indirect tensile stress and a corresponding deformation in orthogonal direction. Assuming a homogeneous, isotropic and - before failure - linearly elastic material, failure is expected at maximum tensile stress, which then can be calculated by Equation 2.24 [149]. The indirect tensile strength test is also known as the Brazilian test. [118]

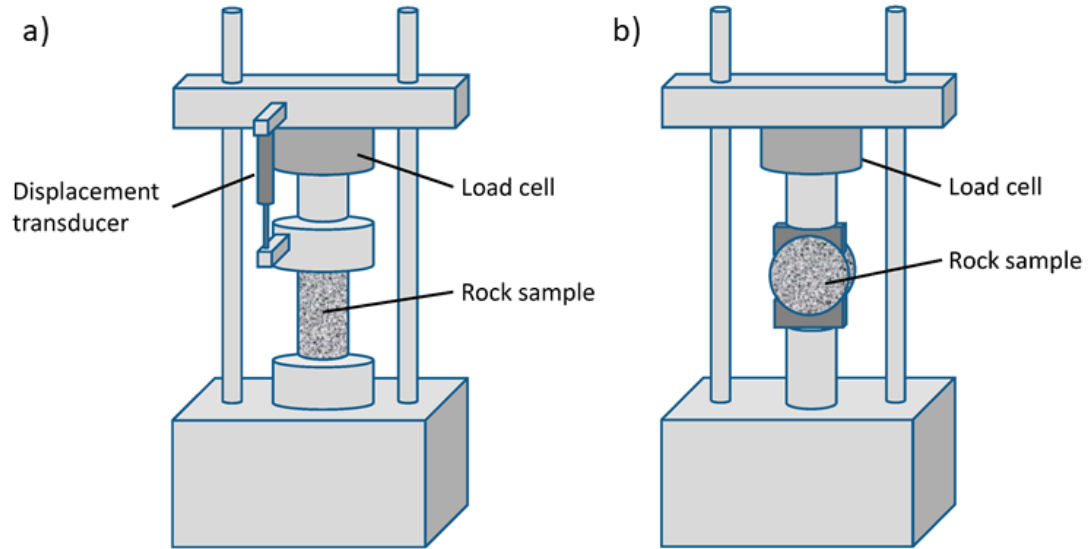$$\sigma_p = \frac{2.8 \, F_{c\,max}}{\pi \, d_p^2} \tag{2.23}$$

Figure 2.31: a) Uniaxial unconfined compressive test b) Indirect tensile
strength test (Brazilian test) [118]

$$\sigma_b = \frac{2\,F_c}{\pi\,d_z\,l} \tag{2.24}$$

σ_p	Particle tensile strength	$[Pa]$
σ_b	Tensile strength at Brazilian test	$[Pa]$
F_c	Compressive load	$[N]$
d_p	Distance between loading points	$[m]$
d_z	Diameter of specimen at Brazilian test	$[m]$
l	Length of specimen at Brazilian test	$[m]$

2.9 Degradation models

Different degradation models for various use cases have been developed to char-
acterize breakage behavior of different materials by describing fines generation,
fragment size distribution or breakage probability. The most relevant for the
degradation of steel-making materials including iron ore sinter are briefly described
in the following Chapter.

2.9.1 Volume breakage constant

Many mathematical models of crushing and grinding processes have been developed for circuit design in the the mineral processing industry. In most of these models, the size degradation is considered as a first-order rate process and it is assumed that results from tumbler drum tests can be treated in a similar manner. For the feed of a single size fraction, the rate of breakage is given by Equation 2.25. When Equation 2.25 is integrated, it can be written as Equation 2.26 or 2.27, with M_0 as the initial mass of the sample in the given size fraction. [37]

$$\frac{dM}{dt} = -kM \tag{2.25}$$

$$\ln\left(\frac{M}{M_0}\right) = -kt \tag{2.26}$$

$$\frac{M}{M_0} = e^{-kt} \tag{2.27}$$

M	Mass of sample remaining in the given size fraction	$[kg]$
M_0	Initial mass of the sample in the given size fraction	$[kg]$
k	Breakage rate constant for the given size fraction	$[-]$
t	Tumbling time	$[min]$

In [55, 61, 62] it is stated that degradation events are discrete and not continuous during drop tests. Assuming first-order breakage kinetics, this results in Equation 2.28 for the volume breakage constant K_V and in Equation 2.29 for the first drop of the sample. Similarly, for the second drop Equation 2.30, which leads to Equation 2.31 for N drops. The numerical value K_V can be determined from the slope of a straight line, when $\log(M_N/M_0)$ is plotted in dependence on N. Thus, K_V is proposed as volume breakage constant and can be considered as an index of strength, where a large K_V means a lower resistance to shatter, a lower bulk strength and a greater extent of breakage. [37]
In [49, 50] the volume breakage constants K_V for coal lumps of different sizes were

determined by dropping the sample onto a steel surface several times from 2.5 m and 7.5 m height. The results from the 2.5 m drop height reveal that, at low drop heights, breakage does not follow a first-order process and there is only a small difference for different lump sizes (see Figure 2.32a). In Figure 2.32b) the graphs of $\log(M_N/M_0)$ versus number of drops N are straight lines, following a first order breakage rate. The gradients of the graphs and the value for K_V increase with increasing lump size for a constant drop height. Thus, the rate of degradation is higher for large lump sizes, which is similar to the findings in [55] and [61, 62]. Large particles preferentially break during initial stages of handling due to in-situ cracks. [37]

Furthermore, the effect of bulk sample mass on the volume breakage constant K_V was investigated in [49, 50]. The results show that an increase in bulk sample mass from 10 kg to 15 kg reduces the volume breakage constant K_V and degradation. It is assumed that with low bulk sample masses a higher percentage of particles collide with the steel surface instead of colliding with other particles. The collisions with other particles, which have not achieved a static state yet after impact, results in smaller impulse forces than colliding with the steel surface. This also agrees with the findings in [55] and [61, 62]. [37]

$$K_V = 1 - \frac{M_1}{M_0} \tag{2.28}$$

$$M_1 - M_0 = -K_V M_0 \qquad or \qquad M_1 = M_0(1 - K_V) \tag{2.29}$$

$$M_2 - M_1 = -K_V M_1 \qquad or \qquad M_2 = M_0(1 - K_V)^2 \tag{2.30}$$

$$M_N = M_0(1 - K_V)^N \tag{2.31}$$

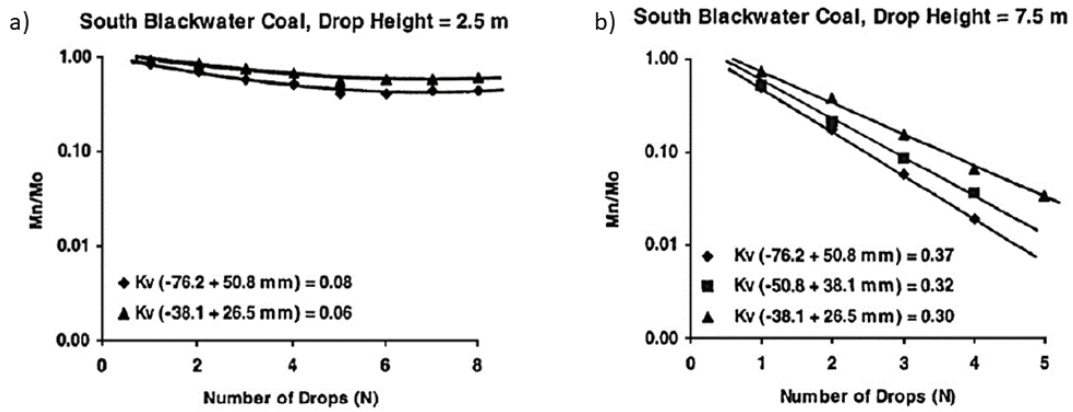| K_V	Volume breakage constant	$[-]$
M_0	Initial mass of the sample in the given size fraction	$[kg]$
M_1	Mass of unbroken material after first drop	$[kg]$
M_N	Mass of unbroken material after N drops	$[kg]$
N	Number of drops	$[-]$

Figure 2.32: Effect of different sizes of coal lumps on volume breakage constant K_V at a) 2.5 m drop height b) 7.5 m drop height [49]

2.9.2 Fines generation model after Sahoo

A fines generation model was developed by Sahoo in [45, 48, 49] to predict the total amount of coal fines generated during handling processes (see Equation 2.32). Orginally developed for coal, it is assumed that it can also be applied to other bulk materials, especially steel-making materials including sinter. In this approach various fines generation effects are tested separately and are represented by a factor. This requires several different trials to obtain each parameter. The most relevant conclusions and some test procedures were already described in Section 2.4. The determination of each parameter is described in detail in [41–50] and reviewed in [37]. With this model, close agreement with experimental data from coal handling at the Gladstone Port was achieved in [48].

$$F = \sum_{j}^{D} \left[\sum_{i}^{N} \{ \lambda_{ij} \phi_{ij} \left(m_{ij} + h_{ij} + w_{ij} - c_{ij} - s_{ij} - st_{ij} \right) \} \right] \qquad (2.32)$$

F	Percentage of produced fines	[%]
λ_{ij}	Percentage of each feed size fraction	[%]
ϕ_{ij}	Percentage of each coal type	[%]
m_{ij}	Fines percentage due to a particular drop height	[%]
h_{ij}	Fines percentage due to handling	[%]
w_{ij}	Fines percentage due to weathering effects	[%]
c_{ij}	Fines percentage due to cushioning effects	[%]
s_{ij}	Fines percentage due to change of impact surfaces	[%]
st_{ij}	Fines percentage due to stabilization effects	[%]
N	Number of feed size fractions	[−]
D	Number of coal types	[−]
i	Size fraction	[−]
j	Coal type	[−]

2.9.3 Surface breakage model after Cavalcanti

Surface breakage or attrition occurs if the stressing level on particles is insufficient to cause volume breakage. In [70] the surface breakage of fired iron ore pellets by impact was investigated for five types of industrial iron ore pellets. Based on the model from Ghadiri and Zhang [150], the average percentage of mass loss due to surface breakage ξ was modeled as a function of particle size, impact energy and impact angle (see Equation 2.33). Impact energy and angle were estimated using DEM in this case. A single material-specific surface breakage parameter κ was able to be identified. The mass-specific impact energy loss $E_{loss,m}$ takes into account normal and shear energy loss. The model was validated with tumbler drum tests. [70]

$$\xi = 100\,\kappa\,d\,E_{loss,m} \tag{2.33}$$

ξ	Average relative mass loss due to surface breakage	$[-]$
κ	Material specific surface breakage parameter	$[kgJ^{-1}m^{-1}]$
d	Particle diameter	$[m]$
$E_{loss,m}$	Mass specific energy loss	$[J/kg]$

2.9.4 Lognormal progeny distribution

Kolmogorov [151] defined the breakage as a random process in which a random number of new fragments is produced [152]. Kolmogorov used the central limit theorem of statistics to prove that the progeny size is lognormally distributed [153, 154]. The probability density function for lognormal distribution follows Equation 2.34.

An alternative expression of Kolmogorov's theory was provided by Halmos [155]. Epstein [153, 156] constructed a statistical model for certain breakage mechanisms and showed that the resulting PSD of the progeny yielded a lognormal distribution for continued repetition of these breakage processes under certain hypotheses. Various studies [157–161], especially in pharmaceutical engineering and powder technology, confirmed Epstein's theory. Delebarre [162] used the Epstein theory to predict the size distribution of coal, coke and iron ore sinter after a number of drop events [1].

Iliev [163] investigated the PSD after crushing unconfined single particles and a particle bed inside a cylindrical container under uniaxial compression by means of numerical simulation. Iliev concluded that single particle crushing produced a lognormal fragment size distribution and that packed bed crushing results in power-law distributed fragments. In Figure 2.33 the simulation of unconfined single particle crushing with different plate heights h is depicted. The corresponding averaged cumulative size distribution and probability density for fragment sizes after 90 realizations are shown in Figure 2.34. In this Figure, the particle diameter is normalized d/d_{max}. [163]

$$P(x) = \frac{1}{x\sqrt{2\pi\sigma^2}} \, exp\left[-\frac{(ln(x) - \mu)^2}{2\sigma^2}\right] \tag{2.34}$$

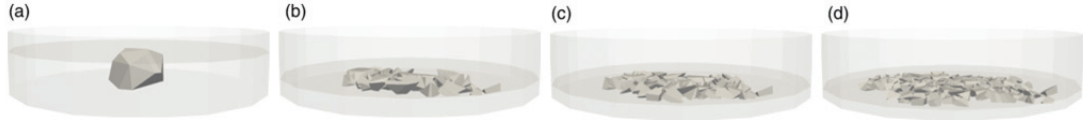| P	Probability density function	$[-]$
μ	Mean	$[-]$
σ	Variance	$[-]$
x	Particle size	$[m]$

Figure 2.33: Simulation of unconfined particle crushing under uniaxial compression with different plate heights: a) h=3 cm b) h=1.125 cm c) h=0.875 cm d) h=0.625 cm [163]
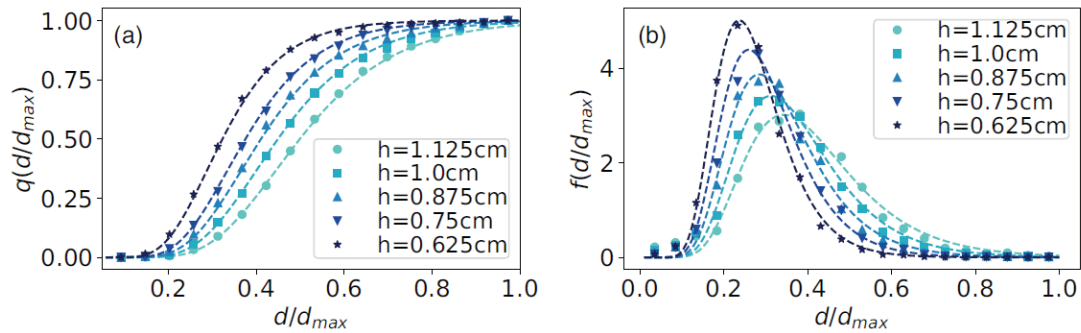

Figure 2.34: Fragment size distributions at different plate heights h averaged over 90 realizations. a) Cumulative PSD b) Probability densities [163]

2.9.5 Weibull statistical model

The Weibull statistics [164], named after W. Weibull, is based on the principle of the weakest link in a chain. The fracture probability P_B for a chain consisting of z links of strength σ_S if a load σ is applied, is given by Equation 2.35. In this equation, m is the shape parameter (sometimes Weibull parameter) of the probability distribution and is not related to a physical property. It has been theoretically and experimentally verified that the tensile strength of brittle materials follows a Weibull distribution [165]. The Weibull statistics were introduced to the field of comminution by Weichert [166, 167] to describe particle fracture energy data of glass beads. In [168] Weibull statistics are applied to describe the fracture of soil particles and in [169] the size effect on the compression breakage strength of glass particles is investigated. The Weibull distribution is also used in mechanical

engineering for lifetime and failure calculations of different systems, like bearings or mechanical wear in an engine, for example.

$$P_B = 1 - exp\left[-z\left(\frac{\sigma}{\sigma_S}\right)^m\right] \tag{2.35}$$

P_B	Probability for breakage	$[-]$
z	Number of links	$[-]$
σ_S	Link strength	$[Pa]$
σ	Applied load	$[Pa]$
m	Shape parameter	$[-]$

2.9.6 Breakage probability after Vogel and Peukert

Following Rumpf's theoretical approach [170] and a fracture mechanical model after Weichert [167], which is based on Weibull statistics [164] (see Section 2.9.5), Vogel and Peukert developed an expression for the breakage probability for different materials in [144, 171, 172]. As the breakable particles were assumed as impacting elastic spheres, the Hertz theory [100] and conclusions from Gildemeister [173] were used for pressure distribution calculations. The probability for breakage P_B due to impact can be calculated by Equation 2.36. A material parameter f_{mat} and a size-independent threshold value $E_{cs,min}$ were introduced, which describe the material influence on the comminution result. Furthermore, the influence of several successive impacts with the same mass-specific energy E_{cs} was taken into account by the parameter k. The model was verified by a trial of single particle tests with a rotary impact tester (see Section 2.8.6). In this trial, different materials including polymers, limestone and glass spheres were accelerated to different velocities up to 140 m/s and the fragments were analyzed by screening. The material parameters f_{mat} and $E_{cs,min}$ were obtained from curve fitting of experimental data. With the material-specific parameters a master curve for the breakage probability was constructed (see Figure 2.35). [144, 171, 172]

$$P_B = 1 - exp\left[-f_{mat}xk\left(E_{cs} - E_{cs,min}\right)\right] \tag{2.36}$$

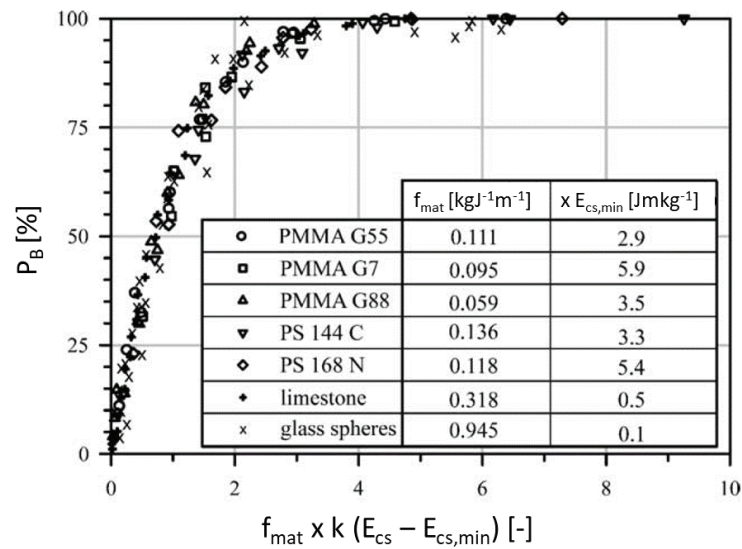|		
P_B	Probability for breakage	$[-]$
f_{mat}	Material parameter	$[kgJ^{-1}m^{-1}]$
x	Particle size	$[m]$
k	Number of successive impacts	$[-]$
E_{cs}	Mass-specific impact energy	$[J/kg]$
$E_{cs,min}$	Minimum mass-specific energy for breakage	$[J/kg]$

Figure 2.35: Master curve for the breakage probability of various materials [144]

2.9.7 The t$_n$-model

The Julius Kruttschnitt Mineral Research Centre (JKMRC) in Brisbane developed a method to estimate the particle size distribution after breakage by defining a parameter set of t_n, where t_n is the cumulative percentage passing $1/n$ of initial particle size [121]. The t_{10} was established as a common breakage index to predict size distributions from the relationship between t_{10} and other t_n curves [174]. Thus, it is also referred to as the t_{10}-approach. The family of t_n curves for a range of ore types in [131] were independently confirmed by using different materials over a wide range of impact energies in [127, 175]. The relationship between energy input and breakage index t_n is given by Equation 2.37. In this equation, A and b are breakage parameters, which have to be fitted from experimental data. [1, 176]

$$t_n = A \left(1 - e^{-bE_{cs}}\right) \tag{2.37}$$

t_n	Cumulative passing 1/n of initial particle size	[%]
E_{cs}	Mass-specific impact energy	[J/kg]
A, b	Model parameters	[−]

Shi and Kojovic [176] modified the breakage probability model by Vogel and Peukert [144, 171, 172] to describe the breakage index t_{10}, also considering the initial particle size, the number of impacts and the threshold energy required to break the particle, which resulted in Equation 2.38. [1]

$$t_{10} = M\{1 - exp\left[-f_{mat}xk\left(E_{cs} - E_{cs,min}\right)\right]\} \tag{2.38}$$

t_{10}	Cumulative passing 1/10 of initial particle size	[%]
M	Maximum t_{10} for a material	[%]
f_{mat}	Material parameter	$[kgJ^{-1}m^{-1}]$
x	Particle size	[m]
k	Number of successive impacts	[−]
E_{cs}	Mass-specific impact energy	[J/kg]
$E_{cs,min}$	Minimum mass-specific energy for breakage	[J/kg]

Various functions have been proposed to describe the cumulative progeny size distribution from drop weight tests. This includes cubic splines [121, 174], the upper-truncated Rosin-Rammler distribution [177, 178] and combined exponential functions [179]. Due to its ability to describe data with great flexibility, the incomplete beta function [180] is often used to describe the progeny size distribution from a given t_{10} value (see Equation 2.39). In this equation, α_n and β_n are model parameters and have to be fitted for each value of n selected. [181]

$$t_n(t_{10}, \alpha_n, \beta_n) = \frac{100}{\int_0^1 x^{\alpha_n-1}(1-x)^{\beta_n-1}\, dx} \int_0^{t_{10}/100} x^{\alpha_n-1}(1-x)^{\beta_n-1}\, dx \qquad (2.39)$$

2.9.8 Tavares breakage model

In contrast to the Vogel and Peukert model or the t_n-model, which are both based on the Weibull distribution, the Tavares breakage model is based on a lognormal distribution. The lognormal distribution was successfully used to describe particle fracture energy or fracture probability of various irregularly-shaped brittle materials in [114, 127, 182] and is given by Equations 2.40 and 2.41 for the cumulative probability. The probability density function is given by Equation 2.34 in Section 2.9.4. The influence of the particle size on particle fracture energy is described by Equation 2.42. $E_\infty, d_{p,0}, \phi$ are model parameters, which have to be fitted from single particle breakage tests. E_∞ the residual-specific fracture energy of the material for large size and $d_{p,0}$ is a characteristic value for the microstructure of the material. E_{50} corresponds to the specific energy that results in breakage of 50% of the particles after a single impact. [99, 183]

$$P(E) = \frac{1}{2}\left[1 + erf\left(\frac{ln(E^*) - ln(E_{50})}{\sqrt{2\sigma_E^2}}\right)\right] \qquad (2.40)$$

$$E^* = \frac{E_{max}E}{E_{max} - E} \qquad (2.41)$$

$$E_{50} = \frac{E_\infty}{1 + k_p/k_s}\left[1 + \left(\frac{d_{p,0}}{d_p}\right)^\phi\right] \qquad (2.42)$$

Using continuum damage mechanics, Tavares and King developed a model for particle fracture by repeated impacts in [183], which was further developed by Tavares in [184]. The specific particle fracture energies at successive impacts are given by Equations 2.43 and 2.44, which have to be solved in an iterative

procedure. Thus, E_n is used for E in Equation 2.40. A simulation procedure for calculating the energy spent in comminution by impact with this model was first presented in [178]. The model was applied to describe breakage rates in a ball mill [185], ore degradation during handling [186] and degradation of iron ore pellets by impact [142]. To additionally describe the progeny size distribution, the t_n-model (see Section 2.9.7) is proposed for further modeling by Tavares in [184]. A review and further validation of the whole procedure with various materials is provided in [181].

$$E_n = E_{n-1}(1 - D_n) \tag{2.43}$$

$$D_n = \left[\frac{2\gamma}{2\gamma - 5D_n + 5} \frac{E_{k,n}}{E_{n-1}} \right]^{\frac{2\gamma}{5}} \tag{2.44}$$

$P(E)$	Cumulative probability for fracture	$[-]$
E	Mass-specific particle fracture energy	$[J/kg]$
E^*	Relative mass-specific particle fracture energy	$[J/kg]$
E_{max}	Mass-specific impact energy below which all particles would break after a single impact	$[J/kg]$
E_{50}	Median of the lognormal distribution	$[J/kg]$
σ_E	Geometric variance of the lognormal distribution	$[-]$
$E_\infty, d_{p,0}, \phi$	Model parameters	$[-]$
k_p	Hertzian stiffness of the particle	$[N/m]$
k_s	Hertzian stiffness of the surface of the test device	$[N/m]$
E_n	Mass-specific fracture energy after n impacts	$[-]$
D_n	Accumulated damage after n impacts	$[-]$
$E_{k,n}$	Kinetic energy of the striker after the n impacts	$[-]$
γ	Damage accumulation constant	$[-]$

2.10 Discrete element method

The discrete element method (DEM) is a numerical method for computing the motion and collisions of particles. The theory of a discrete element model was introduced by Alder and Wainwright in [187] for molecular dynamics studies. The principles of the discrete element method, sometimes also called the distinct element method, were developed by Cundall and Strack in [188]. In contrast to the continuum approach, e.g. Finite Element Method (FEM) or Computational Fluid Dynamics (CFD), the discrete approach models each single particle as a distinct entity and represents granular material as a simplified assembly of particles. The macroscopic system behavior results from individual particle interactions, which makes the discrete approach well suitable for investigating phenomena occurring at the scale of particle diameter and simulating bulk behavior of particles.

DEM has become widely established as an efficient method addressing a variety of engineering problems in granular and discontinuous materials like granular flows, powder mechanics, rock mechanics, fluidized beds and comminution. DEM is applied in various fields: the mining and steel industry, soil, rock and sand handling, agriculture, the food industry, the pharmaceutical and chemical industry, waste management, mass product handling, etc. (see Figures 2.11 and 2.36).
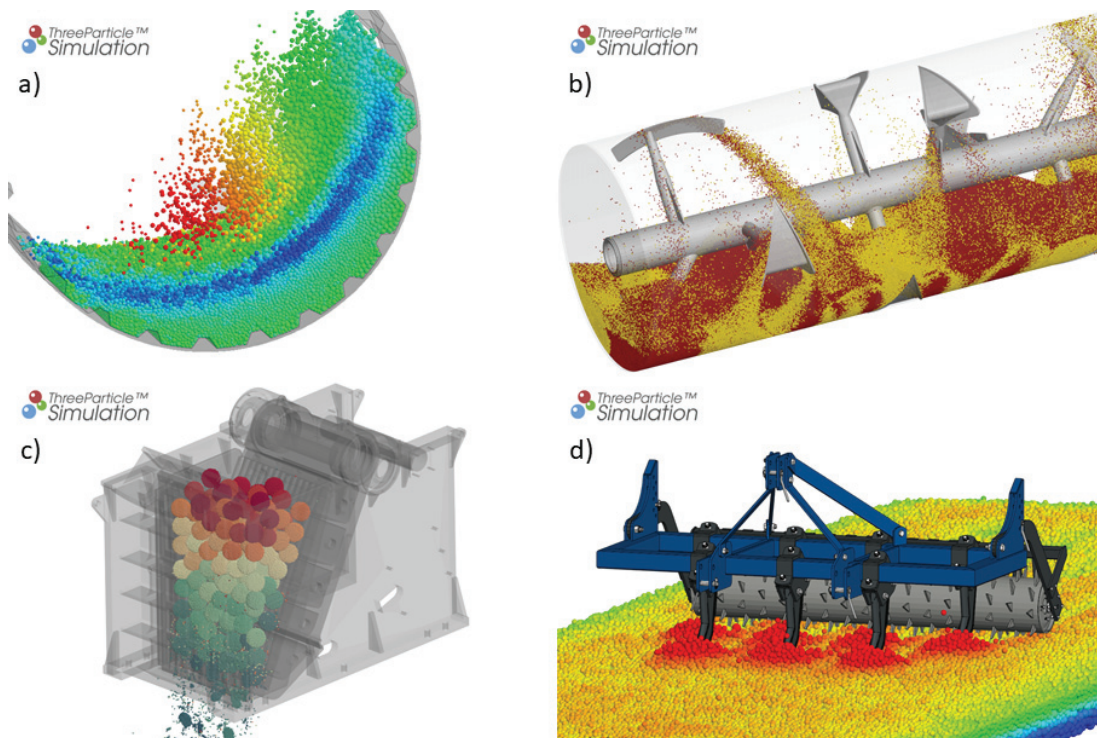
Figure 2.36: Examples for applications of DEM using ThreeParticle a) SAG mill b) plow mixer c) jaw crusher (BPM) d) chisel plow [189]

Also related to DEM is the method of smoothed particle hydrodynamics (SPH), introduced by Gingold and Monaghan in [190] and Lucy in [191]. SPH uses particles to represent continuum media, which is particularly suitable for numerical simulation of fluids. [192, 193]

2.10.1 The DEM computation scheme

The entire computation process of a DEM simulation can be described as a repetitive loop (see Figure 2.37). In this loop a series of subordinate systems is calculated iteratively. Fundamentally, the DEM solves Newton's equations of motion (Newton's second law, see Equation 2.45) by numerical integration (see Equations 2.46 and 2.47) to compute translational and rotational accelerations, velocities and positions of the particles.

Then all contacts, including inter-particle and particle-wall contacts, are detected by contact detection algorithms. In these algorithms, the computation domain is divided into cubic cells, the size of which depends on the smallest particle. The optimum cell in terms of computational efficiency and detection accuracy should be 1.5-2 times the smallest particle radius, as proposed in [194].

Afterwards the contact forces are calculated using the force-displacement laws according to a suitable contact model (contact mechanics). The contact forces are separated in normal and tangential direction with different requirements. Material and interaction properties are defined by the user. There are various contact models to describe elastic, plastic and cohesive behavior. Cohesion contact models allow to simulate pasty materials as in [195, 196], for example. Additional multiphysics like heat transfer, electrostatics, tribocharge, moisture and sintering can also be implemented. A multiphysical model to describe thermal expansion was developed by Mitterlehner and Kartnig in [197] to describe the stress increase on the walls of packed-bed thermal energy storages (TES) and load modification due to several loading and unloading processes (thermal ratcheting phenomenon) [198]. The most common contact model is the Hertz-Mindlin model (see Section 2.10.3). Other common contact models are the Hooke, Linear Spring, Linear Cohesion, Johnson-Kendall-Roberts (JKR) [199] and Hysteretic Spring model, to name a few [200].

Most DEM software programs use the soft-sphere approach (in contrast to the hard-sphere approach), where particles are assumed to be rigid (not deformable) but small overlaps δ are allowed to represent deformations during contact (see Figure 2.38). Overlaps, relative velocity, normal and tangential vectors are calculated by Equations 2.48, 2.49, 2.50 and 2.51. [192, 193, 201, 202]
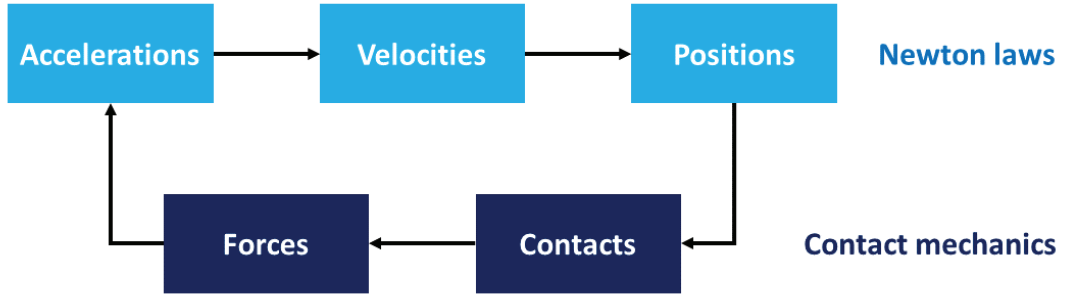
Figure 2.37: Basic DEM computation loop [193]

$$\sum_i \vec{F}_i = m\ddot{\vec{x}} \qquad and \qquad \sum_i \vec{M}_i = \mathbf{I}\ddot{\vec{\varphi}} \qquad (2.45)$$

$$\vec{x}(t + \Delta t) = \vec{x}(t) + \dot{\vec{x}}(t)\Delta t \qquad and \qquad \vec{\varphi}(t + \Delta t) = \vec{\varphi}(t) + \dot{\vec{\varphi}}(t)\Delta t \qquad (2.46)$$

$$\dot{\vec{x}}(t + \Delta t) = \dot{\vec{x}}(t) + \ddot{\vec{x}}(t)\Delta t \qquad and \qquad \dot{\vec{\varphi}}(t + \Delta t) = \dot{\vec{\varphi}}(t) + \ddot{\vec{\varphi}}(t)\Delta t \qquad (2.47)$$

$\vec{F}$	Force	$[N]$
$\vec{M}$	Torque	$[Nm]$
m	Mass	$[kg]$
$\mathbf{I}$	Moment of inertia tensor	$[kg\,m^2]$
$\vec{x}$	Distance	$[m]$
$\dot{\vec{x}}$	Velocity	$[m/s]$
$\ddot{\vec{x}}$	Acceleration	$[m/s^2]$
$\vec{\varphi}$	Rotation angle	$[rad]$
$\dot{\vec{\varphi}}$	Rotational speed	$[s^{-1}]$
$\ddot{\vec{\varphi}}$	Angular acceleration	$[s^{-2}]$
t	Time	$[s]$
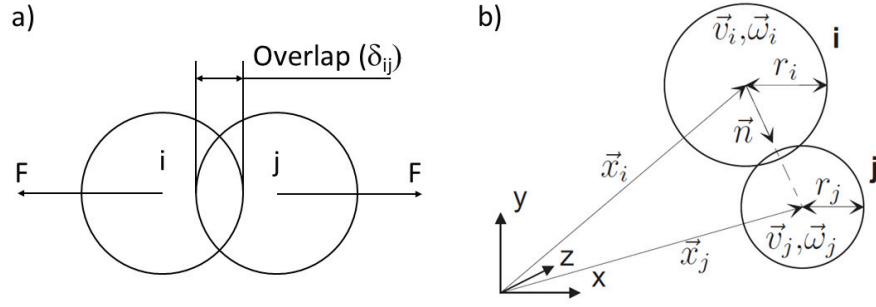
Figure 2.38: a) Soft-sphere approach allowing small overlaps for calculation of forces b) Contact calculation in a three-dimensional simulation space [202]

$$\delta_{ij} = max(0\,,\, r_i + r_j - |\vec{x}_j - \vec{x}_i|) \tag{2.48}$$

$$\vec{n}_{ij} = \frac{\vec{x}_j - \vec{x}_i}{|\vec{x}_j - \vec{x}_i|} \qquad and \qquad \vec{t}_{ij} = \frac{\vec{v}_{ij} - (\vec{v}_{ij} \cdot \vec{n}_{ij})\vec{n}_{ij}}{|\vec{v}_{ij} - (\vec{v}_{ij}\dot{\vec{n}}_{ij})\vec{n}_{ij}|} \tag{2.49}$$

$$\vec{v}_{ij} = \vec{v}_i - \vec{v}_j + \vec{\omega}_i \times (r_i\vec{n}_{ij}) - \vec{\omega}_j \times (-r_j\vec{n}_{ij}) \tag{2.50}$$

$$\vec{v}_{n,ij} = (\vec{v}_{ij} \cdot \vec{n}_{ij})\vec{n}_{ij} \qquad and \qquad \vec{v}_{t,ij} = (\vec{v}_{ij} \cdot \vec{t}_{ij})\vec{t}_{ij} \tag{2.51}$$

$x_{i/j}$	Position vector of particle i or j	$[m]$
$\vec{v}_{i/j}$	Velocity vector of particle i or j	$[m/s]$
$\vec{\omega}_{i/j}$	Angular velocity vector of particle i or j	$[s^{-1}]$
δ_{ij}	Overlap between particle i and j	$[m]$
$\vec{n}_{ij}$	Normal vector	$[-]$
$\vec{t}_{ij}$	Tangential vector	$[-]$
$\vec{v}_{ij}$	Relative velocity vector	$[m/s]$
$\vec{v}_{n,ij}$	Normal relative velocity vector	$[m/s]$
$\vec{v}_{t,ij}$	Tangential relative velocity vector	$[m/s]$

2.10.2 Time step

Choosing the right time step Δt is of critical importance in DE simulations for the following reasons. The choice of the right time step is always a compromise between computational efficiency on the one side and numerical stability and accuracy on the other side. On the one hand, small time steps lead to higher computational effort as more time steps have to be computed, which leads to longer computing times to reach the required simulation time. On the other hand, the time step has to be chosen sufficiently small to prevent excessive overlaps, which result in unrealistically high forces. This depends on particle radii and maximum velocities. Furthermore, the time step has to be chosen small enough to avoid the effect of disturbing Rayleigh waves, considering to wave propagation along surfaces of elastic solids based on the work by Rayleigh [203]. In addition to contacts with its immediate neighbors, the movement of a particle in a granular flow is also affected by disturbance propagations from particles far away. The Rayleigh time step is approximated from Rayleigh surface wave propagation speed and is calculated by Equation 2.52. To ensure realistic force transmission and avoid numerical instability, a fraction of the Rayleigh time step should be chosen. Further parameters affecting time step choice are bondings and complex particle geometries, especially geometries with sharp edges, as used in this thesis. Further work dealing with time step dependency in DEM is provided by O'Sullivan and Bray in [204]. A typical time step range for DEM is 10^{-4} to $10^{-6}\,s$. [193, 205]

$$T_R = \frac{\pi R \sqrt{\frac{\rho}{G}}}{0.1631\,\nu + 0.8766} \tag{2.52}$$

T_R	Rayleigh time step	$[s]$
R	Particle radius	$[m]$
ρ	Particle density	$[kg/m^3]$
G	Shear modulus	$[Pa]$
ν	Poisson's ratio of the particle	$[-]$

2.10.3 Hertz-Mindlin contact model

The Hertz-Mindlin (no-slip) contact model is the default model used in many DEM software programs, inlcuding EDEM and ThreeParticle, which are used in this thesis. It has been established as default model due to its accurate and efficient force calculation. The normal force component is based on the Hertzian contact theory [100]. The tangential force component is based on the work of Mindlin and Deresiewicz [206, 207]. In this model both normal and tangential forces have an elastic and a damping component (see Figure 2.39). The damping constant is related to the coefficient of restitution (see Section 2.5.3) as described in [208]. The tangential friction force is calculated by Coulomb's law of friction, as described in [188].

For the contact between two particles i and j the Hertz-Mindlin model uses an equivalent mass m^*, radius R^* and Young's modulus E^*, which are calculated by Equations 2.53 and 2.54. With the Poisson's ratio, the equivalent shear modulus G^* can be determined by Equation 2.55. When a particle-wall contact is computed, the particle radius and mass are considered as equivalent radius and equivalent mass. The overall contact force is calculated by Equation 2.56. The tangential force term is limited by the Coulomb friction force $|\vec{F_{Cf}}|$, given by Equation 2.57. Especially in the software ThreeParticle, which is mostly used in this thesis, a distinction is made between a normal overlap δ_n and a tangential overlap vector $\vec{\delta_t}$. In this case the tangential (shear) force is a "history" effect, which accounts for the tangential displacement or tangential overlap for the duration of the contact [201]. At the Hertz-Mindlin contact model the elastic constants k_n and k_t are functions of the normal overlap δ_n and are computed by Equation 2.58. The damping constants γ_n and γ_t are calculated by Equation 2.59 with Equations 2.60 and 2.61. [200, 201]

$$\frac{1}{m^*} = \frac{1}{m_i} + \frac{1}{m_j} \qquad and \qquad \frac{1}{R^*} = \frac{1}{R_i} + \frac{1}{R_j} \tag{2.53}$$

$$\frac{1}{E^*} = \frac{1 - \nu_i^2}{E_i} + \frac{1 - \nu_j^2}{E_j} \tag{2.54}$$
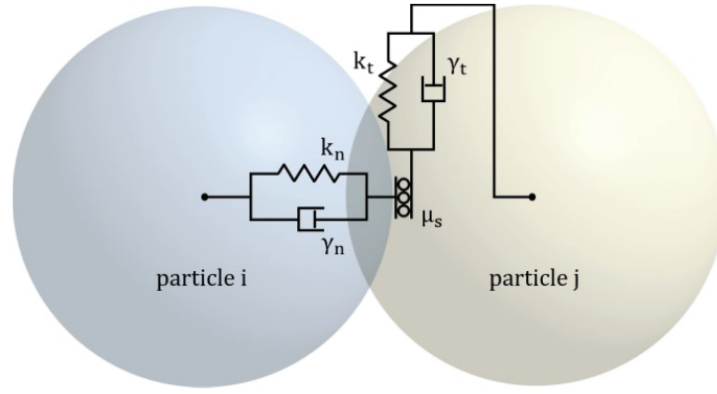
Figure 2.39: Hertz-Mindlin contact model [205]

$$G^* = \frac{E^*}{2(1+\nu)} \qquad (2.55)$$

m^*	Equivalent particle mass	$[kg]$
$m_{i/j}$	Particle mass of particle i or j	$[kg]$
R^*	Equivalent particle radius	$[m]$
$R_{i/j}$	Particle radius of particle i or j	$[m]$
E^*	Equivalent Young's modulus	$[Pa]$
$E_{i/j}$	Young's modulus of particle i or j	$[Pa]$
G^*	Equivalent shear modulus	$[Pa]$
e	Coefficient of restitution	$[-]$

$$\vec{F}_{contact} = (k_n \delta_n \vec{n}_{ij} - \gamma_n \vec{v}_{n,ij}) + (k_t \vec{\delta_t} - \gamma_t \vec{v}_{t,ij}) \qquad (2.56)$$

$$|\vec{F}_{Cf}| = \mu_s k_n \delta_n \geq k_t |\vec{\delta_t}| \qquad (2.57)$$

$$k_n = \frac{4}{3} E^* \sqrt{R^* \delta_n} \qquad and \qquad k_t = 8 G^* \sqrt{R^* \delta_n} \qquad (2.58)$$

$$\gamma_n = -2\sqrt{\frac{5}{6}} \beta \sqrt{S_n m^*} \qquad and \qquad \gamma_t = -2\sqrt{\frac{5}{6}} \beta \sqrt{S_t m^*} \qquad (2.59)$$

$$S_n = 2 E^* \sqrt{R^* \delta_n} \qquad and \qquad S_t = 8 G^* \sqrt{R^* \delta_n} \qquad (2.60)$$

$$\beta = \frac{ln(e)}{\sqrt{ln^2(e) + \pi^2}} \qquad (2.61)$$

$\vec{F}_{contact}$	Contact force	$[N]$
k_n	Elastic constant of the normal contact	$[N/m]$
k_t	Elastic constant of the tangential contact	$[N/m]$
γ_n	Viscoelastic damping constant for normal contact	$[kg/s]$
γ_t	Viscoelastic damping constant for tangential contact	$[kg/s]$
$\vec{v}_{n,ij}$	Normal relative velocity vector	$[m/s]$
$\vec{v}_{t,ij}$	Tangential relative velocity vector	$[m/s]$
δ_n	Normal overlap	$[m]$
$\vec{\delta_t}$	Tangential displacement vector	$[m]$
$\vec{F}_{Cf}$	Coloumb friction force	$[m]$
μ_s	Coefficient of static friction	$[-]$

Additionally, rolling friction can be implemented, mostly using the contact-independent constant directional torque (CDT) model as described in [209, 210]. A torque $\vec{M}_i$ directed against the rotation is applied to the contacting surfaces of the particle i. The torque $\vec{M}_i$ is calculated by Equation 2.62 and defined by a rolling friction coefficient μ_r. A rolling friction model allows to model non-spherical behavior for round particles. [200, 201]

$$\vec{M}_i = -\mu_r k_n \delta_n \, \vec{R}_i \times \vec{\omega}_i \tag{2.62}$$

$\vec{M}_i$	Torque due to rolling friction	$[N/m]$
μ_r	Coefficient of rolling friction	$[-]$
$\vec{R}_i$	Distance vector from contact point to the center of mass	$[m]$
$\vec{\omega}_i$	Angular velocity vector of the particle at the contact point	$[s^{-1}]$

2.10.4 Hooke contact model

Very similar to the Hertz-Mindlin contact model, but with a slight difference, is the Hooke contact model in the DEM software ThreeParticle. In contrast to the Hertz-Mindlin model (compare Equations 2.58), the elastic constants k_n and k_t are independent of the normal overlap δ_n and calculated by Equations 2.63. Thus, the contact force $\vec{F}_{contact}$ is linearly dependent on the normal overlap δ_n. In the Hertz-Mindlin contact model, the contact force $\vec{F}_{contact}$ is dependent on $\delta_n^{\frac{3}{2}}$ (see Equation 2.56). [201]

$$k_n = \frac{4}{3} E^* \sqrt{R^*} \qquad and \qquad k_t = 8 G^* \sqrt{R^*} \tag{2.63}$$

2.11 Particle breakage models in DEM

In general, three different principles are established to simulate particle breakage embedded in DEM and are implemented and ready to use in various DEM software programs including EDEM, ROCKY and ThreeParticle. A comparison of these models, simulating the impact on particle beds is provided in [192].
A different approach, in which DEM is only used to obtain the collision history and breakage predicted by a post-processing routine, is provided in [211]. For mills, approaches coupling DEM with populations balance models (PBM) are established due to the high number of fine particles resulting from grinding [212]. An example of a one-way DEM-PBM coupling is given in [185]. An example of a two-way DEM-PBM coupling, in which the DE simulation is rerun with updated PSD after significant changes in PSD, is given in [213].

It has to be considered that there is no general solution for all comminution and degradation processes in DEM and the optimum solution that fits for the specific problem has to be selected [212].

2.11.1 Bonded particle model

The bonded particle model (BPM) was developed by Potyondy and Cundall [214] to mimic the behavior of agglomerates containing cemented granular materials. In this model, a meta-particle of any shape is assembled by numerous smaller sub-particles, which are bonded together by a virtual cylinder. The bonds between the particles break when a critical stress is exceeded.

In general, two types of bondings are distinguished: longitudinal-only bondings and beam-theory-based bondings. Longitudinal-only bondings can only transmit longitudinal loads, such as tension and compression. The transmitted force can be calculated with a stress-strain relation, for example, using the Young's modulus and a cross-sectional bonding area. Beam-theory-based bondings can handle and transmit tension, compression, shear, torsion and bending, and are used for general load cases (see Figure 2.40). The forces and torques acting on a single bond are calculated by Equations 2.64, 2.65 and 2.66. The criterion for rupture is the excess of a critical normal stress σ_c or a critical shear stress τ_c, which are model parameters and are defined by the user. As the bond radius R_b usually depends on the diameter of the smallest particle in contact, inhomogeneous agglomerates can be created by varying particle sizes. Inhomogeneous agglomerates can be modeled, for example, by using bimodally [124] or normal-distributed [215] particle sizes. Most commonly, the bond is modeled as a homogeneous cylindrical beam element as this does not require additional orientation. The use of beam theory approaches including the Timoshenko beam theory [216–218] have been proven to be suitable for DEM bonding applications. [192, 205]

The BPM model can explain several aspects of the mechanical behavior of a particle [219]. The BPM is widely established to investigate and simulate the behavior of single rock particles. Potyondy and Cundall demonstrated in [214] that the BPM was able to simulate the strain-softening response of granite during confined and unconfined compression. In [220] it was shown that the frequency of bond breakage correlated to acoustic emissions. Individual particle studies with the BPM are not limited to slow compression, as demonstrated by Kafui and Thornton in [221], where the impact of spherical, face-centered cubic agglomerates on a target wall was simulated. Further investigations regarding breakage of bonded agglomerates during impacts were conducted by Metzger

and Glasser in [222]. In these investigations, the effects of impact velocity and bond strength on the force exerted on the wall and the bond breakage were investigated. The breakage of quasi-brittle materials, which exhibit crack growth prior to catastrophic failure, was simulated in [223, 224] by Khanal et al. The BPM has also been used to simulate size reduction equipment including ball mills [225], wheat mills [226] and crushers. Quist [124, 227] used the BPM to simulate the breakage of granite in a cone crusher. However, simulations of crushers with the BPM require either severe simplifications or high computational effort [192]. Simulations of complex-shaped particle breakage using the BPM were conducted by Platzer in [228]. Fimbinger [205] developed a methodology for dynamic belt simulation based on the BPM, also published in [229–232], and applied in [233] for the simulation of round balers pressing hay in agricultural machines. [192]
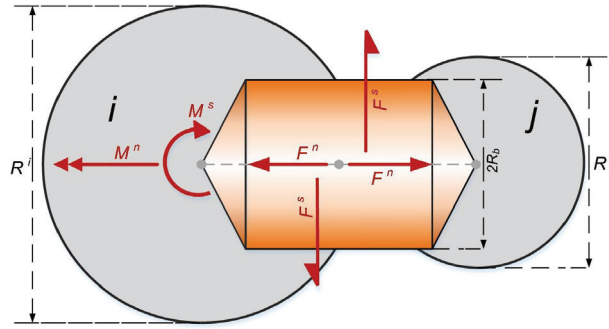
Figure 2.40: Illustration of the bonded particle model (BPM). Two spherical particles cemented by a cylindrical bond [192]

$$\Delta F_n = -k_n \, A \, v_n \, \Delta t \qquad and \qquad \Delta F_s = -k_s \, A \, v_t \, \Delta t \qquad (2.64)$$

$$\Delta M_n = -k_n \, J \, \omega_n \, \Delta t \qquad and \qquad \Delta M_s = -k_s \, J \, \omega_t \, \Delta t \qquad (2.65)$$

$$A = \pi R_b^2 \qquad\qquad I = \frac{1}{4}\pi R_b^4 \qquad\qquad J = \frac{1}{2}\pi R_b^4 \qquad (2.66)$$

$$\sigma = \frac{F_{b,total}}{A} + \frac{2M_b}{J}R_b > \sigma_c \qquad and \qquad \tau = \frac{F_{s,total}}{A} + \frac{2M_b}{J}R_b > \tau_c \qquad (2.67)$$

F_n	Normal force	$[N]$
F_s	Shear force	$[N]$
M_n	Torque acting in normal direction	$[Nm]$
M_s	Torque acting in shear direction	$[Nm]$
k_n	Normal bond stiffness	$[Nm^{-3}]$
k_s	Tangential bond stiffness	$[Nm^{-3}]$
A	Cross-sectional area of bond	$[m^2]$
J	Polar moment of inertia	$[m^4]$
I	Moment of inertia	$[m^4]$
R_b	Bond radius	$[m^4]$
v_n	Normal velocity	$[m/s]$
v_t	Tangential velocity	$[m/s]$
ω_n	Normal angular velocity	$[s^{-1}]$
ω_t	Tangential angular velocity	$[s^{-1}]$

2.11.2 Particle replacement model

In the particle replacement model (PRM), originally proposed by Cleary [234, 235], the particles are instantaneously replaced by several smaller progeny particles when the criterion for failure is met (see Figure 2.41). The progeny particles are usually spheres, sometimes also clumped spheres or superquadrics. The failure criterion can be the excess of a critical force, for example. A major benefit of the replacement method is that the progeny sizes can be defined, which leads to high accuracy in terms of the resulting fragment size distributions. Another advantage is that no additional calibration is needed, as it is the case for other breakage models, such as the bonded particle model (BPM) [124, 214] (see Section 2.11.1), in which the bond calibration requires great effort.

The PRM was used to describe particle breakage under confined conditions [192, 236–238], in geotechnical applications [192, 239] and in comminution equipment including different types of crushers [240–242]. The vast majority of the established and commonly used particle replacement models use spheres as progeny particles for computational efficiency. However, the major disadvantage here is the volume loss which occurs when a large sphere is replaced by several smaller spheres. Even with the densest sphere packing, which is a face-centered cubic lattice arrangement,

as stated by J. Kepler and proven by many mathematicians, a packing density of only 74.05% can be achieved [243]. To ensure mass constancy, the fragment density was adjusted in [244], which is negligible in mills and crushers, but less suitable for conveying processes with high mass flows because flow behavior and loads on conveying equipment would be distorted.

In the work of Tavares et al. [245] volume and mass constancy is ensured by overlapping the following smaller spheres and defining damping factors for the following time steps to avoid explosions. Thus, the fragments drift apart, which is realistic in many cases, but is also assumed to lead to "swelling effects" in a bulk sample and might be disadvantageous in some applications. Further limitations of spherical particles are the description of particle shape and applications when severe rebreakage occurs, which is not the case for polyhedral particles [212].

On the other hand, the replacement by spheres is advantageous in terms of computational efficiency. With spherical particles, the least effort in contact detection and force calculation is necessary and a straight forward conversion to size distribution is possible [212]. The particle replacement with overlapping spheres and damping factors was implemented in EDEM [246], where it is referred to as the Tavares breakage model because the degradation model is also based on the work of Tavares [99] and was further developed by his group at the Federal University of Rio de Janeiro (UFRJ), which is described in Section 2.9.8.

In ROCKY version 4.1, a breakage algorithm was introduced, also called the Tavares breakage model. Here the degradation model is based on the work of Tavares [99] and for fragment generation, the Voronoi subdivision algorithm (see Section 2.12) is used for mass and volume conservation [247, 248]. The implementation of this model in ROCKY was validated in [249] by simulation of single particle drop weight tests using non-round particles. In [248] this model was used to simulate coal breakage in a conveyor transfer chute. [7, 192]
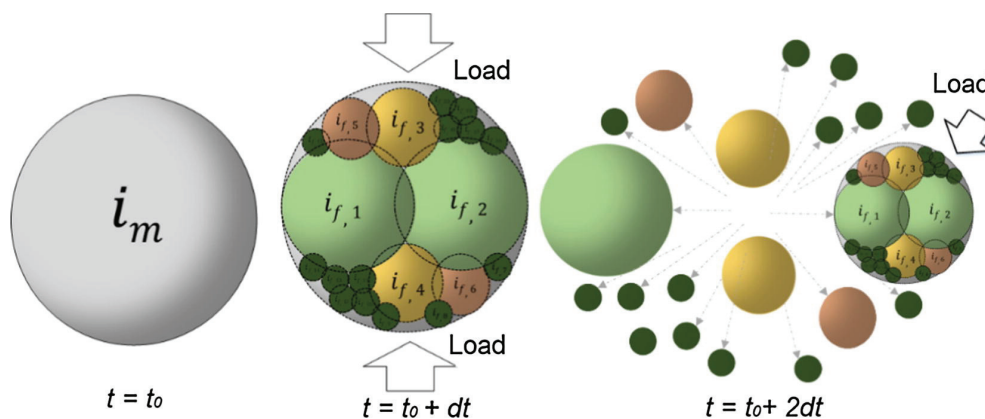
Figure 2.41: Illustration of the particle replacement model (PRM) [192]

2.11.3 Fast breakage model

Potapov and Campbell [250] first introduced a model involving polyhedral particles to describe the breakage of individual particles. This approach was also used to model the breakage in particle beds by Potapov and Campbell in [251] and Paluszny et al. in [252]. Furthermore, it was applied to simulate comminution equipment in by Lichter in [253] and Herbst in [254].

The original model described the interaction of each polyhedral element during stressing, which was called discrete grain breakage [254]. Due to the large computational effort of the original model, a simplified version was developed. The simplified version also includes polyhedral elements, is more suitable for large particle amounts and is called the fast breakage model (FBM). The FBM was first published by Potapov et al. in [255] and is a type of particle replacement model (see Section 2.11.2). In the FBM, instantaneous breakage occurs the first time the collision energy exceeds the minimum fracture energy. Therefore, the Laguerre-Voronoi tessellation, as described in [256, 257] is used to segment the particle in 2D polygons or 3D polyhedrons (see Figure 2.42). Contacts between individual particles are computed using the linear hysteresis contact model [258, 259].

The FBM coupled with submodels using the Vogel and Peukert approach [144, 171, 172] for the breakage probability (see Section 2.9.6) and the t_n approach [176, 177] for the progeny size distribution (see Section 2.9.7) is implemented in ROCKY version 3.11. In this model, fragments may be further broken until a minimum particle size is reached. To mimic the typical brittle material breakage response during fragmentation, finer debris is replaced in the vicinity of the contact points and coarser fragments are replaced away from the contact points [98]. [192]
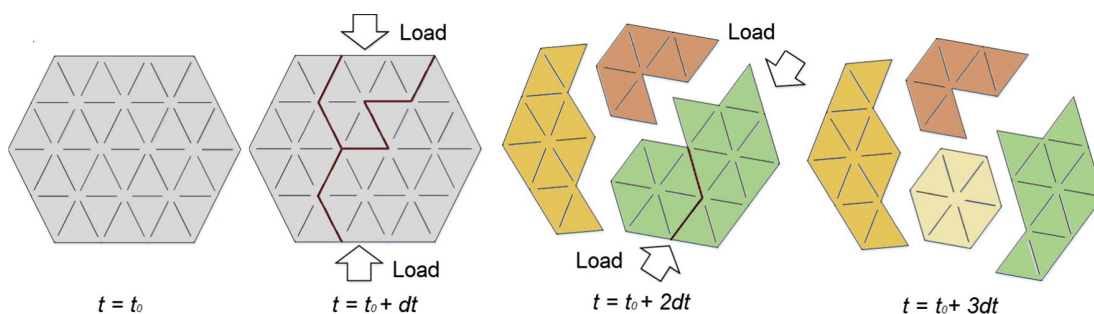
Figure 2.42: Illustration in 2D of multiple breakage events using the fast breakage model (FBM) [192]

2.11.4 Discrete breakage model

The discrete breakage model (DBM) is also based on the work of Potapov and Campbell [250, 260] and has recently been implemented in ROCKY. In the DBM the particles are discretized into a number of elements of simple geometrical shapes, such as Voronoi triangles or Dealunay tetrahedra. This approach is similar to the one in the FBM (see Section 2.11.3). Every element interacts with other elements and bounding geometries, which results in an internal stress state. The elements within each particle are additionally bonded to their neighboring elements by a joint. Each of the joints can be set to break under different circumstances, which is similar to the BPM (see Section 2.11.1). After a joint is broken, neighboring elements only interact by overlapping. Thus, the particle loses its integrity, which models the breakage of the particle. In [261] Petit et al. recently simulated the breakage of iron ore pellets with the DBM in order to validate it and observe its main features, advantages and disadvantages. [261]

2.12 Voronoi tessellation

The Voronoi tessellation, named after G. Voronoi [262, 263], is an efficient way to tessellate areas and volumes. In the Voronoi tessellation algorithm randomly-distributed points (seeds) are generated. Then the area or volume is split half way between all neighboring seeds along lines perpendicular to the (imaginary) connecting lines of two seeds. This partitions the area or volume into polygons or polyhedrons (see Figure 2.43). Each polygon or polyhedron contains exactly one seed and every point in a polygon or polyhedron is closer to its generating seed than to any other seed. The resulting pattern is called Vornoi diagram, regions or cells and is sometimes also referred to as Dirichlet regions [264] or Thiessen polytopes [265]. The Voronoi tessellation algorithm is already established in 3D-animation and in the gaming industry. [5, 7, 17, 266]
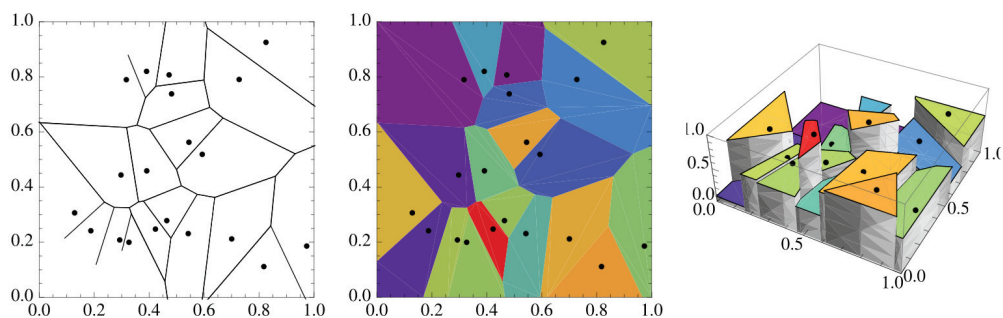
Figure 2.43: Illustration of a Voronoi tessellation of an area [266]

Voronoi diagrams have practical and theoretical applications in many fields, such as science, technology or visual arts [267]. In science, they are employed in a wide variety of areas including material science [268], for example in astrophysics to find galaxy clusters [269], in mining to predict the location of mineral resources [270], in meteorology to predict and model rainfall patterns [271], in biology to describe bone structure [272] and to model biological cells [273] and in medical diagnostics [274]. Voronoi patterns frequently occur in nature, for example in dried mud, honeycombs, the fur of giraffes, foam, the structure of dragonfly wings and plant leaves, on sea turtles, etc. (see Figure 2.44). [275]
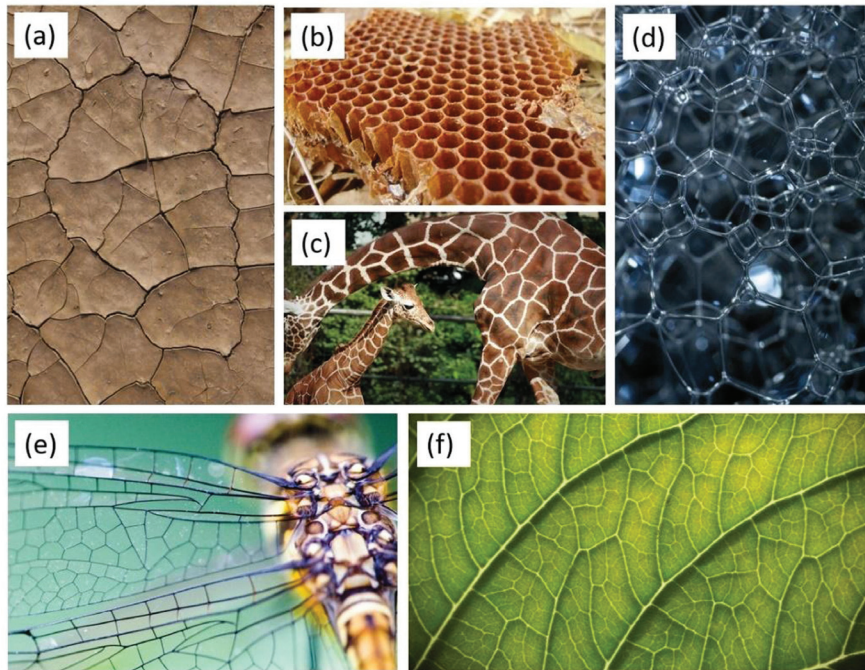
Figure 2.44: Examples of Voronoi patters in nature a) dried mud (J. Beaufort) b) honeycombs (Joydeep) c) giraffes (B. Hautzenberger) d) foam (M. Hetto) e) dragonfly (J. Ito) f) leaf (D. Emmenegger) [275]

3 Task

The aim of this thesis is to provide a model which allows to predict particle breakage of blast furnace sinter during transport and handling. In doing so, a special focus should be placed on the prediction of fines because return fines are mainly responsible for additional energy consumption, emissions and costs.

To evaluate the behavior of bulk material during handling, the discrete element method (DEM) is commonly used. Thus, the model should allow to simulate particle breakage using DEM. Different conveying processes should be simulated with this model in order to evaluate them in regard to particle damaging effects. A prediction of particle size distribution (PSD) after potentially damaging events is needed. This will be used to analyze and optimize existing equipment in regard to bulk material degradation and also help to develop new, innovative equipment for sinter transportation and storage.

To simulate sinter breakage, further understanding of the breakage behavior of sinter is needed. Therefore, a suitable test method should also be developed to analyze sinter breakage characteristics at damaging events, which occur during conveying processes.

The following scientific contributions are expected from this thesis:

- Test method to analyze breakage behavior of blast furnace sinter due to transport and handling processes

- Further understanding of breakage characteristics of blast furnace sinter: what is the resulting PSD and how much return fines are generated in dependence on mechanical stress?

- Model to simulate particle breakage of blast furnace sinter using DEM

- Prediction of particle breakage of blast furnace sinter during conveying processes, with special focus on fines generation

4 Research strategy
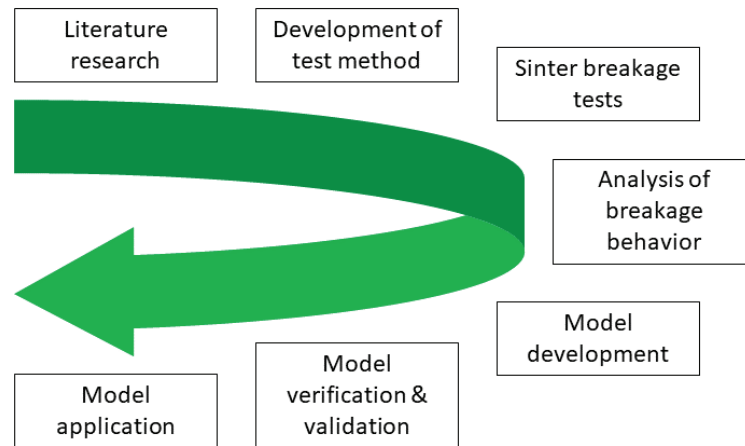
Figure 4.1: Illustration of the research strategy in this thesis

First of all, the state of the art is evaluated in a comprehensive literature research (see Chapter 2), including the sintering process itself, the following path of the sinter from the sinter plant to the blast furnace, various degradation effects on steel-making materials in general, relevant fundamentals of impact processes and particle breakage mechanisms, different breakage test methods, several degradation models, DEM and established particle breakage models in DEM.

Secondly, a suitable test method and a test rig for sinter breakage tests are developed. After testing, the breakage behavior of sinter is analyzed and possible trends are derived from the breakage test results.

Based on the breakage behavior and on the breakage test results, a suitable model is developed to simulate sinter breakage during conveying processes using DEM, allowing to predict the resulting PSD after damaging events with a special focus on fines generation. This model is then verified and validated with a simple experiment. Lastly, applications of the model are shown. An illustration of the research strategy can be found in Figure 4.1.

5 Material

All trials in this work were performed with sinter produced in a sinter plant of a steel manufacturer. All samples were sieved by the manufacturer and were provided in closed containers.

5.1 Particle size and shape

Depending on the manufacturer, the following size fractions are used, which refer to squared mesh sizes of conventional screens. Sinter A and C were produced by the same manufacturer, but on different dates. Sinter C was produced 3 years later than sinter A. Sinter quality depends on input material quality and on a variety of process parameters during sintering. Thus, each batch of sinter is different.

- Sinter A: <6.3; 6.3–10; 10–16; 16–25; 25–40; 40–50; >50 mm

- Sinter B: <6.3; 6.3–8; 8-10; 10–16; 16-31.5; 31.5-50; >50 mm

- Sinter C: 25-40 mm

As sinter particles are fragments of a sinter cake, particles are all irregular in shape. In [276] a sample of 25 particles of each size fraction of sinter A was measured by P. Pirstinger with a self-built Arduino-based 3D-scanner. Particle mass and the diameters along three orthogonal axes were measured. d_{max} is the largest, d_{med} the medium and d_{min} the smallest diameter. A boxplot of particle diameters for each fraction was created to illustrate the large scattering of particle sizes (see Figure 5.1). The average diameters for each fraction and the calculated shape factors d_{max}/d_{min} are listed in Table 5.1.

With different diameters along all three orthogonal axes, on average, the particles have an ellipsoidal shape. For most sorting processes the minimum diameter d_{min} is relevant because it determines the passing diameter. To characterize the ellipsoidal shape, the shape factor d_{min}/d_{max} was introduced. When the shape factor is plotted against d_{min}, a linear decreasing trend is noticed (see Figure 5.2).
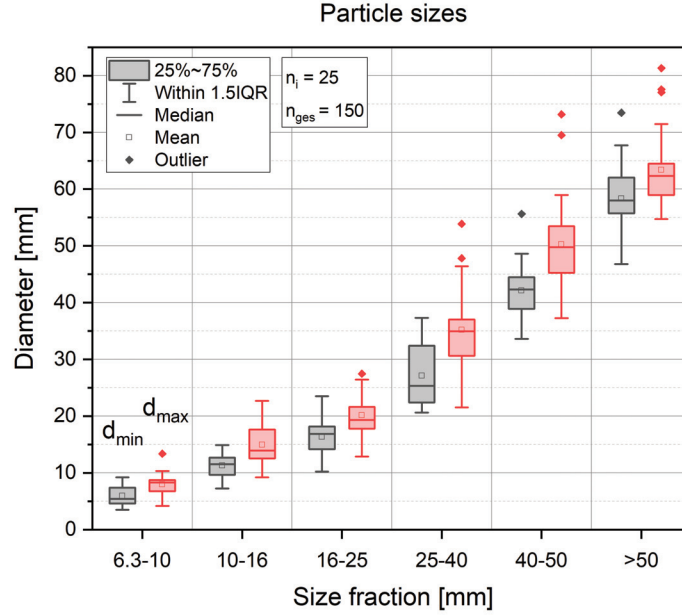
Figure 5.1: Boxplot of minimum and maximum particle diameters (d_{min}, d_{max}) of a sample of 25 particles for each size fraction, based on [276]

Size fraction [mm]	d_{min} [mm]	d_{med} [mm]	d_{max} [mm]	d_{max}/d_{min} [-]
6.3-10	5.9	7.2	8.0	1.22
10-16	11.5	14.2	15.2	1.23
16-25	16.3	19.3	20.2	1.18
25-40	27.1	31.3	35.2	1.15
40-50	42.1	46.7	50.3	1.11

Table 5.1: Average dimensions of sinter particles, based on [276]

5.2 Particle mass

When the particle masses from [276] are plotted in dependence on the minimum diameter d_{min}, an exponential trend is noticed. In contrast to spheres, where the mass grows to the power of 3 with diameter, mass grows to the power of 2.3 for sinter particles. It is assumed that this is due to the ellipsoidal shape. Furthermore, it is noticed that the mass scatter range decreases with increasing particle diameter. The specific weight of the material is 3717 kg/m³, as measured in [277]. The bulk density is dependent on the PSD. A bulk density of 1642 kg/m³ was measured in [277] for the PSD listed in Table 6.4. A particle density of 1990 kg/m³ for the particle size fraction 50-150 mm and 1470 kg/m³ for the particle size fraction 16-25 mm was measured. Specific weight, bulk and particle density measurements were conducted with Sinter A.
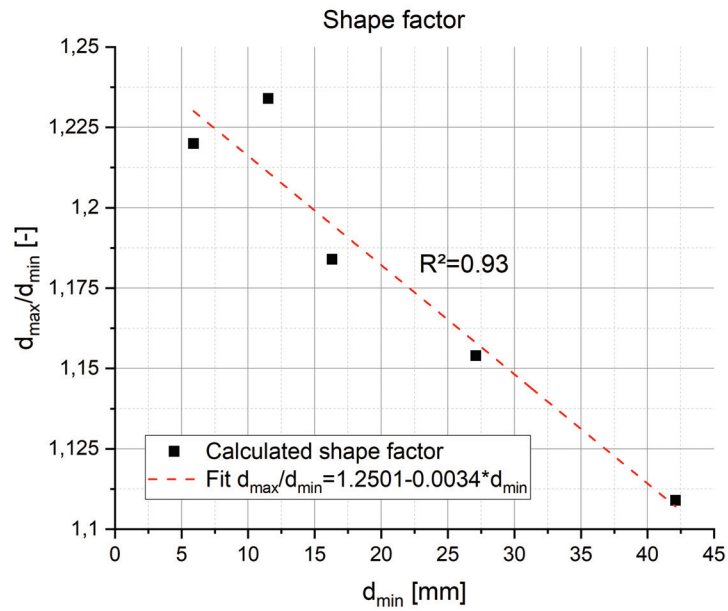
Figure 5.2: Shape factor d_{min}/d_{max} in dependence on the minimum particle diameter d_{min}, based on [276]
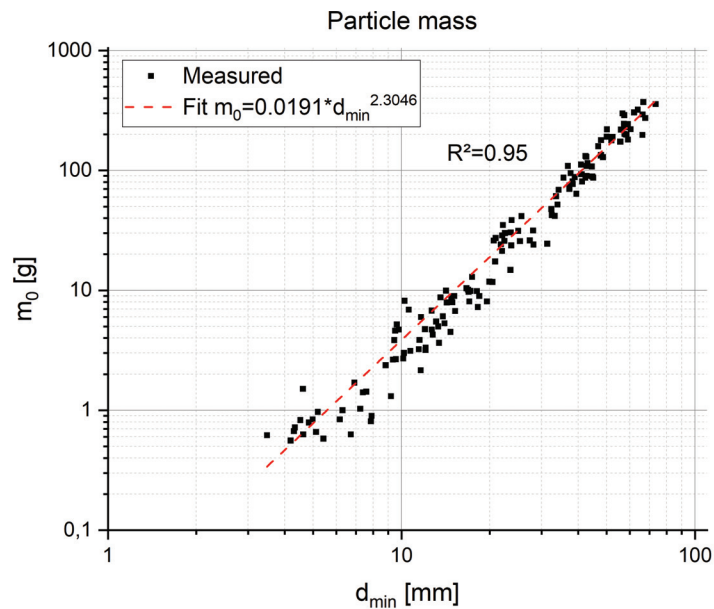
Figure 5.3: Particle mass m_0 in dependence on the minimum diameter d_{min}, based on [276]

6 Analysis of sinter breakage behavior

In the following Chapter methods and procedures to analyze breakage characteristics of blast furnace sinter are described. This includes preliminary studies carried out in order to develop a suitable method for sinter breakage tests, the test rig development, a detailed description of the test procedure and a detailed discussion of the breakage test results. This investigation is focused on aspects, which are relevant to application, which are breakage mechanisms due to transport and storage processes. In this context, common size fractions from sinter production and the steel-making industry are of interest. Most of the content in Chapter 6 was already published in [1, 6] and is based on the MinSiDeg project report D1.3 [13], which has already been submitted to the EU and the research consortium and will be published after project closing.

6.1 Compression tests

To determine the breakage behavior of sinter under slow compression as it occurs in bunkers and other storage facilities, compression tests were carried out. It must be stated that in this test series a uniaxial load was applied, whereas in bunkers a multiaxial load occurs due to interlocking effects and multiple contact points. Although it is not intended to be the standard test procedure, it is an additional investigation for comparison with impact tests and further investigations regarding particle breakage due to quasi-static compressive loads in bunkers. The compression tests were conducted with sinter A.

6.1.1 Modified hydraulic press

For uniaxial compression tests a hydraulic press was modified and equipped with a load cell (HBM-U3, 50kN) and an inductive displacement transducer

(HBM-W5TK), which is shown in Figure 6.1. The cylinder is powered by a 0.4 kW hydraulic unit. A flow valve was installed before the cylinder to reduce the downward velocity to 7.8 mm/s in unloaded conditions. The cylinder was controlled manually by a 4/3-way valve with a hand-operated lever.
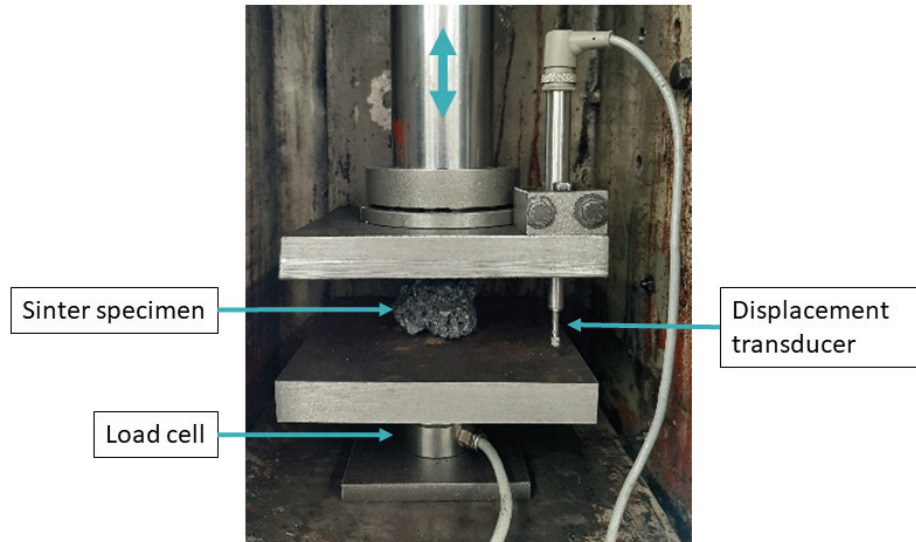
Figure 6.1: Modified hydraulic press

6.1.2 Test procedure

In total 250 compression tests were carried out, 50 for each size fraction (6.3-10; 10-16; 16-25; 25-40; 40-50 mm). The specimens were weighed with a laboratory scale before being placed in the press. The measurement was started manually when the cylinder was about 10 mm above the specimen. Measurement rate was 2400 Hz. The cylinder was moved downwards until volume breakage occurred, which could clearly be noticed by a cracking sound. Afterwards the cylinder was immediately moved upwards again and the fragments were collected from the chamber. The manual cylinder control meant that further crushing after first volume breakage could eventually occur, depending on the reaction time of the machine operator.

Furthermore, manual fragment collecting means that only particles of a certain size can be collected and fines are usually lost, but will be calculated as the difference to the initial mass. Because sieves are too damaging and conventional sieve analysis would have been too much effort for 250 tests, the collected fragments were analyzed by the specially developed vibrating sorter described in Section 6.3.4. The tests were performed by G. Mattathil. The first data evaluation and some mass dependent trends regarding breakage force and energy are described

in [278]. For each test the following data was collected (see Figure 6.2):

F	Measured force	$[N]$
s	Measured displacement	$[mm]$
t	Time	$[s]$
m_0	Initial particle mass	$[g]$
m_i	Fragment weights for each size fraction	$[g]$

6.1.3 Data evaluation

The following parameters were determined from the compression tests:

F_{max}	Maximal force a particle can withstand	$[N]$
E_c	Comminution energy, by numerical integration of the force-displacement-curve (see Figure 6.2)	$[J]$
E_{cs}	Mass specific comminution energy	$[J/kg]$
F_{1p}	First force peak with 50 N prominence (see Figure 6.2)	$[N]$
x_f	Fictitious particle diameter	$[mm]$
σ_P	Particle strength	$[MPa]$

The input energy E_c was determined in MATLAB by numerical integration of the force-displacement-curve with the trapezoidal method "trapz" (see Figure 6.2). The first force peak F_{1p} was determined in order to investigate when the first chipping and thus return fines production would occur. This was performed using MATLAB's peakfinder function "findpeaks". A peak was defined by a minimum prominence of 50 N.

The fictitious particle diameter x_f was calculated with Equation 6.1. The mass of a spherical particle with this fictitious particle diameter x_f and a density of $\rho = 1470 \, kg/m^3$ equals the measured initial particle mass m_0. The fictitious particle diameter is larger than the passing diameter because of the irregular particle shape. Due to a lack of data, the particle density of $\rho = 1470 \, kg/m^3$, which was measured for the particle size fraction 16-25 mm, was applied for all size fractions in this case.

According to [146], the tensile strength of an irregular shaped rock can be approximated by Equation 6.2. This simple equation is derived from complex expression of the stress state of a sphere subjected to compression. The numerator is defined

as the critical force for failure F_C multiplied by a factor (2.8) given by the loading condition, geometrical features and Poisson's ratio. The denominator is defined as the area of a disc where D is the distance between the loading points. [124]

It must be stated that Hiramatsu's approach [146] is suitable for rocks, where volume breakage occurs due to the local exceeding of a critical tensile stress yielded by compression of the particle (see indirect tensile strength test or Brazilian test in Section 2.8.7). This is not always the case for sinter particles, because chipping and other breakage mechanisms also occur during a compression test. It is considered that this approach provides results for a rough estimation of particle strength.
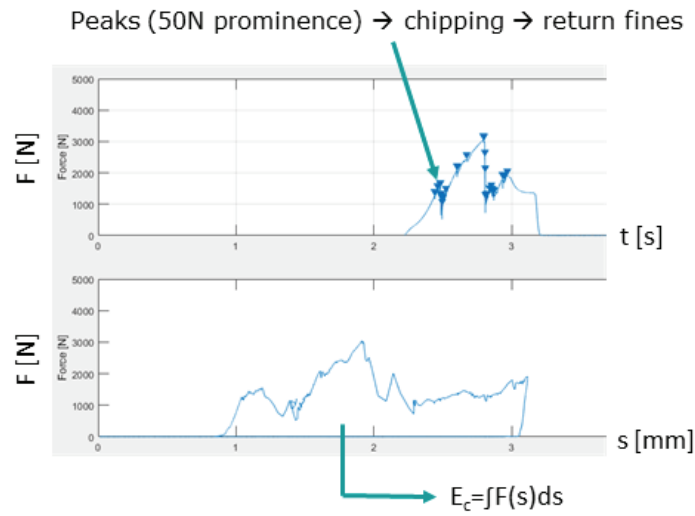
Figure 6.2: Plots of the force in dependence on time and displacement during a compression test, exemplary for a 40-50 mm particle (sinter A)

$$x_f = \sqrt[3]{\frac{6m_0}{\rho\pi}} \tag{6.1}$$

$$\sigma_P = \frac{2.8F_C}{D^2\pi} \tag{6.2}$$

ρ	Particle density	$[kg/m^3]$
F_C	Critical force for failure	$[N]$
D	Distance between the loading points	$[m]$

6.1.4 Results

Under assumption of spherical particles and a particle strength calculated by the approximation of [146], the following trend is noticed when the particle strength σ_P is plotted against the fictitious particle diameter x_f (see Figure 6.3). The particle strength decreases with increasing particle size, which meets experiences from handling. The decrease follows a power function.
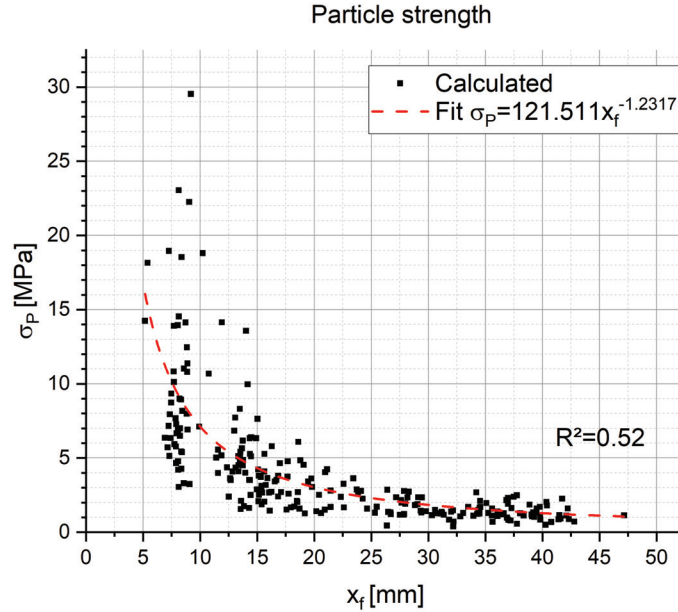
Figure 6.3: Particle strength under uniaxial compression (sinter A, particle sizes 6.3–50 mm, n=250)

In Figure 6.4 the particle strength σ_P, the calculated mass-specific comminution energy $E_c s$, the maximum force until volume breakage F_{max} and the force for first chipping F_{1p} are plotted with standard deviations as function of the fictitious particle diameter x_f for an overview. Every data point in this diagram represents one particle size fraction and is calculated as the average of 50 tests. The particle strength and the mass-specific comminution energy follow a similar trend. The maximum force until volume breakage increases unsteadily with similar values for the fractions 10-16 mm and 16-25 mm. The force for first chipping remains almost constant for large particles.

In Figure 6.5 the particle size distribution (PSD) for each size fraction after volume breakage is presented in relation to the initial particle mass m_0. The values presented for the mass fraction m_i/m_0 are calculated as the average of 50 tests for each size fraction. The return fines are presented in orange as <6.3 mm. The average mass-specific comminution energy is given at the top of the bars.
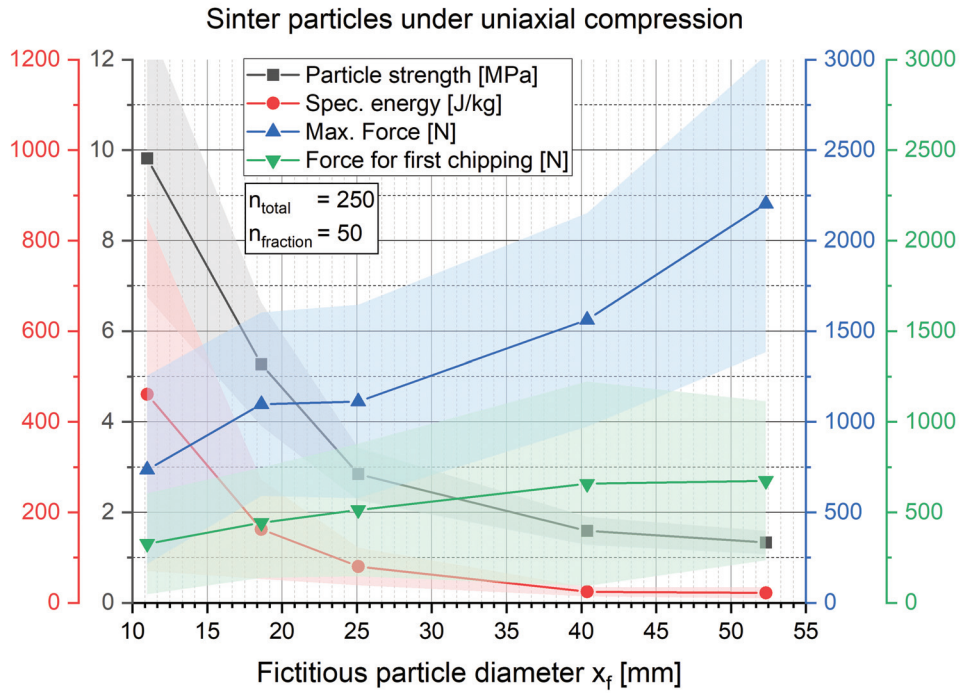
Figure 6.4: Overview of sinter properties under uniaxial compression (sinter A, particle sizes 6.3-50 mm, n=250)
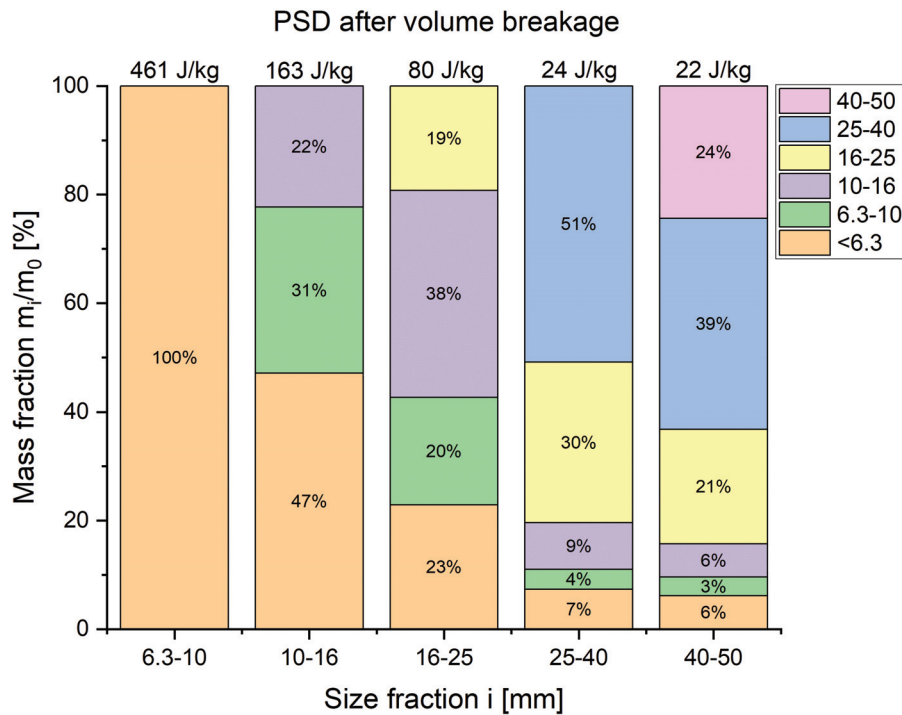
Figure 6.5: Particle size distribution for each size fraction after volume breakage under uniaxial compression (sinter A, particle sizes 6.3-50 mm, n=250)

6.2 Drop tests

A preliminary study containing single particle drop tests onto a 20 mm steel plate was carried out with sinter A in [279]. Absolute energy values for probable and improbable breakage were determined for each particle size fraction by the following drop procedure. Single sinter particles were dropped from a certain height, depending on their mass to achieve the desired impact energy. Absolute energy values for probable breakage and improbable breakage were then determined for each particle size fraction. To estimate the energy for a probable breakage, the energy was stepwise increased (0.005 J) until 10 consecutive samples broke. Chipping was also defined as breakage because return fines were produced. For an improbable breakage, the energy was stepwise decreased (0.005 J) until no breakage was detected with 10 consecutive samples. The results of this investigation are listed in Table 6.1. A complete investigation of the fraction >50 mm was not performed due to limited samples and high fragility.

Size fraction	No breakage		Breakage	
[mm]	E_c [J]	m_0 [g]	E_c [J]	m_0 [g]
6.3-10	0.010	0.6	0.12	1.4
10-16	0.015	2.8	0.30	6.4
16-25	0.025	15.2	0.50	14.7
25-40	0.025	42.2	1.10	51.8
40-50	0.035	116.3	1.10	113.3
>50	0.045	301.0	-	-

Table 6.1: Results from single particle drop tests in [279]

The data from [279] was further evaluated. In [279] E_c describes the kinetic energy of the particle before impact, which was simply calculated from the drop height without air drag. It must be stated that for small particles and large drop heights the air drag has a significant influence. When the mass-specific breakage energy E_{cs} (see Equation 6.3) is plotted over the average particle mass m_0 of a size fraction, a clear trend can be noticed in Figure 6.6, which indicates a size effect and mass-specific energy as the key factor. Large particles show a greater tendency to break than small particles, which is consistent with the results in [92]. As concluded from drop test results, the mass-specific impact energy should be in the range of 0.1–100 J/kg (10-10000 mm or 0.4-14 m/s) to cause breakage.

$$E_{cs} = \frac{E_c}{m_0} \qquad (6.3)$$
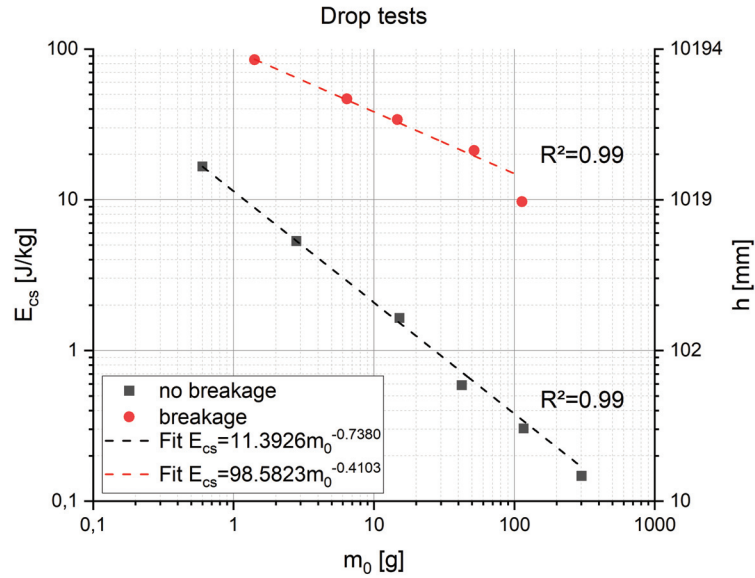
Figure 6.6: Mass-specific impact energy E_{cs} for probable and improbable breakage in dependance of particle mass m_0, based on drop tests in [279]

6.3 Automated single particle impact tester

The content of this Section was already published in [1]. One of the main causes of sinter breakage during transport and handling are impacts against equipment or other particles. Thus, accelerating the particle itself and shooting it against a target was considered closer to reality than a drop-weight or pendulum hammer test. This assumption was later confirmed in [280], whereby breakage matrices were determined to predict particle attrition in pneumatic conveyors. A drop-weight test would have been simple but energy input by two contacting surfaces could have resulted in different fragmentation behavior.

The following challenges were faced in test rig development. For an accurate determination of breakage behavior, single particle tests are necessary. As known from the preliminary study with drop tests (see Section 6.2), a wide range of energies were to be covered. Furthermore, the particles had to be accelerated carefully to avoid breakage during acceleration. The major challenge in sinter testing is that due to great heterogeneity and varying shape, a reliable statement about breakage behavior can only be achieved by high sample numbers [93]. This requires a high grade of automation, but the undefined shape and fragility of the sinter complicate handling.

Consequently, a highly-automated test rig with separation, weighing system, two different acceleration concepts for low and high energy testing and integrated automated fragment analysis was developed (see Figure 6.7).

Figure 6.7: Automated test rig for rapid single particle impact testing to determine sinter breakage behavior [1]

6.3.1 Concept

In Figure 6.8 a flow diagram and an overview of the test rig is presented. A bulk sample is placed into the vibratory bowl feeder, where the particles are separated along a spiral. When a particle drops out and is detected by a light gate, the feeder is switched off and the particle slides along guide plates onto the padded weighing station. After weighing, the particle is carefully pushed by a pneumatic cylinder and slides into the air cannon. To ensure correct placement in the cannon, the particle is guided by a moveable system of guide plates, which is coupled to the movement of the pneumatic cylinder. The automation of the separation and the loading mechanism of the air cannon were developed by B. Waidbacher in [281]. The loading closure of the cannon is also moved pneumatically. Meanwhile the air tank has been filled with the desired pressure. When shooting valve opens, the sabot in the cannon is accelerated and the particle is fired against a 20 mm thick steel plate in a housing. The particle speed is measured by two Arduino-based self-built light gates directly after the muzzle and in front of the steel plate. After collision the fragments are led via several padded slides into the vibrating sorter, where the received particles are carefully sorted by size. Under the vibrating

sorter, collecting boxes on weigh cells are placed for each fraction. All weigh cells are zero balanced before a new shot is fired. The weights of each fraction after breakage m_1 to m_7, the initial particle mass m_0 and the measured impact velocity v is then saved to a CSV-file on an SD-card. Consequently, PSD and return fines production as functions of impact energy and initial particle mass can be determined. After the data has been saved, the bowl feeder starts again and the process begins anew. The whole process takes approximately one minute. Particles >50 mm are placed manually on the drop module due to their size and fragility. Separation in a rotary bowl feeder could cause significant damage, as known from drop tests in Section 6.2. The height of the drop module is adjusted by a spindle drive. A weighing platform is integrated. The maximum drop height is 900 mm, which is equivalent to 8.8 J/kg. After weighing, the particle is carefully pushed and falls into a box with a 20 mm steel plate at the bottom. While the box is tilted, the front side of the box opens with a couple mechanism and the fragments slide into the padded receiving Section of the vibrating sorter. From here onwards, the automated fragment analysis is the same procedure as for the high-energy tests by air cannon.
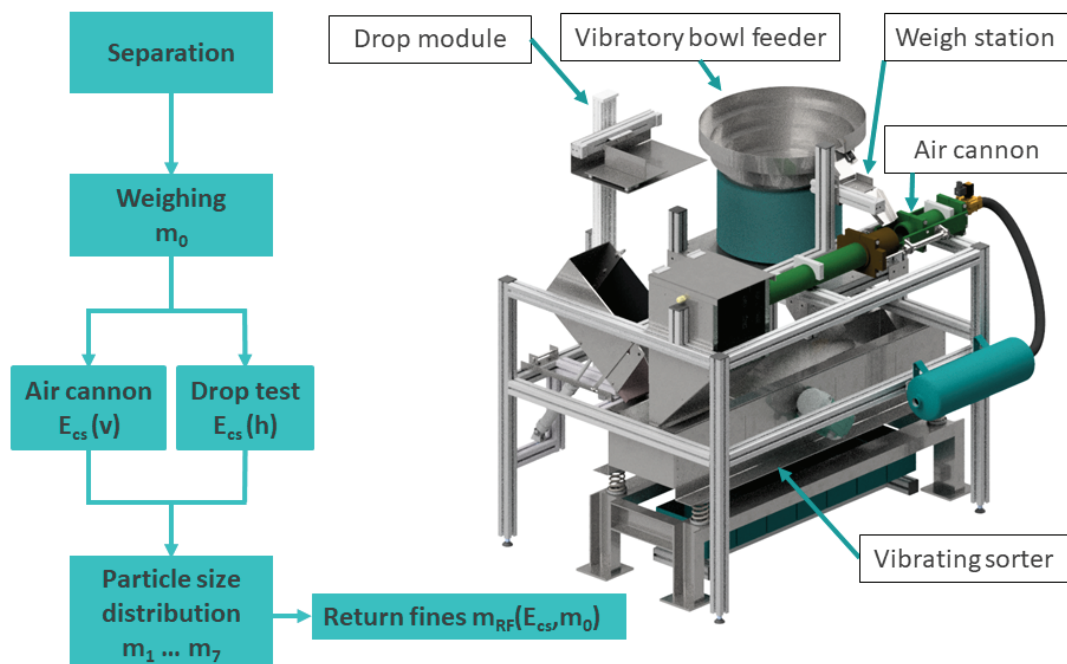
Figure 6.8: Flow diagram and concept of the automated single particle impact tester [1]

6.3.2 Separation

A vibratory bowl feeder operates on the micro-jerk principle and was considered as the most careful way of separating a bulk sample. A stepped pot was considered most suitable for this application. The steps have a width of 37 mm, which allows separation of all fractions except >50 mm, which have to be separated manually anyway because of their fragility.

Because the manufacturer could not guarantee proper operation for this application, a discrete element simulation with calibrated sinter particles from [277] was carried out with EDEM (see Figure 6.9a). The aim of this simulation was to determine separation behavior and estimate mechanical loads during separation. The following vibratory bowl feeder was used: TFH400R/S560VA from the manufacturer AVITEQ [282].
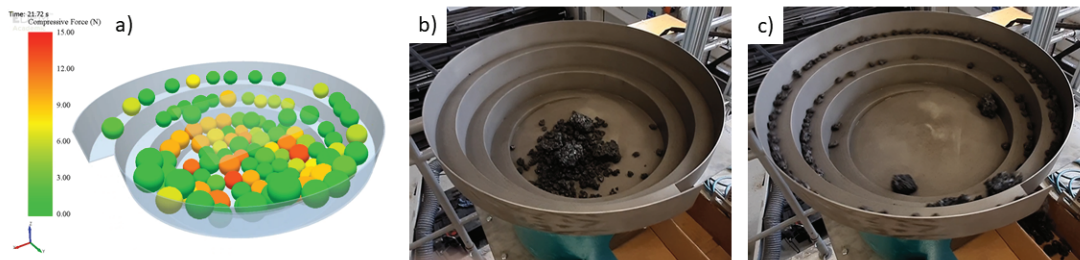
Figure 6.9: a) Discrete element simulation b) bulk sample c) separation test in rotary bowl feeder [1]

Material and interaction parameters are listed in Tables 6.2 and 6.3. These were determined with angle of repose and slip tests in [277] for sinter A with a sample from the sinter plant with the PSD listed in Table 6.4. A cone angle of 32° was noticed in these tests. These parameters were calibrated with spherical particles with capped angular velocity, which turned out to be suitable to represent the behavior of highly irregularly-shaped sinter particles in this case. As angular velocity of the particles is capped, rolling friction is irrelevant in this case. It must be stated that the density of sinter and the interaction parameters for sinter-sinter depend on particle sizes. Thus, these parameters were not exact for the used PSD in the following simulation, but it was assumed that the difference in static friction for sinter-sinter could be neglected as sinter-sinter interactions would not have a great effect on the conveying behavior in the vibratory bowl feeder in this case. For the evaluation of compressive forces, the exact density is not needed as long as the calibration and simulation are performed with the same density.

Material	Density [kg/m³]	Poisson's ratio [-]	Shear modulus [MPa]
Sinter A	3717	0.25	9
Steel	7850	0.25	9

Table 6.2: Material parameters for discrete element simulations [277]

Interaction	Restitution [-]	Static friction [-]
Sinter-Sinter	0.5	0.25
Sinter-Steel	0.5	0.839

Table 6.3: Interaction parameters for discrete element simulations [277]

Passing [mm]	Mass fraction [-]
100	9.393
50	6.404
40	17.033
25	14.925
16	17.560
10	22.043
6	12.642

Table 6.4: Particle size distribution for a sample from the sinter plant in [277], determined with a conventional sieve with quadratic mesh

In the simulation, a bulk sample with a total mass of 20 kg consisting of 50% 50 mm and 50% 40 mm particles was placed in the vibratory bowl feeder. For this purpose, a CAD file of the vibratory bowl feeder was created according to data sheets [282]. Vibration kinematics of the vibratory bowl feeder were defined with 100 Hz, 0.125 mm vertical oscillation and 0.25° rotating oscillation, according to data sheets. As contact model EDEM's default model Hertz-Minldin was used. Time step and target save interval in the simualtion were $4 \cdot 10^{-5}\,s$. Operation of the vibratory bowl feeder was simulated for 40 s in total. To compare fictitious compressive forces in the simulation with reality, drop tests with the same parameters were simulated at different drop heights of 0-125 mm (see Figure 6.10). Simulation results show that the maximum compressive force on a 40 mm particle ($m_0 = 124\,g$ in simulation) due to the vibratory motion does not exceed 26.4 N, which corresponds to a drop height of 26.02 mm according to Figure 6.10. According to drop test experiments (compare Figure 6.6), this load corresponds to a mass-specific energy input slightly above the trend line for no breakage. This

means that marginal breakage may occur but is rare for the particle size fraction 40-50 mm, which is the most fragile in this case. The simulation results also show that loads during vibratory motion are lower than gravitational static loads in the bulk sample.

Some tests with sinter samples were then carried out (see Figure 6.9b) and c). All fractions 6.3–50 mm were tested and the results show that a sufficiently careful separation for all fractions 6.3–40 mm is possible and minimal chipping in the fraction 40–50 mm occurs, which is consistent with the simulation results.
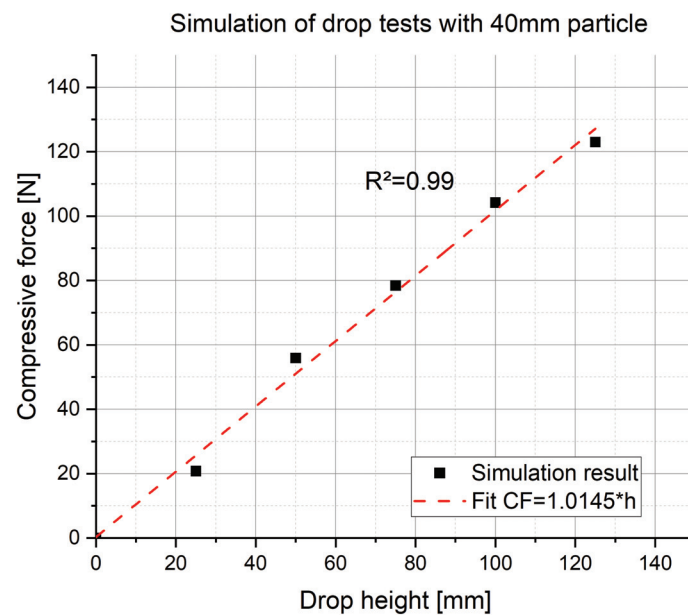
Figure 6.10: Drop tests simulated with a 40 mm sinter particle in EDEM in order to determine the resulting compressive force due to impact on a steel plate

6.3.3 Air cannon

The air cannon shown in Figure 6.11, has a caliber of 70 mm and a barrel length of 1100 mm. The challenge in its development was to shoot projectiles of undefined geometric shape with a desired velocity. For this purpose, particles are loaded into a sabot with an inner diameter of 60 mm and a 60x60 mm opening for loading. First trials showed that particles of 40–50 mm could be shot when placed manually but tended to cause problems when loaded automatically due to varying shape. The sabot glides directly on the barrel, which is honed and minimally lubricated. Due to clearance fit no additional seals are needed. To avoid particle breakage during acceleration a foam damper is mounted at the back of the sabot. When

shot, the sabot crashes against a spring pack at the muzzle to reduce impact forces. First sabots were made of POM-C because of its excellent tribological properties and good machinability, but could not withstand high impact loads when crashing against the spring pack. Polyamide turned out to be the more suitable material for this application.

To prevent possible chippings from blocking the barrel, the sabot is flushed with air after each shot in its front position. After flushing, the shooting valve is opened again and the sabot returns to its loading position by a retaining spring. To ensure the correct loading position, a centering ring is mounted at the back. First trials showed that the retaining spring force was insufficient in rough operation and a suction module was installed additionally.

400 shots each with the lightest and the heaviest sinter particles in this trial have been evaluated to determine the air cannon shooting characteristics, which are plotted in Figure 6.12. The plot shows only a minimal influence of projectile mass on muzzle velocity. This is because average particle masses are relatively small in relation to sabot mass ($m_{sabot} = 240\,g$, $m_{10-16} = 3\,g$, $m_{25-40} = 36\,g$). Shooting performance follows a nonlinear trend as described in [283]. Shots with <4 m/s are possible but problematic in terms of speed measurement.
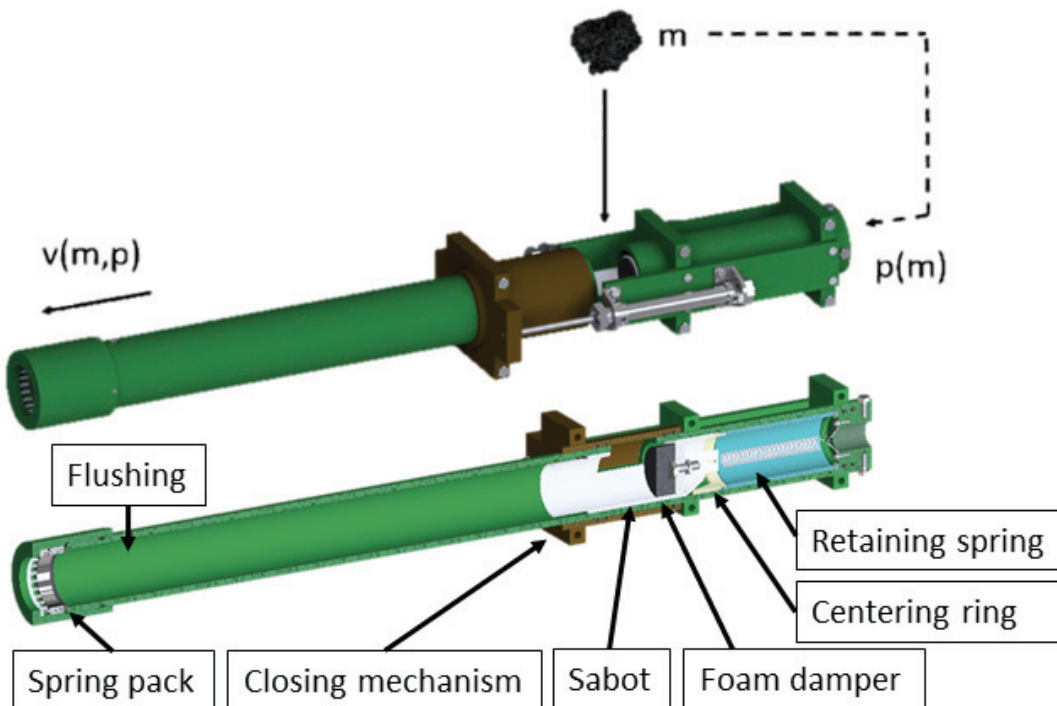
Figure 6.11: Air cannon for high energy impact tests [1]
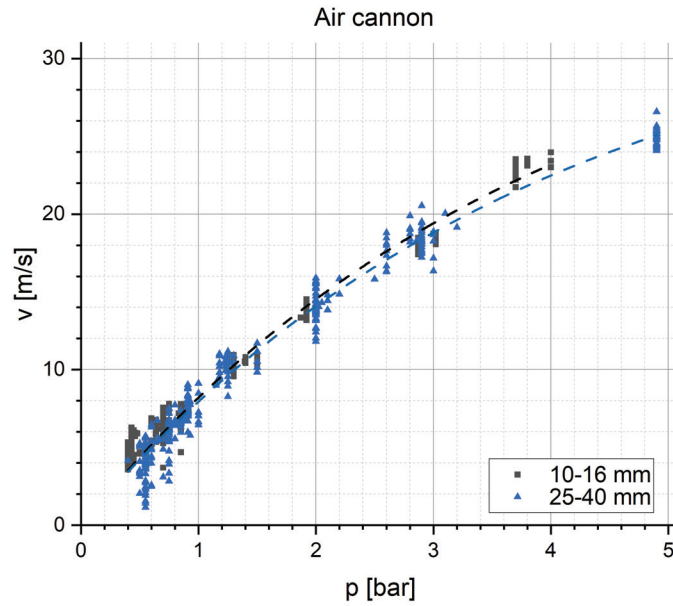
Figure 6.12: Measured particle impact velocity v in dependence on pressure p in air tank [1]

6.3.4 Automated fragment analysis

For a detailed investigation of breakage behavior, an individual fragment analysis for every single test was desired. In contrast to simply analyzing all debris at once after each trial, individual fragment analysis has the advantage of being able to determine the fragment size distribution and mass fractions in relation to the individual initial particle mass. This increases accuracy, especially when testing highly heterogeneous particles, which greatly differ in mass within the same size range. Furthermore, this method generates more information which quantifies individual particle heterogeneity [284]. Additionally, it allows a more detailed prediction of comminution machine performance [284], which is irrelevant for sinter, but useful when testing other materials. A high number of tests and short testing duration require a rapid and automated fragment analysis. Additionally, the fragment analysis must be performed as careful as possible to avoid further breakage.

Various sieving concepts were considered. To check functionality and determine loads on fragments discrete element simulations were carried out (see Figure 6.13). Simulations revealed that a screen slide as in Figure 6.13b) (in this case only return fines are screened out) is considered unsuitable for this application because too much construction height would be required to sort all fractions.
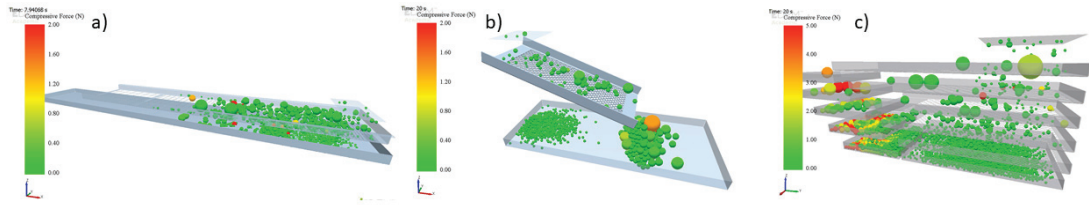
Figure 6.13: Discrete element simulations of a) screen line b) screen slide c) multi-deck sieve [1]

As it was considered that conventional sieving of sinter would cause too much load on fragments and could lead to further breakage and falsification of impact breakage test results, a more careful concept was developed – the vibrating sorter (see Figure 6.14). The vibrating sorter is a V-shaped channel with a slit at the bottom which opens up stepwise in conveying direction and corresponds to particle size fractions. It must be stated that this sorting principle is based on a one-dimensional passing in contrast to a two-dimensional passing through conventional sieves. The whole channel is exchangeable for rapid change of size fractions. The sorter is driven by two counterrotating unbalance motors, which can be adjusted in work angle and speed by a frequency converter. This results in a vibration in the work angle. The vibrating part is mounted with springs to a heavy framework with rubber bumpers for vibration isolation. Under the vibrating sorter, a row of collecting boxes on weigh cells is placed, which allows quick determination of mass fractions for each size fraction.
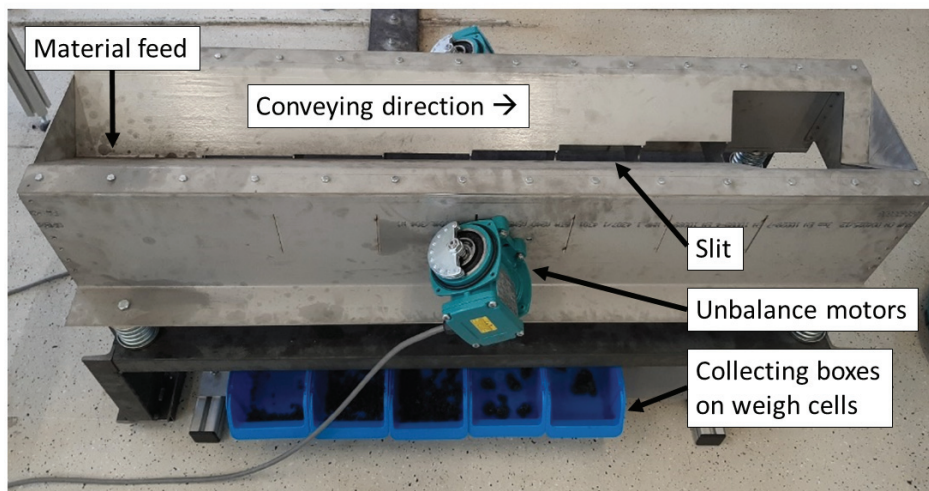
Figure 6.14: Vibrating sorter for rapid automated fragment analysis [1]

Discrete element simulations, shown in Figure 6.16, were carried out to estimate parameters like frequency, oscillation amplitude and work angle. Tests showed that optimum operation with regard to conveying speed, load on fragments, jamming and sound emissions was at 45° work angle and 2100 min^{-1} rotation speed. A detailed analysis of the vibration behavior of the vibrating sorter was conducted by G. Steiner in [285] for the purpose of testing a newly developed acceleration sensor (see Figure 6.15). In the diagrams, X is the conveying direction and Z is the vertical axis.
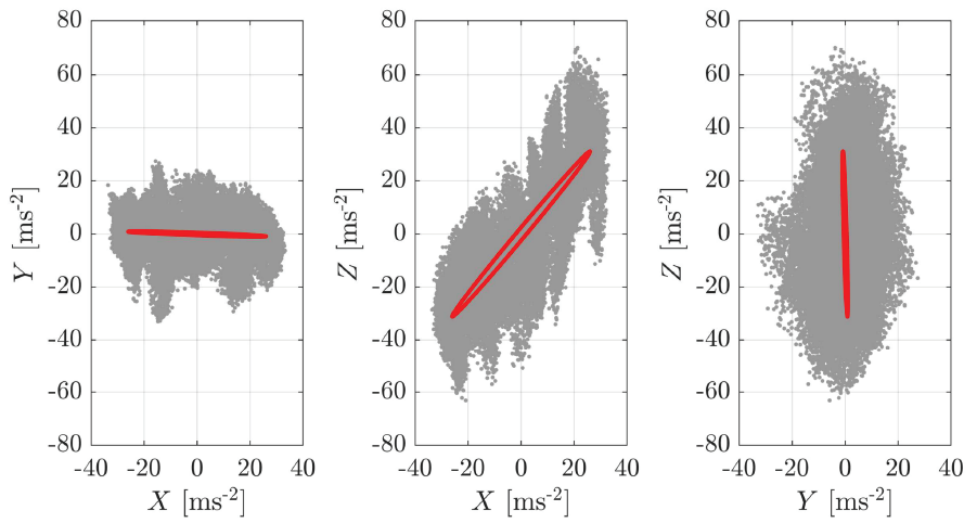
Figure 6.15: 2D projections of data and vibration orbits in the machine frame coordinate system of the vibrating sorter at 3072 Hz sampling frequency [285]
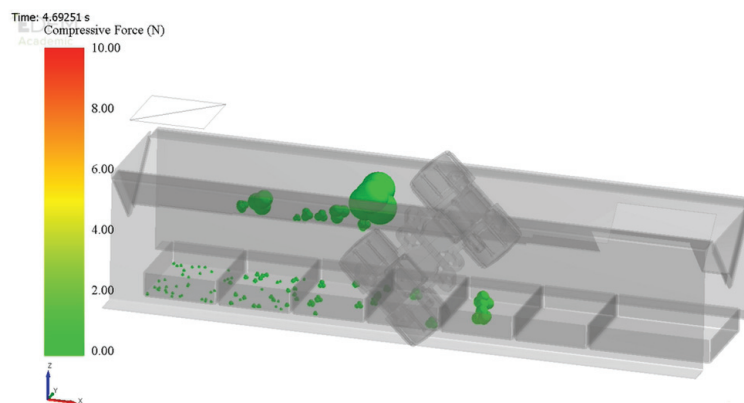
Figure 6.16: Discrete element simulation of vibrating sorter [1]

For discrete element simulations the same material and interaction parameters as for the vibratory bowl feeder simulations were used. They are listed in Tables 6.2 and 6.3, and were determined in [277]. For simulations of the vibrating sorter rollable clustered particles were used. Simulations were carried out with the Hertz-Mindlin contact model, a time step of $4 \cdot 10^{-5}\,s$ and a target save interval of $4 \cdot 10^{-2}\,s$. It must be stated that very low shear moduli were used for calculation efficiency. Thus, the resulting compressive forces listed in Table 6.5 are not realistic, but can be used for direct comparison. In Table 6.5 maximum compressive forces during conveying and sorting are compared for 40 mm particles. Drops into collecting boxes are excluded. The results confirm that the vibrating sorter - operating on the microjerk principle - causes much less damage than conventional screens.

Screening concept	Max. compressive force [N]
Screen line	27.8
Multi-deck sieve	35.1
Vibrating sorter	9.5

Table 6.5: Simulation results for 40 mm particles in different sorting concepts

Because the vibrating sorter works on a one-dimensional passing principle and conventional sieves work on a two-dimensional passing principle, the classification methods are compared in Table 6.6. 5 kg each of the size fractions 10–16 mm and 16–25 mm of sinter A, which had been screened by the manufacturer with conventional sieves with quadratic meshes, have been sorted by the vibrating sorter. The results show a significant shift of relative mass fraction values to the smaller size fraction, when sorted by the vibrating sorter, which has to be considered when interpreting the results in Section 6.5.

The influence of the sorting principle is due to the ellipsoidal shape of sinter particles (see Table 5.1). Owing to the importance of particle shape when classifying particles into size fractions with different methods, additional investigations regarding particle shapes were carried out in [276] (see Section5.1). The shape factor d_{min}/d_{max}, which provides information about different passing behavior at a 2D-mesh and a 1D-slot, linearly decreases with particle size (see Figure 5.2). Thus, the difference between different sorting principles decreases with increasing particle size.

Unfortunately, a comparison with the largest size fraction 25–40 mm was not carried out due to a lack of test material. Based on the fact that a linear trend for

the shape factor was noticed in Figure 5.2, also a linear trend for the mass fraction sorted into the same size fraction by the vibrating sorter as by conventional sieves was assumed. On this assumption and the given data from Table 6.6, the missing data for the size fraction 25-40 mm was extrapolated (25-40 mm: 89%, 16-25 mm: 11%), which is shown Figure 6.17.

| | | Sieve (2D-passing) | |
		10-16 mm	16-25 mm
	6.3-10 mm	63.1%	0%
Sorter (1D-passing)	10-16 mm	36.9%	45.2%
	16-25 mm	0%	54.8%
	$\sum$	100%	100%

Table 6.6: Comparison of vibrating sorter and conventional sieve
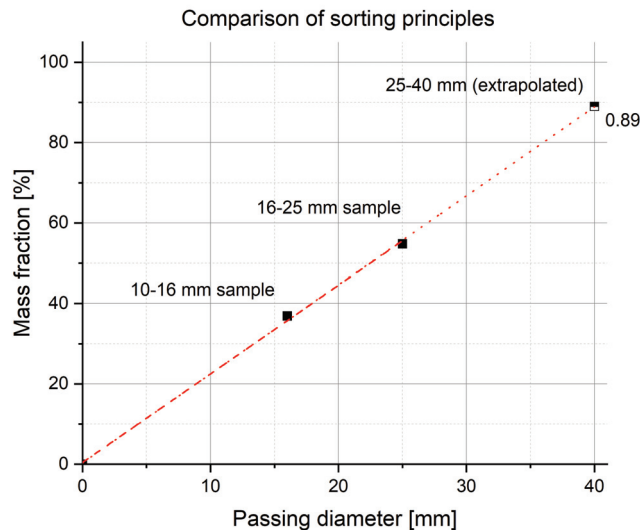
Figure 6.17: Mass fraction sorted into the same size fraction by the vibrating sorter as by conventional sieves [1]

6.3.5 Low-cost automation by Arduinos

The high grade of automation requires a complex control system, which is able to manage pneumatic, electric and measurement components. Due to a tight budget the whole test rig is controlled by Arduinos. Of course, Arduino components are less reliable than professional industry equipment, but for prototyping with a tight budget, it was considered the best compromise.

The control system consists of 1 master- and 2 slave-Arduinos. The splitting provides more input/output pins (an Arduino Mega 2560 has 54 input/output pins)

and allows faster and more accurate measurement. One slave controls the weigh cells under the sorter, the other the speed measurement and both communicate via serial communication with the master. The master collects data from both measurement slaves, is connected to all control panels, switches relays for load circuits and saves data to the SD card.

All weigh cells are operated by HX711 chips, which are high precision 24-bit A/D load cell amplifiers and communicate via I2C bus with Arduinos. Speed measurement is performed by self-built light band sensors with an IR-LED and several phototransistors, inspired by a chronograph in [286].

Full automatic operation as well as manual control is possible by control panels. A connection to a computer is not necessary for normal operation, only to adjust machine parameters. The whole test rig only needs a 230 V connection and a compressed air supply.

6.4 Test procedure

As mass-specific energy input turned out to be the key factor, breakage at certain specific energy levels was determined. A minimum of 50 valid tests were carried out with the same air pressure, resulting in approximately the same impact velocity. A test was regarded as valid if the sum of all fragment masses deviated <5% from the initial particle mass, which meant that no large fragments had been lost. Due to high heterogeneity and wide dispersion, average values from minimum 50 valid tests are represented by one data point in the result diagrams. For each fraction 6–9 data points have been created, which is equivalent to a minimum of 300–450 tests for each size fraction. In Figures 6.18 and 6.19 pictures captured by a high-speed camera are depicted, which show the completely different breakage behavior for two sinter particles from the same batch and initial size fraction at the same impact velocity.
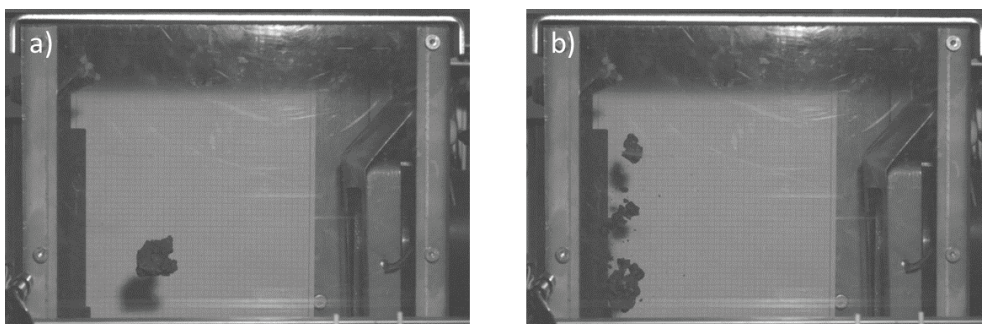
Figure 6.18: Volume breakage of sinter particle (sinter B, 16-31 mm, $m_0 = 39\,g$) at impact with $10\,m/s \cong 50\,J/kg$. a) before impact b) after impact
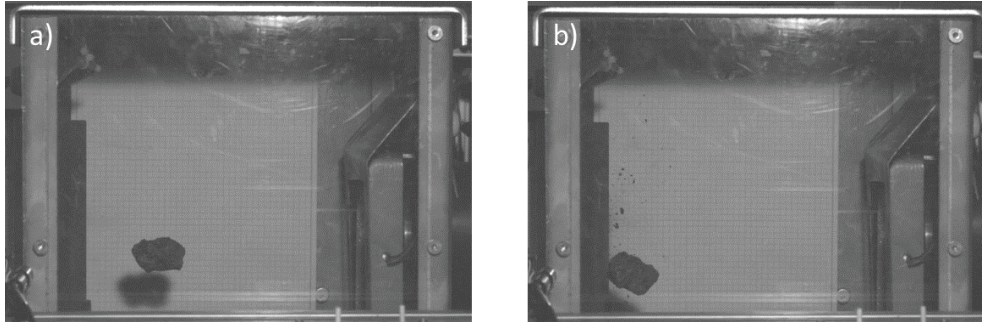
Figure 6.19: Chipping of sinter particle (sinter B, 16-31 mm, $m_0 = 51\,g$) at impact with $10\,m/s \mathrel{\widehat{=}} 50\,J/kg$. a) before impact b) after impact

6.5 Impact test results

From sinter A, the fractions 10–16 mm, 16–25 mm and 25–40 mm were tested. A detailed breakage characterization was carried out for sinter A because the channel in the vibrating sorter with its size fraction classification had been designed for sinter A. From sinter B, the size fractions 10-16 mm, 16-31.5 mm, 31.5-50 mm and >50 mm were tested. From sinter C, the fraction 25-40 mm was tested subsequently. Trials with particles <10 mm were not conducted because hardly any breakage occurred at impact velocities of 4-25 m/s with the size fractions 6.3-10 mm of sinter A and 8-10 mm of sinter B.

6.5.1 Particle size distribution

For every impact test the sorted fragment masses m_2 to m_7 were set in relation to the individual initial particle mass m_0 to calculate the relative mass fraction m_i/m_0. PSD after impact was then calculated as the average of each mass fraction m_i/m_0 from 50 valid tests for each specific energy level. Thus, each data point in the result diagrams represents the average of 50 tests, which also applies to fines generation, breakage probability and t_n-curves.

In Figures 6.20, 6.21 and 6.22 the PSD after impact tests with initial particle sizes 10-16, 16-25 and 25-40 mm are plotted against the mass-specific impact energy E_{cs}. Each data point represents the average of 50 valid tests at a certain specific energy level. For $E_{cs} = 0$ the initial values from Table 6.6 and the extrapolated value for the size fraction 25-40 mm from Figure 6.17 have been used. The average initial particle masses m_0 of all tested particles in these size fractions are 2.9 g (10-16 mm), 10.4 g (16-25 mm) and 36.4 g (25-40 mm).

The initial particle size decreases exponentially. Also for smaller sizes fractions clear trends are observed. The 16-25 mm data in Figure 6.22 follows a lognormal distribution and the 10-16 mm data in Figure 6.22 has been fitted with a biphasic Hill curve [287]. The 6.3-10 mm curves in Figures 6.21 and 6.22 can be fitted with a Bigaussian peak function [288]. A sharp peak is noticed for the 6.3-10 mm in Figure 6.20, which cannot be fitted with a continuous function with Origin's curve fitting tool. The data at the peak was confirmed by a second trial of 50 tests. After the peak the data follows an exponential decrease.

Compared with compression test results in Figure 6.5, the PSD after impact tests at the same energy is generally finer and more fines are produced. It is assumed that this is because of further breakage at subsequent impacts and the fact that more elastic energy is absorbed by the test rig during compression tests.

m_0	Initial particle mass	$[g]$
m_{RF}	Mass of return fines	$[g]$
m_{1-7}	Fragment masses for size fractions <6.3, 6.3-10,	
	10-16, 16-25, 25-40, 40-50 and >50 mm	$[g]$
i	Size fraction	$[-]$
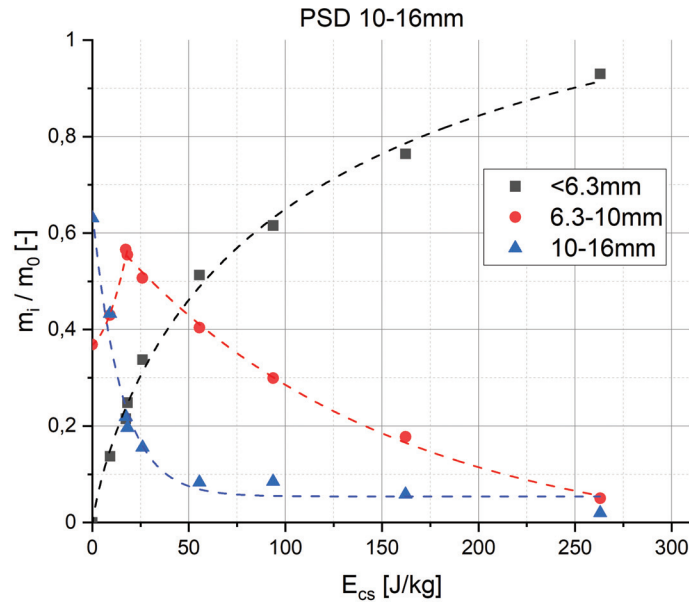
Figure 6.20: Particle size distribution after impact tests for initial size fraction 10-16 mm (sinter A) [1]
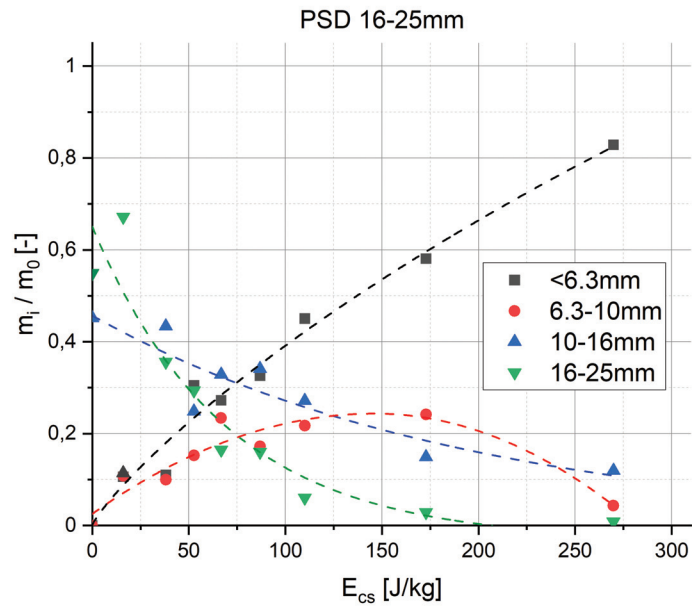
Figure 6.21: Particle size distribution after impact tests for initial size fraction 16-25 mm (sinter A) [1]
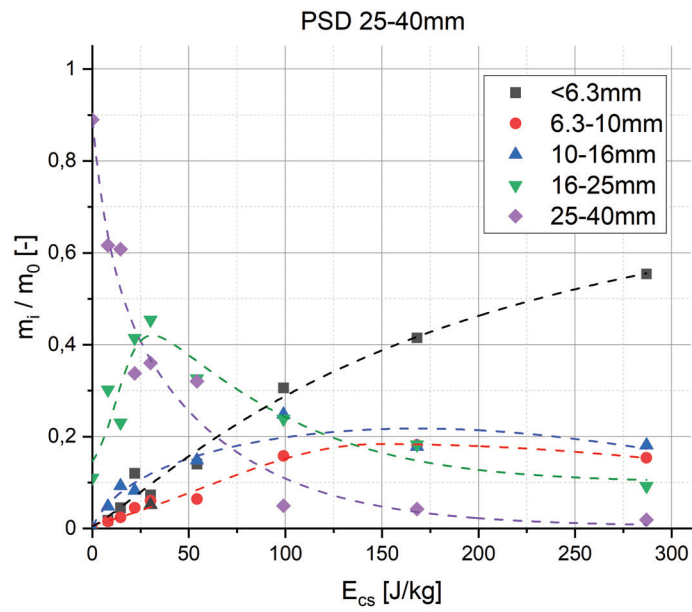
Figure 6.22: Particle size distribution after impact tests for initial size fraction 25-40 mm (sinter A) [1]

6.5.2 Return fines

Return fines m_{RF} were calculated as the difference between initial particle mass m_0 and the sum of all other fragments except m_1 because it could not be ensured that every fine particle was collected (see Equation 6.4). Thus, the mass m_1 in the first collecting box for return fines was only used as a check value.

In Figure 6.23 the absolute return fines production is plotted depending on specific impact energy input, calculated by Equation 6.4. The results show a limited growth trend of fines, following Equation 6.5, which has the same form as Equation 2.37, a and b are fit parameters.

$$m_{RF} = m_0 - \sum_{i=2}^{7} m_i \geq m_1 \tag{6.4}$$

$$m_{RF} = a(1 - e^{-bE_{cs}}) \tag{6.5}$$
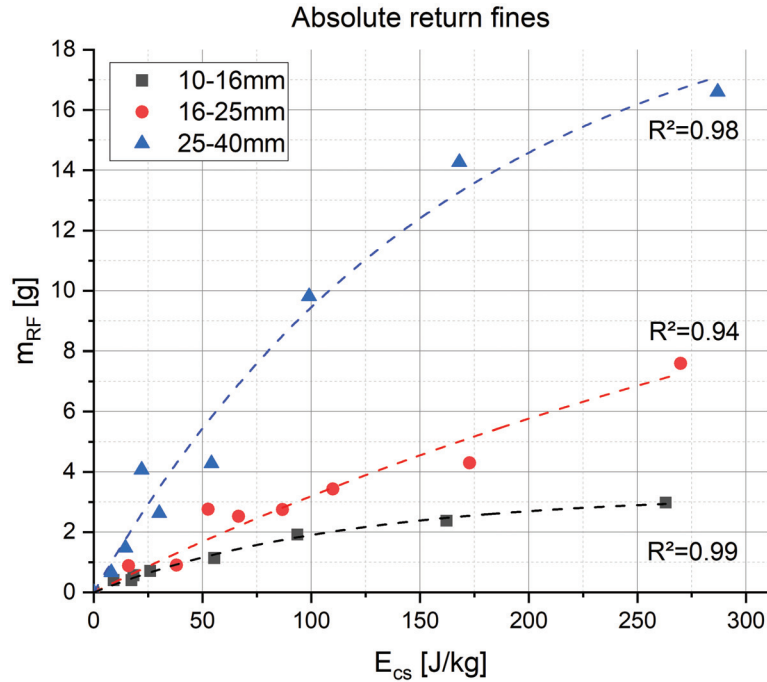
Figure 6.23: Absolute return fines production for various initial particle sizes of sinter A [1]

In Figure 6.24 the relative return fines production in relation to initial particle mass m_{RF}/m_0 is plotted for different initial particle sizes. This plot summarizes the <6.3 mm curves from the PSD diagrams in Figures 6.20-6.22. The plot shows that smaller particles produce a higher percentage of return fines, which is consistent with the findings in [92]. The data can well be described as a logistic growth trend [289], following Equation 6.6. E_0 is the initial value, E_∞ the final value, E_t the turning point and p is the power value. The turning points for fines curves of sinter A are at very low impact energies $E_t \approx 0$, but are higher for sinter B (see Section 6.5.5), which clarifies the use of the logisitc growth model for relative fines production instead of a limited growth model following Equation 6.5.

$$m_{RF}/m_0 = \frac{E_0 - E_\infty}{1 + (E_{cs}/E_t)^p} + E_\infty \qquad (6.6)$$
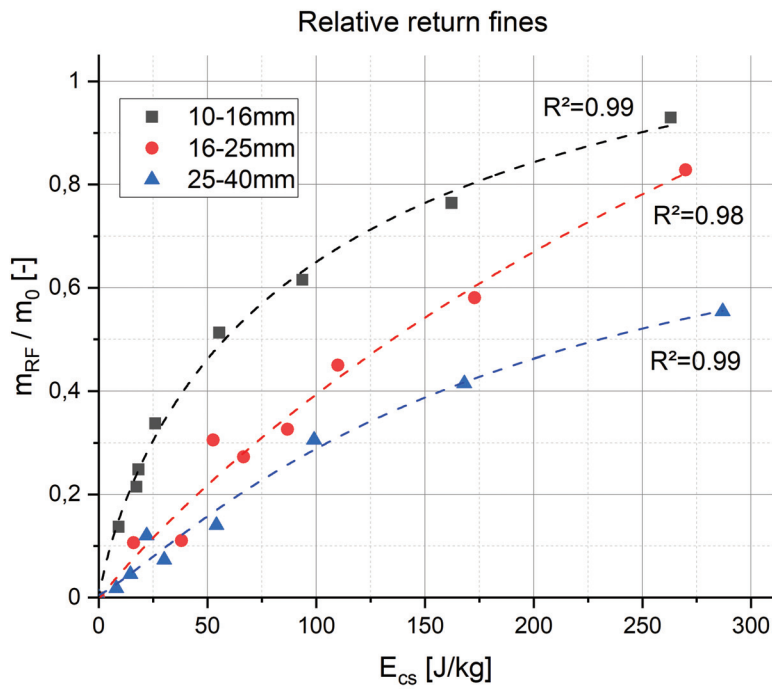
Figure 6.24: Relative return fines production for various initial particle sizes of sinter A [1]

In Figure 6.25 an attempt for a size-independent return fine prediction has been made. A size factor $1/x^2$ has been introduced, where x is the initial particle size. In this case x is 16 mm, 25 mm or 40 mm. When the relative return fines are plotted over the specific energy multiplied by this size factor (E_{cs}/x^2), the fines production data from all fractions fit well into a logistic growth trend following Equation 6.6. For better visualization, the data is presented in semi-logarithmic scale.
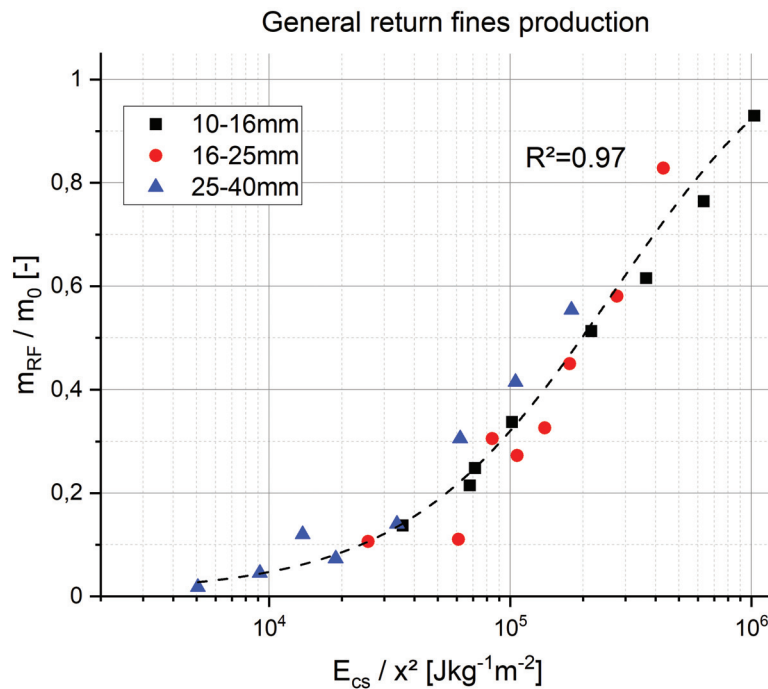
Figure 6.25: Construction of a general return fines production curve for sinter A by introducing a size factor $1/x^2$ [1]

A further advantage of individual fragment analysis in contrast to simply analyzing all debris at once for each trial is that the variability of fines production can be investigated, which gives more detailed information. In Figures 6.26-6.28 the variability for the relative return fines production for each size fraction at similar specific energy levels is illustrated by box plots. Each box plot represents a minimum of 50 particles. The results quantify the great variability in particle strength of the tested sinter.
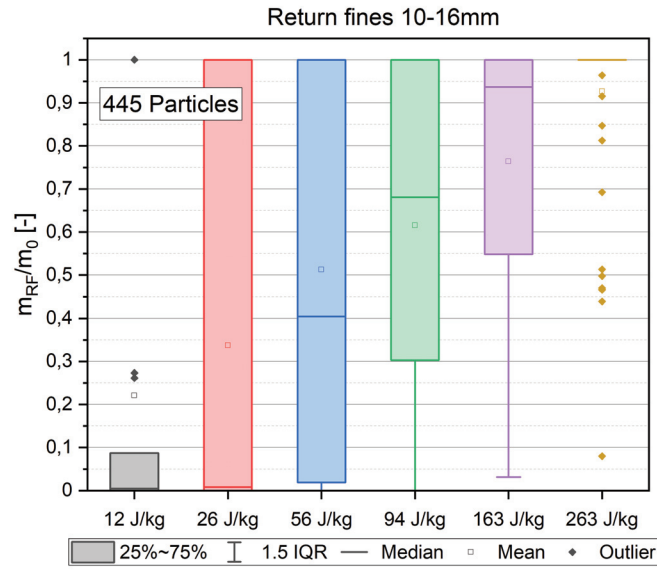
Figure 6.26: Variability of relative return fines production for size fraction 10-16 mm of sinter A [1]
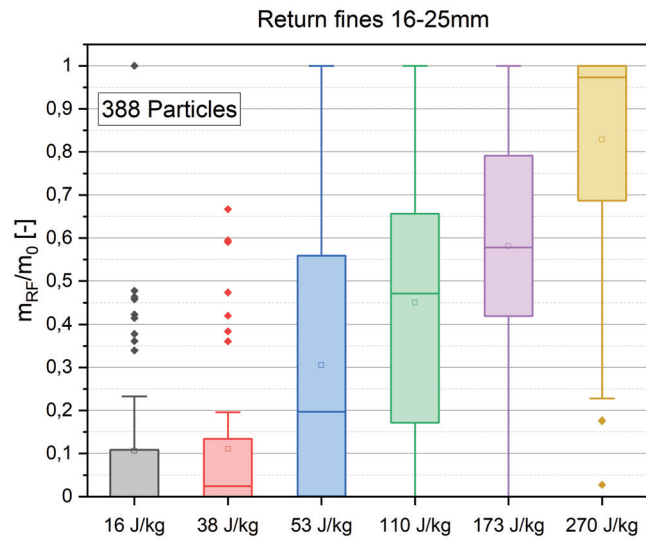
Figure 6.27: Variability of relative return fines production for size fraction 16-25 mm of sinter A [1]
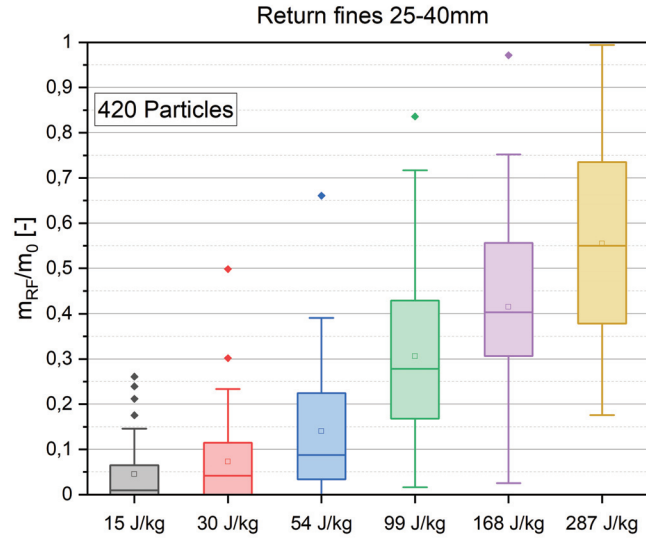
Figure 6.28: Variability of relative return fines production for size fraction 25-40 mm of sinter A [1]

The standard deviation (STD) of relative return fines production has also been investigated. Plotted against the mass-specific impact energy E_{cs}, clear trends are noticed, which all follow an exponentially modified Gaussian peak curve [290] (see Figure 6.29). Furthermore, Figure 6.29 clearly points out that the variability, or rather, the STD of generated return fines peaks at a certain impact energy. This peak shifts to higher impact energies with increasing particle size.
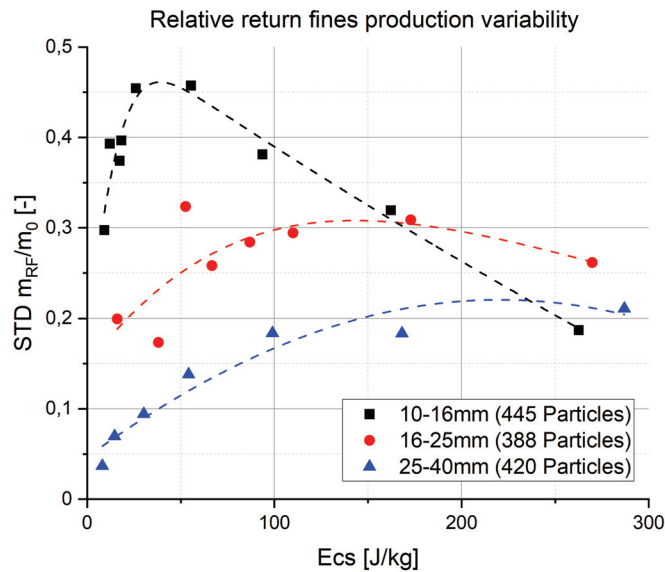
Figure 6.29: Standard deviation of relative return fines production

6.5.3 Breakage probability

As in [291] a particle is defined as broken when its mass is decreased by 10% due to a damaging event. Thus, a particle counts as broken if the fragment mass m_i is <90% of the initial particle mass m_0. m_i is the fragment mass, which corresponds to the initial particle size. In this study, however, it is necessary to include the fragment mass below m_i (m_{i-1}). This is because of the fact that the vibrating sorter works on a one-dimensional passing principle and some particles are classified into a size fraction lower than they were classified by the two-dimensional sieves of the manufacturer. Thus, a particle counts as broken if $m_i + m_{i-1}$ is <90% of the initial particle mass m_0 (see Equation 6.7).

$$m_i + m_{i-1} < 0.9\,m_0 \tag{6.7}$$

The breakage probability is plotted depending on the mass-specific impact energy E_{cs} for each fraction. Breakage is defined as a 10% mass decrease of the initial particle. The Vogel and Peukert model (Section 2.9.6) and the t_n-model (Section 2.9.7) both suggest a Weibull fit for the breakage probability. The Tavares breakage model (Section 2.9.8) suggests a lognormal fit. For comparison, both regression models are depicted in Figures 6.30 and 6.31 with their coefficients of determination R^2. For all tested size fractions both regression models are suitable. The Weibull model provides a slightly more accurate fit in this case, considering $\sum_{i=1}^{3} R_i^2$. The largest particles 25–40 mm are more likely to break, which meets expectations derived from material handling.
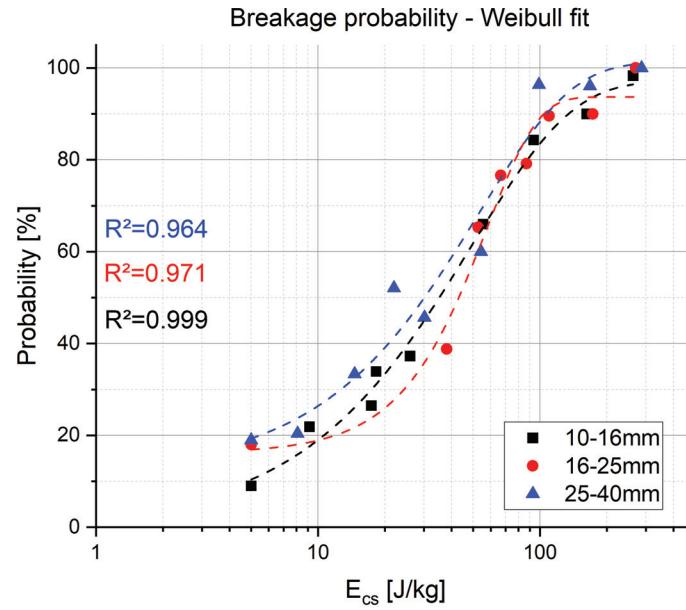
Figure 6.30: Breakage probability for sinter A with Weibull regression, breakage defined as 10% mass decrease
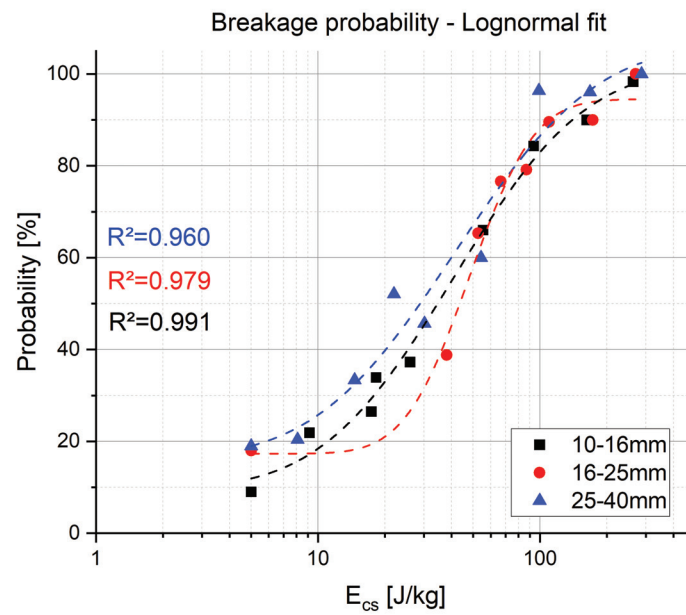
Figure 6.31: Breakage probability for sinter A with lognormal regression, breakage defined as 10% mass decrease

6.5.4 Breakage characterization with the t_n-model

The breakage behavior of sinter A has been characterized with the t_n-model (see Section 2.9.7). The tested particle size range in this investigation was 10–40 mm. All particles smaller than 6.3 mm are not suitable for blast furnace charging and were declared as return fines. Consequently, 6.3 mm is the finest mesh size in this investigation and determination of a t_{10} value was considered irrelevant in this case. In Table 6.7 the resulting n-values for each mesh size are listed.

Thus, a size-independent characterization of breakage behavior was be performed by creating t_4 and $t_{2.5}$ curves (see Figures 6.32) and 6.33. The data for all initial particle size fractions can be fitted with a limited growth trend following Equation 2.37. In Figure 6.33 no data for the 10–16 mm size fraction is available because no sieving finer than 6.3 mm was carried out. The results show that general breakage behavior is independent of particle size for this material, which meets expectations because all size fractions are fragments from the same sinter cake.

Size fraction [mm]	Passing [mm]	n for mesh size				
		6.3 mm	10 mm	16 mm	25 mm	40 mm
10-16	16	2.5	1.6	1.0	-	-
16-25	25	4	2.5	1.56	1.0	-
25-40	40	6.3	4	2.5	1.6	1.0

Table 6.7: n-values for different mesh sizes and size fractions
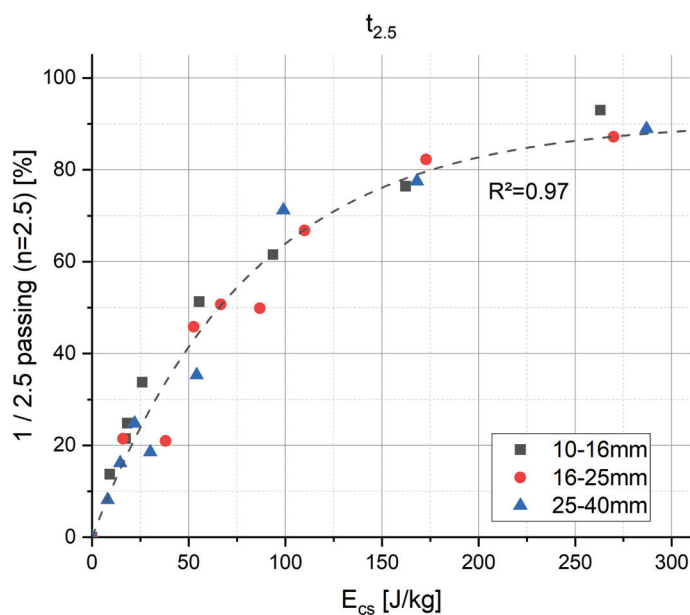
Figure 6.32: Size-independent breakage characterization of sinter A with t_n-model, n=2.5 [1]
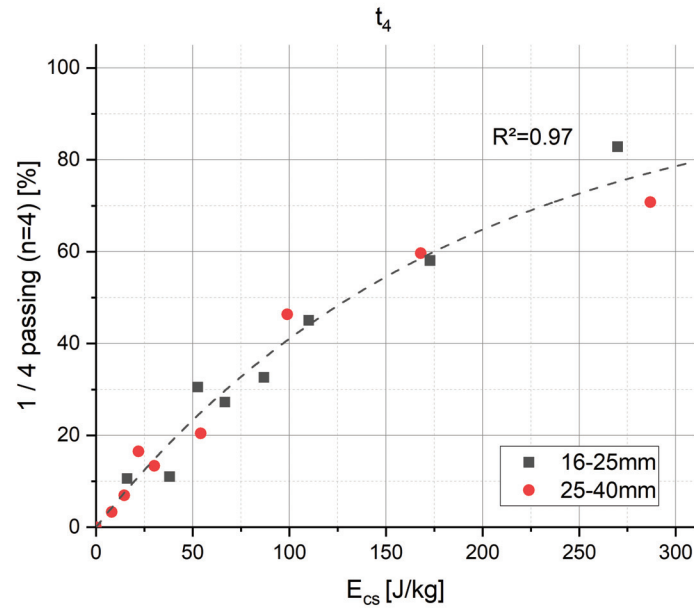
Figure 6.33: Size-independent breakage characterization of sinter A with t_n-model, n=4 [1]

6.5.5 Sinter B

The same test procedure as for sinter A was conducted for sinter B for the particle size fractions 10-16, 16-31.5 and 31.5-50 mm. The average initial particle masses m_0 of tested particles were 2.7 g (10-16 mm), 10.2 g (16-31.5 mm) and 59.9 g (31.5-50 mm). The PSD for these fractions in dependence on specific impact energy is depicted in Figures 6.34-6.36. Similar to sinter A, larger size fractions decrease exponentially. For the particles with the initial size 31.5-50 mm in Figure 6.36 the fractions between initial sizes and fines (16-25 mm and 10-16 mm) peak at low energies and can also be described by biphasic Hill curves [287]. An additional investigation with the size fraction >50 mm at low impact energies was performed with the drop module (see Figure 6.37).
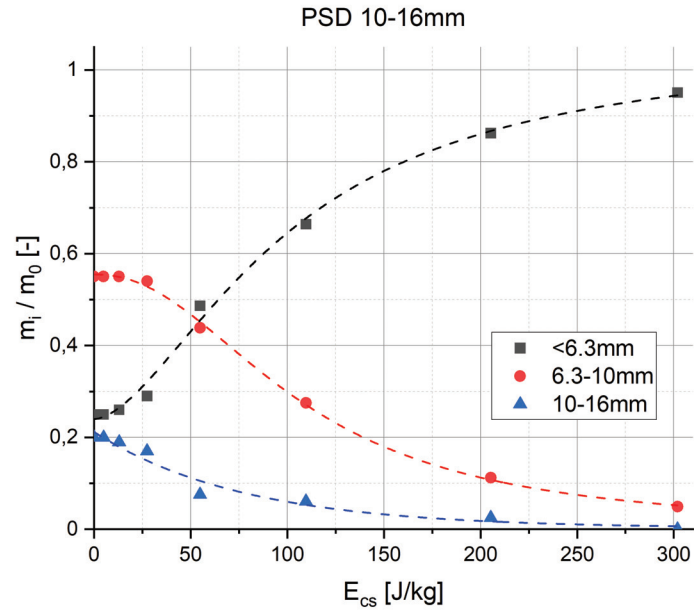
Figure 6.34: Particle size distribution after impact tests for initial size fraction 10-16 mm (sinter B)
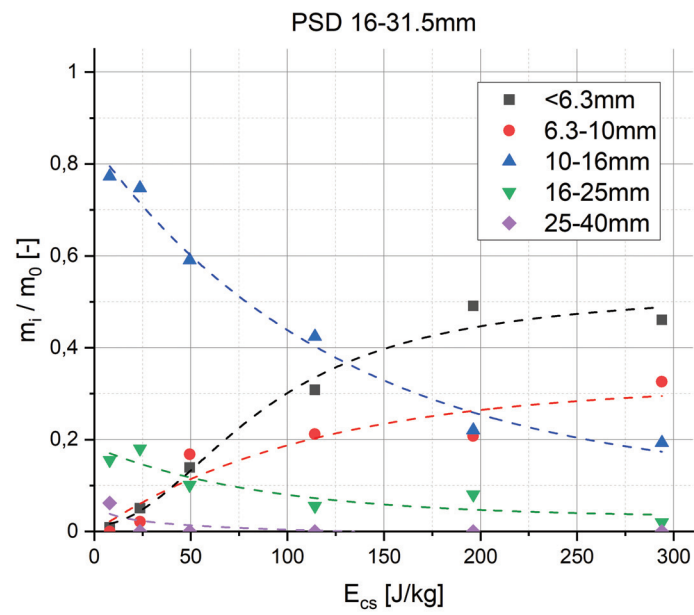
Figure 6.35: Particle size distribution after impact tests for initial size fraction 16-31.5 mm (sinter B)
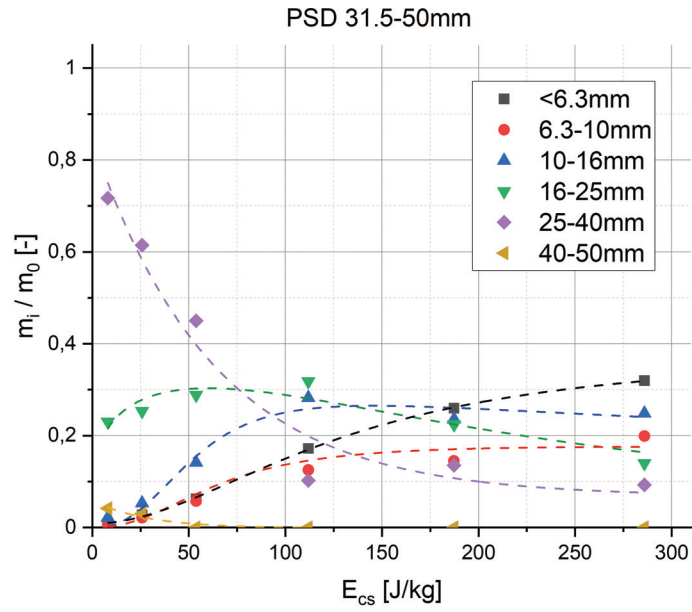
Figure 6.36: Particle size distribution after impact tests for initial size fraction 31.5-50 mm (sinter B)
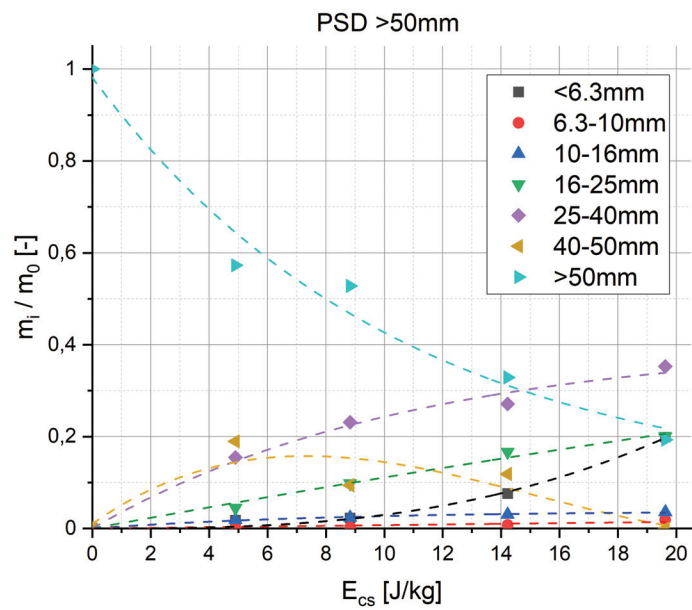
Figure 6.37: Particle size distribution after low-energy impact tests by drop module for initial size fraction >50 mm (sinter B)

The absolute return fines production of sinter B is shown in Figure 6.38. The mass of the produced return fines m_{RF} for the smallest initial particle size 10-16 mm follows a limited growth trend (see Equation 6.5). For the larger initial particle sizes 16-31.5 mm and 31.5-50 mm, the trends seem to be linear for these impact energies, but it is assumed that for higher impact energies the curves would also follow a limited growth trend because the return fines mass is limited by the particle mass.
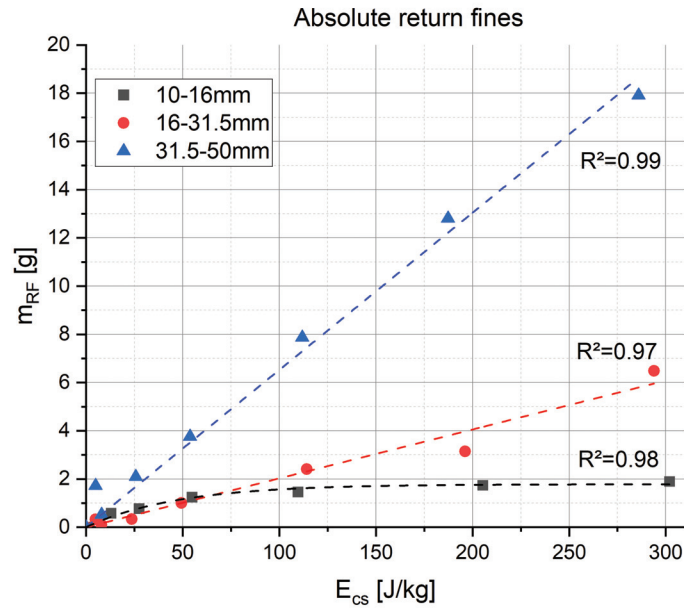
Figure 6.38: Absolute return fines production for various initial particle sizes of sinter B

The relative return fines production of sinter B is depicted in Figure 6.39. In contrast to sinter A, a lower gradient at low impact energies is noticed, which can well be described as a logistic growth trend [289].
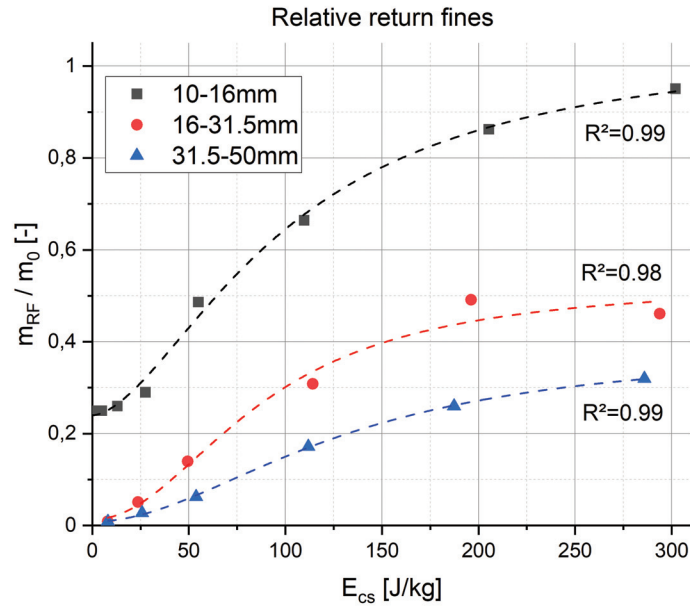
Figure 6.39: Relative return fines production for various initial particle sizes of sinter B

6.5.6 Sinter C

Sinter C was tested subsequently for verification and validation of the simulation model with shatter tests (see Section 11.1). In contrast to sinter A and B, sinter C was re-sorted with the vibrating sorter before the impact tests. This reduced statistical scattering and allowed to reduce the tests to 30 valid tests per specific energy level. The maximum specific test energy for this trial was $E_{cs} = 103$ J/kg because higher energies did not occur in the performed shatter tests. Only the size fraction 25-40 mm was tested with sinter C. The average particle mass m_0 for all tested particles is 47 g.

The PSD after impact tests is depicted in Figure 6.40. Similar to sinter A and B, the initial particle size decreases exponentially. The fragment sizes 16-25 mm, 10-16 mm and 6.3-10 mm are assumed to peak at low impact energies and to decrease with increasing impact energy, which is not visible in this diagram due to the low energy range. The fines appear almost linear at this impact energy range, but are assumed to follow a logistic growth trend [289] if the trial was continued with higher impact energies.
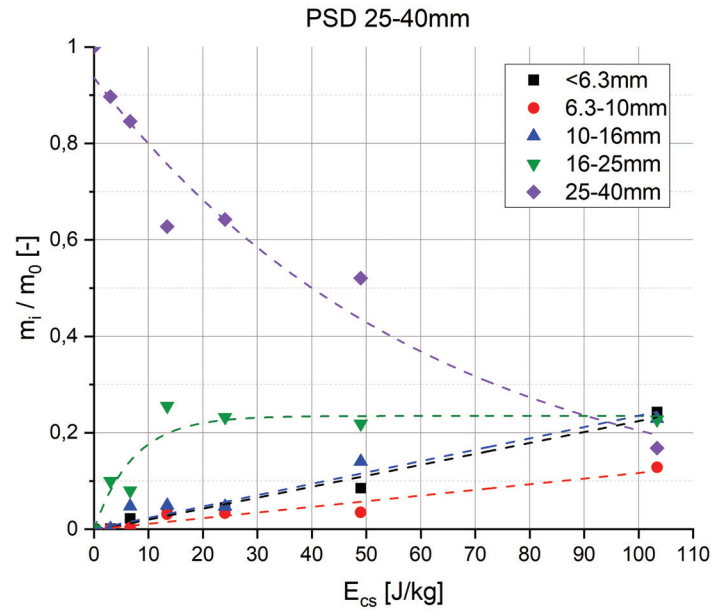
Figure 6.40: PSD after impact for initial size 25-40 mm (sinter C) [2, 7, 9]

6.5.7 General return fines production curve

As seen in Figure 6.25, relative return fines production m_{RF}/m_0 of all fractions fits well into a curve when plotted over the specific impact energy multiplied by a size factor $1/x^2$, whit x being the initial particle size. If the data from sinter B and sinter C are added to this plot, the data from all three batches of sinter also can well be described by a logistic growth trend following Equation 6.6, which is presented in a semi-logarithmic scale (see Figure 6.41). It must be stated that in the fraction 10–16 mm of sinter B initially 25% of the particles were declared fines when re-sorted by the vibrating sorter before testing, however, the data converges the fit curve with increasing impact energy.

The fact that the data from three different batches from two different manufacturers can be fitted into one curve justifies the construction of a size-independent return fines production curve. It is assumed that the constructed curve allows a general evaluation of return fines production for these materials, but needs to be confirmed by further investigations. This general return fines production curve can be a very useful tool to estimate return fines production when impact velocities or drop heights are known. It can be used for the development or optimization of conveying and storage processes, for example. It must be stated that this specific curve is only valid for sinter particles which hit steel plates. This is due to the test method, which can be adapted for other impact surfaces.
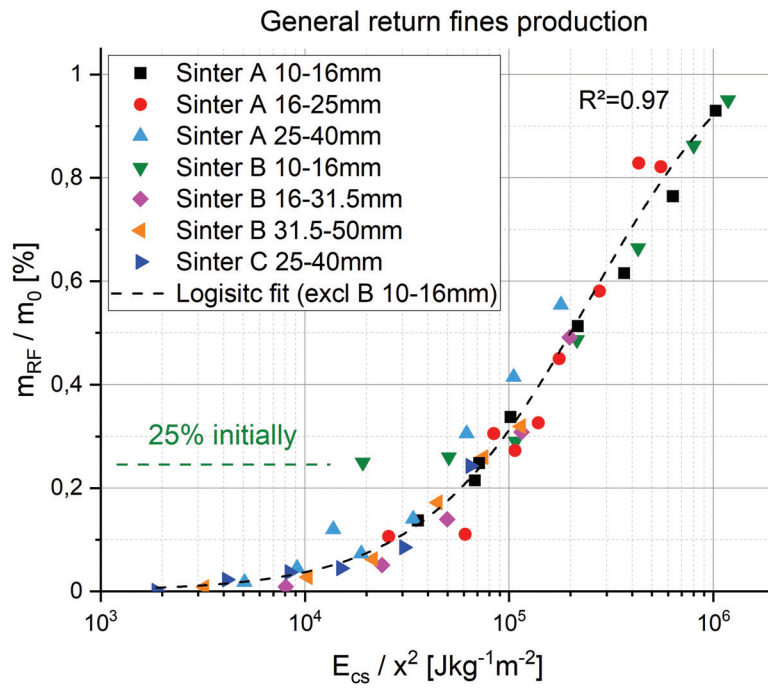
Figure 6.41: General return fines production curve, based on three different batches of sinter from two different manufacturers

7 Conveying tests

The content of this chapter 7 was already published in [5, 11] and documented in the project report [16]. It was desired to verify and validate sinter breakage simulations by means of realistic conveying processes. This was conducted by comparative trials with a standard chute and an innovative dynamic transfer system (FlowScrape), which was further developed and tested during the project MinSiDeg.

7.1 Dynamic transfer system FlowScrape

The team Conveying Technology and Design Methods at the Chair of Mining Engineering and Mineral Economics is currently developing a dynamic transfer device in a parallel project in cooperation with the companies ScrapeTec Trading GmbH, ScrapeTec GmbH and Wanggo Gummitechnik GmbH. This device has been tested and investigated with regard to its applicability to particle breakage reduction in MinSiDeg. The content of Section 7.1 is based on [292, 293].

The design of the dynamic transfer chute system FlowScrape is shown in Figure 7.1. The system is constructed from at least three rubber chains, joined together to form a trough. The chain structure and the associated supporting elements are based on the function of rubber track excavator undercarriages. A cardanic connection of the chain wheel axles ensures synchronous running of the chains. The dynamic transfer chute is mounted between the discharging and the receiving conveyor (see Figure 7.2).

The drive of the transfer chains can be realized in two ways. Basically, the transfer chains are driven by the receiving conveyor belt via a friction wheel. For this purpose, the friction wheel is pressed onto the middle chain and the receiving belt conveyor. The chain system is pivoted for this purpose (parallel to the drum axles of the receiving belt). If the weight of the transfer chains is not sufficient, an additional pressing device can be implemented. As an alternative to the friction wheel drive, the system can also be driven by an electric motor. The prototype of the dynamic transfer system is depicted in Figure 7.3a).
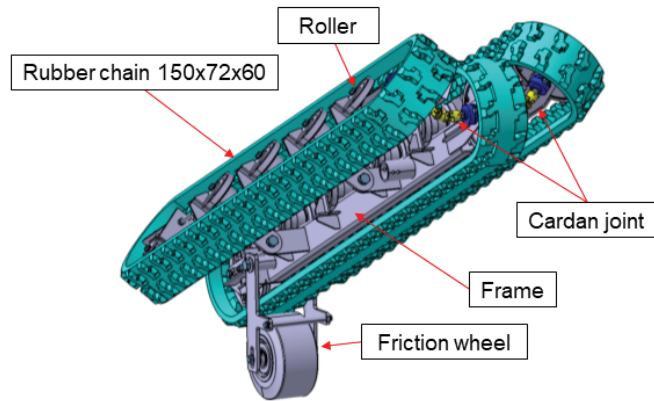
Figure 7.1: Design of the dynamic transfer system FlowScrape [292]
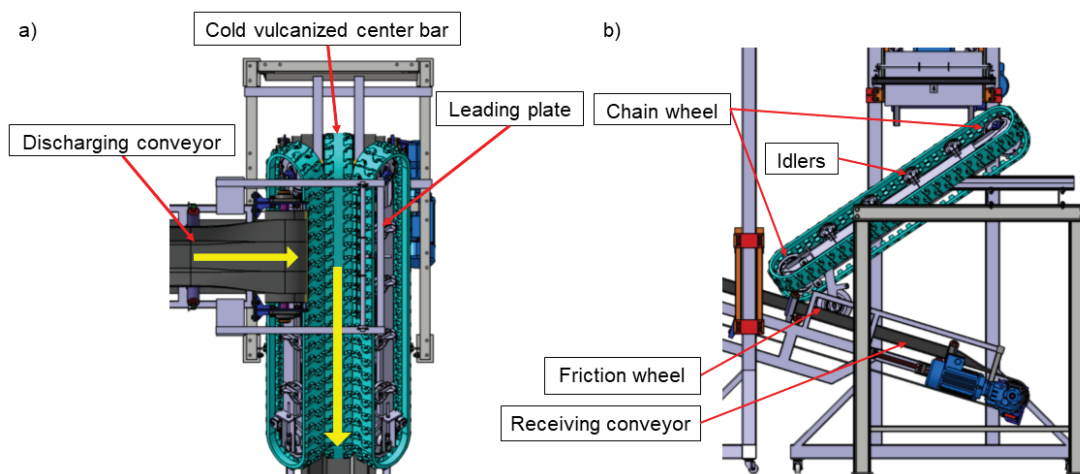
Figure 7.2: Operating principle of the FlowScrape (CAD model) a) top view b) side view [292]

Depending on the properties of the transported bulk material, the sealing of the longitudinal chain transitions can be implemented as follows. For bulk materials without fines, the longitudinal chain edges can be pressed together for sealing. However, due to manufacturing tolerances of the chains, small opening and closing gaps eventually occur when the edges are pressed together, through which fine material can pass. In the case of fine-grained bulk material, the outer chains are overlapped with the middle chain to ensure a seal and thus prevent the fines from passing through. Depending on the incline of the transfer chains, they can be designed with or without cross cleats. The dynamic transfer system has been patented in [293]. Further details regarding development and first tests are described in [292].

In addition to reducing particle breakage, the transfer system has other advantages. Compared to conventional rigid transfer chutes, the chute wear is not punctual but distributed over the entire circulating chain surface. A significantly longer service

life can therefore be expected. With sufficient mass flow and height difference, the resulting downhill forces are sufficient to overcome the movement resistance of the chain system. The dynamic chute must then be braked by the receiving conveyor or an electric drive. In this process, some energy recovery occurs [292]. In combination with the reduction of the drive power of the receiving belt and the energy recovery, this results in an energy-efficient system. Due to the design, clogging due to caking is unlikely. Only massive unintentional overfilling can cause problems. Compared to conventional accelerator belts, the chain system has a central guiding device on the chain running side. This forced guidance means that, in contrast to conventional accelerator belts, no belt misalignment can occur, regardless of the feed direction.

The system always leads to a directed transfer in the conveying direction of the discharging belt (soft loading). This means that the bulk material has to be accelerated less (reduction of drive power) and there is less belt load and thus less wear on the receiving conveyor. In contrast to simple chutes, this soft-loading effect can be achieved with the FlowScrape even at low drop heights. Simple chutes would tend to clog at low drop heights due to the large decrease in speed of the bulk material if a standard soft loading chute or device is used.

7.2 Comparative trails with conventional chute

In order to quantify the reduction of stresses on the bulk material during transfer with the FlowScrape, the resulting particle breakage was compared with the particle breakage during transfer with a conventional chute. Such conventional chutes are also used for the transport of blast furnace sinter. The conventional transfer chute consists of a cuboidal wooden structure with a steel baffle plate on the rear wall and additional covers near the belt to prevent material loss (see Figure 7.3b). Most of the bulk material collides with the baffle plate and then falls onto the outgoing belt. The total drop height is 1600 mm. Such drop chutes are installed as an alternative to rock boxes. In a rock box, a deliberate accumulation of material is caused. This leads to a reduction of wear on the chute because the mass flow impacts onto the material accumulation. Thus, the stresses are transferred from the chute to the bulk material itself and partially promote degradation of the bulk material. However, since rock boxes tend to clog and thus cause problems, existing rock boxes are in some cases replaced by conventional chutes.
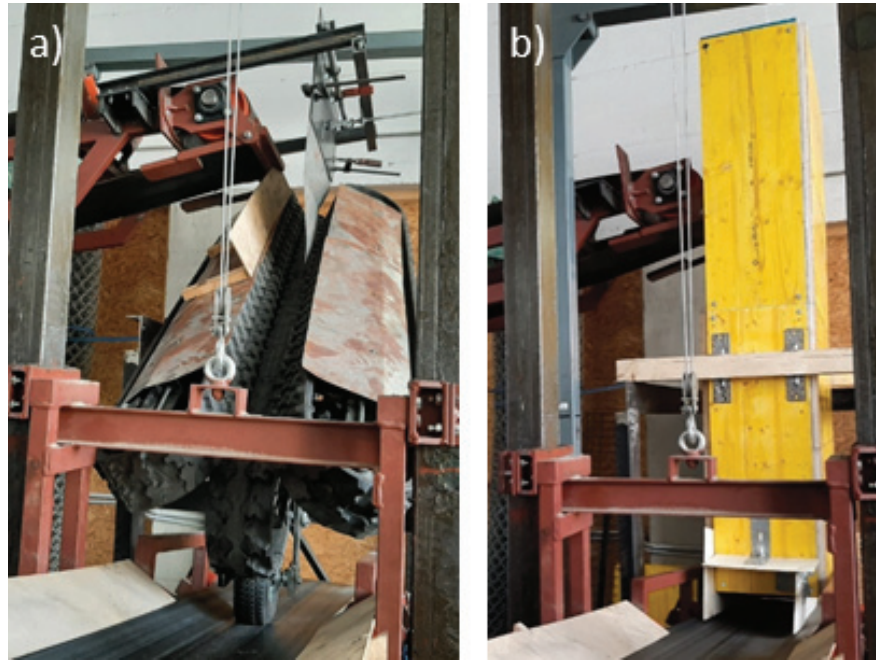
Figure 7.3: Transfer point with a) FlowScrape b) Conventional transfer chute [5, 11]

The test series was carried out on the chairs' own conveyor circuit (see Figure 7.4). This consists of four belt conveyors with a width of 400 mm each. Inclinations, trough angles and belt conveyor speeds can be individually adjusted. Three of the four transfer points are equipped with simple baffle plates. One transfer point is intended as a test stand, in order to be able to assemble a wide variety of transfer systems there and test them in the circuit.

Two series of tests were carried out with the particle size fractions 16-31.5 mm and 31.5-50 mm from sinter B, the latter being the critical fraction for particle breakage. For each test, 10 kg (31.5-50 mm) and 5 kg (16-31.5 mm) of material were used. The actual particle size distribution within these conventionally sieved (2D sorting principle) size fractions was determined in each case prior to the tests by means of the vibrating sorter (1D sorting principle), which is described in detail in Section 6.3.4. Since the particle size distribution varies within the size fraction provided by the manufacturer and the classification by means of the vibrating sorter depends on the orientation of the particles in the vibrating sorter, the samples were sorted three times in each case and the arithmetic mean of the results was defined as the particle size distribution before the test. At constant belt speeds and drop heights, 6 tests each were carried out with the FlowScrape (see Figure 7.3a) and 5 tests each with the conventional chute (see Figure 7.3b) as transfer device. In the case of the FlowScrape, an additional baffle plate was mounted at the upper end to prevent material loss and to load the FlowScrape

centrally. The bulk sample was placed and distributed manually at the beginning of the discharging belt so that no particles overlapped. The belt velocities of the discharging and receiving belts were 1.5 m/s. The bulk sample was collected in a plastic trough at the end of the outgoing belt. The drop height into the plastic trough was also the same for all tests and was approximately 0.5 m. Finally, the particle size distribution was measured again after the test by sorting three times in the vibrating sorter. These trials were carried out together with P. Wagner and are also documented in [294].

Figure 7.4: Conveying circuit with operating FlowScrape [5, 11]

Figure 7.5 shows the mass-related particle size distributions of the test series with initial size fractions 31.5-50 mm and 16-31.5 mm before and after transfer with a conventional chute. The particle size distributions before and after transfer with the FlowScrape are shown in Figure 7.6. The values are derived from the arithmetic mean of all 6 or 5 tests. A direct comparison of the particle breakage between the FlowScrape and the conventional transfer chute is shown in Figure 7.7, where the increase in mass per size fraction is depicted. The results show that with both the FlowScrape and the conventional transfer chute, the larger particles tend to break and their mass fractions decrease. At the same time, the mass fractions of the smaller size fractions increase.

The significant difference in the increases and decreases of mass fractions between the FlowScrape and the conventional transfer chute proves that less particle breakage occurs during transfer with the FlowScrape. The difference is particularly

significant in the case of return fines (<6.3 mm), which is quite important for the steel industry. In the test series with the size fraction 31.5-50 mm, 50% less fine material was produced during the transfer with the FlowScrape compared to the transfer with a conventional chute.

The test results of the trial with the initial size fraction 16-31.5 mm show significantly less particle breakage than those of the trial with size fraction 31.5-50 mm. This meets expectations, since large particles are generally more likely to break than small ones and the larger fraction is regarded as more critical in the industry. A similar amount of fines was produced with the 16-31.5 and 31.5-50 mm size fraction with both transfer devices. It is assumed that this is not only due to volume breakage of the larger particles, but that particle abrasion, especially with smaller particles, also has a relevant influence on the production of fines. Since the number of particles in the test series with the initial size fraction 16-31.5 mm is significantly higher than that in the test series with the size fraction 31.5-50 mm, the influence of particle abrasion due to particle interactions thus also increases.
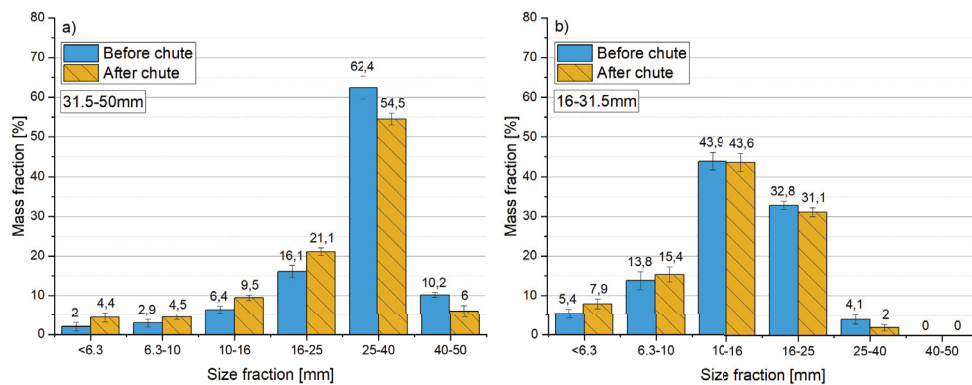
Figure 7.5: Particle size distribution before and after the conventional chute for initial size fraction a) 31.5-50 mm b) 16-31.5 mm [5, 11]
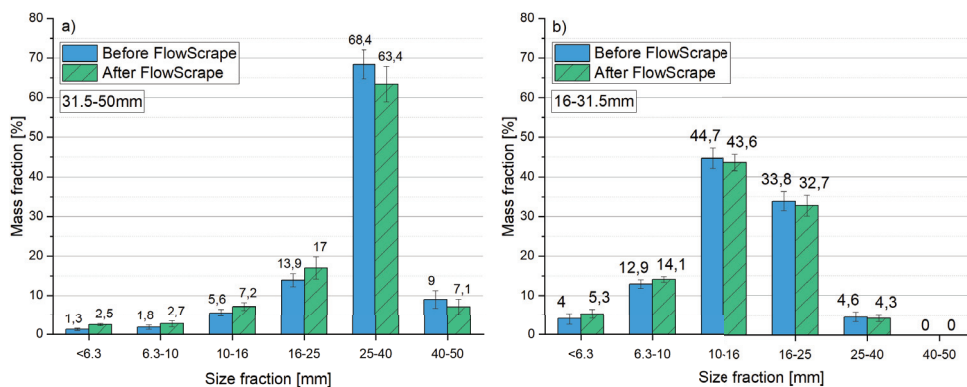
Figure 7.6: Particle size distribution before and after the FlowScrape for initial size fraction a) 31.5-50 mm b) 16-31.5 mm [5, 11]
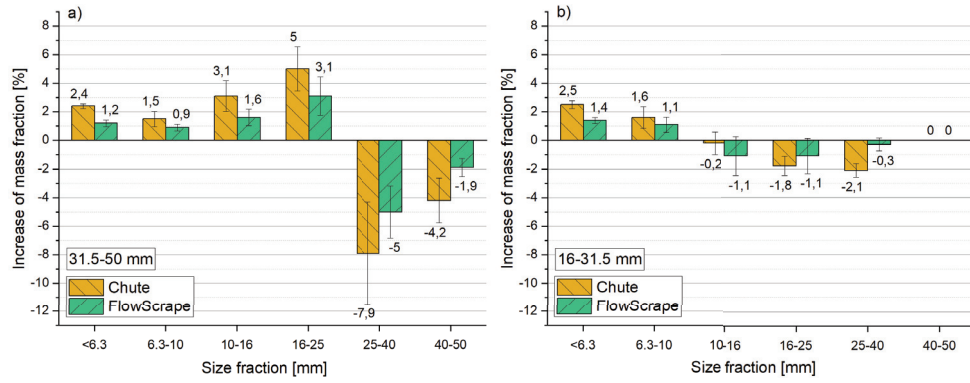
Figure 7.7: Increase of mass fraction due to transfer with conventional chute and FlowScrape for initial size fraction a) 31.5-50 mm b) 16-31.5 mm [5, 11]

7.3 Material calibration

As static friction between sinter particles is dependent on particle size in this case, angle of repose tests as in [277] were performed with size fractions 16-31.5 mm and 31.5-50 mm from sinter B, which were used in the following simulations in Section 7.4. In these tests, a steel cylinder with inner diameter $\varnothing = 212\,mm$ on a steel plate was filled with the sinter sample (m=25.06 kg for 16-31.5 mm and m=29.84 kg for 31.50 mm). The PSD of the sinter samples were analyzed with the vibrating sorter and are listed in Table 7.1. The steel cylinder was lifted with a crane with a constant velocity of 67 mm/s until the whole bulk sample slid out and formed a bulk cone. The lifting velocity was measured with a high-speed camera.

	Mass fraction [%]	
Size fraction [mm]	16-31.5 mm	31.5-50 mm
<6.3	5.7	1.5
6.3-10	13.4	2.8
10-16	44.2	6.3
16-25	32.7	16.4
25-40	4.0	62.5
40-50	0	10.5

Table 7.1: Particle size distribution of sinter samples (sinter B) in the angle of repose tests, analyzed with the vibrating sorter

Then the angle of repose tests for each size fraction were simulated with EDEM in order to calibrate the static friction for sinter-sinter interaction coefficient. Spherical particles with capped angular velocity were used. The simulation was performed with capped angular velocity. Hereby the static friction coefficient was initially estimated and iteratively adjusted until the cone angle in the simulation matches the cone angle from the tests, which is depicted in Figures 7.8 and 7.9. The calibration results are listed in Table 7.2.
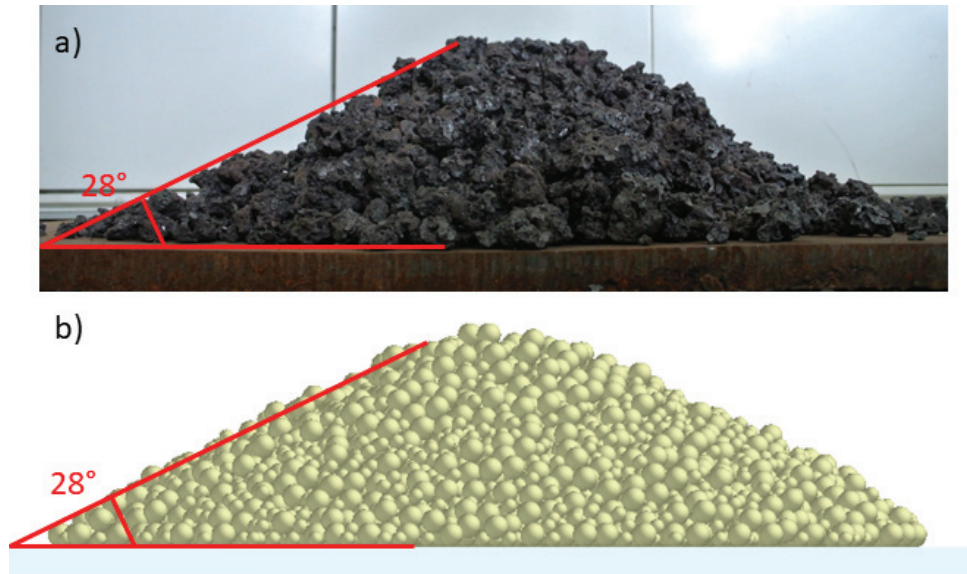
Figure 7.8: Comparison of cone angles from angle of repose test and corresponding simulation for the size fraction 16-31.5 mm (sinter B) a) angle of repose test b) simulation
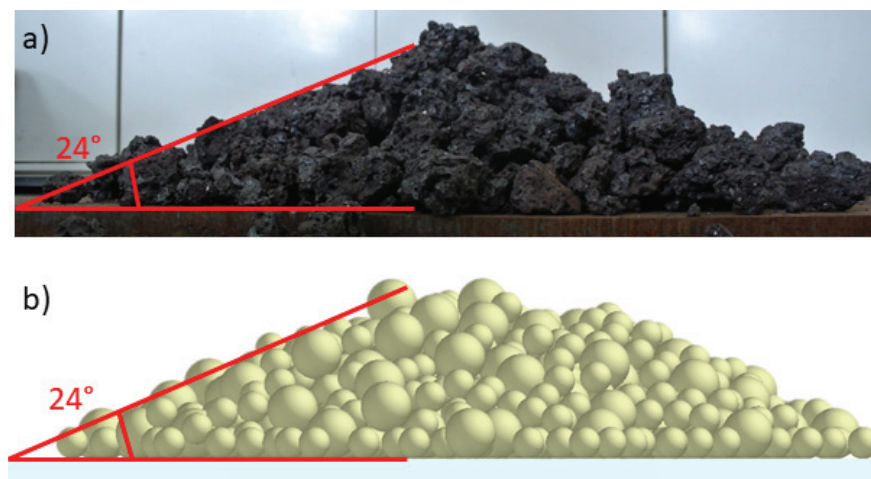
Figure 7.9: Comparison of cone angles from angle of repose test and corresponding simulation for the size fraction 31.5-50 mm (sinter B) a) angle of repose test b) simulation

Size fraction [mm]	Static friction (sinter-sinter) [-]
16-31.5	0.2
31.5-50	0.15

Table 7.2: Calibration results from angle of repose tests with spherical particles and capped angular velocity (sinter B)

7.4 Simulation

Transfer by FlowScrape and transfer by conventional chute were simulated using the DE software EDEM (see Figure 7.10). The cleats movement on the rubber tracks of the FlowScrape were realized by translation and rotation along the circulation curve. The initial size fractions used (31.5-50 mm and 16-31.5 mm) were represented by round particles with averaged diameters of d=40 mm and d=22 mm. From the breakage tests, the average particle masses of these size fractions are known ($m_0 = 59.9\,g$ and $m_0 = 10.2\,g$). The resulting numbers of particles (z=167 and z=490) for a bulk sample of $m_s = 10\,kg$ and $m_s = 5\,kg$, were also placed on the discharging belt conveyor in the simulation. The density ρ (1788 kg/m³ for 40 mm and 1830 kg/m³ for 22 mm) was adjusted to particle number z and sample mass m_s (see Equation 7.1).

$$\rho = \frac{6\,m_s}{z\,\pi\,d^3} \tag{7.1}$$

Material and interaction parameters are listed in Tables 7.3 and 7.4. Friction parameters were determined using slip tests in [277]. The static friction coefficients for sinter-sinter from Table 7.2 were used. Coefficients of restitution for sinter-sinter, sinter-FlowScrape, sinter-conveyor belt, and sinter-steel were determined using bounce tests and high-speed imaging from two perspectives in [295]. Shear and Young's moduli were set to very small values due to computational reasons but in a proper ratio for each material.

In order to detect the contact forces on the individual particles with sufficient accuracy, the time step and storage interval - depending on particle size, Young's moduli and contact velocities - must be small enough. However, a too small time step leads to high computational effort, and a too small storage interval to a flood of data and also to increased computational times. The relative deviations in contact force at various larger time steps and storage intervals were determined

in [296] in comparison to $10^{-7}\,s$ for particles of 6 mm and 40 mm in diameter at velocities which commonly occur in sinter conveying. An optimum between accuracy, computational effort and amount of data was found for these particle sizes and the impact velocities encountered in this simulation at a time step of $10^{-5}\,s$ and a storage interval of $10^{-4}\,s$. The relative deviations in contact force compared to $10^{-7}\,s$ here are 6.62% (6 mm) and 0.15% (40 mm). The simulation with a time step of $10^{-5}\,s$ and a storage interval of $10^{-4}\,s$ with particle diameters of 22 mm and 40 mm is thus sufficiently accurate for contact force detection in this case.
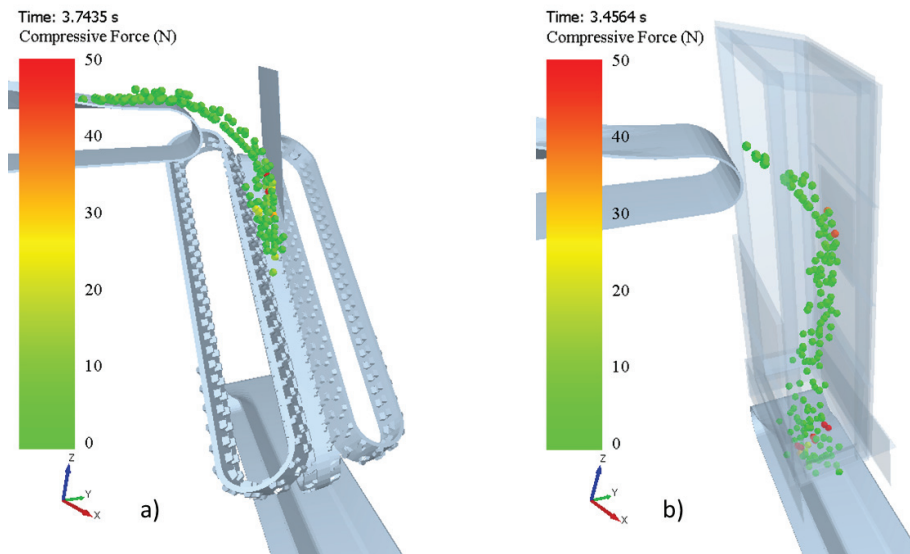
Figure 7.10: DE simulation of conveying tests with EDEM a) FlowScrape b) conventional chute [5, 11]

Material	Density [kg/m³]	Poisson's ratio [-]	Shear modulus [MPa]
Sinter B (16-31.5 mm)	1830	0.25	1
Sinter B (31.5-50 mm)	1788	0.25	1
Steel	7850	0.25	8400
FlowScrape	1400	0.5	2
Conveyor belt	1400	0.5	2

Table 7.3: Material parameters for conveying test simulations

Interaction	Restitution [-]	Static friction [-]
Sinter-Sinter (16-31.5 mm)	0.75	0.2
Sinter-Sinter (31.5-50 mm)	0.75	0.15
Sinter-Steel	0.43	0.839
Sinter-FlowScrape	0.49	0.7
Sinter-Conveyor belt	0.4	0.7

Table 7.4: Interaction parameters for conveying test simulations [277, 295]

8 Post-processing approach: evaluation of compressive force

The first attempt to simulate sinter breakage was made by evaluating compressive forces on particles in post-processing in order to predict breakage and the resulting particle size distribution based on breakage test results. The following approach was used: A particle breaks when a certain compressive force is applied. This approach was applied to the simulations of the conveying tests, described in Section 7.4 and conducted with EDEM. The content of Chapter 8 was already published in [5, 11] and documented in the project report [16].

8.1 Correlation between compressive force and impact velocity

The compressive forces required for establishing the correlation between compressive force and impact velocity were determined by simulating breakage tests with the parameters listed in Tables 7.3 and 7.4 (see Figure 8.1). For this purpose, the impact test against a steel plate was simulated at different velocities (see Figure 8.2). Time step and storage interval were again defined as $10^{-5}\,s$ and $10^{-4}\,s$, to determine the compressive force with sufficient accuracy as described in 7.4. A nonlinear correlation between maximum compressive force and impact velocity was noticed (see Figure 8.3). With this correlation and breakage test results, a prediction of eventual particle fracture was then able to be made.

To avoid an unnecessarily low time step and thus higher computation times, very low Young's moduli were chosen in the simulation. However, in order to take into account the different damping behavior of the impact surfaces and thus the influence on the compressive force, the Young's moduli of steel, belt and FlowScrape were defined in the correct ratio to each other. The Young's modulus of sinter was set to the smallest possible value. The coefficients of restitution also contribute to the damping are obtained from rebound tests in [295].
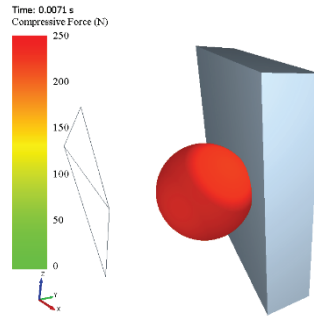
Figure 8.1: Simulation of impact test with EDEM [5, 11]
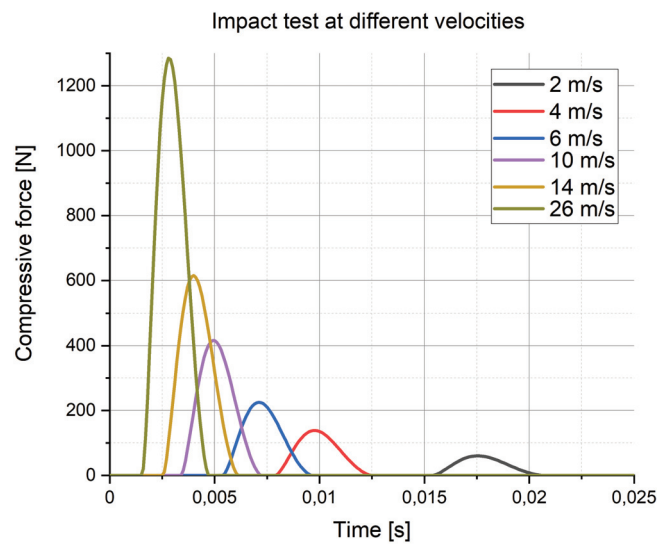
Figure 8.2: Compressive force at various impact velocities [5, 11]
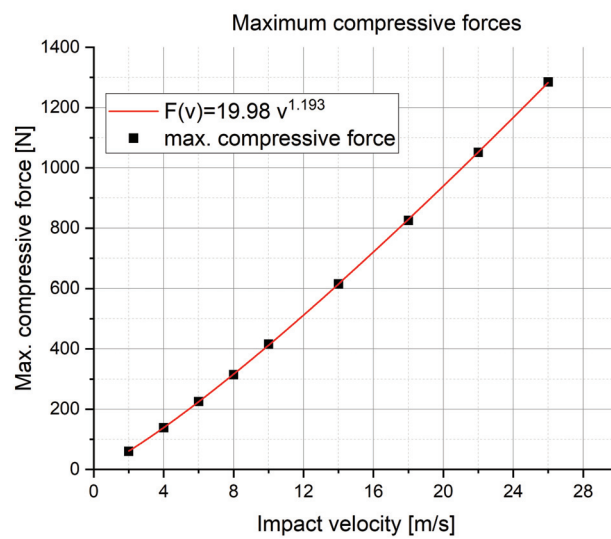
Figure 8.3: Maximum compressive force dependent on impact velocity [5, 11]

8.2 Breakage prediction

For particle breakage prediction, the compressive force of each particle was considered individually over the entire conveying time. Since EDEM can only export the compressive force or the particle ID at a time, a Matlab routine which links the result tables was programmed so that the compressive force was able to be determined for each particle for every time step and the compressive force plot was able to be evaluated (see Figure 8.4). Starting time for both plots in Figure 8.4 is the moment of discharge at the discharging belt conveyor.
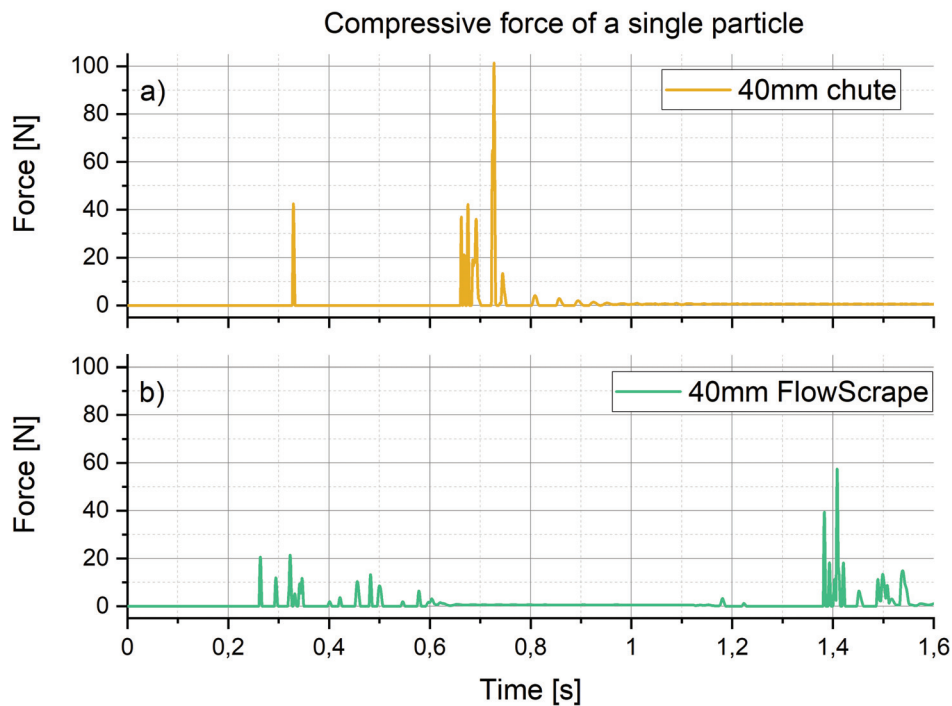
Figure 8.4: Exemplary compressive force plot for a single particle (40 mm) during conveying with a) conventional chute b) FlowScrape [5]

With both the FlowScrape and the conventional chute, there are two events which are mainly responsible for breakage: firstly, the collision with the baffle plate and the drop onto the FlowScrape, and secondly the fall onto the receiving belt conveyor. Thus, the largest and the second largest peak compressive force values were determined for each particle. Then force intervals were defined and the numbers of particles with peak value in the respective force intervals were determined. For this purpose, a histogram was created for the largest (Figure 8.5) and the second largest peak value in each case. As can be seen in Figure 8.5, the maximum compressive forces occurring are lognormally distributed in each case. The mean value of each force interval was then converted into a corresponding

velocity using the relationship in Figure 8.3. With the velocity, the mass-specific energy [J/kg] was able to be calculated and the expected PSD after breakage based on the breakage test results in Figure 6.36. The calculated expected PSD for each corresponding force interval was then weighted by the number of particles per force interval, resulting in the expected PSD of the entire bulk sample after the largest occurring load. This methodology was first described in [11]. The procedure was repeated for the second largest peak compressive force value and the increases or decreases in the mass fractions of the respective particle size fractions were added to the results of the largest peak compressive force value.
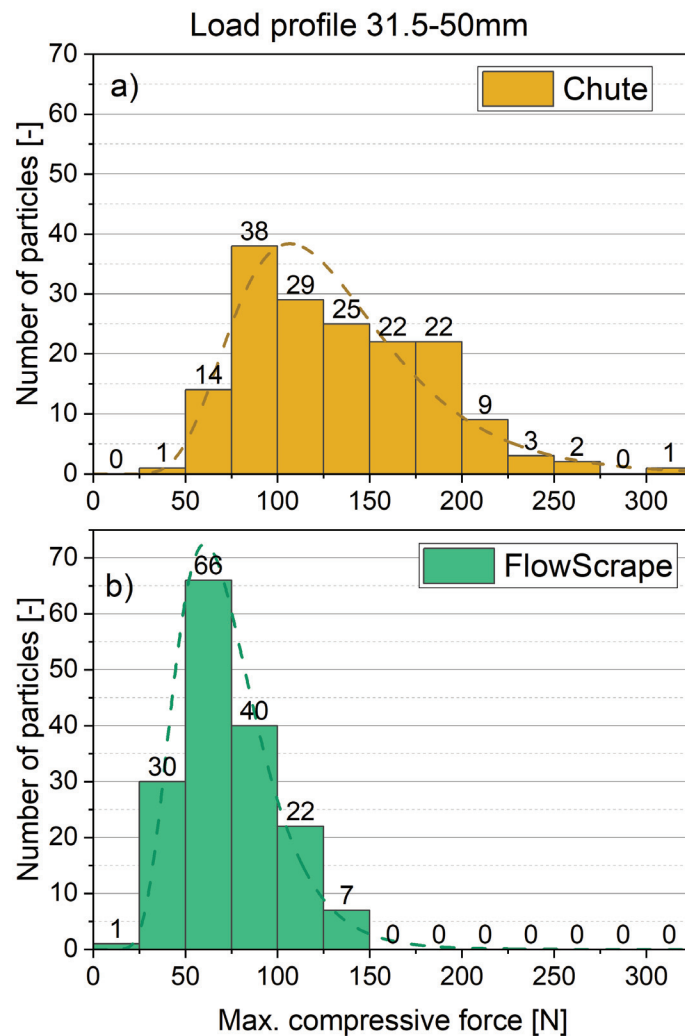
Figure 8.5: Load profile of 40 mm particles during conveying with a) conventional chute b) FlowScrape [5]

The simulation results show a particle-preserving effect during transfer with the FlowScrape. A comparison of the simulation results for the particle size fraction 31.5-50 mm with the tests in Figure 8.6 and 8.7 shows partly significant deviations for the larger size fractions, but only slight deviations for the smaller size fractions. Especially for the return fines, only 0.3 and 0.2% more fines are produced in the test than predicted by simulation. This may be due to the fact that the fall into the plastic trough at the end of the discharging belt was not taken into account in the simulations and possibly additional fines were produced when the fragments were sorted three times with the vibrating sorter after the test.
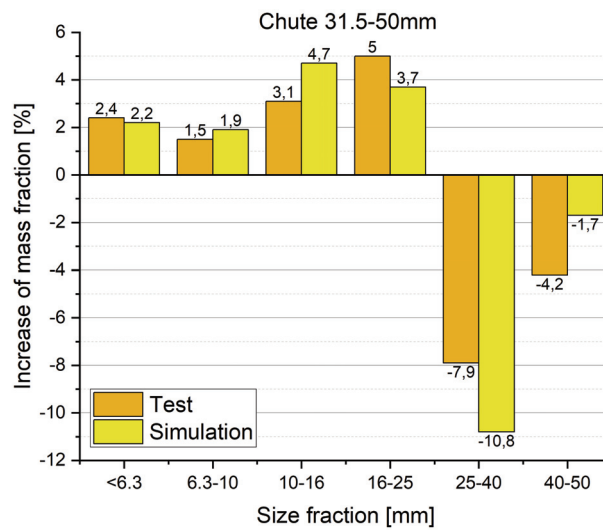
Figure 8.6: Particle breakage due to transfer with the convential chute [5, 11]
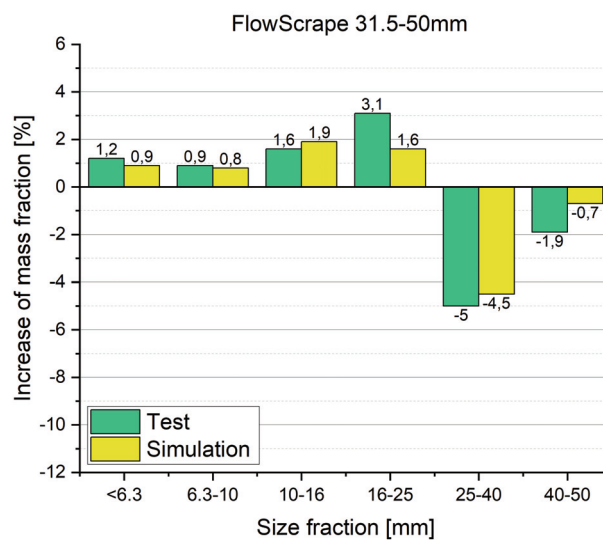
Figure 8.7: Particle breakage due to transfer with the FlowScrape [5, 11]

The compressive forces in the simulation with the initial particle size fraction 16-31.5 mm were also converted to corresponding velocities and mass-specific energies using a separate calibration curve (similar to that in Figure 8.3). The predicted return fines production is also slightly lower than the actual value from the tests. However, except for the return fines production, no satisfactory results were able to be obtained for the particle breakage prediction for the initial size fraction 16-31.5 mm using the methodology described above, which is why they are not depicted. This is presumably due to the fact that the specific energy inputs encountered in this case are unlikely to result in significant breakage in this initial size fraction, because smaller particles are generally less prone to break than larger ones.

8.3 Further simulations

Further simulations were carried out in order to increase the accuracy of the particle breakage prediction and thus to reduce the deviations from the real tests in [294]. The transfer with FlowScrape as well as the transfer with the conventional chute was simulated again. An improvement was expected by adjusting the Young's modulus of the sintered particles, also in the correct ratio to the impact surfaces. The shear modulus, and thus the Young's modulus, of sinter was chosen as small as possible in the original simulation for simulation reasons. Due to the heterogeneity of the sinter and the irregular shape of the sinter particles, the Young's modulus cannot be determined exactly. In [294] an attempt to determine an averaged Young's modulus for sinter particles was made by evaluating compression tests from Section 6.1 in which force and deformation were also measured.

However, the simulations in [294] with an adjusted Young's modulus showed only a slight improvement over the original simulation with a smaller Young's modulus of the particles. This suggests that in the conveying processes studied here, for volume breakage the interactions between the particles play a minor role compared to the interactions with the conveyors or the transfer systems. It is also expected that the simulation results would improve if the PSD in the simulation was adjusted to the actual PSD in the bulk material instead conducting the simulation with an averaged diameter. However, this would require a finer classification of size fractions and breakage tests would have to be repeated accordingly, which would take a lot of effort.

8.4 Conclusion

The approach of evaluation of compressive forces during post-processing described here leads to satisfying results in the fraction 31.5-50 mm, but not in the smaller fraction 16-31.5 mm, which is assumed to be due to too low specific impact energies in this case, leading to hardly any significant breakage in this size fraction. An advantage of this approach is that it can be performed with the standard version of EDEM and no additional programming or extension modules for the DEM software are needed. This allows a simple and in some cases sufficient prediction of particle breakage.

A big disadvantages of this approach is that the particle amount is quite limited for this approach. For sufficient compressive force evaluation small storage intervals are needed, which leads to a flood of data depending on simulation time and particle amount. Also, the data post-processing with the specially programmed Matlab routine leads to oversized matrices when linking particle ID and compressive force for every time step when used for a high amount of particles. A further disadvantage is that only a certain number of compressive force peaks can be taken into account and an eventual breakage of a particle is not considered in the following simulation. This could influence simulation accuracy, especially in terms of material flow behavior and interactions with equipment. As the breakage itself is not simulated, no further breakage of fragments can be simulated with this method either. This makes this method unsuitable for long and complex conveying processes with multiple breakage or high mass flows. Other breakage models, which allow to simulate breakage itself, are considered in the following Chapters.

However, a chute at a sinter manufacturer was investigated and optimized in [297]. The compressive forces were evaluated, but a fines generation prediction was not able to be performed because of the high mass flow and high number of particles leading to oversized matrices in the post-processing Matlab routine. This reaffirms the demand for a model in which breakage is embedded in DEM.

9 Bonded particle approaches

In the following Chapter approaches with bonded particles to simulate breakage are briefly described. This includes the established BPM and a different approach combining bonds with Voronoi-tessellated particles. The advantages, disadvantages and reasons why these are no purposeful approaches for sinter breakage simulations in this case are discussed.

9.1 Bonded particle model

As described in Section 2.11.1, the well-established BPM was developed and successfully applied in various cases to simulate breakage of agglomerates. As sinter is also an agglomerate, it was assumed that the BPM would also be suitable to simulate sinter breakage. These simulations would also be close to reality. The following content was partly published in [2, 9]. The following simulations were conducted in ThreeParticle due to a wider variety of adjustable parameters regarding bondings compared to EDEM. In ThreeParticle beam-theory-based bondings are used.

In this approach a sinter meta-particle was built from many small spherical sub-particles. For the sake of simplicity this approach was tested for a 16 mm particle of sinter A. The sub-particles were originally intended to have the size of the biggest relevant fragments, in this case 6.3 mm in diameter. A 16 mm meta-particle, would only consist of 3-5 sub-particles, which was insufficient as first simulations revealed. Therefore, the sub-particle diameter was defined by 2 mm. To create the meta-particle a virtual spherical mold was generated in order to arrange the sub-particles in a spherical shape. When the movements of the sub-particles was almost zero, bondings were created with the implemented bonding tool in ThreeParticle. In this process, bondings between two sub-particles are created if their contact radii overlap. The contact radius can be defined independently from the physical radius. In this case the contact radius was defined 20% greater than the physical radius.

The idea in this approach was to calibrate the critical stress by impact tests (see Figure 9.1). The critical stress for bonding failure σ_c was varied in order to achieve the same average PSD after impact in the simulations as in the breakage tests. The bonding cylinder was defined by a radius of 0.0015 m and a Poisson's ratio of 0.25, which both remained fixed. The general parameters from [277], listed in Tables 6.2 and 6.3, and a time step of $2 \cdot 10^{-6}\, s$ were used.

As first simulations revealed, the Young's modulus E of the bondings also had a great influence on the breakage behavior and also had to be adjusted successively. Every time a parameter was adjusted, the impact test was repeated with 5, 10, 15 and 20 m/s to detect trends and characterize breakage behavior (see Figure 9.3). As breakage test results were the average of 50 tests and sinter is a very inhomogeneous material, the BPM approach was extended to take this into account. In [124, 215], for example, inhomogeneous breakage behavior was modeled by normally or bimodally-distributed sub-particle sizes, which affected the bond radii in these cases. As the bond radii were fixed and sub-particles were all of the same size, inhomogeneous breakage behavior was modeled in a different way. ThreeParticle allows to define the critical stress for each individual bond failure following a normal distribution with a given mean value μ and standard deviation σ. Thus, every bonded meta-particle breaks in a different way. The impact of 50 particles with the same impact velocity was then simulated simultaneously (see Figure 9.2 for an image section). A different breakage behavior for each particle was able to be achieved with this approach.
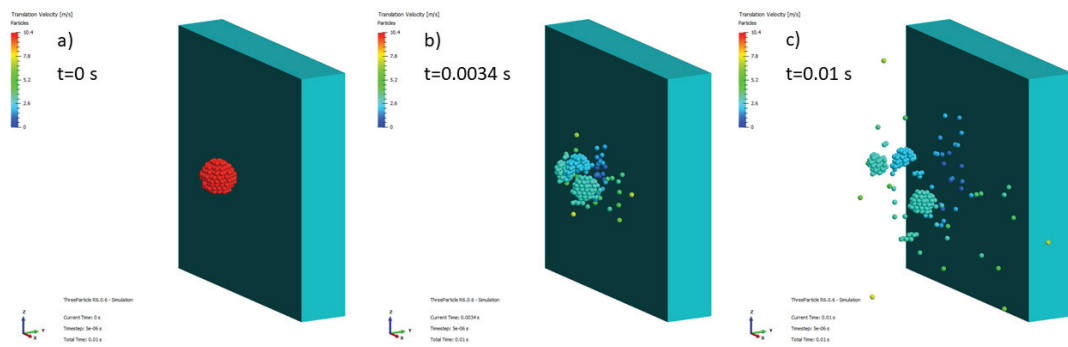
Figure 9.1: Simulation of an impact test of a 16 mm particle at 10 m/s with the bonded particle model at a) before b) during c) after breakage. Color scale represents translational velocity.
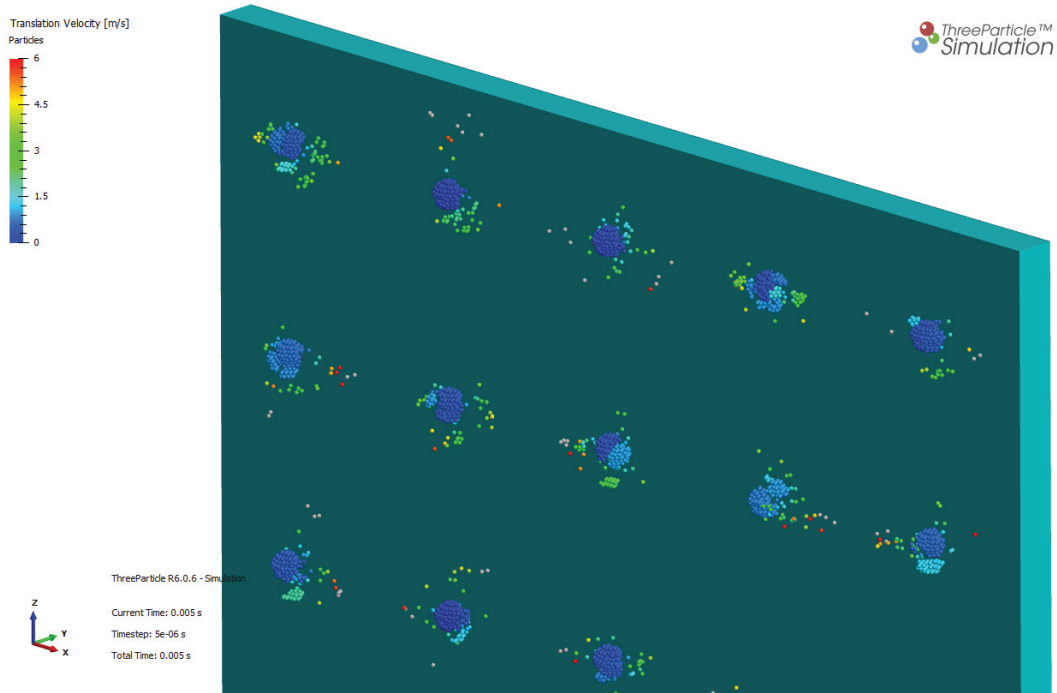
Figure 9.2: Different breakage behavior due to normally-distributed stress for bond failure (image section of impact tests with 50 particles sized 16 mm at 5 m/s). Color scale represents translational velocity.
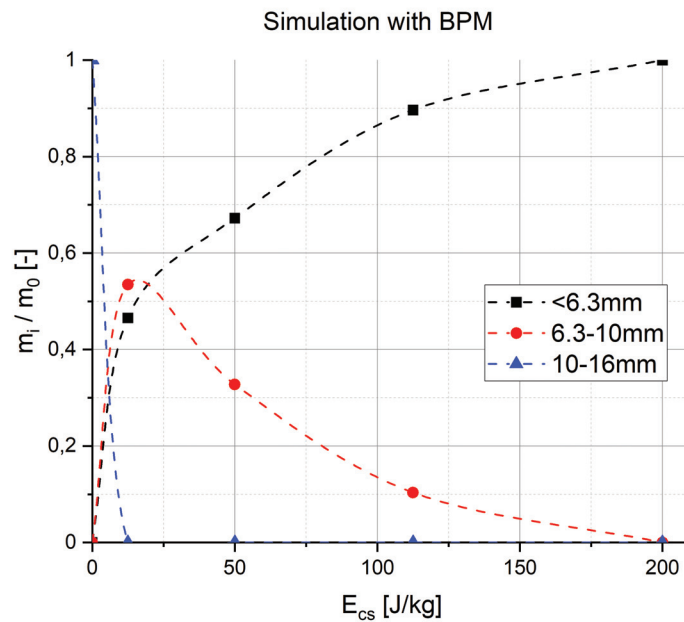
Figure 9.3: PSD after impact in simulation with the BPM for a 16 mm particle with 2 mm sub-particles ($\sigma_c = 6$ MPa, $E = 3000$ MPa)

9.1.1 Fragment identification and size analysis

A challenge in this approach is the fragment size analysis after impact. This is because of different fragment shapes and the fact that every meta-particle is built from the same sub-particles. Before the fragment size can be determined, a fragment has to be defined as such. Fragment definition and size analysis were all done during post-processing with specially programmed Matlab routines.

The first approach to define a fragment was by same translational velocities: Every sub-particle in the same fragment move with approximately the same translational velocity if the fragments do not rotate and particles and bondings are stiff enough. This approach turned out to be too inaccurate because fragment rotation speed was too high and stiffnesses too low in this case. A more accurate approach was then programmed and used, in which a sub-particle was defined as part of a certain fragment when it was bonded to any other sub-particle of this same fragment. This approach is very reliable and independent of rotation speeds and stiffness, but could lead to oversized calculation matrices.

An accurate way to determine the fragment size is by calculating the distance from every sub-particle to every other sub-particle in a fragment. The maximum of these values is the distance to the furthermost other sub-particle in the same fragment. Thus, the minimum value of these maxima would be the passing diameter for a one-dimensional sorting principle like the vibrating sorter. This approach is very accurate but leads to oversized calculation matrices in Matlab and requires too much computing power. A simpler but less accurate approach to determine the fragment size is with a fictitious enveloping box. The position values for all sub-particles are listed separately for every direction. With the difference between each maximum and minimum values the box dimensions in each direction can then be calculated. Thus, the smallest box dimension is the passing diameter for a one-dimensional sorting principle. This approach was used for evaluating simulation results because it required less computational effort.

9.1.2 Results and conclusion

In Figure 9.3 the PSD after impacts with different velocities in the simulation is exemplarily depicted with successively adjusted Young's modulus $E = 3000$ MPa and critical stress for bonding failure $\sigma_c = 6$ MPa. It must be stated that the lines in this diagram are spline interpolated. When compared with breakage test results for 10-16 mm in Figure 6.20, qualitatively similar trends are noticed. Thus, a simulation with this approach would be possible, but a quantitative match

would need further calibration.

Further calibration was not performed because this approach was not considered purposeful for this application for the following reasons. Firstly, too much calibration effort would have been required due to the fact that three interacting parameters (Young's modulus E, mean value μ and standard deviation σ for the critical stress for bonding failure) would have had to be calibrated. Secondly, the BPM generally requires relatively high computational effort compared to replacement models because of high sub-particle amounts and the many bonds, which have to be calculated additionally. Thus, the BPM is not considered suitable for simulation of sinter breakage in high mass flows.

9.2 Bonded Voronoi fragments

The recently introduced Voronoi-tessellation tool in ThreeParticle allows an approach which has been considered to require less computing power than the classic BPM with small spherical sub-particles. In this approach predefined bonded Voronoi fragments are used. For this purpose, a polyhedral particle is tessellated with the Voronoi algorithm. Then bondings are created between the Voronoi fragments. Thus, the initial particle shape remains the same, but the particle is breakable. The critical stress for bonding failure is then calibrated by impact tests (see Figure 9.4). As both individual Voronoi fragment sizes and bonded cluster sizes vary, an additional subsequent size analysis is required. This was done by simulating the sorting process in the vibrating sorter. Figure 9.5 shows the simulation of the impact test with subsequent fragment analysis by the vibrating sorter.

This approach requires less computing power than the classic BPM described in Section 9.1 due to bigger sub-particles, which are Voronoi fragments in this case, and thus also less bondings. However, due to the requirement of the subsequent sorting simulation and the need for at least two interacting bonding parameters (Young's modulus E, critical stress for bonding failure σ_c), if no normally-distributed critical stress for bonding failure is needed, this approach also involves too much calibration effort. Thus, it is not considered suitable for the simulation of sinter breakage either, especially when simulations with several particle sizes from different manufacturers are desired.
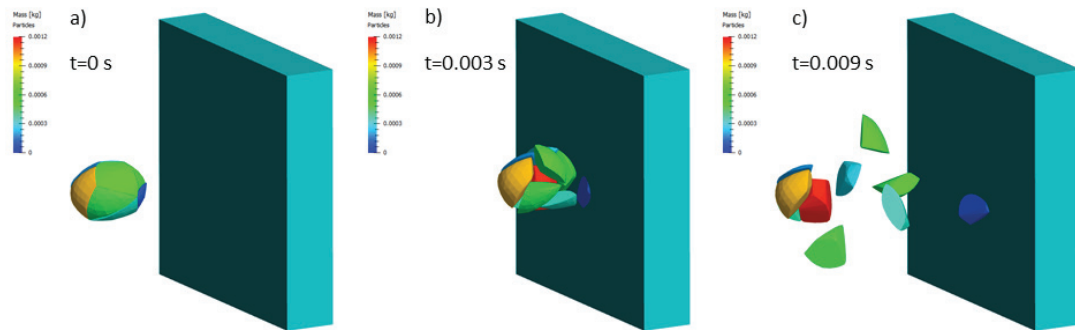
Figure 9.4: Impact test of a bonded Voronoi-tessellated 16 mm particle at 10 m/s at a) before b) during c) after breakage. Color scale represents mass.
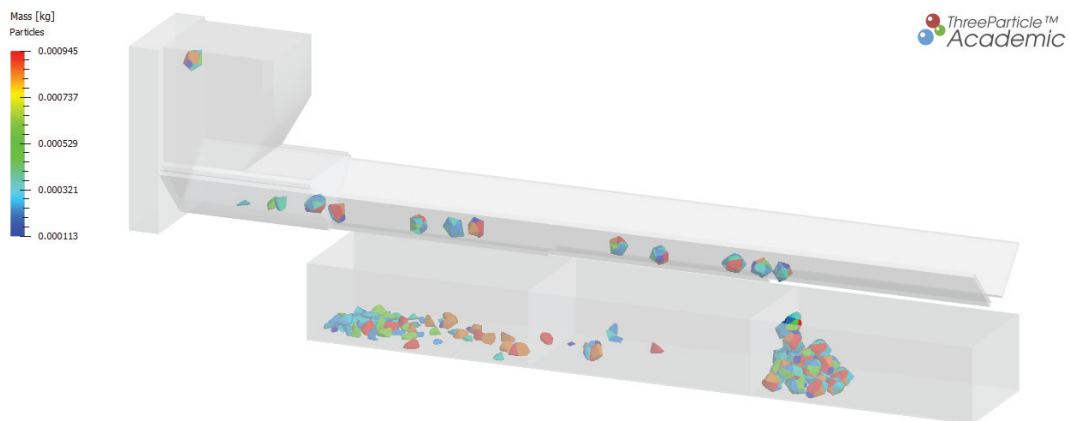
Figure 9.5: Impact test of bonded Voronoi-tessellated particles and subsequent sorting process in the vibrating sorter (16 mm particles at 10m/s). Color scale represents mass.

10 Probabilistic particle replacement with Voronoi fragments

In order to simulate bulk material degradation in high mass flows with high accuracy in terms of fragment size distribution and a reasonable computing efficiency, a novel particle breakage model has been developed for DEM. The model is based on a probabilistic particle replacement with fragments, which are previously tessellated with the Voronoi algorithm. The model has been developed in ThreeParticle's particle replacement API (Application Programming Interface) with C++ using the recently implemented Voronoi tessellation tool in ThreeParticle. The content of this Chapter was partly published in [2, 4, 7–9].

10.1 Concept

For Voronoi tessellation polyhedral particles are required. In this case the initial particles are of spherical shape, but can be of any convex shape. The polyhedral particles were created in the visualization software ParaView and imported to ThreeParticle as STL-file. Here a spherical mesh was created with a diameter of 40 mm and a resolution of 18 in both directions ($\varphi = \theta = 18$), which is shown Figure 10.1.

Depending on the stress, initial particles are probabilistically replaced by different particles, similar to [245]. In contrast to [245] and other particle replacement models, the initial particle is replaced by different breakage patterns instead of several smaller spheres. The different breakage patterns have the same mass and volume as the initial particle, which ensures mass and volume constancy. The breakage patterns are predefined and are copies of the initial particle, but have been tessellated with the Voronoi algorithm (see Figure 10.2). The replacement with previously defined breakage patterns is much more efficient in terms of computational effort than tessellating the particle at the event of breakage, which

would mean that the the Voronoi algorithm would have to be performed at every event of breakage.
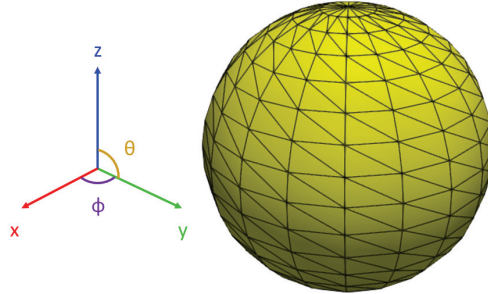
Figure 10.1: Polyhedral particles of spherical shape created in ParaView with a resolution of $\varphi = \theta = 18$
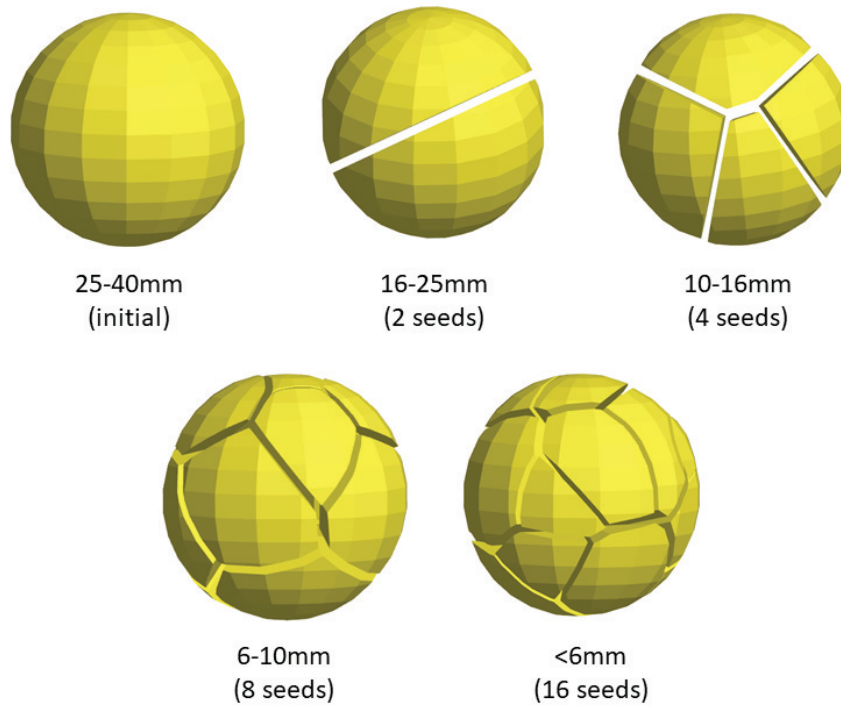
Figure 10.2: Breakage patterns, which are Voronoi-tessellated polyhedral particles (exploded view for better visualization) [7]

As described in Section 2.12, the Voronoi algorithm is an efficient way to tessellate areas or volumes. For Voronoi-tessellation randomly distributed points (seeds) are generated. Then the area or volume is divided in the middle of two neighboring seeds. Thus, the average fragment size in this application depends on the number of seeds. These fragments are sharp-edged polyhedral particles and are of random shape. This requires more computing power and usually smaller simulation time

steps than with spheres, but ensures mass and volume constancy. No fictive overlaps and temporary damping factors are necessary for the fragments to ensure volume constancy, as needed for a replacement with spheres in [245].

It must be stated that due to the random shape of individual fragments, individual fragment masses do not correspond to average particle mass in the respective size fraction. To ensure that the average fragment mass within a breakage pattern approximately corresponds to the average particle mass in the respective size fraction $m_{fraction}$, the number of seeds s can be defined by Equation 10.1, with m_0 as the initial particle mass. It has to be stated that in this case the number of seeds s was defined lower in the example of sinter C for computational efficiency. However, deviations from the calculated value s do not affect breakage probabilities. Fragments are only represented larger in the simulation. This could affect material flow behavior in some cases, but was assumed to be negligible for the application with sinter C in Section 11.1.

$$\lfloor s \rceil = \frac{m_{fraction}}{m_0} \qquad (10.1)$$

The concept is described using the example of sinter C because the first verification and validation was conducted with sinter C (see Chapter 11). In Figure 10.2 a particle of 40 mm corresponding to the initial particle size fraction 25-40 mm (sinter C) is depicted. Four different breakage patterns were defined for the different resulting fragment sizes corresponding to the size fractions 16-25, 10-16, 6-10 and <6 mm. To reduce computing power, fines are represented larger and summarized as 6 mm fragments.

Depending on the stress, the initial particle is completely replaced by fragments of a defined size. The probability for each breakage pattern or resulting fragment size is determined from breakage test results (see Figure 6.40) for breakage test results of sinter C. A piecewise linear regression is conducted in order to allow simple calculation of the replacement probability at any specific impact energy E_{cs} using linear interpolation (see Figure 10.3).

The piecewise linear regression was conducted with Matlab by means of [298] using the least squares method, in which the breakpoints have to be defined by the user (in this case at $E_{cs} = 14\,J/kg$ and $E_{cs} = 49\,J/kg$). The linear equations resulting from this Matlab calculation were then slightly adjusted manually in order to ensure that the sum of all probabilities is 100 at every point. This was achieved by adjusting the gradients that the sum of all gradients in all intervals was 0. These linear equations were then implemented in the particle replacement API. The

adjustment is simple and can be performed manually for linear regressions, but could be mathematically complex for other types of regression, which could be more accurate in some cases. For this application a linear regression is considered sufficiently accurate.

The relation between maximum compressive force at an impact and impact velocity is determined by simulating impact tests at several velocities (see Section 10.4). At every compressive force maximum a corresponding impact velocity and a specific energy is then calculated by the API. If the maximum compressive force exceeds a minimum breakage force, a random algorithm is started. At the event of breakage, one of the pre-defined breakage patterns is determined by the random generator. The probability for each breakage pattern is equivalent to the average mass fraction of the corresponding fragment size after impact at this specific impact energy. When the initial particle size is determined by the random generator, no replacement occurs. This leads to the correct PSD in the bulk sample when applied to a high number of particles.
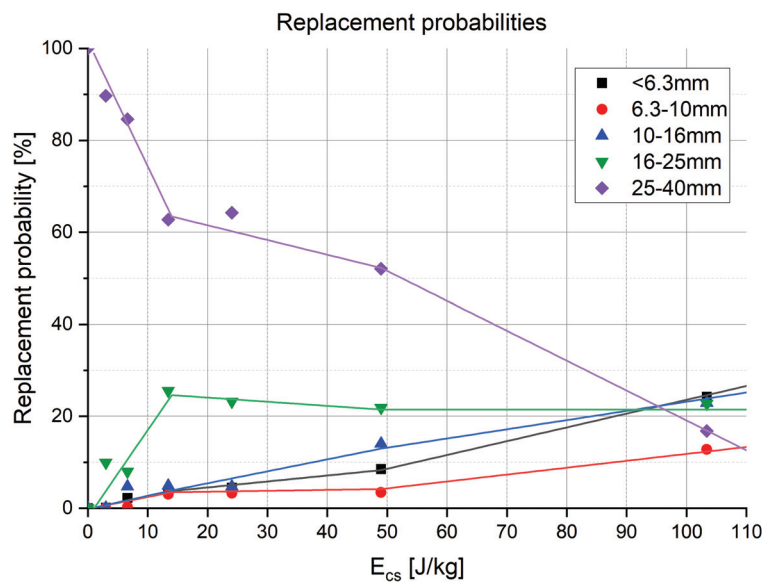
Figure 10.3: Replacement probabilities for following particles from piecewise linear regression based on breakage tests in Figure 6.40 (25-40 mm, sinter C)

In Figure 10.4 the breakage model is demonstrated with the impact on a 20 mm steel plate, in a similar way as in Figures 9.1 and 9.4. As the model is based on probabilities, a number of particles are necessary. The impact of 25 identical initial particles (40 mm, sinter C) is simulated at different velocities. Figure 10.4a) shows the particles before the impact, moving towards the steel plate. Figures 10.4b)-d) show the particles after the impact with different velocities, moving away from the steel plate.

The color scale represents the particle or fragment mass (0 to 47 g). Shortly after the impact process is completed, the initial particles are replaced by one of the breakage patterns from Figure 10.2, following the probabilities of Figure 10.3. The initial 40 mm particles appear red, the 16-25 mm fragments appear green and all smaller fragments (10-16, 6-10, <6 mm) appear blue in this case.
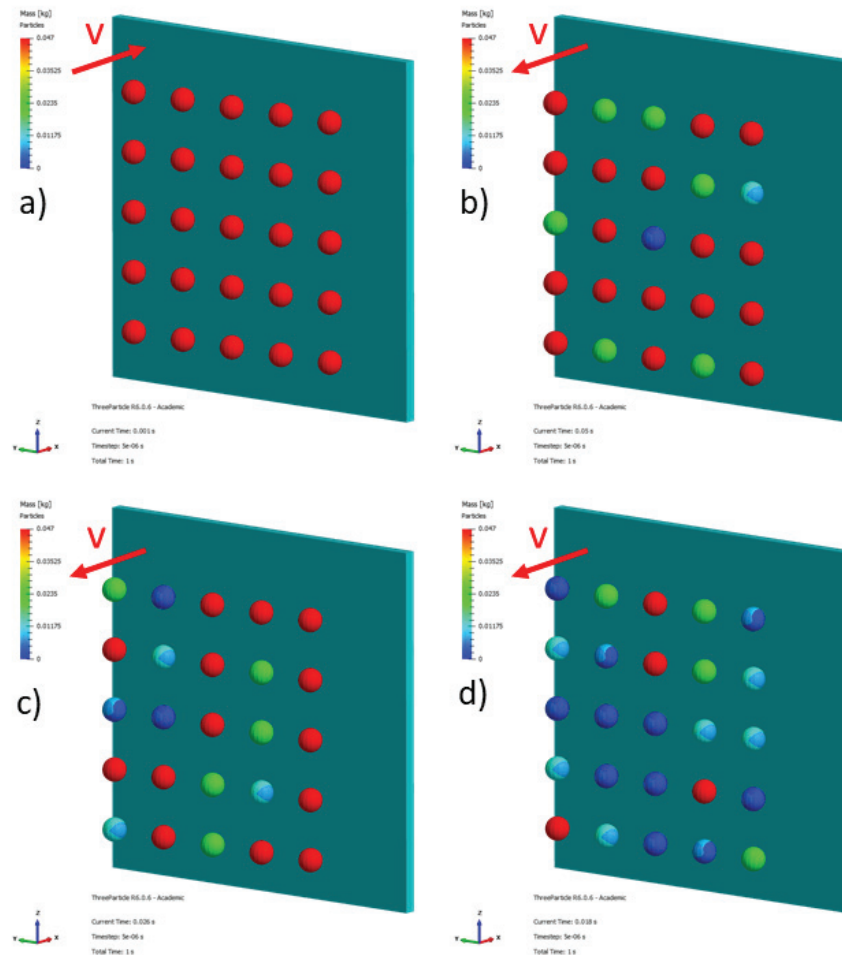
Figure 10.4: Impact simulation with 25 identical initial particles a) before impact and after the impact with b) 5 m/s (12.5 J/kg) c) 10 m/s (50 J/kg) d) 15 m/s (112.5 J/kg). Color scale represents fragment mass from 0 to 47 g.

10.2 Energy balance

In contrast to reality, the fragments in Figure 10.4 do not fly apart in this case. This is due to the fact that the replacement occurs a few time steps after the impact process is completed, which is necessary to avoid unrealistic explosions and a false increase in kinetic energy. If the particle were replaced by smaller

fragments during the impact process, which would mean that there was still a certain overlap with the impact surface, this could lead to extraordinary overlaps for the small fragments with the impact surface and thus to extraordinary reaction forces and explosions.

If the replacement occurs after completion of the impact process, the kinetic energy of the fragments after the breakage is also higher than in reality. The fragments all have the same velocity after impact, which is only reduced by a damping factor calculated from the coefficient of restitution. The coefficient of restitution also has to be calibrated, because it depends on the contact model and various parameters. This is not physically correct because the breakage energy is not taken into account. Thus, it must be stated that the energy balance is not correct in the following simulations with this model, because the proportion of kinetic energy is too high.

One method to consider the breakage energy would be to decrease the velocity after the impact by a factor, which could easily be implemented with the API. For this purpose, further investigations regarding the breakage energy would be needed. Alternatively, the breakage energy could be estimated by means of the Griffith criterion [64], as described in Section 2.6, whereby the breakage energy is proportional to the creation of new surfaces [101] with a given surface energy.

Breakage with fragments flying apart could be visualized with this model by defining an initial overlap among the Voronoi fragments. This could be defined by the recently implemented explosion offset in ThreeParticle, which shifts the Voronoi fragments toward or away the center of the particle after tessellation. Figure 10.2 was created with an explosion offset of +2 mm for better visualization, for example. A negative explosion offset would lead to overlaps among the Voronoi fragments. This function was not used in simulations described in this thesis and the explosion offset was set to 0 in order to avoid a further increase in kinetic energy in the simulations, which could affect material flow behavior during conveying processes.

10.3 Parameters

A time step of $5 \cdot 10^{-6}\,s$ was used for all simulations involving polyhedral particles in this thesis. To evaluate the correlation between compressive force and impact velocities in Section 10.4 a save interval of $5 \cdot 10^{-5}\,s$ was used. These values are smaller than proposed by [296] due to the use of polyhedral particles, in contrast to smooth spheres in [296]. Sharp-edged particles including polyhedral particles

generally require a smaller time step than particles with smooth surfaces, which leads to higher computational effort and simulation times.

Furthermore, the parameters listed in Tables 10.1 and 10.2 were used for breakage simulations with sinter C. With the measured initial particle mass $m_0 = 47\,g$ from breakage tests in Section 6.5.6 and a defined diameter of $d = 40\,mm$, the density $\rho = 1455\,kg/m^3$ was adjusted following Equation 10.2. Restitution coefficients and the static friction coefficient for the sinter-steel were used from [277, 295].

Material	Density [kg/m³]	Poisson's ratio [-]	Shear modulus [MPa]
Sinter C (40 mm)	1455	0.25	10
Steel	7850	0.25	210000

Table 10.1: Material parameters for simulations with polyhedral particles

Interaction	Restitution [-]	Static friction [-]	Rolling friction [-]
Sinter-Sinter	0.75	0.62	0.5
Sinter-Steel	0.43	0.839	0.5

Table 10.2: Interaction parameters for simulations with polyhedral particles [277, 295]

$$\rho = \frac{6\,m_0}{\pi\,d^3} \tag{10.2}$$

The static friction coefficient for the sinter-sinter contact had to be determined again from angle of repose simulations as described in Section 7.3, but in this case with polyhedral particles, without capped angular velocity (compare Figure 7.9) and with the Hooke contact model. Due to the sharp-edged polyhedral particles and fragments, particle rotation was necessary. Additionally, the rolling friction coefficients had to be calibrated. Initial estimations for static and rolling friction coefficients were based on [299, 300]. An angle of repose of 24°, like in experiments, was able to be simulated with a static friction of 0.62 and rolling friction coefficients of 0.5 each (see Figure 10.5 and Table 10.2). It has to be stated that various combinations of these parameters are possible as these parameters affect each other.

Furthermore, it must be stated that the calibration described here and shown in Figure 10.5 was performed with sinter B (31.5-50 mm) with a size distribution

listed in Table 7.1, but was also used for simulations with sinter C. No angle of repose experiments with sinter C were performed due to a lack of test material. It is assumed that the difference in static and rolling friction coefficients between sinter C and B is relatively small and negligible for the following simulations.
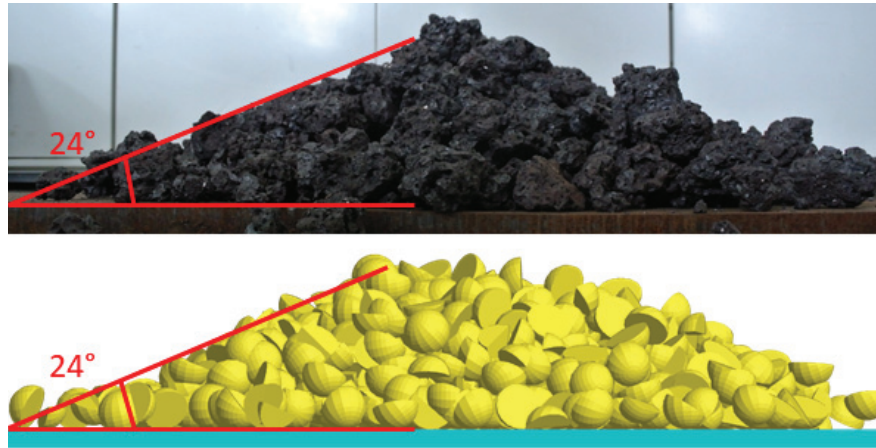
Figure 10.5: Comparison of angles of repose from tests (sinter B 31.5-50 mm) and corresponding simulation a) angle of repose test b) simulation with polyhedral particles and capable of rotation

10.4 Correlation between impact velocity and compressive force

In order to calculate the corresponding impact velocity in experiments with a fictive compressive force in the simulation, a correlation is needed. This correlation between impact velocity and compressive force is determined by simulations of impact tests, similar to the procedures described in Sections 6.3.2 and 8.1, but with polyhedral particles instead of perfect spheres.

In the previously mentioned procedures perfect spheres with smooth surfaces were used as particles, whereby the overlap at a contact and thus the computed compressive force was independent from the alignment of the particle. Although the polyhedral particles are of spherical shape as a whole, the overlap and thus the computed compressive force are dependent on the alignment. This is due to the fact that mesh particles are only approximately spherical and consist of many small plane surfaces and sharp edges. Thus, the impact with an edge leads to a higher computed compressive force than the impact with a plane surface.

Taking into account the dependence on the compressive force on the alignment, the

impact tests were simulated with 1000 particles with random alignment for each impact velocity (see Figure 10.6). The median of the maximum compressive forces of these 1000 impacts is then used. Depending on the contact model, different correlations are determined (see Section 10.5).
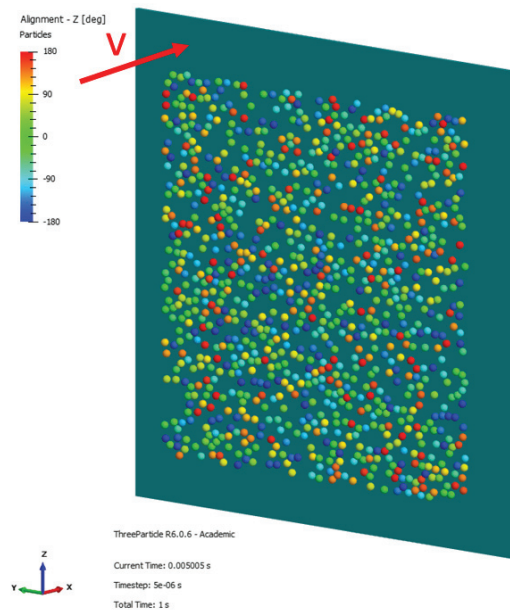
Figure 10.6: Impact test simulation with 1000 polyhedral particles of spherical shape with random alignment (sinter C, 40 mm). Color scale represents alignment in z-direction from -180° to +180°.

10.5 Hertz-Mindlin vs. Hooke contact model

First the Hertz-Mindlin contact model (see Section 2.10.3) was used for this breakage model as it is well established as the standard contact model in EDEM and ThreeParticle. No problems occurred during simple simulations and calibration processes with the Hertz-Mindlin contact model. However, the first more complex simulations including conveying processes (see Sections 11.3 and 11.2) revealed that the Hertz-Mindlin contact model was not suitable for polyhedral particles and thus for this breakage model. Extraordinarily high reaction forces which led to explosions were noticed in some cases.

Movement on a belt conveyor is usually implemented as virtual movement, which sets the translational velocity of the particle to the belt speed as long as the particle contacts the belt. Especially in these simulations explosions were noticed after a certain time of conveying. Detailed investigations considering contact

forces, overlaps and translational and rotational velocities revealed the following numerical phenomenon (in ThreeParticle). When a sharp-edged particle contacts the belt at two points with different surface normal vectors, as depicted in Figure 10.7, in some cases the particle could begin to oscillate between these two contact points. This could lead to extraordinary overlaps and reaction forces until the particle is pushed away with a very high force resulting in high velocity.
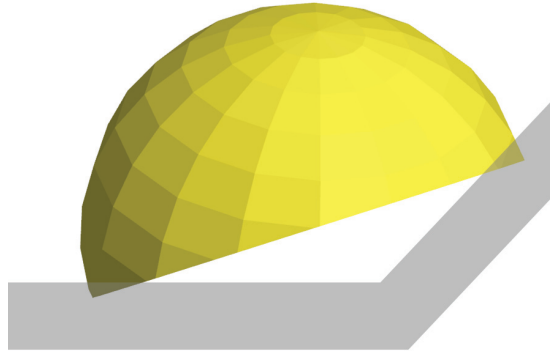
Figure 10.7: Sharp-edged particle jammed at a simplified model of a conveyor belt resulting in high overlaps with the Hertz-Mindlin contact model

At first it was assumed that the high rotational speeds due to the eccentric forces and oscillations caused these extraordinary overlaps, but limiting the rotational speed did not solve this problem. According to literature, the Hertz-Mindlin contact model is generally suitable for elastic particles with smooth surfaces [301]. The same simulations were then conducted with the Hooke contact model (see Section 2.10.4). With this model no oscillations and explosions were noticed. Thus, the Hooke contact model is more suitable for sharp-edged particles including polyhedral particles used for this breakage model. All calibrations with polyhedral particles presented in this thesis were simulated with the Hooke contact model. As described in Section 2.10.4, with the Hooke contact model the contact forces are calculated differently than with the Hertz-Mindlin contact model. The difference between the two contact models was evaluated with impact simulations. In this process, the impacts of 1000 polyhedral particles with random alignment and the parameters described in Section 10.3 were simulated with different velocities (3-24 m/s). A time step of $5 \cdot 10^{-6}$ s, a save interval of $5 \cdot 10^{-5}$ s and the parameters from Tables 10.1 and 10.2 were used. The maximum compressive forces for each particle during the whole impact process were determined with an specially programmed Matlab routine. The median of all 1000 maximum compressive force values is depicted in Figure 10.8.
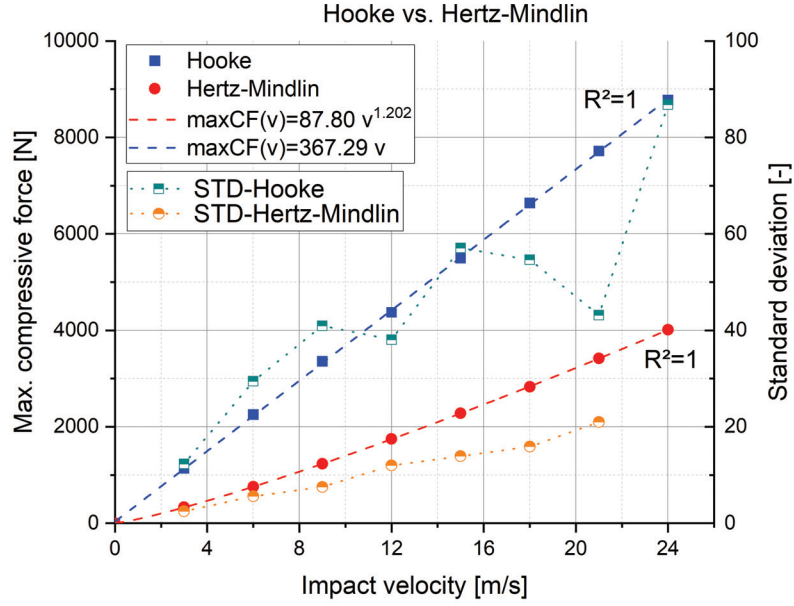
Figure 10.8: Maximum compressive forces and their standard deviations at an impact of 1000 polyhedral particles on a plane surface, calculated with the Hooke and Hertz-Mindlin contact models (sinter C, 40 mm)

As seen in Figure 10.8, significantly higher contact forces are calculated with the Hooke model than with the Hertz-Mindlin model. The maximum compressive force $maxCF$ is linearly dependent on the impact velocity v if the Hooke model is used, following the form of Equation 10.3. The linear parameter a, in this case $a = 367.29$, will then be used to calculate the corresponding impact velocity and energy with the detected compressive force in the API. If the compressive force is calculated with the Hertz-Mindlin model, the maximum compressive force $maxCF$ follows a power function with the form of Equation 10.4, in which a is the linear and b the power parameter.

$$maxCF(v) = a \cdot v \tag{10.3}$$

$$maxCF(v) = a \cdot v^b \tag{10.4}$$

Furthermore, the standard deviations (STD) of the maximum compressive forces of all 1000 particles were calculated for each impact velocity and added to the diagram in Figure 10.8. A lower standard deviation is noticed with the Hertz-Mindlin model, but only until a certain velocity. For velocities >21 m/s extraordinarily high maximum compressive forces are calculated for some of the 1000 polyhedral particles, which is not the case with the Hooke model. This could explain the numerical phenomenon described above leading to extraordinarily high reaction forces. The distributions of the maximum compressive forces for both contact models are exemplarily depicted in Figure 10.9 for an impact velocity of 9 m/s. The values are significantly more widely dispersed for the Hooke model than for the Hertz-Mindlin model.

It is concluded that the Hertz-Mindlin model could lead to extraordinarily high contact forces in some cases for sharp-edged particles, especially from a certain impact velocity. The Hertz-Mindlin model is only suitable for particles with smooth surfaces, which is consistent with statements in [301]. The Hooke model leads to higher and more widely dispersed contact forces than the Hertz-Mindlin model, but does not lead to extraordinary contact forces due to sharp edges. Thus, the Hooke model is more suitable for particles with non-smooth surfaces.
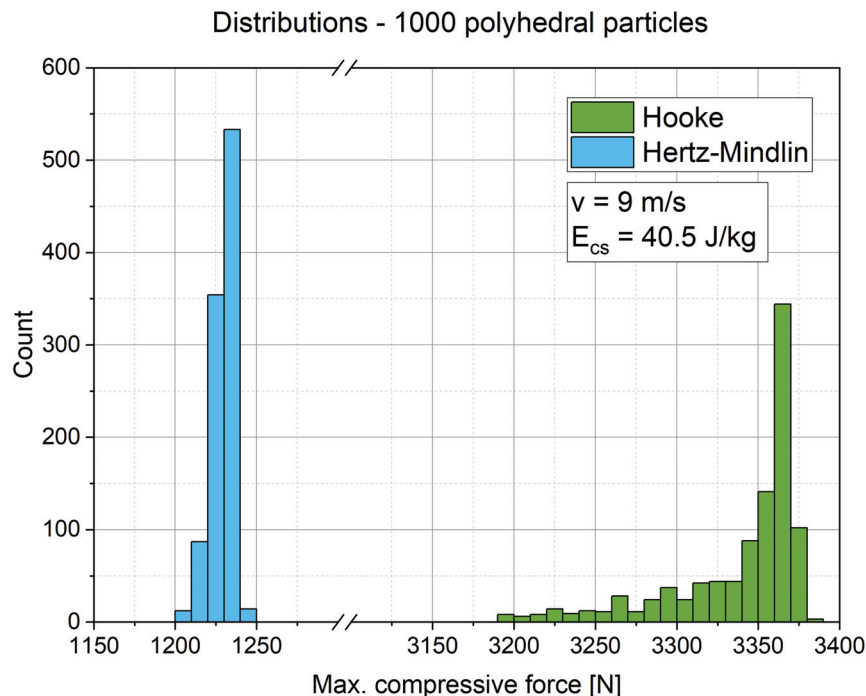
Figure 10.9: Distributions of calculated maximum compressive forces for 1000 polyhedral particles with random alignment, exemplarily depicted for an impact velocity of 9 m/s (sinter C, 40 mm)

Subsequent detailed investigations revealed that median rebound velocities v_2 are higher in the simulations with polyhedral particles for both contact models than they should be, according to Equation 10.5. The Hooke model leads to higher deviations than the Hertz-Mindlin model if coefficients of restitution e from experiments are used. For example, for an impact velocity $v_1 = 15\,m/s$ a rebound velocity $v_2 = -11.6\,m/s$ (e=0.77) for the Hooke model and a rebound velocity $v_2 = -7.4\,m/s$ (e=0.49) for the Hertz-Mindlin model was noticed in the simulations for a defined coefficient of restitution e=0.43 in both cases. This is due to large overlaps with the polyhedral particles. Thus, it has to be stated that rebound velocities in simulations in this thesis are higher than in reality, which further falsifies kinetic energy balance additionally to neglecting the breakage energy (see Section 10.2). This could be avoided by either reducing the time step or calibrating the coefficient of restitution e, which was not done in this case because all simulations and calibrations had already been performed with the measured coefficient of restitution from experiments in [295]. Furthermore, rebound velocities are not assumed to be the crucial factor for breakage in the simulations in this thesis and kinetic energy balance is not correct anyway. Additionally, a comparison with the simulation results from Section 7.4 and 8.2 was desired.

For future simulations it is strongly recommended to first calibrate the coefficient of restitution and then calibrate the static and rolling friction with angle of repose tests. As these parameters affect each other, it has to be considered that various combinations of all parameters are possible. Otherwise a small enough time step could be chosen, which would increase computational effort.

$$v_2 = -e \cdot v_1 \tag{10.5}$$

10.6 Fragment size analysis

Due to the Voronoi tessellation process, fragments are of random shape and individual fragment sizes vary. In contrast to other breakage models where spheres are used and fragment sizes can be simply determined by diameter, mass or volume, in this model fragment sizes are identified by particle names. When particles are defined, every particle is assigned a name containing its size in the first characters by the user. Thus, also for breakage patterns a name corresponding to their size fraction must be assigned. In ThreeParticle the Voronoi fragments resulting from a tessellation are numbered and the name of the initial particle with the

suffix _voronoi_x_ is automatically assigned. Here x is the number of the fragment, which starts the count at 0. Thus, every fragment can later be associated with its breakage pattern and categorized into a certain size fraction, independent of its actual size and mass in the simulation.

Fragment size analysis is conducted during post-processing with specially pro-grammed Matlab routines. First, the particle (fragment) names and their masses are exported from ThreeParticle as .csv files. In this case, ThreeParticle's PSD sensors are only used to define the cuboid volume, which is to be analyzed. Then, Matlab routines identify fragment sizes by prefixes in particle names and calculate the mass-related fragment size distribution.

10.7 Multiple breakage

For longer and complex conveying processes with several damaging events, it can be necessary to generate further breakable fragments. The model presented here allows further breakage of fragments as the generated fragments are also polyhedral particles, which were able to be further tessellated with the Voronoi algorithm.

As individual fragments have different masses and shapes, for each fragment a correlation between impact velocity and compressive force has then to be determined, following the procedure described in Section 10.4 using the Hooke contact model. Evaluations revealed that also for relatively irregularly shaped and sharp-edged fragments impact simulations with 1000 fragments with random alignment were accurate enough in most cases. Maximum compressive force values are more widely dispersed in this case, which reaffirms using the mean value instead of the average value to reduce the impact of outliers.

How often a particle and its resulting fragments can be further broken is described with the breakage level L in the following. For example, a breakage level of $L = 2$ means that the initial particle for this breakage process is a fragment of a previous breakage process at $L = 1$.

Multiple breakage was implemented for sinter B because the conveying tests (Section 7) had also been conducted with sinter B. In the conveying tests with sinter B the particles were exposed to more damaging events than in the shatter tests with sinter C (Section 11.1), which made this application a more suitable application for further breakage of fragments. Multiple breakage was implemented on three breakage levels ($L = 3$) with a constant number of seeds ($s = 2$) for each breakage level (see Figure 10.10).
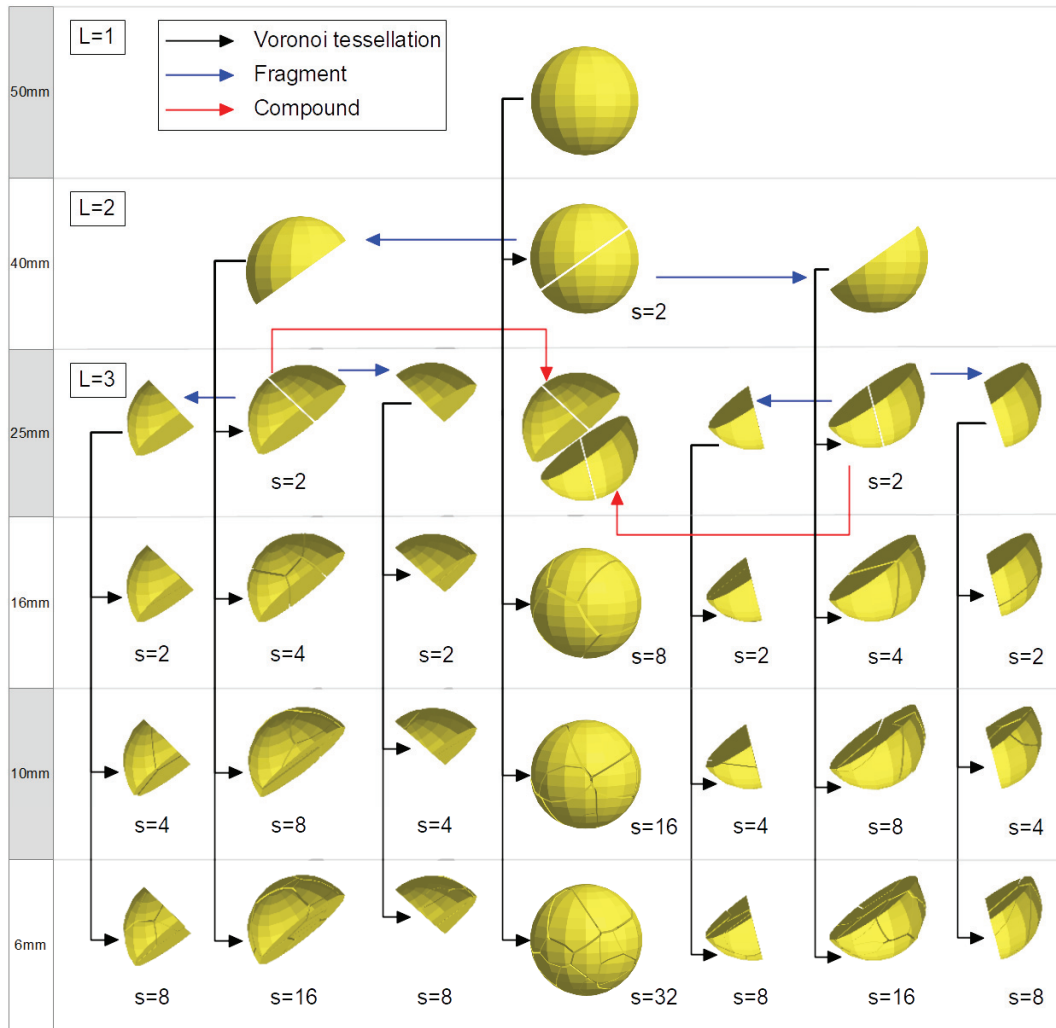
Figure 10.10: Multiple breakage on 3 breakage levels (sinter B, L=3, s=2)

The initial 50 mm particle is of spherical shape. At breakage level $L = 1$ the intial particle is able to break into one of five breakage patterns (40, 25, 16, 10, 6 mm), which are aligned below the initial particle in Figure 10.10. Breakage by replacement of a breakage pattern tessellated from the same particle is indicated with a black line (Voronoi tessellation). When the 50 mm initial particle breaks into the 40 mm size fraction, $s = 2$ is applied, which results in two fragments approximately shaped like a half sphere, in this case.

The particles in the 40 mm size fraction are then further breakable into the four smaller size fractions at breakage level $L = 2$. When the 40 mm size fraction breaks into the 25 mm size fraction, again $s = 2$ is applied, which splits the half spheres into quarter spheres in this case.

The 25 mm size fraction is then further breakable into the three smaller size fractions at breakage level $L = 3$. When the 50 mm particle directly breaks into

the 25 mm size fraction, it is replaced by a compound particle assembled from its further broken fragments to ensure that the same fragments are generated as from breakage in two steps (via $L = 1$ and $L = 2$). $L = 4$ would be further breakage of the 16 mm size fraction in this case, which was not implemented.

As fragment size distribution is determined by names of particles during post-processing with Matlab routines (see Section 10.6), the assignment of suitable particle names is very important for this model. An example of systematic naming is depicted in Figure 10.11 for this case of sinter B.
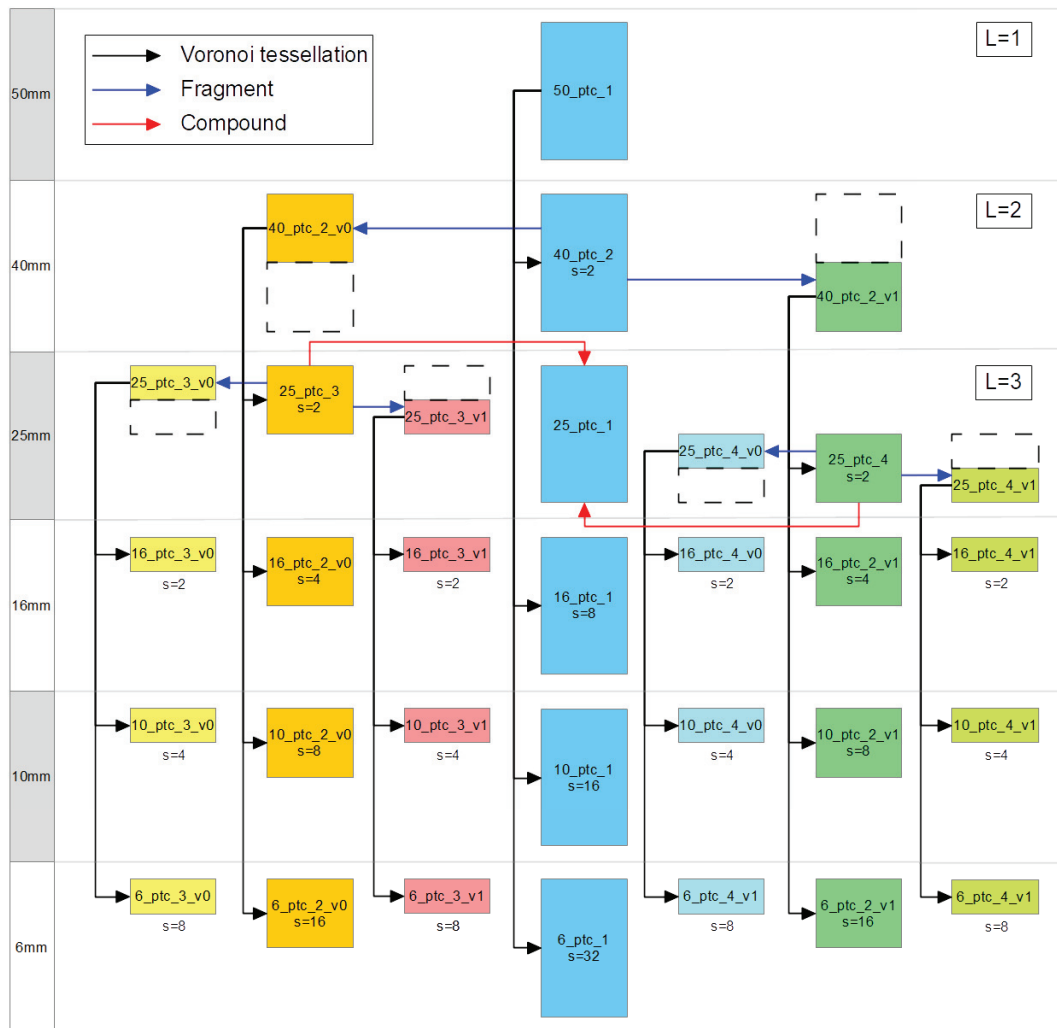
Figure 10.11: Example of particle naming for multiple breakage (sinter B, L=3, s=2)

The number of required correlations between impact velocity and maximum compressive force c also depends on the number of seeds s, which describes how many fragments are generated at a breakage process. The number of correlations c can easily exceed to high numbers requiring high calibration and pre-simulation

effort. For a constant number of seeds s for each breakage level L, the number of required correlations c follows Equation 10.6. As the procedure to determine these correlations (Section 10.4) is the same for every fragment, this could be automatized by Keyword editing and Simulation queuing in ThreeParticle with subsequent Matlab routines for evaluation.

The linear parameters a to calculate the corresponding impact velocity from the maximum compressive force following Equation 10.3 for sinter B including fragments until breakage level $L = 3$ are listed in Table 10.3. If the linear parameters a are plotted against the fragment mass, a trend following a power function is noticed (see Figure 10.12). Thus, the linear parameter a is only dependent on the fragment mass and is independent of the fragment shape. This fact will significantly reduce the pre-simulation effort to determine the correlation between maximum compressive force and impact velocity for multiple breakable particles in future simulations.
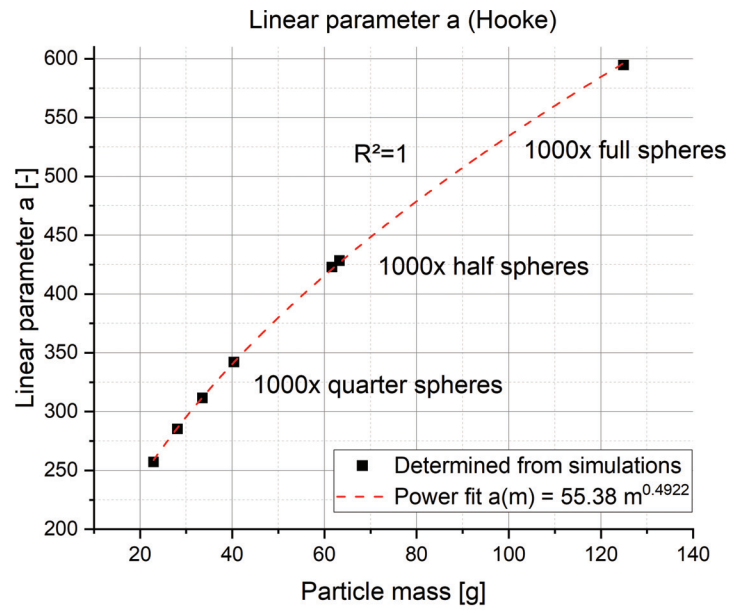
Figure 10.12: Mass dependency of the linear parameter a for the correlation between maximum compressive force $maxCF$ and impact velocity v with the Hooke contact model following Equation 10.3

$$c(s, L) = \begin{cases} 1 & \text{for } L = 1 \\ \sum\limits_{i=1}^{L-1} s^i + 1 & \text{for } L > 1 \end{cases} \quad \text{with} \quad s, L \in \mathbb{N} \qquad (10.6)$$

Particle name	a [-]	Mass [g]	Approximate form
50_ptc_1	594.72	124.9	Full sphere
40_ptc_2_v0	422.90	61.6	Half sphere
40_ptc_2_v1	428.37	63.3	Half sphere
25_ptc_3_v0	285.30	28.1	Quarter sphere
25_ptc_3_v1	311.65	33.5	Quarter sphere
25_ptc_4_v0	342.11	40.4	Quarter sphere
25_ptc_4_v1	257.23	22.9	Quarter sphere

Table 10.3: Linear parameters a for sinter B with the Hooke model, following $maxCF(v) = a \cdot v$

10.8 Computational scheme

The breakage model was developed using ThreeParticle's Particle Replacement API, which allows the user to extend the simulation software with additional features. Customized functions can be programmed with C++ in the API. The default simulation cycle of ThreeParticle is shown in Figure 10.13. The Particle Replacement Plugin is executed after the Keyword Plugin.
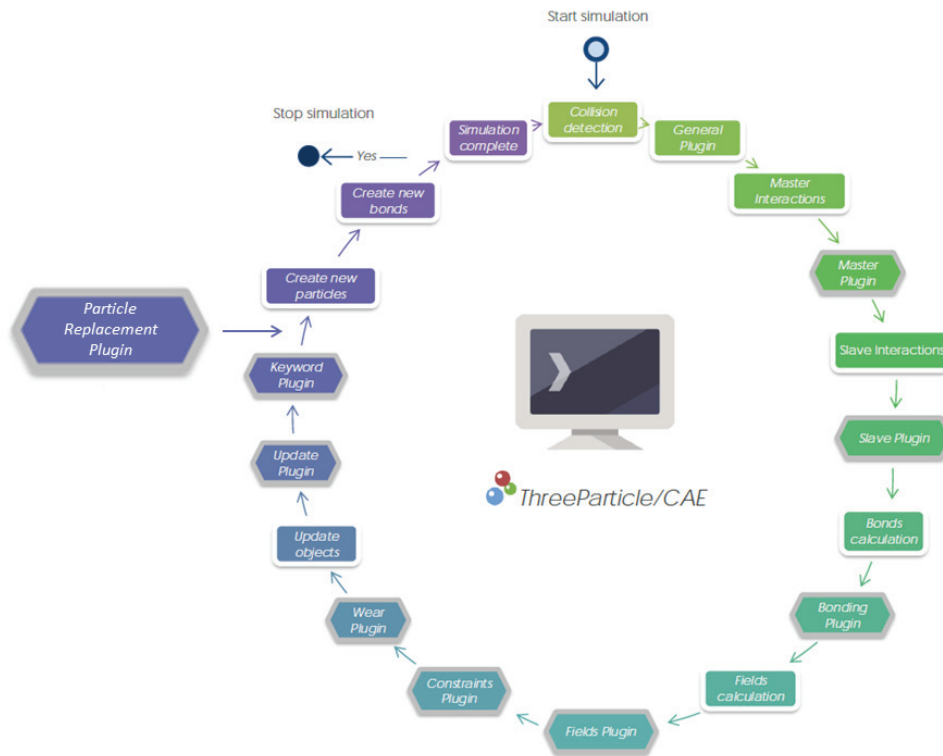
Figure 10.13: Simulation cycle in ThreeParticle [302]

10.8.1 Custom properties

In ThreeParticle custom properties have been introduced to ease the user's handling of custom variables, which are stored as a common string and can be easily written and read via predefined functions [302]. The custom properties are not deleted when a new simulation cycle starts. In this case, the custom properties are used to take into account the particle history. The custom properties string is assembled from comma-separated values and is converted into a vector of type double with four entries. A description of the custom properties vector is given in Equation 10.7. In various steps values (type double) are written to and read from the custom properties vector. The first two entries customProperties(0,1) are updated at the end of the algorithm. This is done by replacing the first value customProperties(0) by the second customProperties(1) and by writing the current compressive force into customProperties(1).

$$\text{customProperties} = \begin{pmatrix} CF(t-2) \\ CF(t-1) \\ maxCF \\ \text{Breakage timer} \end{pmatrix} \tag{10.7}$$

10.8.2 Breakage delay

The breakage delay is necessary to avoid extraordinarily high overlaps and explosions due to almost instant replacement (delayed by one time step) as described in Section 10.2. To implement a breakage delay in the algorithm, a breakage timer is introduced which is reduced by 1 each time step. The value for the breakage timer or breakage delay is dependent on maximum velocities, particle size and time step. For the simulations with sinter B in Section 11.3 and 11.2, a breakage delay of 100 time steps was defined. For simulations with sinter C in Section 11.1 a breakage delay of 50 time steps was defined.

10.8.3 Breakage algorithm

A schematic flow diagram of the algorithm of the model is depicted in Figure 10.14. All computational procedures before or after this Plugin, according to Figure 10.13, are summarized as previous or following computation steps of the DEM software in this flow diagram. The computational scheme is executed in every simulation cycle and parallelized for every single particle.

In the first step it is checked if the particle is defined as breakable, by comparison of the particle name with predefined Strings, which correspond to the names of the breakable particles. If not, the whole particle replacement procedure including several if-clauses is skipped for this certain particle, which reduces computational effort.

If the particle is defined as breakable, its custom properties are checked. Generally, when a new particle is created, no custom properties are assigned by default. Thus, the custom properties are empty (no value) for new particles, which leads to errors when compared with values of the type double. Therefore, the custom properties have to be initialized with 0 values for newly created particles.

In the next step the current compressive force CF on the particle in this time step is compared with a minimum value for breakage. The minimum compressive forces for breakage are calculated with the linear parameter a from Equation 10.3 and from minimum specific impact energies E_{cs}, which are determined from drop tests in Figure 6.6.

Then it is evaluated if the compressive force CF peaked in the previous time step $(t-1)$. For this purpose, the compressive force values of the two time steps before (t-2) and (t-1) from customProperties(0,1) are compared with the current compressive force in this time step $CF(t)$ with the condition in Equation 10.8. If a peak for the previous time step $(t-1)$ is detected, the maximum compressive force value $maxCF$ in customProperties(2) is set as $CF(t-1)$ and the breakage timer is set to a defined value (see Section 10.8.2).

When the breakage timer is 1 and a value is set for the maximum compressive force $maxCF \neq 0$ the actual particle replacement procedure starts. With the correlation from Equation 10.3, the impact velocity is back-calculated. Then the mass-specific impact energy E_{cs} is calculated with the impact velocity v and Equation 2.13. With a given specific impact energy E_{cs} the breakage probabilities for each breakage pattern can be interpolated (see Figure 10.3).
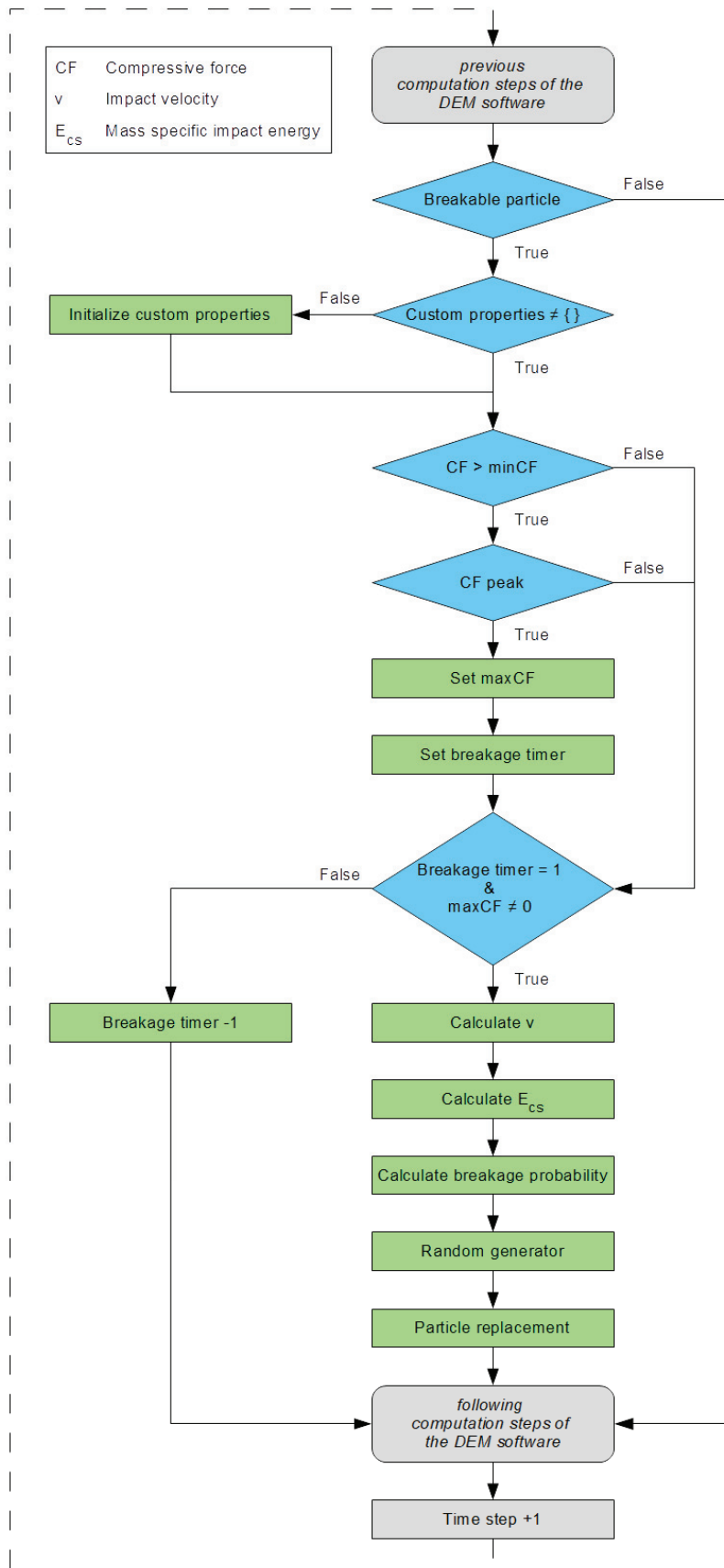
Figure 10.14: Schematic flow diagram of the breakage algorithm

Then a random procedure is started. It has to be considered that there is no real randomness in numerics and random generators are actually pseudo-random generators, which deliver the same set of values depending on the seed. Always different sets of values can be obtained when the pseudo-random generator is seeded with a value depending on the absolute time, for example. Most pseudo-random generators deliver normally-distributed values, which is not desired here. Evenly-distributed values are needed. For this model the Mersenne Twister MT19937 is used [303], which is an equidistributed uniform pseudo-random generator. A pseudo-random value is generated in the range of 0 to 10000.

With the previously calculated replacement probabilities, intervals in the range of 1 to 10000 are then defined for comparison with the pseudo-random value. Each interval corresponds to a different breakage pattern. Depending on the pseudo-random value, a breakage pattern is selected and the initial particle is replaced. For the following particle, all custom properties are set 0.

$$CF(t-2) \; < \; CF(t) \; < \; CF(t-1) \tag{10.8}$$

11 Verification and validation

The novel breakage model from Chapter 10 was verified and validated with a trial of shatter tests with sinter C. Furthermore, simulations of the conveying trials described in Chapter 7 including a standard chute and the dynamic transfer system FlowScrape were repeated with the novel breakage model and compared with results from the experiments for further validation. The content of this Chapter was already published in [2, 7, 9].

11.1 Shatter tests

To verify and validate the breakage model, a trial of shatter tests was conducted. In these shatter tests, a drop apparatus with a quick-opening flap from [304] was used (see Figure 11.1). The drop apparatus had a drop height of 3.8 m and the bulk material was dropped onto a steel plate at the bottom. The flap was held closed by an electromagnet and was quickly opened by gravity, when triggered. Three tests with 7.5 kg and one test with 5.7 kg sinter C of the size fraction 25-40 mm were conducted. More than four tests would have been desirable, but could not be carried out due to a lack of material. The bulk sample was analyzed before and after the test with the vibrating sorter, described in Section 6.3.4.

The test was simulated with the DE-software ThreeParticle using the novel breakage model, described in Chapter 10. A time step of $5 \cdot 10^{-6}\,s$ and the parameters listed in Tables 10.1 and 10.2 were used. In Figure 11.2 the collision of the material with the steel plate at the bottom during the shatter test is depicted at different points in time. The color scale represents the particle or fragment mass (blue=0 g, red=48 g). The particle breakage is clearly visible in the simulation. The fines (dark blue fragments, <6.3 mm) are represented larger in the simulation. Due to the probabilistic approach, accurate simulation results in terms of fragment size distribution require a high amount of particles. The particle mass in the shatter test was 7.5 kg, which is equivalent to 160 particles with an average mass of 47 g. Due to the low particle amount, the simulation was conducted 25 times and the arithmetic average of all simulations was further used.
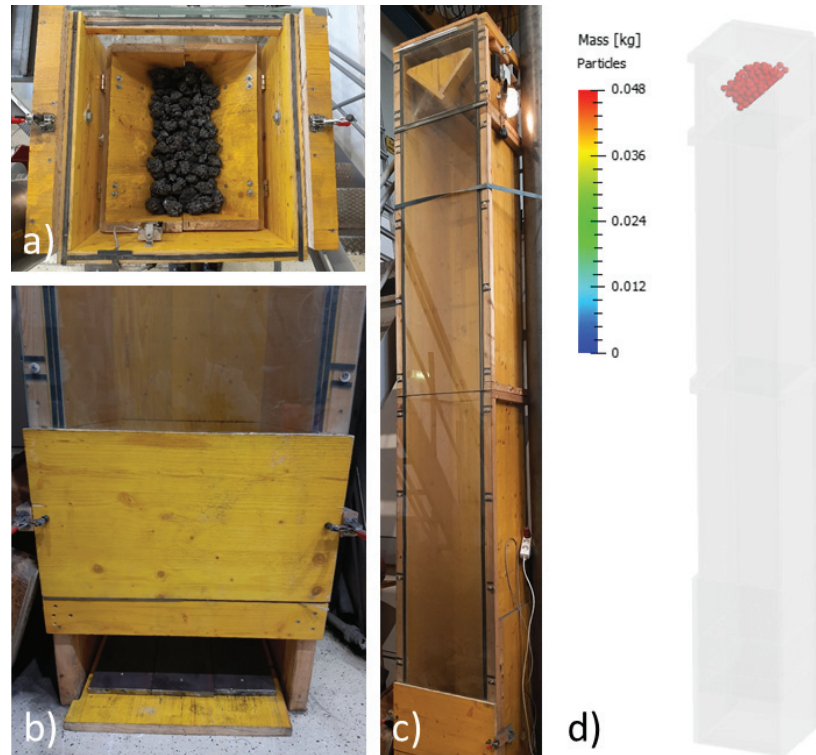
Figure 11.1: Drop apparatus a) bulk material in quick-opening flap b) steel plate at bottom c) front view d) DE-simulation with ThreeParticle [7, 9]

The comparison of test and simulation results from shatter tests is shown in Figure 11.3. The fragment size distribution after the drop is displayed (100% 25-40 mm before the drop). Minimal mass losses are considered as fines (<6.3 mm) due to dust generation and losses during fragment collection. The arithmetic average from the four tests and 25 simulations with standard deviations are depicted. The comparison shows satisfying agreement between test and simulation results.
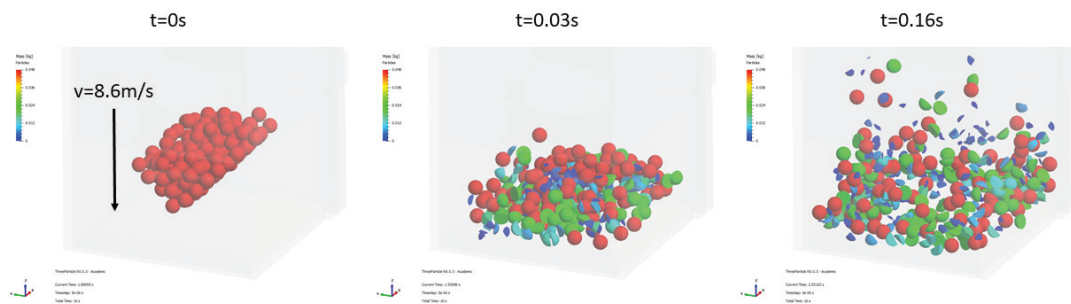
Figure 11.2: DE-simulation of the shatter test using the novel breakage model showing the collision of the material with the steel plate at different points in time. Color scale represents mass (0-48 g). [7, 9]
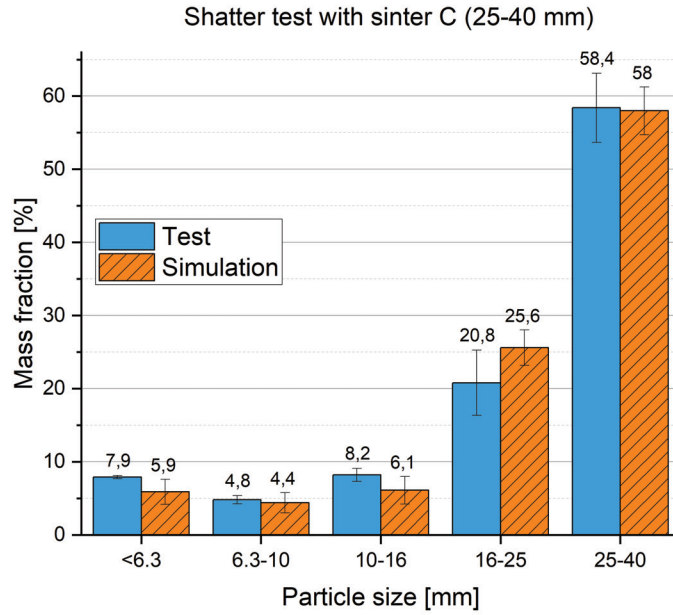
Figure 11.3: Comparison of test and simulation results from shatter tests [7, 9]

Additionally, the minimum amount of particles for sufficiently accurate simulation results in terms of PSD with this probabilistic method was determined for this case. For this purpose, the cumulative average mass fraction for each size fraction in the simulation S_i was determined and the squared deviation R_i from the test results T_i was calculated with i referring to a fragment size fraction (<6.3 to 25-40 mm). The sum of the squared deviations R_i of all fragment size fractions is then calculated with Equation 11.1 and is shown in Figure 11.4. The accuracy of the simulation asymptotically approaches a constant deviation from the tests. No significant change of simulation results is noticed over 3000 particles. Thus, a minimum of 3000 particles is required for an accurate prediction of fragment size analysis in this case.

$$\sum_{i=1}^{5} R_i{}^2 = \sum_{i=1}^{5} (T_i - S_i)^2 \tag{11.1}$$
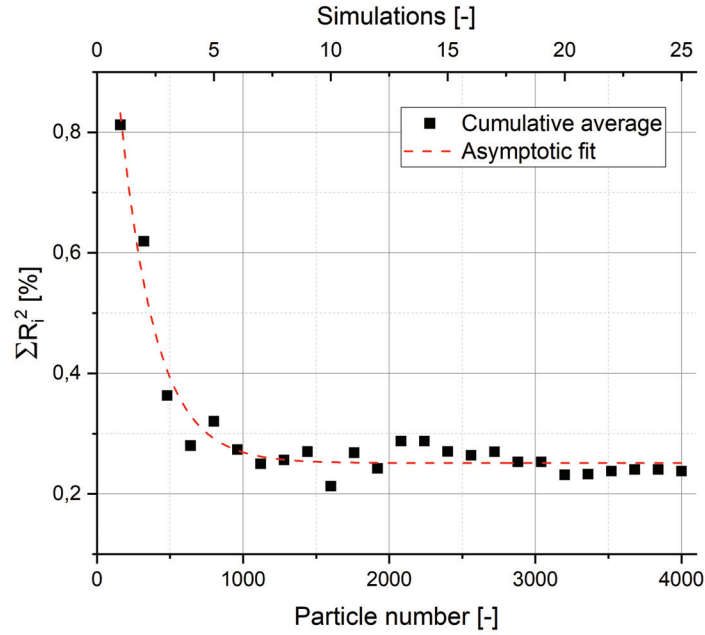
Figure 11.4: Evaluation of simulation accuracy in dependence on particle amount [7, 9]

11.2 Dynamic transfer system FlowScrape

For further validation the simulation of the conveying trial with the FlowScrape, described in Chapter 7 was repeated with the novel breakage model and polyhedral particles in ThreeParticle. For this simulation, the size fraction 31.5-50 mm of sinter B with further breakable fragments was used as described in Section 10.7. The size fraction 31.5-50 mm was defined as a mix of 25, 40 and 50 mm particles in the simulation according to measurements with the vibrating sorter before the conveying trial (compare Figure 7.6). As it was assumed that the breakage of smaller size fractions was negligible at these low impact energies, the smaller size fractions <6.3, 6-10 and 10-16 mm were excluded, which increased the mass fractions of the other particle sizes (see Table 11.1). According to the individual masses of the breakable particles, the individual mass fractions for the simulation were then calculated and listed in Table 11.2.

A time step of $5 \cdot 10^{-6}\,s$ and the parameters listed in Tables 11.3 and 11.4 were used. A different density than in Table 7.3 was used because in this case the density was adjusted with a mass of $m_0 = 124.9\,g$ for the initial 50 mm particle (compare Figure 10.10) using Equation 10.2. The correlations between compressive force and impact velocities from Table 10.3 were used.

Size fraction [mm]	Measured mass fraction [%]	Small size fractions excluded [%]
<6.3	1.3	0
6.3-10	1.8	0
10-16	5.6	0
16-25	13.9	15.2
25-40	68.4	74.9
40-50	9	9.9

Table 11.1: PSD for sinter B (31.5-50 mm) measured before experiments with the FlowScrape and adjusted for simulation

Particle name [-]	Particle mass [g]	Mass fraction [%]
25_ptc_3_v0	28.1	3.4
25_ptc_3_v1	33.5	4.1
25_ptc_4_v0	40.4	4.9
25_ptc_4_v1	22.9	2.8
40_ptc_2_v0	61.6	37.0
40_ptc_2_v1	63.3	38.0
50_ptc_1	124.9	9.8

Table 11.2: PSD for sinter B (31.5-50 mm) in breakage simulation with FlowScrape

Material	Density [kg/m³]	Poisson's ratio [-]	Shear modulus [MPa]
Sinter B (31.5-50 mm)	1908	0.25	10
Steel	7850	0.25	21000
FlowScrape	1400	0.5	7600
Conveyor belt	1400	0.5	7600

Table 11.3: Material parameters for conveying test simulations

Interaction	Restitution [-]	Static friction [-]	Rolling friction [-]
Sinter-Sinter	0.75	0.62	0.5
Sinter-Steel	0.43	0.839	0.5
Sinter-FlowScrape	0.49	0.7	0.5
Sinter-Conveyor belt	0.4	0.7	0.5

Table 11.4: Interaction parameters for conveying test simulations with polyhedral particles [277, 295]

It must be stated that, unfortunately, the breakage tests for the size fraction 31.5-50 mm of sinter B (see Section 6.5.5) were performed without sorting with the vibrating sorter before testing. Thus, no individual result diagrams for the fractions 16-25, 25-40 and 40-50 mm can be obtained. Only a diagram for the mix of these fractions (31.5-50 mm) can be obtained (see Figure 6.36). The breakage behavior depends on the PSD of the mix. As no sorting with the vibrating sorter was performed before the breakage tests, the PSD before the breakage tests can only be estimated by extrapolating the fits to $E_{cs} = 0\,J/kg$. For future investigations, it is strongly recommended to sort the specimens before breakage testing with exactly the same device as used for the fragment analysis, as it was conducted for sinter C.

With only the breakage test results for the size fraction 31.5-50 mm given, the replacement probabilities for the breakable particles 25, 40 and 50 mm had to be estimated so that the mix of these matched breakage test results for the size fraction 31.50 mm (Figure 6.36). As it was assumed that the specific impact energies in this application did not exceed $E_{cs} = 110\,J/kg$, the replacement probabilities only until $E_{cs} = 110\,J/kg$ were estimated. This significantly simplified the estimation procedure because the data in Figure 6.36 were able to be approximated very well with linear fits until $E_{cs} = 110\,J/kg$ (see Figure 11.5). The linear fit equation for the fraction 40-50 mm was able to be directly used as the replacement probability for this fraction because it is not influenced by the smaller size fractions. The linear fits of test results for the smallest size fractions <6.3, 6.3-10 and 10-16 mm were also directly used as breakage probabilities and defined the same for the particles 25, 40 and 50 mm, which were then independent of the mix of these. The replacement probabilities for the size fractions 16-25 and 25-40 mm had to be estimated iteratively due to the previously mentioned lack of data. In this process it was considered that the sum of all gradients for the replacement probabilities was 100.

As a high amount of particles was necessary, the simulation was conducted three times with 2773 particles, which was equivalent to 157 kg sinter for this material mix. This resulted in a total of 8319 particles or 471 kg material in this case. To achieve the same mass flow in simulations as in the experiments, the belt was loaded on a longer Section. The simulation is depicted in Figure 11.6. The color scale represents the particle mass (0 to 0.13 kg).
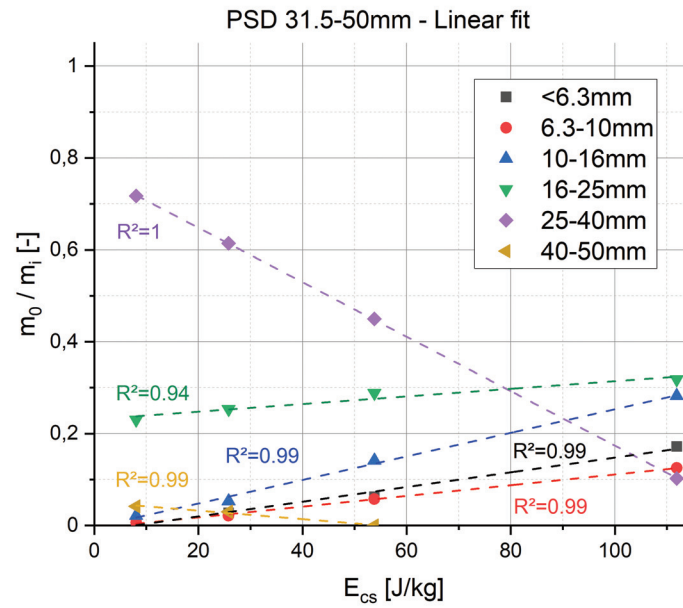
Figure 11.5: Particle size distribution after impact tests for initial size fraction 31-50 mm (sinter B) with linear fit until $E_{cs} = 110 J/kg$
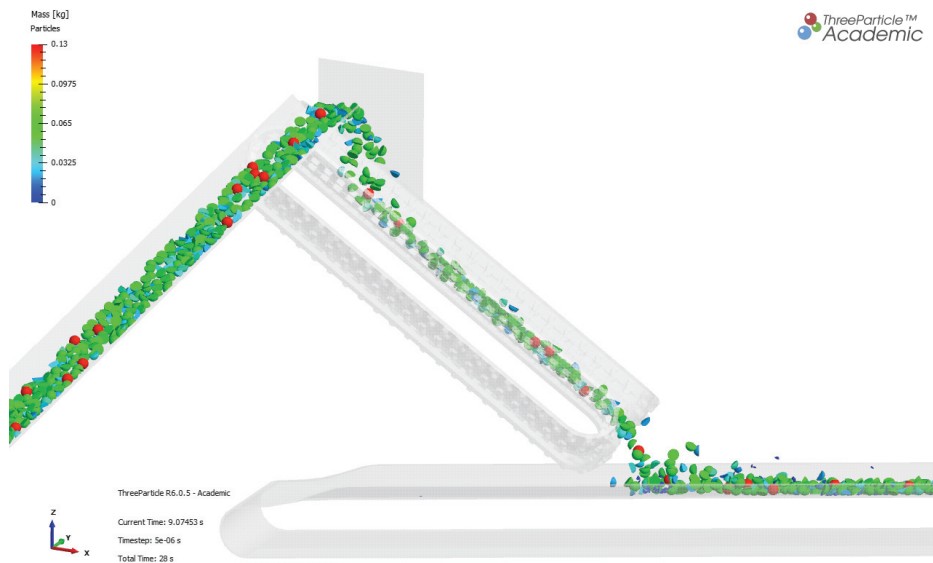
Figure 11.6: Simulation of the FlowScrape using the novel breakage model with polyhedral particles in ThreeParticle (sinter B, 31.5-50 mm). Color scale represents mass (0-0.13 kg). [7]

The simulation results are compared with the results of the experiments in Figure 11.7. The increase of each mass fraction for every size fraction is depicted with the standard deviations calculated from the six experiments and 3 simulations. The comparison shows a satisfying agreement of test and simulation results. Especially

for the fines (<6.3 mm) a very good agreement is noticed, which was the main purpose of the breakage simulation. A significant improvement to the breakage simulations by using the post-processing approach of evaluating the compressive force described in Chapter 8 was also noticed (compare with Figure 8.7).
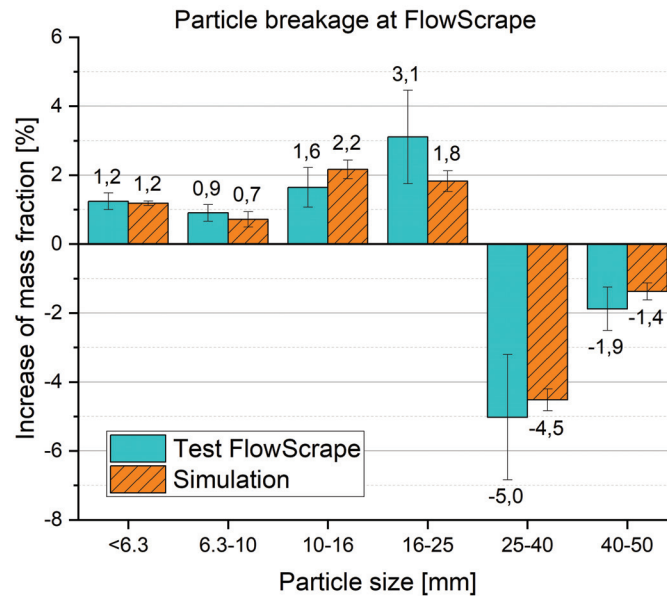
Figure 11.7: Increase of mass fractions due to transfer with the FlowScrape. Comparison of test and simulation results (sinter B, 31.5-50 mm) [7]

11.3 Conventional chute

Also for further validation, the simulation of the conveying trial with the conventional chute described in Chapter 7 was repeated with the novel breakage model and polyhedral particles in ThreeParticle. As described in Section 11.2, the size fraction 31.5-50 mm of sinter B with further breakable fragments was used as described in Section 10.7. In contrast to the simulations with the FlowScrape in Section 11.2, a different material mix of the size fraction 31.5-50 mm was defined containing 25, 40 and 50 mm particles in the simulation according to measurements with the vibrating sorter before the conveying trial, compare Figure 7.5. The PSD for the simulations with the conventional chute were also adjusted to exclude the smaller size fractions <6.3, 6-10 and 10-16 mm, which increased the mass fractions of the other particle sizes (see Table 11.5). According to the individual masses of the breakable particles, the individual mass fractions for the simulation were then calculated and listed in Table 11.6.

Size fraction [mm]	Measured mass fraction [%]	Small size fractions excluded [%]
<6.3	2	0
6.3-10	2.9	0
10-16	6.4	0
16-25	16.1	18.2
25-40	62.4	70.3
40-50	10.2	11.5

Table 11.5: PSD for sinter B (31.5-50 mm) measured before experiments with conventional chute and adjusted for simulation

Particle name [-]	Particle mass [g]	Mass fraction [%]
25_ptc_3_v0	28.1	4.1
25_ptc_3_v1	33.5	4.9
25_ptc_4_v0	40.4	5.9
25_ptc_4_v1	22.9	3.3
40_ptc_2_v0	61.6	34.7
40_ptc_2_v1	63.3	35.6
50_ptc_1	124.9	11.5

Table 11.6: PSD for sinter B (31.5-50 mm) in breakage simulation with conventional chute

As also in this case a high amount of particles was necessary, the simulation was conducted three times with 2773 particles, which was equivalent to 153 kg sinter for this material mix. This resulted in a total of 8319 or 459 kg material. The simulations were conducted with the same mass flow as in the experiments. The simulation is depicted in Figure 11.8. The color scale represents the particle mass (0 to 0.13 kg).

The simulation results are compared with the reuslts of the experiments in Figure 11.9. The increase of each mass fraction for every size fraction is depicted with the standard deviations calculated from the five experiments and three simulations. Also in this case the comparison shows a satisfying agreement of test and simulation results. For the fines (<6.3 mm), a very high agreement is noticed again. A significant improvement to the breakage simulations by using the post-processing approach of evaluating the compressive force described in Chapter 8 was also noticed, compare with Figure 8.6.
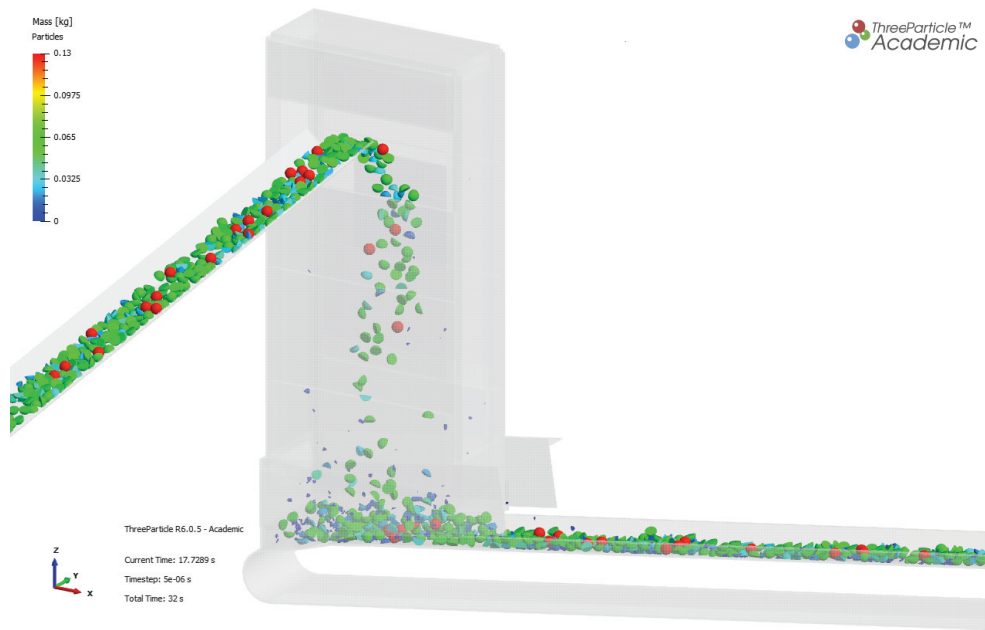
Figure 11.8: Simulation of the conventional chute using the novel breakage model with polyhedral particles in ThreeParticle (sinter B, 31.5-50 mm). Color scale represents mass (0-0.13 kg). [7]
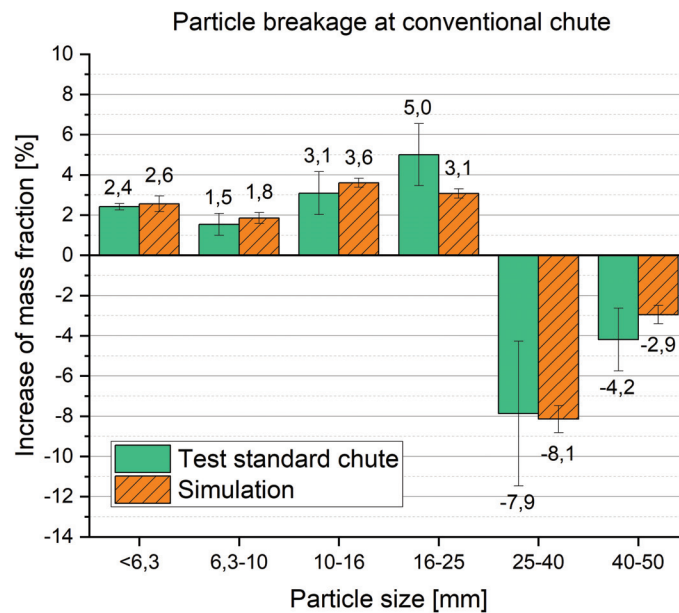
Figure 11.9: Increase in mass fractions due to transfer with the conventional chute. Comparison of test and simulation results (sinter B, 31.5-50 mm) [7]

12 Application for a solid state material driven turbine

Another objective of the project MinSiDeg besides minimization of sinter degradation, was to reduce segregation effects during transport and storage processes. A solid state material driven turbine, which was originally developed and patented in [305] for energy recovery [306–308], was further developed and optimized to reduce segregation effects. To quantify material degradation due to the solid state material driven turbine, simulations using the novel breakage model with multiple breakage were conducted. The content of this Chapter was already published in [4, 6, 8].

12.1 Segregation effects during bunker filling

Bunkers are mostly used for storage or buffering. Particle size segregation effects at the bunker outflow lead to fluctuations in particle size distribution. In most applications and for their following processes, an evenly-distributed bunker discharge is desired in terms of particle size distribution. This especially applies to blast furnace sinter bunkers as a constant particle size distribution for blast furnace operation is needed to ensure a sufficient gas flow.

Significant segregation effects during bunker filling mainly occur due to the following two effects. Due to vibrations during transport by conveyor belt, small particles accumulate at the bottom and large particles at the top of the bulk material heap in the conveyor belt. Thus, the large particles have a different trajectory than the small particles when discharged. Depending on the belt incline and speed, at discharge the large particles could have a higher velocity than the small particles due to the greater distance of the large particles to the center of the discharge pulley. This could lead to an accumulation of large particles in the conveying direction and an accumulation of small particles against the conveying direction of the discharging conveyor belt in the bunker. [309]

The second segregation effect is noticed every time a bulk material pile is formed. As larger particles have a greater forward momentum than smaller particles, the coarse material continues moving down the side of the pile more than the fine material. The material that tumbles down the slope of a pile is called overrun. Larger particles tend to roll down the entire length of the slope and fine particles tend to settle into the side of the pile. This effect of overrun causes the outer and bottom zones of the pile to consist of coarser material, while the inner and upper zones of the pile consist of more fine material. [309]

12.2 Current state

The current state at a steel manufacturer, which produces sinter A, was investigated. Sinter is stored in square-shaped bunkers with filling levels of up to 600 t, which are filled by conveyor belts with a mass flow of 300 t/h and an almost constant particle size distribution (see Figure 2.6). Low filling levels lead to high drop heights, which is assumed to be one of the main reasons for material degradation.

The current state was simulated by means of DEM with EDEM by M. Prenner [6] (see Figure 12.1). The parameters listed in Tables 6.2 and 6.3 were used. In the simulations the bunker was filled with 350 t with the PSD listed in Table 6.4. The small fractions 6, 10 and 16 mm were combined (52.245% in total). All particles were upscaled by the factor 3 for computational efficiency.
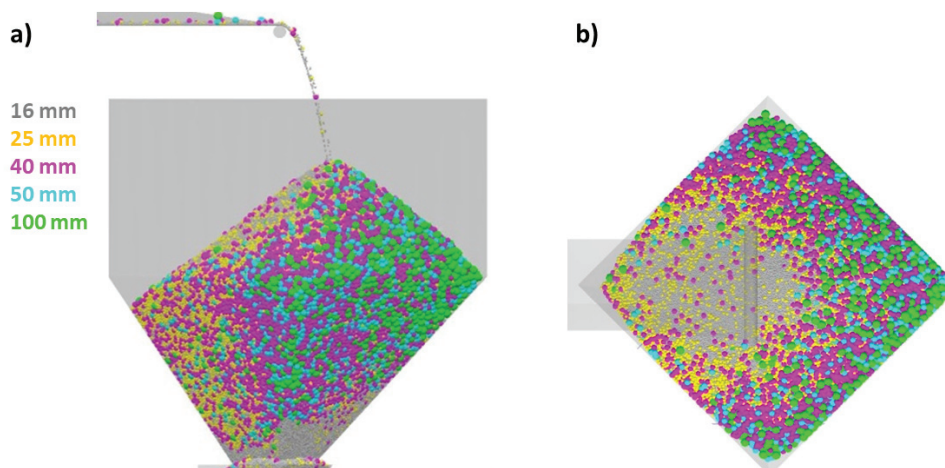
Figure 12.1: DE simulation of current state of bunker with significant segregation a) side view b) top view [4, 6]

At a filling level of 350 t, the bunker was discharged and the particle size distribution at the outflow was determined in the simulation. In Figure 12.2 the mass fraction for each particle size in connection with the bunker filling level is shown. Small particles (6+10+16 mm) contribute with approximately 80% to the total mass flow at the beginning and decrease to around 10% at the end of the discharging process. As shown in Table 6.4, an optimum would be a constant flow of 52.245% for the small particles during the whole discharging process. In contrast to this, the mass fraction of large particles is relatively small at the beginning of the discharging process and starts to increase at approximately 50% of the filling level. This phenomenon can be explained by the core flow effect, which means that a core flow forms during discharging. This leads to an early discharge of material in the inner zones of the bunker, which consists of the smaller particles. The larger particles (overrun) are accumulated at the outer zones.
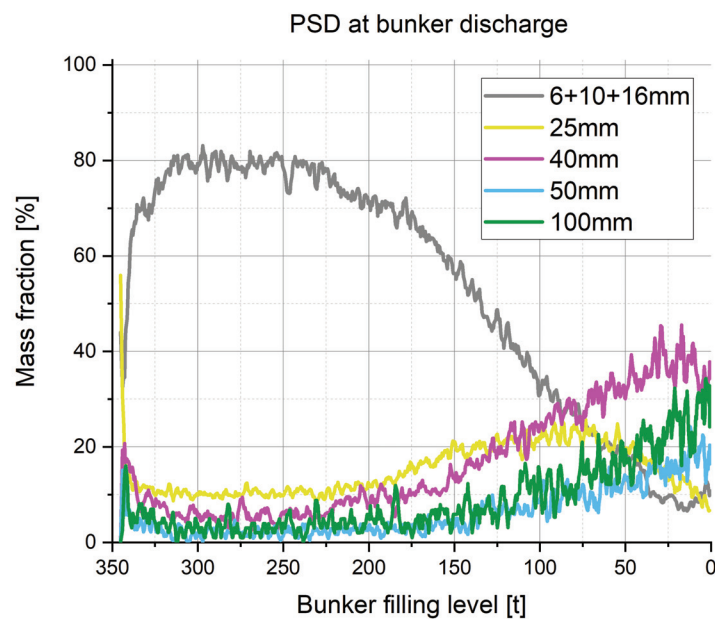
Figure 12.2: PSD at bunker discharge at current state [4]

12.3 Cross flow turbine

Various types of installations to reduce segregation effects during bunker filling were tested in simulations with EDEM by M. Prenner in [4]. Thereby, the discharge from a conveyor belt was simulated with and without different installations including bucket chains and different types of turbines. To determine segregation,

the top view of the bulk material pile with only one particle size at a time faded in was evaluated. The best results were achieved with a cross flow turbine at low rotation speeds of 5 rpm (see Figure 12.3).
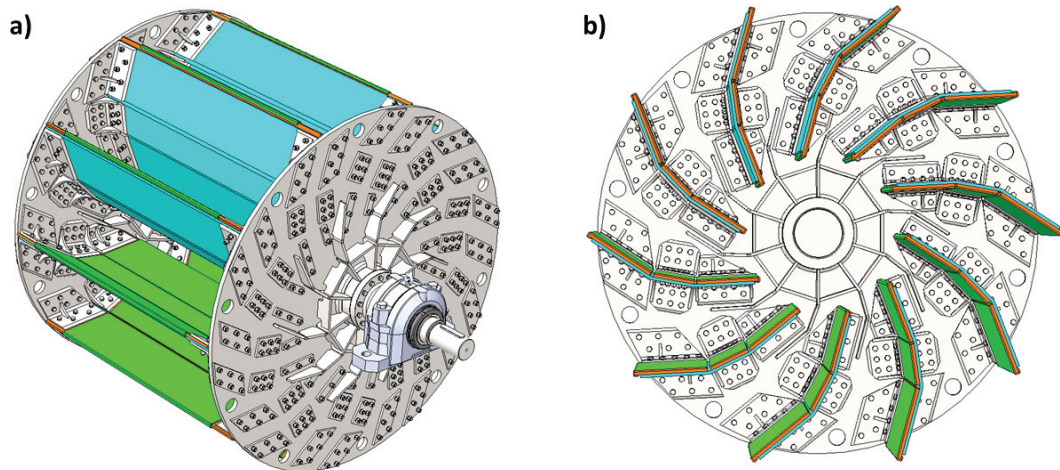
Figure 12.3: Cross flow turbine a) isometric view b) side view [4]

.

The cross flow turbine was engineered by M. Prenner and G. Lux in [4] and consists of 10 segmented blades, which form an ideal curvature for material flow. The center of the cross flow turbine is hollow, which allows the material to flow through the turbine. Depending on the mass flow, the above-mentioned low rotation speed can be achieved by regenerative braking or by an electric drive at low mass flows. An optimum for reducing size segregation effects was found at 5 rpm, for energy recovery at 30-40 rpm. Further investigations regarding power output and wear are described in [4].

The bunker filling process was simulated again with the cross flow turbine in EDEM by M. Prenner (see Figure 12.4). The 100 mm particles were represented by 50 mm particles, otherwise, they would not have passed the turbine due to the up-scaling by a factor of 3. A significant reduction of segregation effects is noticed when the bunker is filled with the cross flow turbine (compare Figure 12.4 with Figure 12.1). This leads to a significant improvement in terms of particle size distribution at bunker discharge in Figure 12.5. An almost constant particle size distribution till a filling level of 100 t is noticed, which is a great improvement compared to Figure 12.2.
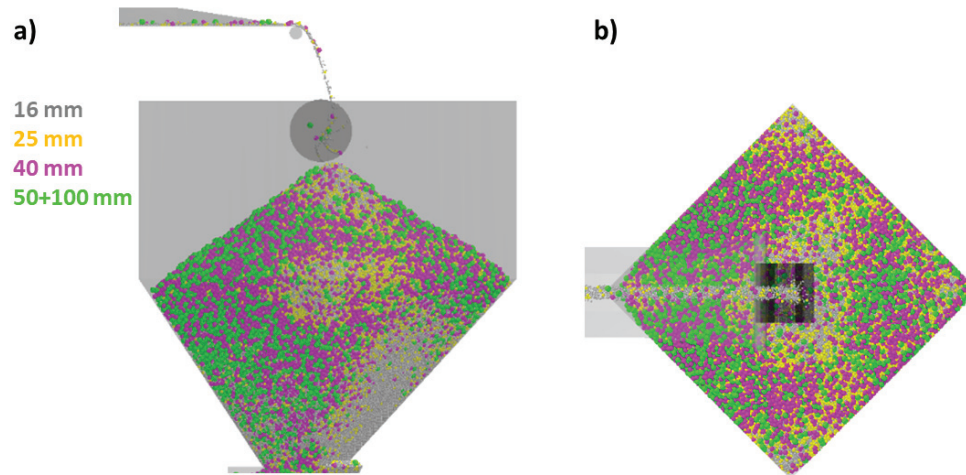
Figure 12.4: DE Simulation of bunker filled with cross flow turbine a) side view b) top view
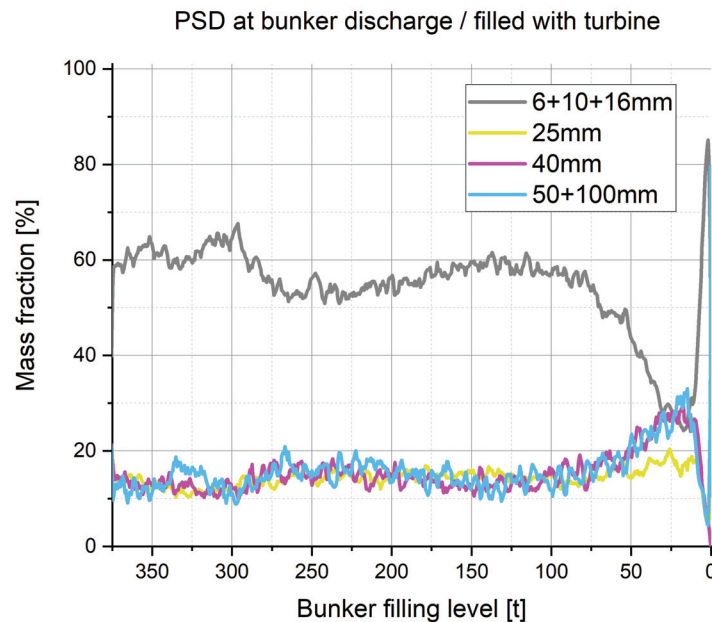
Figure 12.5: PSD at bunker discharge. Bunker filled with cross flow turbine [4]

12.4 Material degradation

The cross flow turbine significantly reduces segregation effects, but could eventually also cause damage to particles. On the one hand, the cross flow turbine reduces drop height into the bunker by its diameter, but on the other hand, it causes additional impacts on the turbine and among particles. To quantify the particle degradation and fines generation caused by the turbine, a detailed investigation

was necessary. For this investigation, the novel breakage model described in Chapter 10 with further breakable fragments was used.

12.4.1 Simulation

To quantify particle breakage caused by the cross flow turbine, a comparison of the drop with the drop and without the turbine was performed in ThreeParticle (see Figure 12.6). For computational efficiency, the simulation was simplified in order to simulate fewer particles in the bunker. To simulate the drop without the turbine, only the pile peak was simulated as a drop into a bulk material bed has a damping effect. The bulk material bed was placed at the same height as the bottom of the turbine, which would allow a direct comparison. The turbine reduced the drop height for the discharged material from h to h_T but caused additional impacts with the turbine and within the material. For evaluation a fragment collecting box was implemented, otherwise, the resulting fragments would have been deleted outside the simulation domain. Very soft material properties were assigned to the collecting box so that no breakage would occur due to impacts on the collecting box (see Tables 12.1 and 12.2 for the parameters). The densities for the different size fractions were adjusted to the measured average particle masses following Equation 10.2. A time step of $5 \cdot 10^{-6}$ and the Hooke contact model were used.
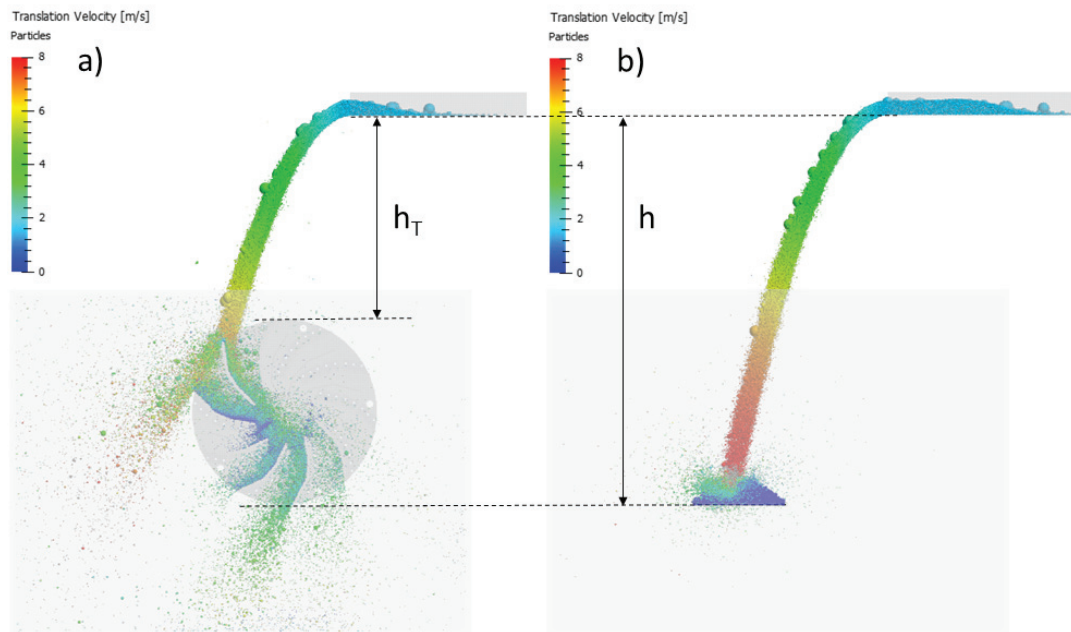
Figure 12.6: Breakage simulation of bunker filling with the novel breakage model a) with cross flow turbine at 5 rpm b) without turbine [4]

Material	Density [kg/m³]	Poisson's ratio [-]	Shear modulus [MPa]
Sinter (10-16 mm)	1371	0.25	10
Sinter (16-25 mm)	1243	0.25	10
Sinter (25-40 mm)	1085	0.25	10
Steel	7850	0.25	210000
Conveyor belt	1400	0.25	7600
Collecting box	100	0.25	10

Table 12.1: Material parameters for simulations with the cross flow turbine

Interaction	Restitution [-]	Static friction [-]	Rolling friction [-]
Sinter-Sinter	0.75	0.62	0.5
Sinter-Steel	0.43	0.839	0.5
Sinter-Conveyor belt	0.4	0.7	0.5
Sinter-Collecting box	0	0.839	0.5

Table 12.2: Interaction parameters for simulations with the cross flow turbine

For comparison of particle damaging effects caused by the turbine, the same process was simulated with the cross flow turbine at different rotational speeds of 5, 10, 20, 30, 40 and 50 rpm. As mentioned in Section 12.3 5 rpm is the optimum for reducing segregation effects and 30-40 rpm for energy recovery. A comparison of Figures 12.7a) and b) shows that at 5 rpm the material flows through the turbine, which results in a mixing effect and reduces segregation. This is not the case at 30 rpm, where the material remains on the same turbine blade and causes a higher torque on the turbine.

The material forms a bulk material bed inside the turbine, which is assumed to have a significant damping effect. As the damping effect depends on the PSD in the material bed and smaller particles lead to higher damping, the small particles were also simulated in this case. The PSD for the simulation equaled the original PSD from the bulk sample of the sinter plant (sinter A), which is listed in Table 6.4. It has to be stated that only the size fractions 10-16, 16-25 and 25-40 mm were breakable in this case, which were represented by polyhedral particles of spherical shape with diameters of 16, 25 and 40 mm in the simulation. No experimental data for the fractions 6-10, 40-50 and 50-100 mm are available. The fines and the non-breakable particles were represented by spheres with a diameter of 6, 10, 50 and 100 mm in the simulations. A total mass of 122.9 kg sinter was simulated, which was equivalent to 160512 particles with this PSD.
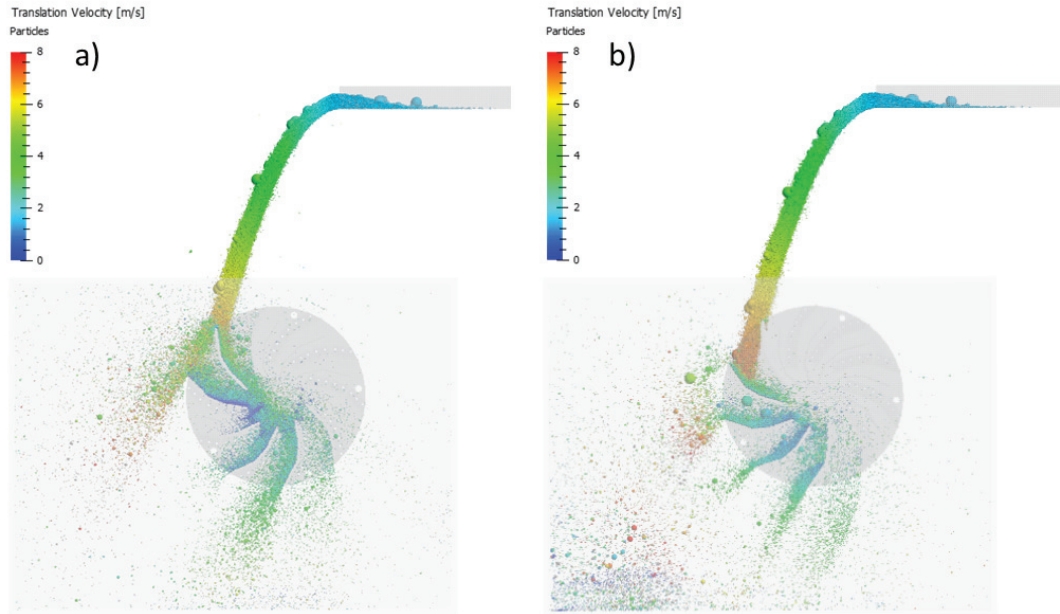
Figure 12.7: Breakage simulation of bunker filling with novel breakage model with cross flow turbine a) at 5 rpm b) at 30 rpm

12.4.2 Multiple breakage

The simulation was conducted with further breakable fragments for the particles 25 and 40 mm. The initial 16 mm particles are breakable, but the resulting fragments were not further breakable in this case ($L = 1$). The schemes for the 25 and 40 mm particles are depicted in Figures 12.8 and 12.9. As the smallest breakable particles were 16 mm in this simulation, the maximum breakage level was $L = 3$ for the initially 40 mm particles and $L = 2$ for the initially 25 mm particles.

The relation between maximum compressive force and impact velocity was determined with impact test simulations at 6, 16 and 22 m/s for 1000 particles, as described in Section 10.4. Impact tests were only simulated for the initial particles 16, 25 and 40 mm (see Table 12.3). As the linear parameter a is only dependent on the particle or fragment mass and independent of the shape (see Figure 10.12), the linear parameters a for the further breakable fragments were calculated by the power function depicted in Figure 12.10.
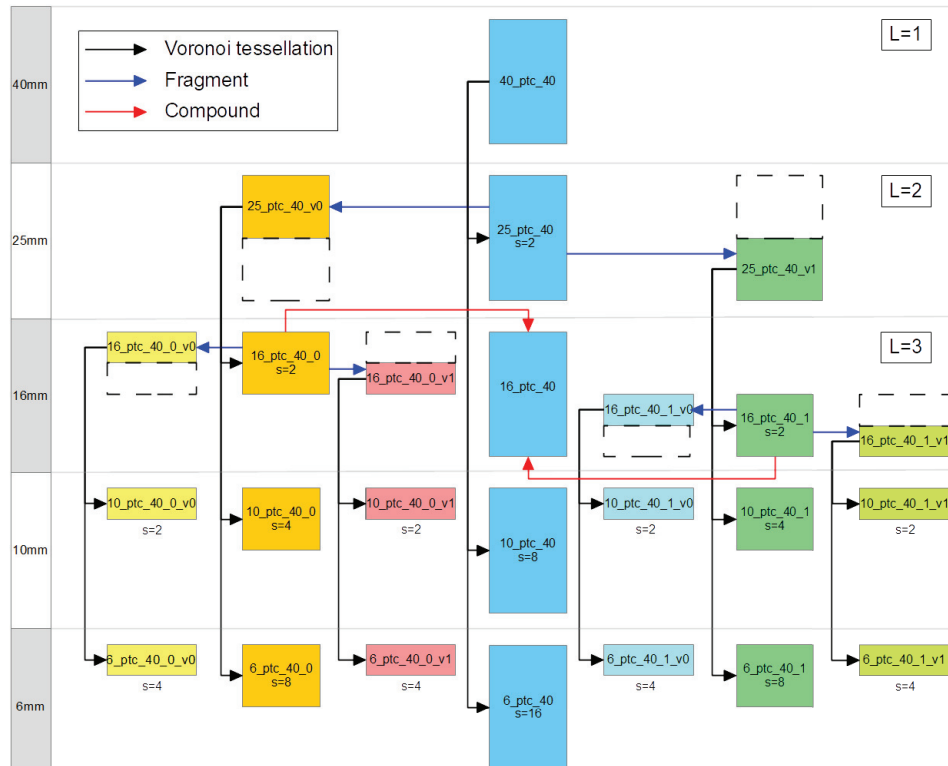
Figure 12.8: Multiple breakage resulting from 40 mm particles (sinter A, L=3, s=2)
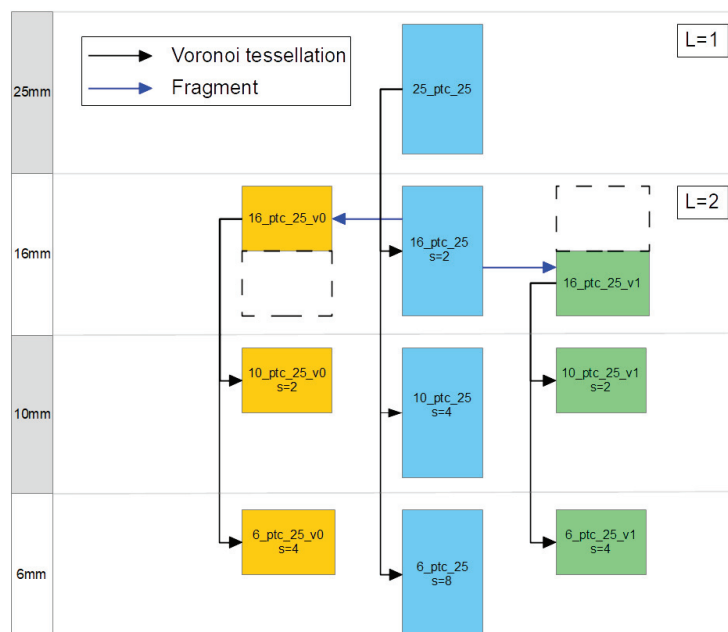
Figure 12.9: Further breakable fragments resulting from 25 mm particles (sinter A, L=2, s=2)

170

Particle name	a [-]	Mass [g]
40_ptc_40	342.02	40.1
25_ptc_25	161.99	9.8
16_ptc_16	88.17	2.6

Table 12.3: Linear parameters a for sinter A with the Hooke model, following Equation 10.3
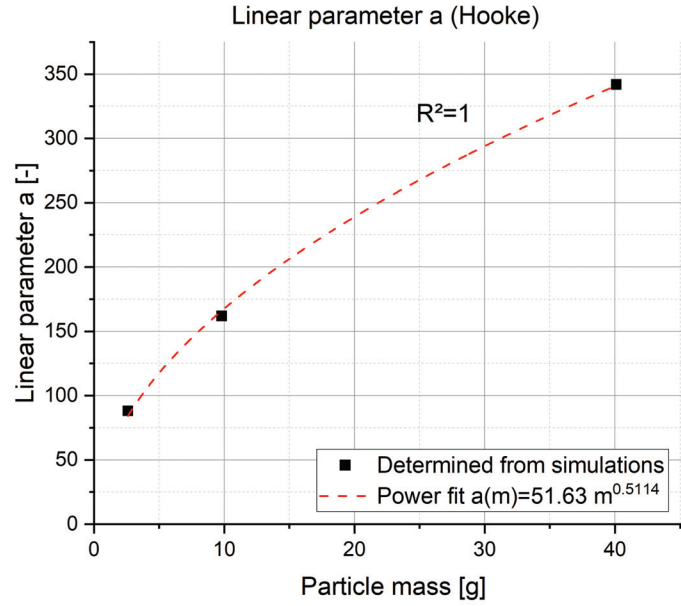
Figure 12.10: Linear parameter *a* for the correlation between maximum compressive force and impact velocity with the Hooke contact model following Equation 10.3

12.4.3 Replacement probabilities

Based on impact test results, the replacement probabilities were defined for the breakable particles. A piecewise linear regression was performed by means of Matlab and [298]. As described in Section 10.1, every set of breakage probabilities was then applied to the corresponding size fraction, independent of where the fragments resulted from. As each size fraction was represented by its passing or maximum diameter, the probabilities at $E_{cs} = 0$ were defined as 1. There was some mismatch for higher specific impact energies, which was negligible in this case because such high impact energies did not occur in the simulations performed here. For higher accuracy at higher specific impact energies, a piecewise linear regression with four segments could be performed.
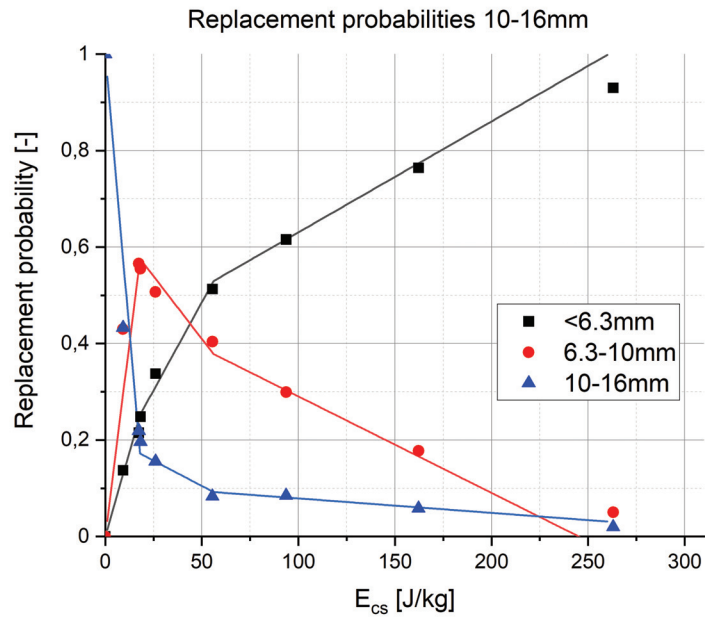
Figure 12.11: Replacement probabilities for 16 mm particles (sinter A) based on impact test results in Figure 6.20
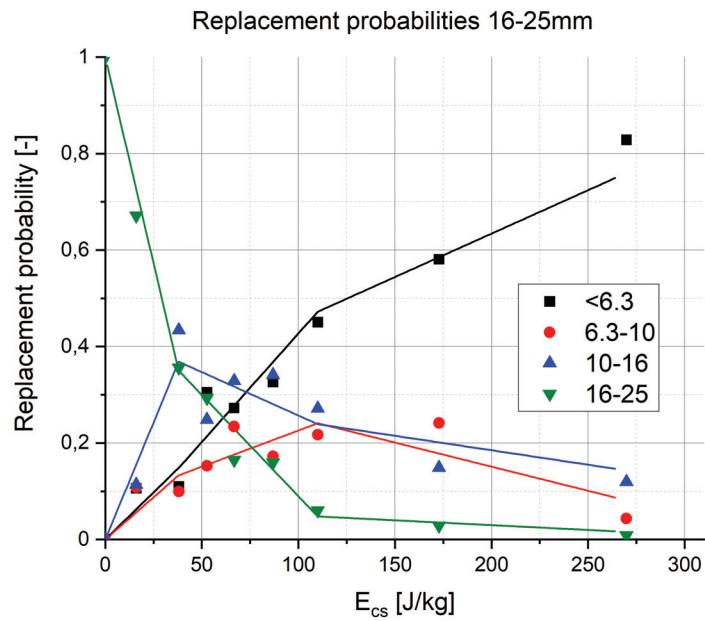
Figure 12.12: Replacement probabilities for 25 mm particles (sinter A), based on impact test results in Figure 6.21
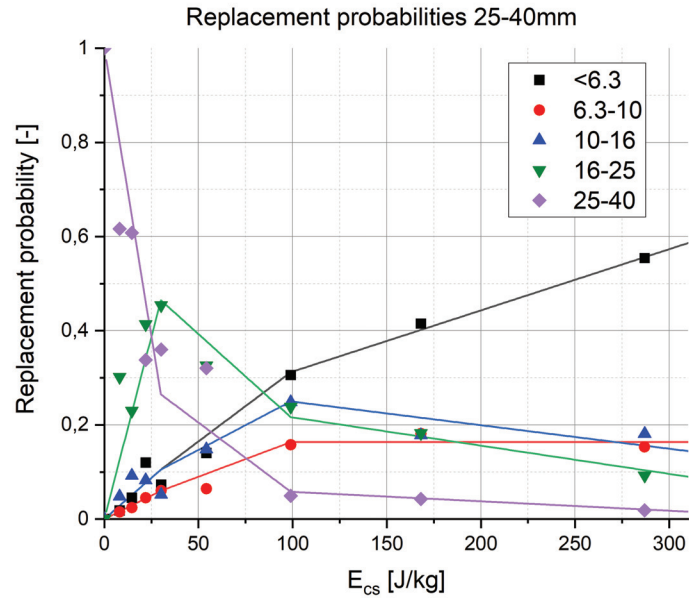
Figure 12.13: Replacement probabilities for 40 mm particles (sinter A), based on impact test results in Figure 6.22

12.4.4 Results

The results of the particle breakage evaluation for 5 rpm (reduce segregation effects) and 30 rpm (energy recovery) are shown in Figure 12.14, which shows the increase in mass fractions for each particle size due to the bunker filling process. The diagram does not include the size fractions 40-50 and 50-100 mm as 50 and 100 mm particles were not breakable in this simulation.

More breakage occurs at the drop with the cross flow turbine at 5 rpm and about 1% more fines are produced in this case, compared to the case without turbine. It is assumed that volume breakage occurs mainly due to impacts on the blade edges, where also the most wear occurs, and generation of fines is mainly due to abrasion among sinter particles inside the turbine.

Significantly less particle breakage occurs if the turbine is operated with a higher rotation speed of 30 rpm for energy recovery. 0.5% less fines are produced at 30 rpm compared to the case without turbine. It was assumed that the turbine has an even more particle-preserving effect at higher rotation speeds, but is limited to a certain rotation speed as the particle preserving effect of a damping material bed on the blades also decreases with higher rotation speeds. For this purpose, the fines production in dependence on the rotation speed was investigated for this case (see Figure 12.16). A minimum for the fines production is noticed at 30 rpm, which confirms the assumption.
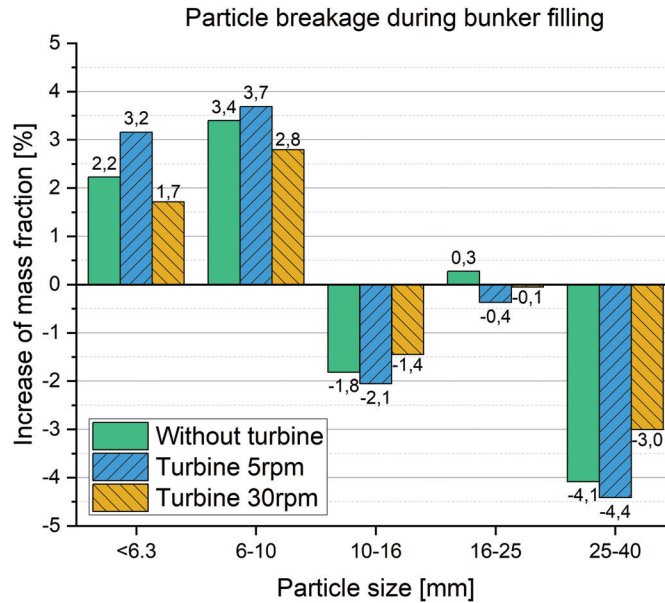
Figure 12.14: Particle breakage during bunker filling without and with the cross flow turbine at 5 rpm (segregation) and 30 rpm (energy recovery)

Various studies confirm that replacing a drop by several smaller drops leads to less particle breakage [37]. Thus, material degradation is not only dependent on the rotation speed, but also on the mounting height of the turbine and bunker filling levels. The reduction of particle breakage due to splitting the drop height into two smaller drops could not be evaluated with the simulations described in Section 12.4.1. Overall, it is assumed that the turbine leads to less particle breakage during a whole bunker filling process, but this needs to be confirmed by further investigations.

Additionally, the torque was evaluated for different rotation speeds (see Figure 12.15). Due to the large scattering, the torque data has been smoothed using the LOWESS method (Locally Weighted Scatterplot Smoothing) in Origin. From the smoothed torque curves, the maximum torque for each rotation speed was determined and the maximum power output was calculated, which are both shown in Figure 12.15. Highest values for power output are noticed at 30 and 40 rpm, which confirms previous investigations with EDEM regarding the optimum rotation speed for energy recovery in [4]. Figure 12.16, shows that the rotation speed with the maximum power output equals the rotation speed for minimum fines generation. It is assumed that a high energy transfer from the bulk material to the turbine leads to a reduction of energy available for particle breakage.
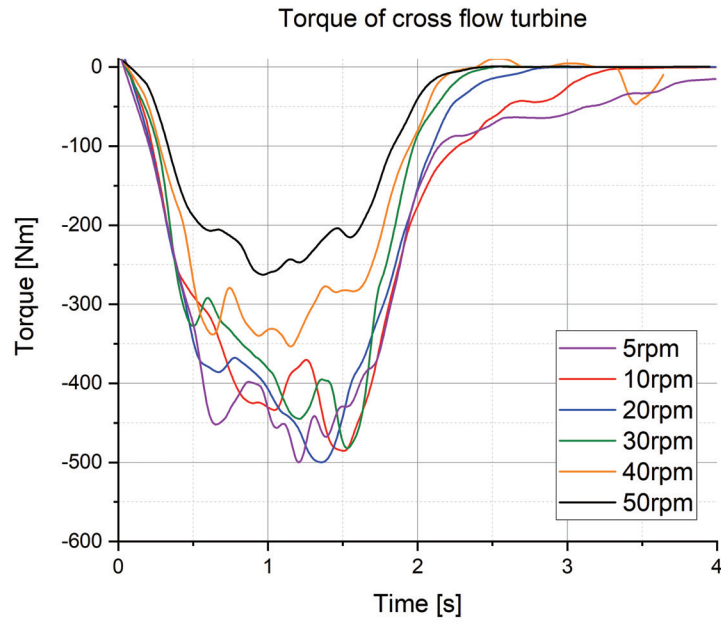
Figure 12.15: Evaluation of the torque (smoothed curves) on the cross flow
turbine at different rotational speeds with 300 t/h sinter
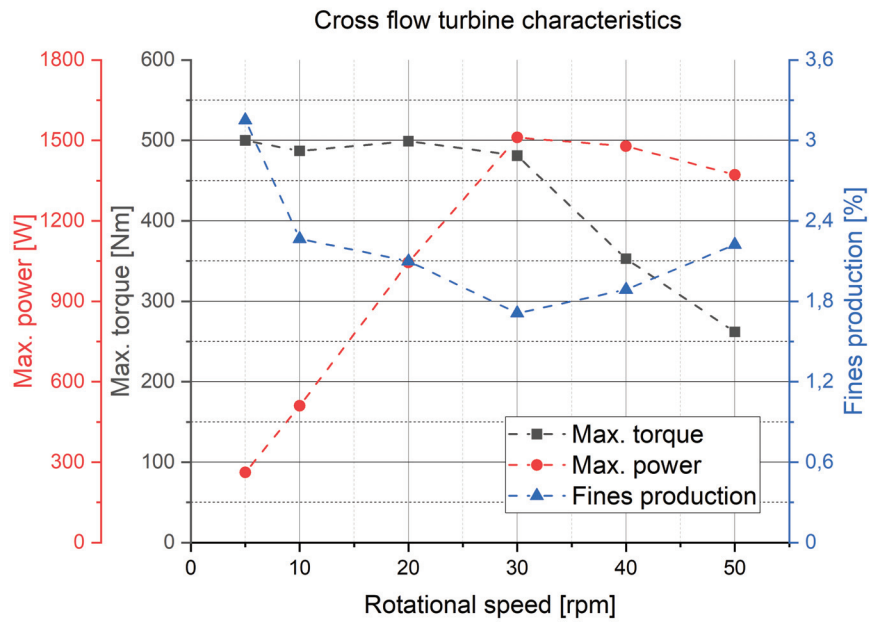
Figure 12.16: Fines production, maximum torque and power output of the
cross flow turbine at different rotational speeds for 300 t/h sinter

13 Summary

In this thesis the breakage behavior of blast furnace sinter was investigated with a special focus on fines generation. Based on breakage test results, a novel breakage model for DEM was developed, which was verified and validated with a trial of shatter tests and two different transfer systems, using sinter from different manufacturers. Additionally, the application of the breakage model for a solid state material driven turbine is described.

In a first step, particle shape and mass were investigated. On average the sinter particles have an ellipsoidal shape. Average dimensions were determined for each size fraction. A linear decrease in the shape factor d_{max}/d_{min} was noticed with increasing particle size. The correlation between particle mass and size was also determined.

With a modified hydraulic press, the particle strength under uniaxial compression was able to be determined, which decreases following a power function. The average mass-specific energy for volume breakage under uniaxial compression was also calculated and the resulting PSD was measured for each size fraction. Further evaluation of data from a preliminary study with drop tests revealed limits for improbable and probable breakage in dependence on particle mass.

As one of the main causes of sinter breakage during transport and handling are impacts on equipment or other particles, an automated single particle impact tester was developed. The test rig consists of a vibratory bowl feeder, a weighing station, a loading mechanism, an air cannon, a drop module and a vibrating sorter for integrated fragment analysis. It provides an efficient tool to analyze single particle breakage behavior due to impacts [1]. A wide range of specific impact energies and particle sizes can be tested. Specific impact energies of 8–312 J/kg (4–25 m/s) and particles up to 50 mm can be tested by air cannon. Low energy tests with 0–8.8 J/kg (0–900 mm) and particles >50 mm can be tested by drop module. The high grade of automation and integrated fragment analysis allow rapid testing by performing one test per minute.

Different size fractions of sinter from two different manufacturers were analyzed in this work. Clear trends in fragment size distributions depending on the initial size fraction were observed. Here it has to be considered that the fragment analysis

with the vibrating sorter works on a one-dimensional passing principle, in contrast to a two-dimensional passing principle with conventional sieves. Compared to compression tests at the same specific energy, the PSD is finer and more fines are produced in impact tests.

Relative return fines production in dependence on specific impact energy can well be described by a logistic growth trend, which only seems linear for low energies, as assumed in [92]. Smaller particles produce more return fines in relation to their initial particle mass, which is consistent with the findings in [92]. Individual fragment analysis allowed to determine the variability of relative return fines production. Clear trends in standard deviations for relative return fines production in dependence on specific impact energy were noticed.

By introducing a size factor $1/x^2$, where x is the initial particle size, a general return fines production curve was able to be calculated. The curve allows a size-independent prediction of return fines production. This approach was successfully repeated with different batches of sinter from a different manufacturer.

When evaluating breakage probability (10% mass decrease), it was noticed that large particles were slightly more inclined to break, which meets expectations from material handling and is also consistent with the findings in [92]. Breakage probability can well be described by a lognormal or Weibull distribution. Furthermore, a size-independent breakage characterization was carried out by the well-established t_n-modeling concept. The t_n-curves show that there is no significant difference in general breakage behavior between size fractions.

Comparative conveying trials with a standard chute and a dynamic transfer system (FlowScrape) were performed and simulated with EDEM. With these simulations a simple post-processing approach to predict particle breakage was conducted. The compressive force during the whole conveying process was evaluated for each particle. With the compressive force peaks and the results from breakage tests, a satisfying breakage prediction was able to be achieved with this approach for large initial particle sizes. However, due to limitations in particle amount, number of damaging events taken into account and post-processing effort this approach is considered unsuitable to simulate long and complex conveying processes with multiple breakage or high mass flows as desired in this case. However, a chute at a sinter manufacturer was investigated and optimized in [297] by means of DEM. Compressive forces were evaluated, but a fines generation prediction was not able to be performed with this approach due to the high mass flow in this case and limitations in particle amount and computing power in the post-processing procedure. This reaffirms the demand for a model in which breakage is embedded in DEM.

An approach to simulate sinter breakage with the well-established bonded particle model [214] was also conducted. Qualitatively similar PSD as in breakage tests was able to be achieved. Due to the much higher computational effort and high calibration effort compared to particle replacement models [234, 235], the bonded particle model was considered unsuitable to simulate sinter degradation during transportation and handling. A breakage model with bonded Voronoi fragments was also considered unsuitable for this application due to high effort in terms of calibration and size analysis of fragments.

In order to simulate bulk material degradation in high mass flows with high accuracy in terms of fragment size distribution and reasonable computing efficiency, a novel breakage model was developed for DEM. The model was developed in ThreeParticle's particle replacement API using C++. The model is based on probabilistic particle replacement with fragments which were previously tessellated with the Voronoi algorithm. Depending on the stress, the particle is replaced by different breakage patterns. The fragments are sharp-edged and of random shape. Slightly more computing power is necessary than for a replacement with spheres as in [245], but mass and volume constancy is ensured. Initial particles are polyhedral and can be of any shape.

Replacement probabilities for breakage patterns are obtained from breakage tests. By temporarily logging the damage history of particles, compressive force peaks are detected. After every compressive force peak, a random procedure is conducted to determine if a particle breaks and which breakage pattern is applied. This leads to the correct PSD in the bulk sample if applied to a high amount of particles. It has to be stated that energy balance is not correct in the simulations performed here because breakage energy was not taken into account. This could be corrected by reducing rebound velocity, when breakage energy was known. For this purpose, further investigations are necessary.

The correlation of compressive force and impact velocity can be obtained from impact simulations with a high number of particles. The Hooke contact model is more suitable for sharp-edged particles than the Hertz-Mindlin model. More widely dispersed contact forces are noticed with the Hooke model, but no extraordinarily high forces occur as with the Hertz-Mindlin model, which could lead to explosions. Impact simulations revealed that the compressive force due to an impact is only dependent on the particle mass and that it was independent of the particle shape for the Hooke model. Before calibrating friction coefficients, the coefficient of restitution needs to be calibrated for both contact models.

Multiple breakage or further breakage of fragments can also be implemented with this model. This allows to simulate long and complex conveying processes with

several damaging events. An example of multiple breakage on three levels is described. The computational scheme of the model is also described in detail.

The novel breakage model was verified and validated with a trial of shatter tests. The results show satisfying agreement of test and simulation results. Further validations were conducted with a different batch of sinter from a different manufacturer in a trial of conveying tests with a conventional chute and a dynamic transfer system (FlowScrape) including multiple breakage. Also in these cases, satisfying agreement of test and simulation results were noticed, especially in terms of fines generation.

Additionally, an application of the breakage model to a solid state material driven turbine is described. The turbine is designed as cross flow turbine and can be used for energy recovery or to reduce segregation effects. The breakage model was successfully applied to quantify material degradation due to the turbine. Investigations with different rotation speeds revealed an optimum to reduce size segregation at 5 rpm and for energy recovery at 30-40 rpm. A minimum for fines production was noticed at 30 rpm.

To sum up, the test method developed in this work is an efficient way to characterize breakage behavior of bulk materials and the validated novel breakage model allows to predict particle breakage by means of DEM. High accuracy in terms of fragment size distribution is achieved if applied to a high amount of particles, especially for fines. The test method and the breakage model were successfully applied to blast furnace sinter, with a special focus on fines generation.

14 Outlook

For a correct energy balance, investigations into breakage energy are necessary. One way to determine breakage energy is to measure fragment velocities. Alternatively, the breakage energy could be calculated as it is proportional to the creation of new surfaces, according to the Griffith criterion [64]. For this purpose, the surface energy has to be determined first.

Additional investigations regarding damage accumulation and multiple breakage are necessary in order to determine the breakage characteristics after repeated impacts. This could also be performed with the automated single particle impact tester by reloading the particles after testing.

In simple processes, where only one main damaging event occurs and the material flow after the damaging event is of minor importance, the actual breakage does not have to be simulated. The particle could also be replaced by an exact copy of the initial particle without tessellation, but with a different name corresponding to the resulting fictitious fragment size, which allows easy analysis of PSD. This would significantly decrease the computational effort.

The novel breakage model will be used to simulate the degradation of Direct Reduced Iron (DRI) pellets and Hot Briquetted Iron (HBI) in two current projects at the Chair of Mining Engineering and Mineral Economics at the University of Leoben.

The novel breakage model will be presented at the 13th International Comminution Symposium (Comminution '23) in Cape Town, South Africa, in April 2023. As usual for this conference, this paper will be invited to be submitted after the conference and, if accepted, will be published in the first available regular issue of Minerals Engineering and included in the Virtual Special Issue of the conference on ScienceDirect.

The findings regarding the solid state material driven turbine to reduce size segregation effects in storage processes will be presented at the 14th International Conference on Bulk Materials Storage, Handling and Transportation in Wollongong, Australia, in July 2023.

List of Figures

List of Tables

Bibliography

[1] Denzel, M., Prenner, M., and Sifferlinger, N. A. "Development of an automated single particle impact tester for iron ore sinter". In: *Minerals Engineering* 175 (2022), p. 107291. ISSN: 08926875. DOI: 10.1016/j.mineng.2021.107291.

[2] Denzel, M. "Partikelbruch in der Fördertechnik: Prüfmethodik und Simulation mittels Diskrete Elemente Methode". In: *Bergbau - Zeitschrift für Rohstoffgewinnung, Energie, Umwelt* 73.10 (2022), pp. 436–440.

[3] Prenner, M. and Denzel, M. "Projekt MinSiDeg". In: *Stein & Kies (Mitgliederzeitschrift - Forum mineralische Rohstoffe)* 180 (2022), p. 11.

[4] Denzel, M., Prenner, M., and Sifferlinger, N. A. "Solid State Material Driven Turbine to Reduce Segregation during Bunker Filling". In: *Berg- und Huettenmaennische Monatshefte (BHM)* 168.2 (2023). DOI: 10.1007/s00501-022-01311-6.

[5] Denzel, M. and Prenner, M. "Partikelbruchvorhersage an einem dynamischen Übergabesystem und Vergleich mit einer herkömmlichen Schurre mittels DEM (Particle breakage prediction on a dynamic transfer system and comparison with a conventional chute using DEM)". In: *BHM Berg- und Hüttenmännische Monatshefte* 167.2 (2022), pp. 66–75. ISSN: 0005-8912. DOI: 10.1007/s00501-022-01197-4.

[6] Denzel, M. and Prenner, M. "Minimierung des Sinterzerfalls mittels DEM (Minimization of Sinter Degradation with DEM)". In: *Berg- und Huettenmaennische Monatshefte (BHM)* 166.2 (2021), pp. 76–81. DOI: 10.1007/s00501-021-01081-7.

[7] Denzel, M., Prenner, M., and Sifferlinger, N. A. "A probabilistic particle replacement model to simulate bulk material degradation during conveying processes using DEM". In: *Proceedings 24th International Conference on Material Handling, Constructions and Logistics (MHCL 2022)*. Ed. by N. Zrnic, G. Kartnig, and S. Bosnjak. Belgrade, 2022, pp. 29–36. ISBN: 978-86-6060-134-8. DOI: 10.34901/mul.pub.2023.02.

[8]   Denzel, M. and Prenner, M. "Solid State Material Driven Turbine to Reduce Segregation Effects in Bunkers". In: *CHoPS 2022 - 10th International Conference on Conveying and Handling of Particulate Solids*. Salerno, Italy, 2022.

[9]   Denzel, M. "Partikelbruch in der Fördertechnik - Prüfmethodik und Simulation mittels Diskrete Elemente Methode (Particle breakage during conveying processes - Test method and simulation with the discrete element method)". In: *10. Kolloquium - Fördertechnik im Bergbau*. Ed. by O. Langefeld. Clausthal-Zellerfeld: Papierflieger Verlag GmbH, 2022, pp. 89–101. ISBN: 978-3-86948-860-8.

[10]   Eroglu, T. et al. "MinSiDeg - Minimise sinter degradation between sinter plant and blast furnace exploiting real-time analytics". In: *ESTEP Dissemination event - Beyond steel research projects* (2022).

[11]   Denzel, M. and Prenner, M. "Dynamisches Übergabesystem zur Reduktion des Partikelbruchs (Dynamic transfer system to reduce particle breakage)". In: *25. Fachtagung Schüttgutfördertechnik 2021* (2021), pp. 233–242. DOI: 10.25673/36794.

[12]   Denzel, M. "Technical State of the Art in Sinter Transportation and Storage". In: *MinSiDeg Deliverable D6.1 - Comprehensive Overview: State of the Art, Problem, Proposed Approach and Outcome* (2019), pp. 5–7.

[13]   Denzel, M., Prenner, M., and Sifferlinger, N. A. "Test Method to Determine Breakage Behaviour of Blast Furnace Sinter". In: *MinSiDeg Deliverable D1.3* (2020), pp. 1–25.

[14]   Denzel, M., Prenner, M., and Sifferlinger, N. A. "Contributions to 1st Periodic Report MinSiDeg". In: *MinSiDeg Reports* (2021).

[15]   Denzel, M., Prenner, M., and Sifferlinger, N. A. "Alternative Design Concepts for Storage Equipment for Sinter". In: *MinSiDeg Deliverable D2.2* (2021), pp. 1–11.

[16]   Denzel, M., Prenner, M., and Sifferlinger, N. A. "Alternative Design Concepts for Transport and Transfer of Sinter". In: *MinSiDeg Deliverable D2.1* (2021), pp. 1–26.

[17]   Denzel, M. and Prenner, M. "Minimization of Sinter Degradation by Means of DEM". In: *MinSiDeg-Workshop (online)* (2022).

[18]   Denzel, M. and Prenner, M. "Dynamic Transfer System to Reduce Particle Breakage". In: *MinSiDeg-Workshop (online)* (2022).

[19] Remus, R. et al. *Best available techniques (BAT) reference document for iron and steel production: Industrial emissions Directive 2010/75/EU : integrated pollution prevention and control.* Luxembourg, 2013. DOI: `10.2791/97469`. URL: `http://bookshop.europa.eu/en/best-available-techniques-bat-reference-document-for-iron-and-steel-production-pbLFNA25521/`.

[20] Marx, K. *Proposal MinSiDeg RFCS-02-2018.* 2018.

[21] Schenk, J. *Vorlesungsskriptum zu Eisen- und Stahlmetallurgie I.* 2019.

[22] ISO 11323. *Iron ore and direct reduced iron - Vocabulary.* 2010.

[23] Malysheva, T. Y. et al. "Mechanism of mineral formation and metallurgical properties of sinter of basicity 1.1–3.1 at OAO MMK". In: *Steel in Translation* 37.2 (2007), pp. 126–130. ISSN: 0967-0912. DOI: `10.3103/S0967091207020118`.

[24] Fabritius, H. and Schnabel, E. "Mechanische Eigenschaften des Stahles 8 CrMoNiNb910 in Abhängigkeit vom Gefügezustand". In: *Archiv für das Eisenhüttenwesen* 47.8 (1976), pp. 495–500. ISSN: 00038962. DOI: `10.1002/srin.197603847`.

[25] Mali, H. *Microscope pictures of blast furnace sinter.* 2020.

[26] Trenkler, H., Krieger, W., and Durrer, G. *Metallurgie des Eisens, Theorie der Stahlerzeugung.* Vol. 5. Springer-Verlag, 1978.

[27] Umadevi, T. et al. "Influence of Iron Ore Fines Feed Size on Microstructure, Productivity and Quality of Iron Ore Sinter". In: *ISIJ International* 51.6 (2011), pp. 922–929. ISSN: 0915-1559. DOI: `10.2355/isijinternational.51.922`.

[28] Fernández-González, D., Piñuela-Noval, J., and Verdeja, L. F. *Iron Ore Agglomeration Technologies.* 2017. DOI: `10.5772/intechopen.72546`.

[29] Kempken, T., Marx, K., and Hauck, T. "Technical State of the Art in Sinter Production". In: *MinSiDeg Deliverable D6.1 - Comprehensive Overview: State of the Art, Problem, Proposed Approach and Outcome.* Ed. by MinSiDeg - Consortium. 2019.

[30] Eurotherm. 27.07.2022. URL: `https://www.eurotherm.com/sv/heat-treatment-articles-sv/sintering/`.

[31] Fernández-González, D. et al. "Iron Ore Sintering: Process". In: *Mineral Processing and Extractive Metallurgy Review* 38.4 (2017), pp. 215–227. ISSN: 0882-7508. DOI: `10.1080/08827508.2017.1288115`.

[32]   Zhou, H. et al. "Effect of flame-front speed on the pisolite-ore sintering process". In: *Applied Thermal Engineering* 75 (2015), pp. 307–314. ISSN: 13594311. DOI: `10.1016/j.applthermaleng.2014.09.050`.

[33]   Loo, C. E. and Dukino, R. D. "Laboratory iron ore sintering studies. 2. Quantifying flame front properties". In: *Mineral Processing and Extractive Metallurgy* 123.4 (2014), pp. 197–203. ISSN: 0371-9553. DOI: `10.1179/1743285514Y.0000000065`.

[34]   Cores, A. et al. "The Influence of Different Iron Ores Mixtures Composition on the Quality of Sinter". In: *ISIJ International* 50.8 (2010), pp. 1089–1098. ISSN: 0915-1559. DOI: `10.2355/isijinternational.50.1089`.

[35]   Unland, E., Ventrella, G., and Jan, J. "Alternate carbon sources for sintering of iron ore (Acasos)". In: *European Commission, Directorate-General for Research and Innovation* (2013). DOI: `10.2777/58105`.

[36]   Fayed, M. E. and Skocir, T. S. *Mechanical conveyors: selection and operation.* Lancaster, PA: Technomic Pub. Co., 1997.

[37]   Sahoo, R. K. "Degradation characteristics of steel making materials during handling". In: *Powder Technology* 176.2-3 (2007), pp. 77–87. ISSN: 00325910. DOI: `10.1016/j.powtec.2007.02.013`.

[38]   Fagerberg, B. and Sandberg, N. *Degradation of lump ores in transport.* Rotterdam, NL, 1974.

[39]   Ooshima, T. et al. "Minimization of Degradation of Sintered Ore During Transportation". In: *3rd Int. Symp. on Agglomeration* (1981), pp. 1112–1124.

[40]   Kelly, S. et al. "Fine coal generation during mining and handling". In: *The Australian Coal Journal* 34 (1991), pp. 31–39.

[41]   Sahoo, R. K., Weedon, D. M., and Roach, D. "Experimental study of several factors effecting Gladstone Port Authority's lump degradation". In: *Bulk Solids Handling 22* (2002), pp. 356–361.

[42]   Sahoo, R. K. and Weedon, D. M. "Factors affecting coal degradation during handling". In: *Bulk Solids Handling 7* 22 (2002), pp. 282–288.

[43]   Sahoo, R. K., Weedon, D. M., and Roach, D. "Degradation Characteristics of Central Queensland coal". In: *4th Int. Conf. on Material Handling and Logistics Systems* (2002), pp. 426–432.

[44]   Sahoo, R. K. and Roach, D. "Degradation characteristics of coal on tumbling tests". In: *Bulk Solids Handling 23* 4 (2003), pp. 252–257.

[45] Sahoo, R. K. and Roach, D. "Degradation modelling of Central Queensland weathered coal". In: *12th Int. Conf. on Coal Science* (2003), pp. 1–10.

[46] Sahoo, R. K., Weedon, D. M., and Roach, D. "Degradation model of the Gladstone Port Authority's coal using drop tests". In: *Bulk Solids Handling 23* 2 (2003), pp. 104–109.

[47] Sahoo, R. K., Weedon, D. M., and Roach, D. "Effect of different types of impact surface on coal degradation". In: *4th Int. Conf. for Conveying and Handling of Particulate Solids* (2003), pp. 845–850.

[48] Sahoo, R. K. and Roach, D. "Degradation of Coal in a Port and Shiploading Environment". PhD Thesis. Central Queensland University, 2004.

[49] Sahoo, R. K., Weedon, D. M., and Roach, D. "Degradation model of Gladstone Port Authority's coal using a twin-pendulum apparatus". In: *Advanced Powder Technology* 15.4 (2004), pp. 459–475. ISSN: 09218831. DOI: 10.1163/1568552041270545.

[50] Sahoo, R. K. and Roach, D. "Quantification of lump coal breakage during handling operation at the Gladstone port". In: *Chemical Engineering and Processing* 44 (2005), pp. 797–804.

[51] van den Berg, T. and Villiers, J. P. R. de. "An assessment of the production of fine material in iron ore sinter". In: *Mineral Processing and Extractive Metallurgy* 118.4 (2009), pp. 214–221. ISSN: 0371-9553. DOI: 10.1179/174328509X455313.

[52] Tavares, L. M. et al. "Fracture probability and fragment size distribution of fired Iron ore pellets by impact". In: *Powder Technology* 336 (2018), pp. 546–554. ISSN: 00325910. DOI: 10.1016/j.powtec.2018.06.036.

[53] Goodwin, P. J. and Ramos, C. M. "Design of belt conveyors in bulk terminal applications". In: *Bulk Solids Handling 5* (1985), pp. 1061–1066.

[54] Goodwin, P. J. and Ramos, C. M. "Degradation of sized coal at transfer points". In: *Bulk Solids Handling 7* (1987), pp. 517–537.

[55] Teo, C. S., Waters, A. G., and Nicol, S. K. "Quantification of the breakage of lump materials during handling operations". In: *International Journal of Mineral Processing* 30.3-4 (1990), pp. 159–184. DOI: 10.1016/0301-7516(90)90013-O.

[56] Devaswithin, A. and Pitchumani, B. "An approach to study the particle degradation during impact". In: *Bulk Solids Handling 7* (1987), pp. 547–550.

[57]   Vogel, J. C. and Quass, F. W. "The friability of South African coals". In: *Journal of the Chemical, Metallurgical and Mining Society of South Africa* (1937), pp. 469–478.

[58]   T. E. Norgate, D. F. Tompsitt, and R. J. Batterham, eds. *Computer simulation of the degradation of lump ores during transportation and handling.* 1986.

[59]   Waters, A. G. and Mikka, R. A. "Segregation of fines in lump ore due to vibration on a conveyor belt". In: *3rd Int. Conf. on Bulk Materials, Storage, Handling* (1989), pp. 89–93.

[60]   Fagerberg, B. and Sandberg, N. "Degradation of lump ores in transport". In: *Proc. of 2nd Int. Symp. on Transportation and Handling of Minerals* (1973), pp. 128–156.

[61]   Waters, A. G., Vince, A., and Lister, J. D. "Measuring the strength of agglomerate materials". In: *Proc. of CHEMECA* (1986), pp. 118–123.

[62]   Waters, A. G., Vince, A., and Teo, C. S. "A technique for determining the resistance to shatter of lump materials". In: *Proc. of CHEMECA* 1071-1078 (1987).

[63]   Teo, C. S. and Waters, A. G. "The effect of drop height and particle size on the extent of degradation of agglomerates". In: *CHEMECA'88 Australian Biocentennial Int. Conf. for the Process Industries* (1988), pp. 665–670.

[64]   Griffith, A. A. "VI. The phenomena of rupture and flow in solids". In: *Philosophical Transactions of the Royal Society of London. Series A, Containing Papers of a Mathematical or Physical Character* 221.582-593 (1921), pp. 163–198. ISSN: 0264-3952. DOI: 10.1098/rsta.1921.0006.

[65]   Griffith, A. A. "The theory of rupture". In: *Proceeding 1st International Congress Applied Mechanics* (1924), pp. 55–63.

[66]   Kowalewski, M. and Gruszczynska-Jacyna, A. "Stabilisierung des Kornaufbaus von Sinter durch Stürzen". In: *Archif für das Eisenhüttenwesen 46* (1975), pp. 567–570.

[67]   Yancy, H. F. and Zane, R. E. "Comparison of methods for determining the friability of coal". In: *U.S. Bureau of Mines Report of Investigations* (1933), pp. 1–24.

[68]   Lister, J. D., Waters, A. G., and Nicol, S. K. "A quantitative measure of coke abrasion". In: *Transaction of the Iron and Steel Institute of Japan* 26 (1986), pp. 704–709.

[69]   Lister, J. D., Waters, A. G., and Nicol, S. K. "Coke degradation by surface breakage in a modified tumble drum". In: *Transaction of the Iron and Steel Institute of Japan* 27 (1987), pp. 3–9.

[70]   Cavalcanti, P. P. et al. "Surface breakage of fired iron ore pellets by impact". In: *Powder Technology* 342 (2019), pp. 735–743. ISSN: 00325910. DOI: `10.1016/j.powtec.2018.10.044`.

[71]   Hocke, H. and Jones, K. T. "Factors affecting the degradation of sinter at a belt conveyor transfer point". In: *Iron and Steel* (1968), pp. 335–340.

[72]   Ramos, C. M. "The real cost of coal degradation". In: *Bulk Solids Handling 12* (1992), pp. 63–67.

[73]   Roberts, A. W. "The dynamics of granular material flow through curved chutes". In: *Mech. Eng. Tran* (1969).

[74]   Kessler, F. and Prenner, M. "DEM - Simulation of Conveyor Transfer Chutes". In: *FEM Transactions* 4.37 (2009), pp. 185–192.

[75]   Nordell, L. K. "Palabora installs curved transfer chute in hard rock to minimize belt cover wear". In: *Bulk Solids Handling 14* 4 (1994), pp. 739–743.

[76]   Nordell, L. K. "Partilce flow modeling: Transfer chutes and other applications". In: *Proc. of the BELTCON 9 International Material Handling Conference* (1997).

[77]   Qiu, X. and Kruses, D. "Design of conveyor chute using discrete element method". In: *Proceedings of the 4th U.S. National Congress on Computational Mechanics* (1997).

[78]   Herzog, M. "Untersuchungen zur Verbesserung der Schüttgutübergabe zwischen Gurtbandförderern". PhD Thesis. TU Dresden, 1999.

[79]   Roberts, A. W. et al. "Flow dynamics and wear considerations in transfer chute design". In: *Proc. of the ICBMH'04 - 8th Internantional Conference on Bulk Materials Storage, Handling & Transportation* (2004).

[80]   Kisters, P. and Gröger, T. "Modifikation einer Übergabeschurre zur Staubreduzierung mit Hilfe der Diskrete Elemente Simulation". In: *10. Fachtagung Schüttgutfördertechnik* (2005).

[81]   Zhao, D. et al. "Three–dimensional discrete element simulation for granular materials". In: *Engineering Computations* 23.7 (2006), pp. 749–770. ISSN: 0264-4401. DOI: `10.1108/02644400610689884`.

[82] Tripathi, A. et al. "Quantitative DEM simulation of pellet and sinter particles using rolling friction estimated from image analysis". In: *Powder Technology* 380 (2021), pp. 288–302. ISSN: 00325910. DOI: `10.1016/j.powtec.2020.11.024`.

[83] Agarwal, A. et al. "Rolling friction measurement of slightly non-spherical particles using direct experiments and image analysis". In: *Granular Matter* 23.3 (2021). ISSN: 1434-5021. DOI: `10.1007/s10035-021-01124-3`.

[84] Chakrabarty, A. et al. "Characterisation of binary mixtures of pellets and sinter for DEM simulations". In: *Advanced Powder Technology* 33.1 (2022), p. 103358. ISSN: 09218831. DOI: `10.1016/j.apt.2021.11.010`.

[85] Rossow, J. and Coetzee, C. J. "Discrete element modelling of a chevron patterned conveyor belt and a transfer chute". In: *Powder Technology* 391 (2021), pp. 77–96. ISSN: 00325910. DOI: `10.1016/j.powtec.2021.06.012`.

[86] Kukreja, K. et al. "Development of transfer chute design through Discrete Element Modelling for using Refused Derived fuel in Indian cement plants". In: *Sustainable Energy Technologies and Assessments* 53 (2022), p. 102567. ISSN: 22131388. DOI: `10.1016/j.seta.2022.102567`.

[87] Ilic, D. "Development of design criteria for reducing wear in iron ore transfer chutes". In: *Wear* 434-435 (2019), p. 202986. ISSN: 00431648. DOI: `10.1016/j.wear.2019.202986`.

[88] Ilic, D. et al. "Modelling bulk solid flow interactions in transfer chutes: Shearing flow". In: *Powder Technology* 354 (2019), pp. 30–44. ISSN: 00325910. DOI: `10.1016/j.powtec.2019.05.058`.

[89] Ilic, D., Roberts, A., and Wheeler, C. "Modelling bulk solid interactions in transfer chutes: Accelerated flow". In: *Chemical Engineering Science* 209 (2019), p. 115197. ISSN: 00092509. DOI: `10.1016/j.ces.2019.115197`.

[90] Chakrabarty, A. et al. "Model Study of Centre Coke Charging in Blast Furnace through DEM Simulations". In: *ISIJ International* 61.3 (2021), pp. 782–791. ISSN: 0915-1559. DOI: `10.2355/isijinternational.ISIJINT-2020-498`.

[91] Mio, H. et al. "Validation of Particle Size Segregation of Sintered Ore during Flowing through Laboratory-scale Chute by Discrete Element Method". In: *ISIJ International* 48.12 (2008), pp. 1696–1703. ISSN: 0915-1559. DOI: `10.2355/isijinternational.48.1696`.

[92] Nistala, S. H. et al. "Study of generation of sinter return fines during transportation". In: *Ironmaking & Steelmaking* 42.3 (2015), pp. 226–232. ISSN: 0301-9233. DOI: 10.1179/1743281214Y.0000000224.

[93] Öfner, W. and Zaunrith, G. "The Drop Weight Test Revisited: Characterization of the Crushability of Hot Sinter and Validation of the Approach with Natural Rocks". In: *BHM Berg- und Hüttenmännische Monatshefte* 161.6 (2016), pp. 277–282. ISSN: 0005-8912. DOI: 10.1007/s00501-016-0501-7.

[94] Hibbeler, R. C. *Technische Mechanik 3 - Dynamik*. 12th ed. Pearson Deutschland GmbH, 2012. ISBN: ISBN 978-3-86894-127-2.

[95] Richard, H. A. and Sander, M. *Technische Mechanik -Dynamik*. 1st ed. Vieweg, 2008. ISBN: 978-3-528-03995-0.

[96] Schönert, K. "Aufbereit.-Tech. 32". In: (1991).

[97] Tavares, L. M. and King, R. P. "ZKG Int. 58". In: (2005).

[98] Tavares, L. M. "Breakage of Single Particles: Quasi-Static". In: *Handbook of Powder Technology* 12 (2007), pp. 3–68. DOI: 10.1016/S0167-3785(07)12004-2.

[99] Tavares, L. and King, R. "Single-particle fracture under impact loading". In: *International Journal of Mineral Processing* 54.1 (1998), pp. 1–28. DOI: 10.1016/S0301-7516(98)00005-2.

[100] Hertz, H. "Ueber die Beruehrung fester elastischer Koerper". In: *Jornal fuer die reine und angewandte Mathematik* 92 (1881), pp. 156–171.

[101] Zehnder, A. T. "Griffith Theory of Fracture". In: (2013), pp. 1570–1573. DOI: 10.1007/978-0-387-92897-5{\textunderscore}259.

[102] Anderson, T. L. *Fracture mechanics Fundamentals and applications*. 2. ed. Boca Raton, Fla.: CRC Press, 1995. ISBN: 0-8493-4260-0.

[103] Kotzur, B. A. et al. "Particle attrition mechanisms, their characterisation, and application to horizontal lean phase pneumatic conveying systems: A review". In: *Powder Technology* 334 (2018), pp. 76–105. ISSN: 00325910. DOI: 10.1016/j.powtec.2018.04.047.

[104] ASTM. *D3402 - Standard Test Method for Tumbler Test for Coke*. 2016.

[105] JIS. *K2151 Coke - Testing methods*. 2018.

[106] ISO 556:2020. *Coke (greater than 20 mm in size) - Determination of mechanical strength*. 2020.

[107] Wills, B. A. and Napier-Munn, T. J. *Mineral processing technology*. 2006.

[108] Korman, T. et al. "Impact of physical and mechanical properties of rocks on energy consumption of jaw crusher: Physicochemical Problems of Mineral Processing; ISSN 2083-3989". In: (2015). DOI: 10.5277/ppmp150208.

[109] Böhm, A., Mayerhofer, R., and Öfner, W. *Energy for rock breakage*. 2016.

[110] Gupta, A. K. and Yan, D. "Jaw Crusher". In: *Mineral Processing Design and Operations* 2 (2016), pp. 123–152. DOI: 10.1016/B978-0-444-63589-1.00004-6.

[111] Barnard, W. J. and Bull, F. A. "Primary breakage of brittle particles". In: *Fourth Tewksbury Symposium, University of Melbourne* (1979), p. 20.

[112] ASTM. "Standard drop shatter test for coal". In: *Annual Book of ASTM Standards* 5 (1991), p. 214.

[113] Tavares, L. M. and Diniz, R. R. "Analysis of self-breakage for modelling media competence in autogenous mills". In: *Proc. VI Southern Hemisphere Meeting on Mineral Technology, Rio de Janeiro* 1 (2001), p. 47.

[114] Dan, C. C. and Schubert, H. "Aufbereit.-Tech." In: 31 (1990), p. 241.

[115] Schönert, K. and Markstscheffel, M. "Liberation of composite particles by single particle compression, shear and impact loading". In: *Proceedings of the 6th European Symposium Comminution* (1986).

[116] Jowett, A. and Weller K.R. "A critical assessment of comminution test methods". In: *Fourth Tewksbury Symposium, University of Melbourne* (1979), p. 18.

[117] Narayanan, S. S. and Bull, F. A. In: *Proc. Australas. Inst. Min. Metall.* 291.49 (1986).

[118] Mwanga, A., Rosenkranz, J., and Lamberg, P. "Testing of Ore Comminution Behavior in the Geometallurgical Context—A Review". In: *Minerals* 5.2 (2015), pp. 276–297. DOI: 10.3390/min5020276.

[119] Morrell, S. "A method for predicting the specific energy requirement of comminution circuits and assessing their energy utilisation efficiency". In: *Minerals Engineering* 21.3 (2008), pp. 224–233. ISSN: 08926875. DOI: 10.1016/j.mineng.2007.10.001.

[120] Bearman, R. A., Briggs, C. A., and Kojovic, T. "The applications of rock mechanics parameters to the prediction of comminution behaviour". In: *Minerals Engineering* 10.3 (1997), pp. 255–264. ISSN: 08926875. DOI: 10.1016/S0892-6875(97)00002-2.

[121] Napier-Munn, T. J. *Mineral comminution circuits: Their operation and optimisation.* Repr. with minor corr. Vol. 2. JKMRC monograph series in mining and mineral processing. Indooroopilly, Queensland: Julius Kruttschnitt Mineral Research Centre, 2005. ISBN: 064628861X.

[122] Genc, Ö. "An investigation on single-particle impact breakage functions of gold ore by drop-weight technique". In: *Bulletin Of The Mineral Research and Exploration* 0.154 (2016). ISSN: 0026-4563. DOI: 10.19111/bmre.78208.

[123] Geng, B. et al. "Experimental study on fabrication and impact characteristics of PTFE/Al/W reactive materials with different molding pressures". In: *Journal of Physics: Conference Series* 1507.6 (2020), p. 062002. ISSN: 1742-6588. DOI: 10.1088/1742-6596/1507/6/062002.

[124] Quist, J. and Evertsson, C. M. "Cone crusher modelling and simulation using DEM". In: *Minerals Engineering* 85 (2016), pp. 92–105. ISSN: 08926875. DOI: 10.1016/j.mineng.2015.11.004.

[125] Narayanan, S. S. and Whiten, W. J. "Breakage characterization of ores for ball mill modelling". In: *Proc. AusIMM* 286 (1983), pp. 31–39.

[126] Eksi, D. et al. "A new method for determination of fine particle breakage". In: *Minerals Engineering* 24.3-4 (2011), pp. 216–220. ISSN: 08926875. DOI: 10.1016/j.mineng.2010.08.006.

[127] King, R. P. and Bourgeois, F. "Measurement of fracture energy during single-particle fracture". In: *Minerals Engineering* 6.4 (1993), pp. 353–367. ISSN: 08926875.

[128] Tavares, L. M. "Energy absorbed in breakage of single particles in drop weight testing". In: *Minerals Engineering* 12.1 (1999), pp. 43–50. ISSN: 08926875. DOI: 10.1016/S0892-6875(98)00118-6.

[129] Bourgeois, F. and Banini, G. A. "A portable load cell for in-situ ore impact breakage testing". In: *Int. J. Miner. Process.* 65 (2012), pp. 31–54.

[130] Abel, F., Rosenkranz, J., and Kuyumcu, H. Z. "Stamped coal cakes in cokemaking technology: Part 1 – A parameter study on stampability". In: *Ironmaking & Steelmaking* 36.5 (2009), pp. 321–326. ISSN: 0301-9233. DOI: 10.1179/174328109X407112.

[131] Narayanan, S. S. "Development of a laboratory single particle breakage technique and its application to ball mill modelling and scale-up". PhD Thesis. The University of Queensland, 1985.

[132] Bond, F. C. "Crushing Tests by Pressure and Impact". In: *Trans. AIME* 169 (1946), pp. 58–65.

[133]   Bond, F. C. "Third Theory of Comminution". In: *Min. Eng. Trans. Aime* 193 (1952), pp. 484–494.

[134]   Bond, F. C. "Crushing and Grinding Calculations". In: *Allis Chalmers Manufacturing Co.* (1961).

[135]   Tavares, L. M. and Carvalho, R. M. "Impact work index prediction from continuum damage model of particle fracture". In: *Minerals Engineering* 20.15 (2007), pp. 1368–1375. ISSN: 08926875. DOI: `10.1016/j.mineng.2007.08.021`.

[136]   Weedon, D. M. and Wilson, F. "Modelling Iron Ore Degradation Using a Twin Pendulum Breakage Device". In: *Int. J. Miner. Process.* 59 (2000), pp. 195–213.

[137]   Hopkinson, B. "A method of measuring the pressure produced in the detonation of high, explosives or by the impact of bullets". In: *Philosophical Transactions of the Royal Society of London. Series A, Containing Papers of a Mathematical or Physical Character* 213.497-508 (1914), pp. 437–456. ISSN: 0264-3952. DOI: `10.1098/rsta.1914.0010`.

[138]   Fandrich, R., Clout, J., and Bourgeois, F. "The CSIRO Hopkinson Bar Facility for large diameter particle breakage". In: *Minerals Engineering* 11.9 (1998), pp. 861–869. ISSN: 08926875. DOI: `10.1016/S0892-6875(98)00073-9`.

[139]   Brown, G. J., Miles, N. J., and Jones, T. F. "A fractal description of the progeny of single impact single particle breakage". In: *Minerals Engineering* 9.7 (1996), pp. 715–726. ISSN: 08926875. DOI: `10.1016/0892-6875(96)00063-5`.

[140]   Brown G.J., M. N. *Applied fractal geometry in impact pulverization.* San Francisco, 1995.

[141]   Meier, M. et al. "Characterization of the grinding behaviour in a single particle impact device: studies on pharmaceutical powders". In: *European journal of pharmaceutical sciences : official journal of the European Federation for Pharmaceutical Sciences* 34.1 (2008), pp. 45–55. ISSN: 0928-0987. DOI: `10.1016/j.ejps.2008.02.120`.

[142]   Cavalcanti, P. P. et al. "Modeling of degradation by impact of individual iron ore pellets". In: *Powder Technology* 378 (2021), pp. 795–807. ISSN: 00325910. DOI: `10.1016/j.powtec.2020.10.037`.

[143] Shi, F. et al. "Development of a rapid particle breakage characterisation device – The JKRBT". In: *Minerals Engineering* 22.7-8 (2009), pp. 602–612. ISSN: 08926875. DOI: `10.1016/j.mineng.2009.05.001`.

[144] Vogel, L. and Peukert, W. "Breakage behaviour of different materials—construction ofa mastercurve for the breakage probability [Vogel, Peukert]". In: *Powder Technology* 129 (2003). ISSN: 00325910. DOI: `10.1016/S0032-5910(02)00217-6`.

[145] Zuo, W. and Shi, F. "Ore impact breakage characterisation using mixed particles in wide size range". In: *Minerals Engineering* 86 (2016), pp. 96–103. ISSN: 08926875. DOI: `10.1016/j.mineng.2015.12.007`.

[146] Hiramatsu, Y. and Oka, Y. "Determination of the tensile strength of rock by a compression test of an irregular test piece". In: *International Journal of Rock Mechanics and Mining Sciences & Geomechanics Abstracts* 3.2 (1966), pp. 89–90. ISSN: 01489062. DOI: `10.1016/0148-9062(66)90002-7`.

[147] Russell, A. R. and Muir Wood, D. "Point load tests and strength measurements for brittle spheres". In: *International Journal of Rock Mechanics and Mining Sciences* 46.2 (2009), pp. 272–280. ISSN: 13651609. DOI: `10.1016/j.ijrmms.2008.04.004`.

[148] Rusnak, J. and Mark, C. "Using the point load test to determine the uniaxial compressive strength of coal measure rock". In: *Proceedings of the 19th International Conference on Ground Control in Mining* (2000), pp. 362–371.

[149] Li, D. and Wong, L. "The Brazilian Disc test for Rock Mechanics Applications: Review and New Insights." In: *Rock Mech. Rock Eng.* 46 (2013), pp. 269–287.

[150] Ghadiri, M. and Zhang, Z. "Impact attrition of particulate solids. Part 1: A theoretical model of chipping". In: *Chemical Engineering Science* 57.17 (2002), pp. 3659–3669. ISSN: 00092509. DOI: `10.1016/S0009-2509(02)00240-3`.

[151] Kolmogorov, A. N. In: *Dokl. Akad. Nauk.* 31.99 (1941).

[152] Dacey, M. F. and Krumbein, W. C. "Models of breakage and selection for particle size distributions". In: *Journal of the International Association for Mathematical Geology* 11.2 (1979), pp. 193–222. ISSN: 0020-5958. DOI: `10.1007/BF01028965`.

[153]   Epstein, B. "The mathematical description of certain breakage mechanisms leading to the logarithmico-normal distribution". In: *Journal of the Franklin Institute* 244.6 (1947), pp. 471–477. ISSN: 00160032. DOI: `10.1016/0016-0032(47)90465-1`.

[154]   Camalan, M. "A computational algorithm for random particle breakage". In: *Physica A: Statistical Mechanics and its Applications* 602 (2022), p. 127640. ISSN: 03784371. DOI: `10.1016/j.physa.2022.127640`.

[155]   Halmos, P. R. "Random alms". In: *Ann. Math. Stat.* 15 (1944), pp. 182–189.

[156]   Epstein, B. "Logarithmico-Normal Distribution in Breakage of Solids". In: *Industrial & Engineering Chemistry* 40.12 (1948), pp. 2289–2291. ISSN: 0019-7866. DOI: `10.1021/ie50468a014`.

[157]   Austin, J. B. "Methods of representing distribution of particle size". In: *Industrial & Engineering Chemistry Analytical Edition* 11.6 (1939), pp. 334–339. ISSN: 0096-4484. DOI: `10.1021/ac50134a014`.

[158]   Steiner, G., Patel, M., and Carstensen, J. T. "Effects of milling on granulation particle-size distribution". In: *Journal of pharmaceutical sciences* 63.9 (1974), pp. 1395–1398. ISSN: 0022-3549. DOI: `10.1002/jps.2600630913`.

[159]   Mehta, A., Zoglio, M. A., and Carstensen, J. T. "Ball milling as a measure of crushing stength of granules". In: *Journal of pharmaceutical sciences* 67.7 (1978), pp. 905–908. ISSN: 0022-3549. DOI: `10.1002/jps.2600670708`.

[160]   Hajratwala, B. R. "Particle size reduction by a hammer mill I: Effect of output screen size, feed particle size, and mill speed". In: *Journal of pharmaceutical sciences* 71.2 (1982), pp. 188–190. ISSN: 0022-3549. DOI: `10.1002/jps.2600710212`.

[161]   Motzi, J. J. and Anderson, N. R. "The Quantitative Evaluation of a Granulation Milling Process II. Effect of Ouput Screen Size, Mill Speed and Impeller Shape". In: *Drug Development and Industrial Pharmacy* 10.5 (1984), pp. 713–728. ISSN: 0363-9045. DOI: `10.3109/03639048409040779`.

[162]   Delebarre, A., Leroy, J., and Negro, P. "Mechanical strength characterization of feed materials used in iron-making industry by Epstein theory". In: *Powder Technology* 105.1-3 (1999), pp. 95–105. ISSN: 00325910. DOI: `10.1016/S0032-5910(99)00123-0`.

[163]   Iliev, P. S., Wittel, F. K., and Herrmann, H. J. "Evolution of fragment size distributions from the crushing of granular materials". In: *Physical review. E* 99.1-1 (2019), p. 012904. DOI: `10.1103/PhysRevE.99.012904`.

[164] Weibull, W. "A Statistical Distribution Function of Wide Applicability". In: *Journal of Applied Mechanics* 9 (1951), pp. 293–297.

[165] Sullivan, J. D. and Lauzon, P. H. "Experimental probability estimators for Weibull plots". In: *J. Mater. Sci. Lett.* 5 (1986), pp. 1245–1247.

[166] Weichert, R. "Fracture physics in comminution". In: *Proc. 7th Eur. Symp. Comminution* 1 (1990), pp. 3–20.

[167] Weichert, R. "Anwendung von Fehlstellenstatistik und Bruchmechanik zur Beschreibung von Zerkleinerungsvorgängen". In: *Zement-Kalk-Gips* 45 (1992), pp. 1–8.

[168] McDowell, G. R. and Amon, A. "The Application of Weibull Statistics to the Fracture of Soil Particles". In: *Soils and Foundations* 40.5 (2000), pp. 133–141. ISSN: 00380806. DOI: `10.3208/sandf.40.5{\textunderscore}133`.

[169] Huang, J. et al. "Size effect on the compression breakage strengths of glass particles". In: *Powder Technology* 268 (2014), pp. 86–94. ISSN: 00325910. DOI: `10.1016/j.powtec.2014.08.037`.

[170] Rumpf, H. "Physical aspects of comminution and new formulation of a law of comminution". In: *Powder Technology* 7.3 (1973), pp. 145–159. ISSN: 00325910. DOI: `10.1016/0032-5910(73)80021-X`.

[171] Vogel, L. and Peukert, W. "Determination of material properties relevant to grinding by practicable labscale milling tests". In: *International Journal of Mineral Processing* 74 (2004), S329–S338. DOI: `10.1016/j.minpro.2004.07.018`.

[172] Vogel, L. and Peukert, W. "From single particle impact behaviour to modelling of impact mills". In: *Chemical Engineering Science* 60.18 (2005), pp. 5164–5176. ISSN: 00092509. DOI: `10.1016/j.ces.2005.03.064`.

[173] Gildemeister, H. H. "Spannungszustände und Bruchphänomene in Prallbeanspruchten Kugeln". Dissertation. Universität Karlsruhe, 1976.

[174] Narayanan, S. S. and Whiten, W. J. "Determination of comminution characteristics from single particle breakage tests and its application to ball mill scale-up". In: *Trans. Inst. Min. Metall. Sect. C Miner. Process. Extr. Metall* 97 (1988), pp. 115–124.

[175] Pauw, O. G. and Maré, M. S. "The determination of optimum impact-breakage routes for an ore". In: *Powder Technology* 54.1 (1988), pp. 3–13. ISSN: 00325910. DOI: `10.1016/0032-5910(88)80043-3`.

[176] Shi, F. and Kojovic, T. "Validation of a model for impact breakage incorporating particle size effect". In: *International Journal of Mineral Processing* 82.3 (2007), pp. 156–163. DOI: 10.1016/j.minpro.2006.09.006.

[177] King, R. P. *Modeling and simulation of mineral processing systems.* Boston: Butterworth-Heinemann, 2001. ISBN: 978-0-08-051184-9.

[178] Tavares, L. "Optimum routes for particle breakage by impact". In: *Powder Technology* 142.2-3 (2004), pp. 81–91. ISSN: 00325910. DOI: 10.1016/j.powtec.2004.03.014.

[179] Ballantyne, G. R., Bonfils, B., and Powell, M. S. "Evolution of impact breakage characterisation: Re-defining t-family relationship". In: *International Journal of Mineral Processing* 168 (2017), pp. 126–135. DOI: 10.1016/j.minpro.2017.10.001.

[180] Carvalho, R. M., Secchi, A. R., and Tavares, L. M. "A new breakage function model and optimization procedure for mechanistic comminution models". In: *14th Eur. Symp. Commin. Classif.* (2015), pp. 42–45.

[181] Tavares, L. M. "Approaches to Deploy Breakage in Conjunction to the Discrete Element Method". In: *ATCx - Altair Technology Conference on the Discrete Element Method* (2022).

[182] Baumgardt, S. et al. "On the comparison of results in single grain crushing under different kinds of load". In: *Proc. 11th Int. Miner. Process. Congr.* (1975), pp. 3–32.

[183] Tavares, L. and King, R. "Modeling of particle fracture by repeated impacts using continuum damage mechanics". In: *Powder Technology* 123.2-3 (2002), pp. 138–146. ISSN: 00325910. DOI: 10.1016/S0032-5910(01)00438-7.

[184] Tavares, L. M. "Analysis of particle fracture by repeated stressing as damage accumulation". In: *Powder Technology* 190.3 (2009), pp. 327–339. ISSN: 00325910. DOI: 10.1016/j.powtec.2008.08.011.

[185] Tavares, L. M. and Carvalho, R. M. de. "Modeling breakage rates of coarse particles in ball mills". In: *Minerals Engineering* 22.7-8 (2009), pp. 650–659. ISSN: 08926875. DOI: 10.1016/j.mineng.2009.03.015.

[186] Tavares, L. M. and Carvalho, R. M. de. "Modeling ore degradation during handling using continuum damage mechanics". In: *International Journal of Mineral Processing* 101.1-4 (2011), pp. 21–27. DOI: 10.1016/j.minpro.2010.07.008.

[187]   Alder, B. J. and Wainwright, T. E. "Studies in Molecular Dynamics. I. General Method". In: *The Journal of Chemical Physics* 31.2 (1959), pp. 459–466. ISSN: 0021-9606. DOI: `10.1063/1.1730376`.

[188]   Cundall, P. A. and Strack, O. D. L. "A discrete numerical model for granular assemblies". In: *Géotechnique* 29.1 (1979), pp. 47–65. ISSN: 0016-8505. DOI: `10.1680/geot.1979.29.1.47`.

[189]   Becker, A. *Becker 3D Three Particle - Showcase.* URL: `https://www.becker3d.com/showcase`.

[190]   Gingold, R. A. and Monaghan, J. J. "Smoothed particle hydrodynamics: theory and application to non-spherical stars". In: *Monthly Notices of the Royal Astronomical Society* 181.3 (1977), pp. 375–389. ISSN: 0035-8711. DOI: `10.1093/mnras/181.3.375`.

[191]   Lucy, L. B. "A numerical approach to the testing of the fission hypothesis". In: *The Astronomical Journal* 82 (1977), p. 1013. ISSN: 00046256. DOI: `10.1086/112164`.

[192]   Jiménez-Herrera, N., Barrios, G. K., and Tavares, L. M. "Comparison of breakage models in DEM in simulating impact on particle beds". In: *Advanced Powder Technology* 29.3 (2017), pp. 692–706. ISSN: 09218831. DOI: `10.1016/j.apt.2017.12.006`.

[193]   Altair Engineering Inc. *What is DEM - Theoretical background behind the Discrete Element Method (DEM).* 2021.

[194]   Mio, H. et al. "Optimum Cell Size for Contact Detection in the Algorithm of the Discrete Element Method". In: *JOURNAL OF CHEMICAL ENGINEERING OF JAPAN* 38.12 (2005), pp. 969–975. ISSN: 0021-9592. DOI: `10.1252/jcej.38.969`.

[195]   Platzer, F. and Fimbinger, E. "Modelling Pasty Material Behaviour Using the Discrete Element Method". In: *Multiscale Science and Engineering* 3.2 (2021), pp. 119–128. ISSN: 2524-4515. DOI: `10.1007/s42493-021-00064-7`.

[196]   Platzer, F. and Fimbinger, E. "Polynomisches Kontaktmodell zur Abbildung pastösen Materialverhaltens in DEM-Simulationen". In: *BHM Berg- und Hüttenmännische Monatshefte* 167.2 (2022), pp. 61–65. ISSN: 0005-8912. DOI: `10.1007/s00501-022-01200-y`.

[197]   Mitterlehner, T. and Kartnig, G. "DEM modelling of charging and discharging cycles in packed bed thermal energy storage". In: *Verein Netzwerk Logistik, Logistik Werkstatt Graz* (2019), pp. 155–174.

[198] Mitterlehner, T., Kartnig, G., and Haider, M. "Analysis of the thermal ratcheting phenomenon in packed-bed thermal energy storage using Discrete Element Method". In: *FME Transactions* 48.2 (2020), pp. 427–431. ISSN: 1451-2092. DOI: 10.5937/fme2002427M.

[199] Johnson, K., Kendall, K., and Roberts, A. D. "Surface energy and the contact of elastic solids". In: *Proceedings of the Royal Society of London. A. Mathematical and Physical Sciences* 324.1558 (1971), pp. 301–313. ISSN: 0080-4630. DOI: 10.1098/rspa.1971.0141.

[200] DEMSolutions. *EDM 2.6 Theory Reference Guide*. 2014.

[201] Becker, A. *ThreeParticle API Guide*. 2022.

[202] Lungfield, A. "Ermittlung von Belastungsgrössen mittels der Diskrete-Elemente-Methode für die Auslegung von Sturzmühlen". PhD thesis. TU Freiberg, 2002.

[203] Rayleigh. "On Waves Propagated along the Plane Surface of an Elastic Solid". In: *Proceedings of the London Mathematical Society* s1-17.1 (1885), pp. 4–11. ISSN: 00246115. DOI: 10.1112/plms/s1-17.1.4.

[204] O'Sullivan, C. and Bray, J. D. "Selecting a suitable time step for discrete element simulations that use the central difference time integration scheme". In: *Engineering Computations* 21.2/3/4 (2004), pp. 278–303. ISSN: 0264-4401. DOI: 10.1108/02644400410519794.

[205] Fimbinger, E. "A Methodology for Dynamic Belt Simulation". PhD thesis. Montanuniversität Leoben - University of Leoben, 2021. DOI: 10.34901/mul.pub.2021.3.

[206] Mindlin, R. D. "Compliance of Elastic Bodies in Contact". In: *Journal of Applied Mechanics* 16.3 (1949), pp. 259–268. DOI: 10.1115/1.4009973.

[207] Mindlin, R. D. and Deresiewicz, H. "Elastic Spheres in Contact Under Varying Oblique Forces". In: *Journal of Applied Mechanics* 20.3 (1953), pp. 327–344. DOI: 10.1115/1.4010702.

[208] Tsuji, Y., Tanaka, T., and Ishida, T. "Lagrangian numerical simulation of plug flow of cohesionless particles in a horizontal pipe". In: *Powder Technology* 71.3 (1992), pp. 239–250. ISSN: 00325910. DOI: 10.1016/0032-5910(92)88030-L.

[209] Sakaguchi, H., OZAKI, E., and IGARASHI, T. "Plugging of the Flow of Granular Materials during the Discharge from a Silo". In: *International Journal of Modern Physics B* 07.09n10 (1993), pp. 1949–1963. ISSN: 0217-9792. DOI: 10.1142/S0217979293002705.

[210]   Ai, J. et al. "Assessment of rolling resistance models in discrete element simulations". In: *Powder Technology* 206.3 (2011), pp. 269–282. ISSN: 00325910. DOI: 10.1016/j.powtec.2010.09.030.

[211]   Cunha, E. R., Carvalho, R. M. de, and Tavares, L. M. "Simulation of solids flow and energy transfer in a vertical shaft impact crusher using DEM". In: *Minerals Engineering* 43-44 (2013), pp. 85–90. ISSN: 08926875. DOI: 10.1016/j.mineng.2012.09.003.

[212]   Tavares, L. M. "Review and Further Validation of a Practical Single-Particle Breakage Model". In: *KONA Powder and Particle Journal* 39.0 (2022), pp. 62–83. ISSN: 0288-4534. DOI: 10.14356/kona.2022012.

[213]   Carvalho, R. M. and Tavares, L. M. "A mechanistic model of SAG mills". In: *28th IMPC* 1-12 (2014).

[214]   Potyondy, D. O. and Cundall, P. A. "A bonded-particle model for rock". In: *International Journal of Rock Mechanics and Mining Sciences* 41.8 (2004), pp. 1329–1364. ISSN: 13651609. DOI: 10.1016/j.ijrmms.2004.09.011.

[215]   Antonyuk, S. et al. "Impact breakage of spherical granules: Experimental study and DEM simulation". In: *Chemical Engineering and Processing: Process Intensification* 45.10 (2006), pp. 838–856. ISSN: 02552701. DOI: 10.1016/j.cep.2005.12.005.

[216]   Timoshenko, S. P. "LXVI. On the correction for shear of the differential equation for transverse vibrations of prismatic bars". In: *The London, Edinburgh, and Dublin Philosophical Magazine and Journal of Science* 41.245 (1921), pp. 744–746. ISSN: 1941-5982. DOI: 10.1080/14786442108636264.

[217]   Timoshenko, S. P. "X. On the transverse vibrations of bars of uniform cross-section". In: *The London, Edinburgh, and Dublin Philosophical Magazine and Journal of Science* 43.253 (1922), pp. 125–131. ISSN: 1941-5982. DOI: 10.1080/14786442208633855.

[218]   Elishakoff, I. "Who developed the so-called Timoshenko beam theory?" In: *Mathematics and Mechanics of Solids* 25.1 (2020), pp. 97–116. ISSN: 1081-2865. DOI: 10.1177/1081286519856931.

[219]   Weerasekara, N. S. et al. "The contribution of DEM to the science of comminution". In: *Powder Technology* 248 (2013), pp. 3–24. ISSN: 00325910. DOI: 10.1016/j.powtec.2013.05.032.

[220] Tan, Y., Yang, D., and Sheng, Y. "Discrete element method (DEM) modeling of fracture and damage in the machining process of polycrystalline SiC". In: *Journal of the European Ceramic Society* 29.6 (2009), pp. 1029–1037. ISSN: 09552219. DOI: `10.1016/j.jeurceramsoc.2008.07.060`.

[221] Kafui, K. and Thornton, C. "Numerical simulations of impact breakage of a spherical crystalline agglomerate". In: *Powder Technology* 109.1-3 (2000), pp. 113–132. ISSN: 00325910. DOI: `10.1016/S0032-5910(99)00231-4`.

[222] Metzger, M. J. and Glasser, B. J. "Numerical investigation of the breakage of bonded agglomerates during impact". In: *Powder Technology* 217 (2012), pp. 304–314. ISSN: 00325910. DOI: `10.1016/j.powtec.2011.10.042`.

[223] Khanal, M., Schubert, W., and Tomas, J. "Oblique Impact Simulations of High Strength Agglomerates". In: *Micro-Macro-Interactions* (2008), pp. 243–253. DOI: `10.1007/978-3-540-85715-0{\textunderscore}19`.

[224] Khanal, M. and Tomas, J. "Oblique impact simulations of high strength agglomerates". In: *Advanced Powder Technology* 20.2 (2009), pp. 150–157. ISSN: 09218831. DOI: `10.1016/j.apt.2008.06.001`.

[225] Metzger, M. J. and Glasser, B. J. "Simulation of the breakage of bonded agglomerates in a ball mill". In: *Powder Technology* 237 (2013), pp. 286–302. ISSN: 00325910. DOI: `10.1016/j.powtec.2012.12.006`.

[226] Patwa, A., Ambrose, R. K., and Casada, M. "Discrete element method as an approach to model the wheat milling process". In: *Powder Technology* 302 (2016), pp. 350–356. ISSN: 00325910. DOI: `10.1016/j.powtec.2016.08.052`.

[227] Quist, J. C. E. "DEM modelling and simulation of cone crushers and high pressure grinding rolls". PhD thesis. Chalmers tekniska högskola, 2017.

[228] Platzer, F. and Fimbinger, E. "Simulation of complex-shaped particle breakage using the Discrete Element Method". In: *Conference: 16. International Conference on Discrete Multiphysics, Modelling Complex Systems with Particle Methods and Discrete Element Method At: Stockholm, Sweden, ISNN: 1307-6892* (2022).

[229] Fimbinger, E. "Simulation von Fördergurten mittels der DEM". In: *8. Kolloquium Fördertechnik im Bergbau.* Ed. by O. Langefeld. Clausthal-Zellerfeld: Papierflieger Verlag GmbH, 2018, pp. 121–133. ISBN: 978-3-86948-621-5.

[230] Fimbinger, E. "Methodology for the Simulation of Conveyor Belts using the Discrete Element Method". In: *A world of engineering simulation.* Hamilton, United Kingdom: NAFEMS Ltd, 2019, pp. 94–95. ISBN: 978-1-910643-52-5.

[231] Fimbinger, E. "Dynamic Conveyor Belt Simulation using the Discrete Element Method". In: *Conference proceedings / 13th International Conference on Bulk Materials Storage, Handling & Transportation (ICBMH) ; 9 - 11 July 2019, Mantra on View, Gold Coast, Queensland, Australia.* Ed. by M. Jones. Barton: Institution of Engineers Australia, 2019. ISBN: 978-1-925627-29-9.

[232] Fimbinger, E. "Berücksichtigung verformbarer Fördergurte in DEM-Simulationen". In: *BHM Berg- und Hüttenmännische Monatshefte* 166.2 (2021), pp. 82–94. ISSN: 0005-8912. DOI: `10.1007/s00501-021-01078-2`.

[233] Fimbinger, E. "Methodik zur Simulation dynamischer Gurtsysteme an Rundballenpressen mittels der DEM". In: *1. Tagung SIMULAND.* Ed. by A. Jahr and A. Batos. Düsseldorf, Germany, 2020, pp. 93–117. ISBN: 978-3-941334-30-4.

[234] Cleary, P. "Modelling comminution devices using DEM". In: *International Journal for Numerical and Analytical Methods in Geomechanics* 25.1 (2001), pp. 83–105. ISSN: 03639061. DOI: `10.1002/1096-9853(200101)25:1{\textless}83::AID-NAG120{\textgreater}3.0.CO;2-K`.

[235] Cleary, P. W. "Recent advances in dem modelling of tumbling mills". In: *Minerals Engineering* 14.10 (2001), pp. 1295–1319. ISSN: 08926875. DOI: `10.1016/S0892-6875(01)00145-5`.

[236] Barrios, G. K., Pérez-Prim, J., and Tavares, L. M. "DEM simulation of bed particle compression using the particle replacement model". In: *Proceedings 14th European Symposium on Comminution and Classification* (2015).

[237] Barrios, G. K., Jiménez-Herrera, N., and Tavares, L. M. "Simulation of particle bed breakage by slow compression and impact using a DEM particle replacement model". In: *Advanced Powder Technology* 31.7 (2020), pp. 2749–2758. ISSN: 09218831. DOI: `10.1016/j.apt.2020.05.011`.

[238] Zhou, W. et al. "Discrete element modeling of particle breakage considering different fragment replacement modes". In: *Powder Technology* 360 (2020), pp. 312–323. ISSN: 00325910. DOI: `10.1016/j.powtec.2019.10.002`.

[239] Cil, M. B. and Buscarnera, G. "DEM assessment of scaling laws capturing the grain size dependence of yielding in granular soils". In: *Granular Matter* 18.3 (2016). ISSN: 1434-5021. DOI: `10.1007/s10035-016-0638-9`.

[240] Barrios, G. K. and Tavares, L. M. "A preliminary model of high pressure roll grinding using the discrete element method and multi-body dynamics coupling". In: *International Journal of Mineral Processing* 156 (2016), pp. 32–42. DOI: 10.1016/j.minpro.2016.06.009.

[241] Cleary, P. W. and Sinnott, M. D. "Simulation of particle flows and breakage in crushers using DEM: Part 1 – Compression crushers". In: *Minerals Engineering* 74 (2015), pp. 178–197. ISSN: 08926875. DOI: 10.1016/j.mineng.2014.10.021.

[242] Delaney, G. W. et al. "DEM modelling of non-spherical particle breakage and flow in an industrial scale cone crusher". In: *Minerals Engineering* 74 (2015), pp. 112–122. ISSN: 08926875. DOI: 10.1016/j.mineng.2015.01.013.

[243] Sloane, N. "The proof of the packing". In: *Nature* 425.6954 (2003), pp. 126–127. ISSN: 0028-0836. DOI: 10.1038/425126c.

[244] Sousani, M. et al. "Simulation of Surface Damage and Body Breakage by using DEM". In: (2019).

[245] Tavares, L. M. and das Chagas, A. S. "A stochastic particle replacement strategy for simulating breakage in DEM". In: *Powder Technology* 377 (2021), pp. 222–232. ISSN: 00325910. DOI: 10.1016/j.powtec.2020.08.091.

[246] Altair Engineering Inc. *Tavares Breakage Model - Particle weakening & fragmentation*. 2020.

[247] Rocky DEM Inc. *Tavares Breakage Model in Rocky DEM*. 2018. URL: https://rocky.esss.co/blog/tavares-breakage-model-in-rocky-dem/.

[248] Potapov, A., Donohue, T., and Ilic, D. "Computer Simulation of Coal Breakage in Conveyor Transfer Chutes with ROCKY Discrete Element Method Package". In: *Rocky DEM Technical Articles* ().

[249] Flavio, A., Potapov, A., and Tavares, L. M. "Simulation of single particle breakage using non-round particles in ROCKY DEM". In: *26th International Mining Congress and Mining Exhibition of Turkey* (2019).

[250] Potapov, A. and CAMPBELL, C. S. "A three-dimensional simulation of brittle solid fracture". In: *International Journal of Modern Physics C* 07.05 (1996), pp. 717–729. ISSN: 0129-1831. DOI: 10.1142/S0129183196000594.

[251] Potapov, A. V. and CAMPBELL, C. S. "The breakage induced by a single grinding ball dropped onto a randomly packed particle bed". In: *Powder Technology* 107.1-2 (2000), pp. 108–117. ISSN: 00325910. DOI: 10.1016/S0032-5910(99)00177-1.

[252] Paluszny, A. et al. "A direct fragmentation method with Weibull function distribution of sizes based on finite- and discrete element simulations". In: *International Journal of Solids and Structures* 80 (2016), pp. 38–51. ISSN: 00207683. DOI: 10.1016/j.ijsolstr.2015.10.019.

[253] Lichter, J. et al. "New developments in cone crusher performance optimization". In: *Minerals Engineering* 22.7-8 (2009), pp. 613–617. ISSN: 08926875. DOI: 10.1016/j.mineng.2009.04.003.

[254] Herbst, J. A. and Potapov, A. V. "Making a Discrete Grain Breakage model practical for comminution equipment performance simulation". In: *Powder Technology* 143-144 (2004), pp. 144–150. ISSN: 00325910. DOI: 10.1016/j.powtec.2004.04.036.

[255] Potapov, A. et al. "A DEM-PBM fast breakage model for simulation of comminution processes". In: *Proc. Computational Modeling* (2007).

[256] Wejrzanowski, T. et al. "Structure of foams modeled by Laguerre–Voronoi tessellations". In: *Computational Materials Science* 67 (2013), pp. 216–221. ISSN: 09270256. DOI: 10.1016/j.commatsci.2012.08.046.

[257] Duan, Q. et al. "Inverting Laguerre Tessellations". In: *The Computer Journal* 57.9 (2014), pp. 1431–1440. ISSN: 0010-4620. DOI: 10.1093/comjnl/bxu029.

[258] Walton, O. R. and Braun, R. L. "Viscosity, granular–temperature, and stress calculations for shearing assemblies of inelastic, frictional disks". In: *Journal of Rheology* 30.5 (1986), pp. 949–980. ISSN: 0148-6055. DOI: 10.1122/1.549893.

[259] Rocky DEM Inc. *Rocky Software version 3.11*. 2015.

[260] Potapov, A. V. and CAMPBELL, C. S. "The two mechanisms of particle impact breakage and the velocity effect". In: *Powder Technology* 93.1 (1997), pp. 13–21. ISSN: 00325910. DOI: 10.1016/S0032-5910(97)03242-7.

[261] Petit, H. A., Potapov, A., and Tavares, L. M. "Simulation of breakage of iron ore pellets using the discrete breakage model". In: *17th European Symposium on Comminution & Classification (ESCC 2022)* (2022).

[262] Voronoi, G. "Nouvelles applications des paramètres continus à la théorie des formes quadratiques. Deuxième mémoire. Recherches sur les parallélloèdres primitifs". In: *Journal für die reine und angewandte Mathematik (Crelles Journal)* 1908.134 (1908), pp. 198–287. ISSN: 0075-4102. DOI: `10.1515/crll.1908.134.198`.

[263] Voronoi, G. "Nouvelles applications des paramètres continus à la théorie des formes quadratiques. Premier mémoire. Sur quelques propriétés des formes quadratiques positives parfaites". In: *Journal für die reine und angewandte Mathematik (Crelles Journal)* 1908.133 (1908), pp. 97–102. ISSN: 0075-4102. DOI: `10.1515/crll.1908.133.97`.

[264] Dirichlet, G. L. "Über die Reduktion der positiven quadratischen Formen mit drei unbestimmten ganzen Zahlen". In: *J. reine angew. Math.* 40 (1850), pp. 209–227.

[265] Burrough, P. A., McDonnell, R., and Lloyd, C. D. *Principles of geographical information systems.* 3. ed. Oxford: Oxford University Press, 2015. ISBN: 978-0-19-874284-5.

[266] Weisstein, E. W. *Voronoi Diagram.* URL: `https://mathworld.wolfram.com/VoronoiDiagram.html`.

[267] Aurenhammer, F. "Voronoi diagrams—a survey of a fundamental geometric data structure". In: *ACM Computing Surveys* 23.3 (1991), pp. 345–405. ISSN: 0360-0300. DOI: `10.1145/116873.116880`.

[268] Pimpinelli, A., Tumbek, L., and Winkler, A. "Scaling and Exponent Equalities in Island Nucleation: Novel Results and Application to Organic Films". In: *The journal of physical chemistry letters* 5.6 (2014), pp. 995–998. DOI: `10.1021/jz500282t`.

[269] Ramella, M. et al. "Finding galaxy clusters using Voronoi tessellations". In: *Astronomy & Astrophysics* 368.3 (2001), pp. 776–786. ISSN: 0004-6361. DOI: `10.1051/0004-6361:20010071`.

[270] Courrioux, G. et al. "3D volumetric modelling of Cadomian terranes (Northern Brittany, France): an automatic method using Voronoi diagrams". In: *Tectonophysics* 331.1-2 (2001), pp. 181–196. ISSN: 00401951. DOI: `10.1016/S0040-1951(00)00242-0`.

[271] Fiedler, F. R. "Simple, Practical Method for Determining Station Weights Using Thiessen Polygons and Isohyetal Maps". In: *Journal of Hydrologic Engineering* 8.4 (2003), pp. 219–221. ISSN: 1084-0699. DOI: `10.1061/(ASCE)1084-0699(2003)8:4(219)`.

[272] Gómez, S. et al. "Design and properties of 3D scaffolds for bone tissue engineering". In: *Acta biomaterialia* 42 (2016), pp. 341–350. DOI: 10.1016/j.actbio.2016.06.032.

[273] Bock, M. et al. "Generalized Voronoi Tessellation as a Model of Two-dimensional Cell Tissue Dynamics". In: (2009). DOI: 10.48550/arXiv.0901.4469.

[274] Sánchez-Gutiérrez, D. et al. "Fundamental physical cellular constraints drive self-organization of tissues". In: *The EMBO journal* 35.1 (2016), pp. 77–88. DOI: 10.15252/embj.201592374.

[275] Dierking, I., Flatley, A., and Greenhalgh, D. "Voronoi patterns in liquid crystal textures". In: *Journal of Molecular Liquids* 335 (2021), p. 116553. ISSN: 01677322. DOI: 10.1016/j.molliq.2021.116553.

[276] Pirstinger, P. "Optische Partikelvermessung". Bachelor thesis. University of Leoben, 2020.

[277] Prenner, M. "Simulationsparameterstudie - Sinterbunker (Simulation parameter study - Sinter bunkers)". Project report. University of Leoben, 2018.

[278] Mattathil, G. "Bruchverhalten spröder und poröser Materialien". Bachelor thesis. University of Leoben, 2020.

[279] Prenner, M. and Fritz, D. "Sinterbruchbestimmung". Projektbericht. Montanuniverstiät Leoben, 2019.

[280] Bradley, M. and Deng, T. "Determining and comparing breakage matrices to predict particle attrition in pneumatic conveyors". In: *CHoPS 2022 - 10th Conference on Conveying and Handling of Particulate Solids* (2022).

[281] Waidbacher, B. "Automatische Beschickung eines Prüfstandes für Hochofensinter (Automated particle feeding of a test rig for blast furnace sinter)". Master's Thesis. Leoben: University of Leoben, 2022.

[282] AVITEQ Vibrationstechnik GmbH. *AViTEQ Teileförderer*. 2020.

[283] Rohrbach, Z. J., Buresh, T. R., and Madsen, M. J. "Modeling the exit velocity of a compressed air cannon". In: *American Journal of Physics* 80.1 (2012), pp. 24–26. ISSN: 0002-9505. DOI: 10.1119/1.3644253.

[284] Faramarzi, F. et al. "The extended drop weight testing approach – What it reveals". In: *Minerals Engineering* 157 (2020), p. 106550. ISSN: 08926875. DOI: 10.1016/j.mineng.2020.106550.

[285] Steiner, G. "MEMS Accelerometers and their Application in Condition Monitoring". Bachelor thesis. University of Leoben, 2021.

[286] Andrews, W. *Arduino playground: Geeky projects for the experienced maker.* San Francisco: No Starch Press, 2017. ISBN: 159327744X.

[287] OriginLab Corporation. *Bigaussian Fit Function.* 14.11.2022. URL: `https://www.originlab.com/doc/Origin-Help/Bigaussian-PAFunc`.

[288] OriginLab Corporation. *BiHill Fit Function.* 14.11.2022. URL: `https://www.originlab.com/doc/Origin-Help/BiHill-FitFunc`.

[289] OriginLab Corporation. *Logistic Fit Function.* 14.11.2022. URL: `https://www.originlab.com/doc/origin-help/logistic-fitfunc`.

[290] OriginLab Corporation. *GaussMod Fit Function.* 14.11.2022. URL: `https://www.originlab.com/doc/Origin-Help/GaussMod-FitFunc`.

[291] Schubert, H. "Zu den Mikroprozessen des Zerkleinerns". In: *Aufbereitungstechnik* 28.5 (1987), pp. 237–246.

[292] Prenner, M. "Dynamische Übergabeschurre zur Effizienzsteigerung von Gurtbandförderern". In: *Berg- und huttenmannische Monatshefte* (2021), pp. 1–6. DOI: `10.1007/s00501-021-01084-4`.

[293] Dünnwald, W. and Prenner, M. "Vorrichtung zum Leiten eines von einem Abwurfende oder Austragsende einer Fördereinrichtung abfließenden Materialstroms (Device for guiding a material flow flowing out from a discharge end or delivery end of a conveying apparatus). Patentnr. DE 10 2019 108 687 A1. Deutschland". 2019.

[294] Wagner, P. "Vergleich zweier Übergabeeinrichtungen in Bezug auf Partikelbruch (Comparison of two transfer systems with regard to particle breakage)". Master's Thesis. University of Leoben, 2022.

[295] Brugger, M. "Rücksprungverhalten von Hochofensinter (Rebound behaviour of blast furnace sinter)". Bachelor Thesis. University of Leoben, 2021.

[296] Kogler, P. "Analyse von Kontaktvorgängen und Optimierung von fördertechnischen Anlagen hinsichtlich Partikelbruchs bei Sinter". Masterarbeit. Montanuniversität Leoben, 2020.

[297] Brenner, F. "Optimierung einer Schurre für Hochofensinter mittels DEM". Bachelor Thesis. University of Leoben, 2023.

[298] Albertin, G. *Piecewise linear least square fit.* 2013. URL: `https://www.mathworks.com/matlabcentral/fileexchange/40913-piecewise-linear-least-square-fit`.

[299]   Barrios, G. K. et al. "Contact parameter estimation for DEM simulation of iron ore pellet handling". In: *Powder Technology* 248 (2013), pp. 84–93. ISSN: 00325910. DOI: `10.1016/j.powtec.2013.01.063`.

[300]   Li, C. et al. "Experimental Study on the Physical Properties of Iron Ore Granules Made from Australian Iron Ores". In: *ISIJ International* 59.2 (2019), pp. 253–262. ISSN: 0915-1559. DOI: `10.2355/isijinternational.ISIJINT-2018-508`.

[301]   Zhao, S., Evans, T. M., and Zhou, X. "Effects of curvature-related DEM contact model on the macro- and micro-mechanical behaviours of granular soils". In: *Géotechnique* 68.12 (2018), pp. 1085–1098. ISSN: 0016-8505. DOI: `10.1680/jgeot.17.P.158`.

[302]   Becker, A. *Discrete Element Method (Becker3D)*. 2022.

[303]   Matsumoto, M. and Nishimura, T. "Mersenne twister. A 623-dimensionally equidistributed uniform pseudorandom number generator". In: *ACM Transactions on Modeling and Computer Simulation* 8 (1998), pp. 3–30.

[304]   Grübler, C. "Evaluierung ausgewählter passiver staubreduktionsmaßnahmen beim Schüttgutumschlag an fördertechnischen Anlagen (Evaluation of passive dust reducing measures at bulk material handling on conveying equipment)". PhD Thesis. Leoben: University of Leoben, 2020.

[305]   Prenner, M. "Solid state material driven turbine: International Patent F03G3/02 F03G3/04". WO 2013/083303 A1. 2013.

[306]   Prenner, M. "Feststoffturbine zur Energierückgewinnung in Kombination mit Gurtförderanlagen". In: *BHM Berg- und Hüttenmännische Monatshefte* 160.1 (2015), pp. 21–31. ISSN: 0005-8912. DOI: `10.1007/s00501-014-0327-0`.

[307]   Prenner, M., Grübler, C., and Zeiler, S. "Vorteile von Feststoffturbinen". In: *Schüttgut* 5 (2018), pp. 68–72.

[308]   Prenner, M. "Energy Recovering System for Moving Bulk Materials". In: *Earth Sciences* 8.1 (2019), p. 20. ISSN: 2328-5974. DOI: `10.11648/j.earth.20190801.13`.

[309]   Nohl, J. and Domnick, B. "Stockpile Segregation: Technical Paper T - 551". In: *Superior Industries* (2000).